



HAL
open science

Advanced Numerical Methods for Nonlinear Water Wave dynamics and Breaking in Boussinesq-type models

Maria Kazolea

► **To cite this version:**

Maria Kazolea. Advanced Numerical Methods for Nonlinear Water Wave dynamics and Breaking in Boussinesq-type models. Numerical Analysis [math.NA]. Université de Bordeaux, 2024. tel-04724479

HAL Id: tel-04724479

<https://hal.science/tel-04724479v1>

Submitted on 7 Oct 2024

HAL is a multi-disciplinary open access archive for the deposit and dissemination of scientific research documents, whether they are published or not. The documents may come from teaching and research institutions in France or abroad, or from public or private research centers.

L'archive ouverte pluridisciplinaire **HAL**, est destinée au dépôt et à la diffusion de documents scientifiques de niveau recherche, publiés ou non, émanant des établissements d'enseignement et de recherche français ou étrangers, des laboratoires publics ou privés.

Habilitation à Diriger des Recherches
Mathématiques appliquées et Calcul Scientifique
Université de Bordeaux

Advanced Numerical Methods for Nonlinear Water Wave Dynamics and Breaking in Boussinesq-Type Models

by

Maria KAZOLEA

HDR Committee:

HDR	Michel Benoit	Reviewer
Prof.	Maurizio Brocchini	Jury
Prof.	Frederic Dias	Reviewer
Prof.	Pilar García-Navarro	Jury
Prof.	James Kirby	Reviewer
Prof.	Volker Roeber	Jury
HDR	Mario Ricchiuto	Garant
HDR	Marissa Yates	Jury

October 3, 2024

To the memory of my beloved mother.

Acknowledgements

I would like to express my deepest gratitude to the reviewers and members of this committee for accepting my invitation.

My sincere thanks to Dr. Mario Ricchiuto for the countless discussions on the whiteboard and for the absolute pleasure of working with him. His guidance and insight have been instrumental to my research journey.

I am deeply grateful to my colleagues at Inria at the University of Bordeaux, with whom I have had the pleasure of working over the past ten years. Special thanks to Andrea Filippini, Luca Arpaia, Ralph Lteif, Subodh Joshi and Martin Parisot for their contributions and friendship. I also express my gratitude to all members of the Cardamom team for their unwavering support and for the unforgettable moments we have shared.

Finally, I owe my deepest gratitude to my family. To my husband, Nikos, and my two children, Akis and Giorgos, your love and support have been my foundation. I would not be here without you.

Contents

0.1	My contributions	1
1	Weakly dispersive Boussinesq-type models	7
1.1	Weakly dispersive Boussinesq PDE models	8
1.1.1	Weakly nonlinear BT equations	9
1.1.2	Fully nonlinear BT modelling: the enhanced Green-Naghdi equations	10
1.1.3	A summary on the model properties	12
1.2	One dimensional benchmarks	17
1.3	Two dimensional benchmarks	30
1.4	Summary	34
2	Numerical methods in 1D	41
2.1	A scheme for the fully nonlinear weakly dispersive model	42
2.1.1	Mathematical Formulation	42
2.1.2	Discretization strategy : elliptic-hyperbolic decoupling	43
2.1.3	Spatial domain discretization and notation	44
2.1.4	Elliptic phase : continuous finite element formulation	44
2.1.5	Hyperbolic phase : Finite Volume Scheme	46
2.1.6	Hyperbolic phase : Finite Element Scheme	48
2.1.7	Well-balancing, wet/dry front treatment, mass conservation	50
2.2	Time integration, boundary conditions, and friction	51
2.2.1	High order time integration methods	51
2.2.2	Boundary conditions and internal source function	52
2.2.3	Friction terms discretization	53
2.3	Semi-discrete error analyses	54
2.3.1	Time continuous analysis	54
2.4	Numerical tests and results	59
2.4.1	Space-time grid convergence	60
2.4.2	Influence of mesh regularity	61
2.4.3	Solitary wave on a composite beach	62
2.5	Summary	63

3	A numerical method in 2D	65
3.1	Solution strategy and geometrical notation	66
3.2	Hyperbolic step: third order FV scheme and derivatives recovery via successive corrections	67
3.2.1	Polynomial expansion and derivative reconstruction via successive corrections	68
3.2.2	Numerical verification for smooth and non-smooth flows	71
3.3	Finite element solver for dispersive effects	73
3.4	Finite element/volume coupling: consistency and well-posedness considerations . .	75
3.4.1	Consistency: using FV data in the FE solver and vice-versa	75
3.4.2	A comment on well-posedness	77
3.5	Stability and dissipation	80
3.6	Boundary conditions and wave generation	82
3.7	Numerical validation and benchmarking	83
3.7.1	Grid convergence for the solitary wave	83
3.7.2	Circular shoal	83
3.7.3	Elliptic shoal	85
3.7.4	Solitary interacting with a cylinder	88
3.7.5	Solitary wave breaking on a 3D reef	89
3.8	Summary	91
4	Wave breaking closures for BT models	95
4.1	Wave breaking closures: a summary	95
4.1.1	Trigger mechanism	99
4.1.2	Hybrid wave breaking model	100
4.1.3	Eddy viscosity closure via a PDE based TKE model	101
4.2	Discussion on the dissipation mechanisms	104
4.3	Numerical results	106
4.3.1	Wave breaking over a bar	106
4.3.2	Solitary waves breaking on a slope	111
4.3.3	Bore propagation and dissipation in function of the Froude number	117
4.3.4	Wave height and setup prediction	120
4.3.5	Application: propagation, breaking, and overtopping of a 2D reef	123
4.4	Parameter sensitivity analysis of selected wave breaking closures	125
4.4.1	Sensitivity Analysis Model	127
4.4.2	Case study: propagation, breaking and runup of a solitary wave	129
4.4.3	Parameter sensitivity analysis	131
4.5	Summary	141
5	Conclusions and future work	145
5.1	Conclusion	145
5.2	Current activity and future work	146

5.2.1	Coupling methods of phase-resolving coastal wave models	146
5.2.2	IMEX schemes for low Froude numbers	149
5.2.3	Discrete well balanced schemes for hyperbolic equations	150
5.2.4	On the design of an improved Boussinesq model for real applications: equilibrium between accuracy and performances	150
5.2.5	European project RESCUER HORIZON-MSCA-2022-DN 101119437 . . .	152
5.2.6	Comparison of different numerical schemes for dispersive flows in real case scenarios	153
5.2.7	Adaptive meshes for tsunami simulations	154
5.2.8	Tidal bore and bathymetry	154
5.2.9	Modeling of wave dispersion including porosity	155

Introduction

My scientific interest lies in the field of applied mathematics and specifically in scientific computation. I work on the creation and improvement of numerical schemes for free surface flow problems. I am also interested in the interaction of numerical schemes with the selected asymptotic mathematical models.

My activity on the topic started as graduate student when I was working on my master thesis and I started studying the nonlinear shallow water equations [63] for the first time. We numerically studied the propagation, run-up and rundown of long surface waves in one and two horizontal dimensions (1HD and 2HD respectively), and the simulation of waves formed by sliding masses using a finite volume (FV) scheme for the nonlinear shallow water equations [62].

During my phd studies we developed and compared two numerical schemes for the solution of the nonlinear shallow water equations (NSWE) on unstructured meshes. A node centered FV scheme (NCFV) and a cell centered FV scheme (CCFV) which are both second order in space and time [65]. At the same time I familiarized myself with the family of asymptotic models [72, 157] and developed a well balanced shock-capturing hybrid FV-Finite Difference (FD) scheme for two extended Boussinesq-type (BT) models in one horizontal direction (1HD) [135]. A follow up is the implementation of an unstructured, higher order, FV numerical scheme for a set of two horizontal dimensions (2HD) BT equations [136] and its numerical treatment when wave breaking occurs [137].

This manuscript presents the core of my scientific activity on numerical schemes for depth averaged models and beyond, after I joined the Inria research center at the University of Bordeaux. Section 0.1 attempts to put my work into context and give a summary of my contributions.

0.1 My contributions

My work over the last ten years can be divided into three main categories:

1. **Study of depth-averaged asymptotic models**
2. **Development of numerical schemes in one and two horizontal dimensions (1HD and 2HD respectively)**
3. **Study of wave breaking for Boussinesq-type models**

The reader can find below a summary of my contributions in the field of nonlinear water wave dynamics in BT models. I owe a big part of these to my colleagues, especially to **Mario Ricchiuto** at Inria of the University of Bordeaux, **Andrea Filippini** at BRGM, **Luca Arpaia** at CNR ISMAR (National Institute of Marine Sciences), Venice, **Subodh Joshi** Shell Technology Center, Bangalore, **Nghi Vu Van** at Ho Chi Minh City University Of Transport in Vietnam and **Paola Bacigaluppi** at Dept. of Civil, Environmental and Geomatic Engineering ETH.

Study of depth-averaged asymptotic modes. The first part, the most recent, comes from the experience I gained over the last ten years working in the Cardamon team at Inria of the University of Bordeaux. Recently in [146] we went back to the fundamental question of whether full nonlinearity in weakly dispersive BT models is a necessity. We reconsidered the tests first used in the literature to address this issue, as well as a number of more demanding issues. We also consider different families of weakly nonlinear BT models, with different shoaling characteristics, especially when nonlinear waves are involved. Our study allows us to point out that for many cases, it is quite hard to conclude whether full nonlinearity is really necessary. There are a few discriminant cases, which are unfortunately not those mostly used in the literature proposing new models or new numerical methods. Two main conclusions can be extracted from this work:

- Benchmarking habits for BT models need to be slightly revised and
- Fully nonlinear models allow us to safely approach problems of different natures and involving highly nonlinear waves. As a rule of thumb, weakly nonlinear models can still be safely used in many problems of practical interest not involving planar nonbreaking wavefronts reflecting on steep coastal structures in deep waters. This is true even for the quite complex urban runup of nonlinear waves.

Numerical schemes for BT models. I have also worked on the implementation of numerical schemes for depth-averaged models in 1HD and 2HD, see for example [97, 138, 92]. The depth-averaged models used, are the enhanced fully non linear weakly dispersive equations of Green-Nagdhi [157] but the schemes proposed can be extend to other weakly nonlinear models, see for example [135], that can be written in a pseudo balanced law form.

The procedure that we follow is a two-step solution composed of a first step where the non-hydrostatic source terms is recovered by inverting the elliptic coercive operator associated to the dispersive effects; a second step which involves the solution of the hyperbolic shallow water system with the source term, computed in the previous phase, which accounts for the non-hydrostatic effects. In this hybrid approach we combine a finite volume (FV) and a finite element (FE) method. The FV method is used to solve the underlying hyperbolic shallow water system, while a standard P^1 finite element method is used to solve the elliptic system associated to the dispersive correction. Of course this is not restrictive and other methods can be used see for example [136, 135, 91]. The most important contributions from these works that we can highlight are:

- We demonstrate the potentially catastrophic results that can occur if one is unaware of the interaction between modeling errors and discretization errors when discretizing BT models. The usage of lower order scheme in space and time can create terms that will significantly affect the dispersion error of your asymptotic model. In other words special attention has to be given to the study of interaction of the error of the scheme and the error of the model.
- The elliptic component has to be discretized with at least a second order method.
- In 2HD on unstructured meshes, when a FV scheme is used in the hyperbolic part and continuous FE in the elliptic part, we must be very careful with the representation of the data and how to handle the incomplete norm that is generated by the variational formulation.

Wave breaking and applications of the BT models. An other part that i have also worked on is the simulation of wave breaking when using BT equations. More precisely during my years in the Cardamom team we attempted to deepen the understanding of the sensitivity of two wave breaking closures. The hybrid, and an eddy viscosity closure that involves a partial differential equation for the main physical quantities (TKE).

The hybrid is one of the most used wave breaking closure in the last fifteen years. This approach is based on a local coupling of the dispersive propagation model with the shallow water equations. It is a simple method in which one first detects breaking regions, and in these the dispersive terms are suppressed. In these breaking regions thus one solves the non-linear shallow water (NSW) equations which allow to model a breaker as a shock. Through this discontinuity mass and momentum are conserved, while total energy is dissipated, thus modeling the energy dissipation due to breaking.

The starting point of this part of my work has been that this technique has a major limitation in the stability of the coupling which introduces spurious oscillations at the interface between the breaking and the non breaking region (see chapter 5 for details). The objective of my work [145] was to study the sensitivity of the two wave breaking closures with respect to the mesh size and with attention to the possibility of obtaining grid independent results. An other objective was to provide some understanding of the sensitivity of this dissipation to the mesh size. We tried to gain an insight into the mechanism actually responsible for wave breaking by providing a quantitative description of the different contributions to the dissipation mechanism, differentiating those associated to the numerical scheme from those introduced at the PDE level. Finally we showed equal capabilities of the approaches studied in reproducing simple as well as complex transformations, while showing the substantial difference in the underling dissipation mechanisms.

A follow up section of this work was to study the sensitivity of wave breaking simulation to the variation of the parameters used from the triggering conditions and the breaking models themselves [129, 142]. Both of them use case depended/ad/hoc parameters which affect the numerical solution while changing. We used the sensitivity indices computed by means of analysis of variance to provide the sensitivity of wave breaking simulation to the variation of breaking parameters. As a result we can safely say that

- Both approaches allow to describe correctly wave transformation and breaking at large scales (at least with a rather standard implementation).
- When using the eddy viscosity approach the numerical dissipation plays a negligible role. This motivates the look for non-dissipative/energy conserving numerical methods.
- We gave some insights into physics of non-linear and dispersive waves, specifically during the breaking and the run-up phases.
- The analysis quantitatively distinguishes between the two prominent approaches for modeling the breaking of the waves, viz., the hybrid method and the TKE model for wave breaking.
- The eddy viscosity approach clearly shows a reduced sensitivity to the mesh compared to the hybrid one.

The problem of oscillations appearing in the hybrid wave breaking closure inspired the work on coupling methods for phase-resolving coastal wave models, with some initial results are discussed in [102] and chapter 5.

In the framework of the French research project TANDEM, dedicated to tsunami modeling, a series of benchmarks has been set up, addressing the various stages of a tsunami event: generation, propagation, run-up and inundation. We presented in [141] the results of five codes involving both depth-averaged Boussinesq and fully 3D Navier-Stokes equations, aimed at being applicable to tsunami modeling. The codes are evaluated on a flow involving propagation, run-up, overtopping and reflection of the waves on two-dimensional reefs, and compared with the experimental data produced from a set of laboratory experiments [228]. We also presented some representative test cases in which we compared different numerical codes to identify the strengths and weaknesses of the models [258]. These benchmarking test cases are part of a database built from existing literature, with validation data from reference simulations, theoretical solutions, or lab experiments. They cover the main stages of a tsunami's life: 1) generation, 2) propagation, 3) run-up and submersion, and 4) impact.

In the same spirit, but with greater emphasis on the context of applications in [143] we presented a numerical study of long wave conditions, in the old Venetian port of Chania (in the island of Crete, Greece) using two different BT models. The two models are used to determine the resonant frequencies, amplitudes and modes of the entire harbor basin.

The manuscript is organized according these outlined divisions: Chapter 1 introduces various weakly dispersive BT models in a pseudo-conservative form. These models are tested using the most classical benchmarking cases available in the literature. Specifically, we examine models with different nonlinear properties. After a brief analysis of their linear and nonlinear characteristics, we compare them to assess the necessity of fully nonlinear models. All of the results are mesh independent solutions obtained by numerical schemes under the same set of reference. The proposed numerical scheme for the fully nonlinear equations in 1HD (but also similar for the other models) is introduced in Chapter 2 while Chapter 3 outlines its extension to 2HD. Each chapter highlights

numerical difficulties and challenges associated to the models and the schemes. Chapter 4 is dedicated to wave breaking for BT models and outlines a sensitivity analysis of different wave breaking closures both for weakly and fully nonlinear BT models. Finally in chapter 5 my current and future activity is discussed.

Chapter 1

Weakly dispersive Boussinesq-type models

No one can dispute the importance of the Boussinesq-type (BT) models in coastal engineering. In the last 50 years, significant developments have been achieved both at the level of modeling, as well as in the development of related numerical methods. BT models are depth-integrated, phase resolving models for surface wave propagation. Two main parameters characterize them. The first is the dispersion parameter μ , which is the ratio of the reference water depth d over the characteristic wavelength L . The second is the non dimensional parameter ϵ , defined as the ratio of the characteristic wave amplitude α_0 over d . Very long waves are characterized by negligible values of μ^2 . In this case, the well known system of shallow water, or Saint-Venant, equations are recovered. In near shore applications, involving wave transformations and their impact in coastal structures, the most widely used models are the so-called weakly-dispersive, obtained for $\mu^2 \ll 1$, and neglecting all effects of order $O(\mu^4)$. This chapter focuses on this class of Boussinesq models. Note that all these PDE systems involve weak dispersive perturbations of the shallow water equations, and usually involve the inversion of an elliptic operator in the time advancement of the depth averaged velocity.

Within weakly dispersive BT equations, we further distinguish two important sub-families. Weakly nonlinear Boussinesq models are obtained assuming that $\epsilon \approx O(\mu^2)$, which allows to neglect all effects of order $O(\mu^4, \epsilon\mu^2)$. This Ansatz results in PDE systems which can be written as the nonlinear shallow water equations with a linear dispersive perturbation. The linearity of the dispersive operator results, in time independence of the elliptic equation.

A large number of the best known models in the coastal engineering community belong to this class. For example, the simple model of Boussinesq [29] and Peregrine's [212] equations. Peregrine's equations, so called the standard Boussinesq equations, written in terms of depth averaged velocity are limited to relatively shallow water. Approximately up to when depth is greater than one fifth of the equivalent deep water wavelength. During the 90's considerable effort has been made to extend the validity and the applicability of the standard Boussinesq equations to deeper waters (or shorter waves). For example the enhanced models by Nwogu [198], Madsen and Sorensen [177] or Beji and Nadaoka [15]. These extended models provide a more accurate representation of phase and group velocities in intermediate water, with a water depth to wavelength ratio of up to 1/2. They are sometimes referred to as low-order enhanced Boussinesq-type equations.

The linear character of the dispersive operator, of these models, translates in its time independent nature which allows efficient implementation strategies for its inversion [222].

There exist a number of known codes implementing these models, e.g., BOUSS-2D by the US Army [197], DHI's commercial platform MIKE21 [70], the code BOSZ initially developed at U. of Hawaii [227], or the more recent open source platform CELERIS [247, 248].

The BT models obtained assuming that $\epsilon = O(1)$ are referred to as fully nonlinear. In this case the depth averaged equations involve a strongly nonlinear dispersive operator, making the associated numerical resolution inherently more expensive. However, this choice is without doubt physically more relevant, and provides the well known models of Serre [231], Green-Naghdi [109], and enhanced variants discussed e.g., in [270], [51], [176], [155],[50], or [59]. A model of this type is implemented in many operational codes among which the most well known are probably FUNWAVE [234, 235, 185], Coulwave [172] and UHAINA [91], but similar models have been implemented in other platforms as the open source projects Basilisk [169], among others.

Note that other parameters may be introduced to characterize depth averaged equations in terms of mild (or not) slope, presence (or not) of surface tension effects etc. For an extensive review on the BT models we refer to [158, 150, 36]. In this work, we will limit our study to the impact of full/weak non-linearity.

As already mentioned, fully nonlinear models are more complex than weakly nonlinear, and require the inversion of a nonlinear, and thus time dependent, elliptic operator at every time step. The natural question arising in this case is whether this additional complexity and computational cost is necessary. Many think that this issue is fully answered in the landmark paper by Wei et al. [270] which concludes that full non-linearity is absolutely necessary to correctly predict water depths. Yet, the literature is still filled with simulations using weakly nonlinear models, showing accurate predictions of wave height and phase, for now almost standard cases, in both small amplitude and configurations close to/or of incipient breaking.

In this chapter, we go back to the question of whether full non-linearity in weakly dispersive BT models is a necessity. We re-consider the tests by [270], as well as a number of more demanding results. We also consider different families of weakly nonlinear BT models, with different shoaling characteristics. As demonstrated, for many cases it is quite hard to conclude in favor of one class of model or another. There are, however, a few discriminant cases in which the water depth predictions are negatively affected by the lack of full non-linearity. However, these cases are rarely used in the literature proposing new numerical methods or, more importantly, dispersive PDE models.

1.1 Weakly dispersive Boussinesq PDE models

In this section we briefly describe the Boussinesq systems used in this work, and recall some of their significant properties. As mentioned in the introduction, the BT models derived since the 1990 are numerous. In this work we use some of the most well known among these.

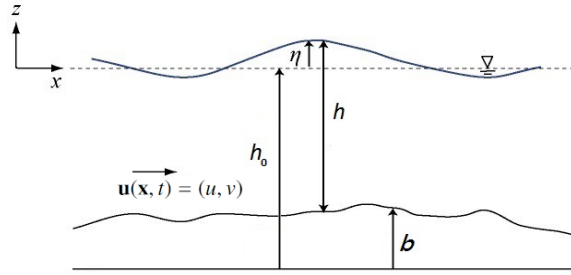


Figure 1.1: Description of the free surface flow problem and main notation.

1.1.1 Weakly nonlinear BT equations

Among the weakly nonlinear models these of Madsen and Sørensen [179, 178] and Nwogu's [198] are two typical and widely used. The two have quite comparable linear dispersion properties, but different shoaling characteristics. For this reason, we also consider the model Nwogu-Abbott introduced in [95], which has the exact same linear properties of the Nwogu equations, but is only equal to the latter within an $\mathcal{O}(\epsilon\mu^2, \mu^4)$ correction allowing to write all the dispersive terms using derivatives of the volume flux rather than of the velocity. As shown in [95], this leads to a system which behaves like Nwogu's for small amplitude waves, but much closer to that one of Madsen and Sørensen in more nonlinear regimes.

All these models are written in a pseudo balanced law form:

$$\begin{aligned} h_t + \nabla \cdot \mathbf{q} &= D_h \\ \mathbf{U}_t + \nabla \cdot (\mathbf{u} \otimes \mathbf{q}) + gh\nabla\eta + c_f(h, \mathbf{q})\mathbf{q} &= \mathbf{D}_q \end{aligned} \quad \text{on } \Omega \times [0, t] \subset \mathbb{R}^2 \times \mathbb{R}^+ \quad (1.1)$$

where h is the total water depth and \mathbf{q} the volume flux $h\mathbf{u}$, with \mathbf{u} as the depth averaged velocity. The free surface is denoted here by $\eta = h + b$ with $b(x, y)$ the topography sources. The friction term $c_f\mathbf{q}$ in this work is approximated with the usual Manning law $c_f = gn_M^2\|\mathbf{u}\|/h^{4/3}$ with n_M as the Manning coefficient. We note that all the dispersive terms are on the right hand sides of (1.1). The definition of D_h , of \mathbf{D}_q , and of the pseud-momentum variables \mathbf{U} allows to distinguish between different models.

The equations of Madsen and Sørensen This system is a dispersion-enhanced variant of the Abbott equations, which are an equivalent of Peregrine's [212] within an $\mathcal{O}(\epsilon\mu^2, \mu^4)$ correction, allowing to write all the dispersive terms using derivatives of the volume flux rather than of the velocity [95]. In two space dimensions, the equations are obtained from (1.1) setting $D_h = 0$, and

$$\mathbf{D}_q = Bgd^2\nabla\nabla \cdot (d\nabla\eta) \quad (1.2)$$

where $d = d(x, y) = h_0 - b(x, y)$ is the still water depth. The momentum variable is defined by

$$\begin{aligned} \mathbf{U} &= \mathbf{q} - \left(B + \frac{1}{3} \right) d^2 \nabla (\nabla \cdot \mathbf{q}) - \\ &- d \left[\frac{1}{3} (\nabla d \otimes \nabla \mathbf{q}) + \frac{1}{6} (\nabla d \otimes (\nabla \mathbf{q})^\perp) - \frac{1}{6} ((\nabla d)^\perp \otimes \nabla \mathbf{q}) \right]. \end{aligned} \quad (1.3)$$

The value of $B = 1/15$ is that for which the phase relation of the system matches a second-order Padé approximation of the exact phase of the Euler equations [179].

The equations of Nwogu Introduced in [198] this BT model is obtained from Peregrine's by replacing the depth averaged velocity with a velocity at an arbitrary distance from the still water level z_θ . The value $z_\theta = -0.531d$ is the one that optimizes the dispersion relation of the system with respect to the Euler equations. The model is defined as in (1.1) with

$$D_h = -\nabla \cdot \left[\left(\frac{z_\theta^2}{2} - \frac{d^2}{6} \right) d \nabla (\nabla \cdot \mathbf{u}) + \left(z_\theta + \frac{d}{2} \right) d \nabla [\nabla \cdot (d\mathbf{u})] \right], \quad (1.4)$$

$$\mathbf{D}_q = -\mathbf{u} D_h + h_t \frac{z_\theta^2}{2} \nabla (\nabla \cdot \mathbf{u}) + h_t z_\theta \nabla (\nabla \cdot d\mathbf{u}) \quad \text{and} \quad (1.5)$$

$$\mathbf{U} = \mathbf{q} + h \left[\frac{z_\theta^2}{2} \nabla (\nabla \cdot \mathbf{u}) + z_\theta \nabla (\nabla \cdot d\mathbf{u}) \right]. \quad (1.6)$$

The equations of Nwogu-Abbott These equations are derived starting from these of Nwogu and in the aim to find an asymptotically equivalent system in an amplitude-volume flux form, which degenerates to the same linearized equations of [198]. This derivation, as described in [95], involves incorporating correction terms of order $\mathcal{O}(\epsilon\mu^2, \mu^4)$ to transition from derivatives of $d\mathbf{u}$ to derivatives of \mathbf{q} . In this case, the equations are written as in (1.1) but now we have $\mathbf{D}_q = 0$ thus:

$$D_h = -\nabla \cdot \left[\left(\frac{z_\theta^2}{2} - \frac{d^2}{6} \right) d \nabla \nabla \cdot \left(\frac{\mathbf{q}}{d} \right) + \left(z_\theta + \frac{d}{2} \right) d \nabla \nabla \cdot \mathbf{q} \right], \quad (1.7)$$

$$\mathbf{U} = \mathbf{q} + \frac{dz_\theta^2}{2} \nabla \left(\nabla \cdot \left(\frac{\mathbf{q}}{d} \right) \right) + dz_\theta \nabla (\nabla \cdot \mathbf{q}). \quad (1.8)$$

1.1.2 Fully nonlinear BT modelling: the enhanced Green-Naghdi equations

Maybe one of the most well know fully nonlinear Boussinesq models are the equations of [109]. The study of improved formulations of these equations and their numerical approximation has been the object of intense efforts in the past 15 years, one can refer e.g., to [26], [103], [190], [202], [159], [217], [59], [80], [164], [205], [158], [214], [250], [259], [47], [48] (and many others). Here we consider the enhanced equations in the form used in [97] and [138] reading as in (1.1) with $D_h = 0$, $\mathbf{U} = [h, \mathbf{q}]^T$ and

$$\mathbf{D}_q = \frac{gh\nabla\eta}{\alpha} + \Psi, \quad (1.9)$$

where Ψ is the solution of the elliptic problem

$$(I + \alpha T) \Psi = W - R. \quad (1.10)$$

We define

$$W = -\frac{gh}{\alpha}\nabla\eta \quad \text{and} \quad R = hQ\left(\frac{\mathbf{q}}{h}\right) \quad (1.11)$$

where the operators T , and Q are, respectively,

$$\begin{aligned} T(\cdot) &= -\frac{1}{3}\nabla\left(h^3\nabla\cdot\left(\frac{\cdot}{h}\right)\right) - \frac{h^2}{2}\left(\nabla\cdot\left(\frac{\cdot}{h}\right)\right)\nabla b + \frac{1}{2}\nabla\left(h^2\nabla b\cdot\left(\frac{\cdot}{h}\right)\right) + \\ &+ h\left(\nabla b\cdot\left(\frac{\cdot}{h}\right)\right)\nabla b, \end{aligned} \quad (1.12)$$

$$\begin{aligned} Q(\cdot) &= \frac{2}{3h}\nabla\left(h^3\left(\nabla(\cdot)_1\cdot\nabla^\perp(\cdot)_2 + (\nabla\cdot(\cdot))^2\right)\right) + \\ &+ h^2\left(\nabla(\cdot)_1\cdot\nabla^\perp(\cdot)_2 + (\nabla\cdot(\cdot))^2\right)\nabla b + \\ &+ \frac{1}{2h}\nabla\left(h^2\left((\cdot)\cdot\left((\cdot)\cdot\nabla\right)\nabla b\right)\right) + \left((\cdot)\cdot\left((\cdot)\cdot\nabla\right)\nabla b\right)\nabla b. \end{aligned} \quad (1.13)$$

$(\cdot)_1$ and $(\cdot)_2$ indicates respectively the first and second component of the vector (\cdot) and ∇^\perp states for the normal gradient operator. α is a parameter used to improve the dispersion properties of the model with respect to those of the full Euler equations. When the parameter a is set to the value of 1.159, it leads to the enhanced Green-Naghdi (eGN) model [155]. By setting $\alpha = 1$ we recover the classical Green-Naghdi equations. We write the operator T in such a way as to guarantee its inversion properties and the coercivity of the operator $(I + \alpha T)$, see [95] and [145] for further details.

The operator $T(\cdot)$ plays a key role, as its inversion is necessary to be able to obtain evolution equations for the physical variables. $T(\cdot)$ can be written in compact form involving two operators $S_1(\cdot)$, $S_2(\cdot)$ and their adjoints $S_1^*(\cdot)$, $S_2^*(\cdot)$, as:

$$T(\cdot) = S_1^*\left(hS_1\left(\frac{\cdot}{h}\right)\right) + S_2^*\left(hS_2\left(\frac{\cdot}{h}\right)\right) \quad (1.14)$$

where

$$S_1(\cdot) = \frac{h}{\sqrt{3}}\nabla\cdot(\cdot) - \frac{\sqrt{3}}{2}\nabla b\cdot(\cdot), \quad S_2 = \frac{1}{2}\nabla b\cdot(\cdot). \quad (1.15)$$

Note that this formulation is essential to show the coercivity of the operator $(I + \alpha T)$, see [97] and referenced therein for further details.

The linear dispersion and shoaling properties of the fully nonlinear GN and eGN models are comparable to those of the weakly nonlinear models of Peregrine and Madsen and Sorensen respectively. The latter are extensively described in [93]. On the other hand, the nonlinear shoaling properties of a weakly/strongly nonlinear model is not easy to be examined analytically. As discussed in [93], one way to test the nonlinear shoaling properties of a model is by performing the test of Grilli et al. [110]. The test consists of a solitary wave with relative amplitude $\alpha/h_0 = 0.2m$, propagating on a water depth of $0.44m$ and shoaling on to a constant slope of $1 : 35$. Ten wave gauges have been placed along the flume to measure the free surface elevation. All of them are placed before the breaking point with the last one being the closest to the breaking point. Figure 1.2 compares the experimental

wave's envelope with the result performed by four weakly non-linear models: Peregrine (P) [212], Abbott (A) [1], Madsen and Sorensen (MS) [178] and the MSP system. The last one is a modified system of Peregrine's equations written in a wave amplitude-velocity form, see [93, 95] for further details. In this work, we performed the same test on the fully nonlinear GN and eGN models and we added the computed results on the figure. Our result has been obtained using the discretization method presented in this work and it is a grid convergent solution, such that the plotted curve can be seen as genuine representations of the behavior of the model. We can observe that as soon as the nonlinear effects dominate (this happens close the breaking region) the phenomenon is better reproduced by the fully nonlinear models and even better by the eGN equations used in this work.

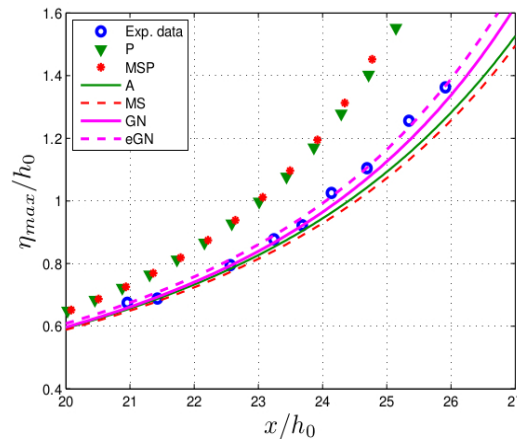


Figure 1.2: Wave envelope on the 9 gauges along the domain. Comparison between different weakly nonlinear models, GN, eGN and the experimental data. A-Abbot model, P-Peregrin model, MS-Madsen and Sorensen, MSP-Madsen and Sorensen in velocity form.

1.1.3 A summary on the model properties

Water waves transform in both phase and energy, due to shoaling, refraction, diffraction and reflection. The degree of refraction, diffraction and reflection depends on dispersion relation while the degree of shoaling mainly depends on the shoaling coefficient which in turns depends on the topography steepness. To highlight the fundamental properties of asymptotic mathematical models, such as those described in subsection 1.1, we turn our focus to the fully nonlinear weakly dispersive model of the GN equation. An analogous process can be applied to other Boussinesq-type (BT) models.

Linear Dispersion Properties

In the BT equations, linear dispersion properties are extracted by linearizing the model around a certain base state, typically the resting state. Linearization involves perturbing the equations about this state and analyzing the resulting linear system. The dispersion relation, governing the propagation of linear waves, can be derived from this linearized system. It characterizes the

relationship between wave frequency and wave number, thereby unveiling how waves of different wavelengths propagate through the medium. More precisely in 1HD, the linearized GN equations without topography terms read as:

$$\eta_t + du_x = 0 \quad (1.16)$$

$$du_t + gd\eta_x = \phi_l \quad (1.17)$$

$$(I + \alpha T_l) \phi_l = T_l(gd\eta_x) \quad (1.18)$$

where

$$T_l = \frac{1}{3}d^2(\cdot)_{xx}. \quad (1.19)$$

Using the above equality in 1.18 we get:

$$\left(I - \frac{\alpha}{3}d^2\partial_{xx}\right) \phi_l = -\frac{g}{3}d^3\eta_{xxx} \quad (1.20)$$

We introduce a solution $W = [h, hu]$ expressed in the form of a Fourier mode $W = \hat{W}e^{\nu t + jkx}$ with $\nu = \xi + j\omega$. ω denotes the phase of the mode, ξ represents the rate of amplification/damping and k is the wavenumber of the Fourier mode. Thus, the system becomes:

$$\nu\hat{\eta} + jkd\hat{u} = 0 \quad (1.21)$$

$$\nu\hat{u} + jkg\hat{\eta} = \frac{g}{3}jk^3d^2\hat{\eta} \left(1 + \frac{\alpha}{3}d^2k^2\right)^{-1}. \quad (1.22)$$

The characteristic polynomial associated with the system's matrix is

$$\nu^2 - (jk)^2gd + \frac{g}{3}(jk)^2k^2d^3 \left(1 + \frac{\alpha}{3}d^2k^2\right)^{-1} = 0 \quad (1.23)$$

and after some calculus we obtain from the imaginary part of 1.23 that $\xi = 0$ and from the real part that

$$\omega_{eGN}^2 = gdk^2 \frac{\left(1 + \frac{\alpha-1}{3}k^2d^2\right)}{1 + \frac{\alpha}{3}k^3d^2}. \quad (1.24)$$

$\alpha = 1.159$ is the indicated value [155] that optimizes the above relation with respect to the Airy theory. The linear dispersion relation for the nominal values of the models' constants proposed in literature is reported on the left picture on 1.3a. In the classical near-shore window of values $kd \in [0, \pi]$, all models provide errors below 2% wrt the Airy theory [239]. We highlight that the Nwogu and Nwogu-Abbott models have the same linearized form, so the same phase relation. The usual choice of parameters provides a monotone relation only for the MS and GN model. The Nwogu and eGN equations pass from phase lag to phase advance when going from long to short waves, the crossing taking place within the frequency window considered for the Nwogu model.

Linear Shoaling Properties

Linear shoaling properties concern the behavior of linear waves as they encounter variations in water depth. Using again the linearized eGN equation, we can investigate wave shoaling by introducing

a slowly depth-varying profile, $b = b(x)$. Higher order derivatives of the bathymetry are neglected. Analyzing how the linearized waves evolve as they propagate into shallower regions provides insights into how wave characteristics, such as amplitude and wavelength, change in response to varying bathymetry. As before we introduce to our system a solution of the form $\eta(x) = \alpha(x)e^{j(\omega t - \psi(x))}$ with $\psi_x = k(x)$ considering that $\alpha(x)$, $h(x)$ and $k(x)$ are slowly varying functions. Collecting the terms containing first order derivatives of α , k and h and after some algebraic manipulations we get:

$$\frac{\alpha_x}{\alpha} = -\mathcal{S} \frac{h_x}{h} \quad (1.25)$$

where \mathcal{S} is called the shoaling coefficient and is defined as:

$$\mathcal{S} = (\alpha_3 - \alpha_2\alpha_4)/\alpha_1. \quad (1.26)$$

For the eGN equations

$$\alpha_1 = 2 \left(1 - \frac{\alpha A}{3B} k^2 d^2 + \frac{4}{3} (\alpha - 1) k^4 d^4 \right), \quad (1.27)$$

$$\alpha_2 = 1 - \frac{\alpha A}{3B} k^2 d^2 + 2(\alpha - 1) k^4 d^4, \quad (1.28)$$

$$\alpha_3 = 1 - \alpha \frac{A}{B} k^2 d^2 + 2(\alpha - 1) k^4 d^4, \quad (1.29)$$

$$\alpha_4 = -\frac{1 - \Omega}{\Omega}, \quad (1.30)$$

with $A = 1 + \frac{\alpha-1}{3}$, $B = 1 + \frac{\alpha}{3}$ and $\Omega = 2(1 + \frac{\alpha-1}{3A} k^2 d^2 - \frac{\alpha}{3B} k^4 d^4)$.

The analysis, for different models, can be found in [178, 72] and more recently in [139] and [93]. Figure 1.3b presents graphically the value of \mathcal{S} for each model. The standard values for the MS equations are optimized in terms of linear shoaling, and this is clearly visible in the picture. In the linear case, the eGN shows an over shoaling behaviour for short waves, while the Nwogu and GN models under-predict the linear increase in height.

Nonlinear Dispersion

In an irregular sea state, waves of various frequencies interact, producing additional waves at combined frequencies, both sums and differences, due to the nonlinear dynamics at the water's surface. These interactions arise from the sea's nonlinear behavior near the surface. Both fully and weakly nonlinear BT equations are able to simulate the generation of the higher order forced waves. Following [198, 179] and having as a model the dimensionless eGN system [155], on a constant bathymetry, we introduce solutions of the form

$$\eta(x) = \alpha_1 \cos(\xi) + \epsilon \alpha_2 \cos(2\xi) \quad (1.31)$$

$$u(x) = u_1 \cos(\xi) + \epsilon u_2 \cos(2\xi) \quad (1.32)$$

where $\xi = \omega t - kx$ and all of the variables are written in a dimensionless form. We collect the terms of order $O(\epsilon)$, this leads

$$\begin{pmatrix} m_{11} & m_{12} \\ m_{21} & m_{22} \end{pmatrix} \begin{pmatrix} a_2 \\ u_2 \end{pmatrix} = \frac{a_1^2}{d} \begin{pmatrix} F_1 \\ F_2 \end{pmatrix} \quad (1.33)$$

where $m_{11} = 2\omega$, $m_{12} = -2kd$, $m_{21} = -2k + \frac{\mu^2}{6}16d^2k^3$, $m_{22} = 2\omega + \frac{8}{3}\mu^2\alpha d^2k^2\omega$, $F_1 = \omega$ and $F_2 = \frac{\omega^2}{2kd} + \frac{4}{3}\mu^2\alpha\omega^2dk - \frac{7}{3}\mu^2dk\omega^2 - 3d^2k^3 \left(\frac{\mu^2}{6}(1 - \alpha) \right)$. Using the dispersion relationship 1.24 we get the solution

$$a_2 = \frac{a_1^2}{d} \left(\frac{F_1 m_{22} - F_2 m_{12}}{m_{11} m_{22} - m_{21} m_{12}} \right). \quad (1.34)$$

The reference for a_2 is the Stokes second-order solution [72]

$$a_s^{Stokes} = \frac{1}{4} \frac{a_1^2}{d} \mu k d \coth(k\mu d) (3 \coth^2(k\mu d) - 1). \quad (1.35)$$

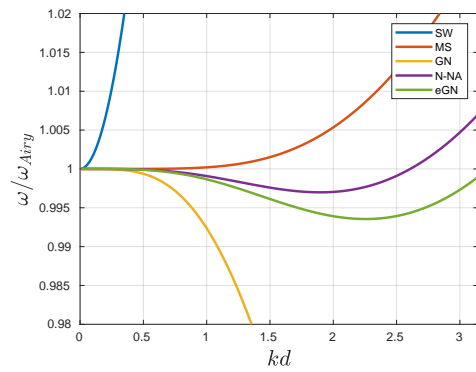
We also report at figure 1.3c, the amplification of second order Stokes-waves obtained with the second order analysis accounting for $\mathcal{O}(\epsilon)$ effects (see also [95]) for all the considered models. The plot shows that amplitudes are systematically under-predicted for the models in amplitude-flux form, and in particular for the MS and NA models considered here. When some non-linearity is accounted for the Nwogu model, an over-prediction in the amplitude occurs up to values $kd \approx 1.7$. The same holds true for all the well known amplitude-velocity models as shown in [95] and in contrast with what the linear shoaling shows. Clearly, this behaviour is not universal for BT models, which is also a part of the motivation of this work.

Numerical approximation, wet/dry treatment, and breaking closure

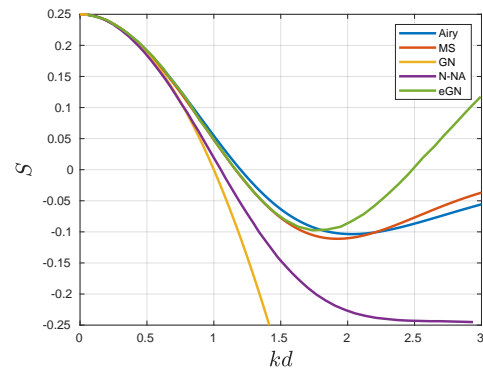
Numerical framework: The numerical discretization of the system (1.1) is performed on unstructured mesh discretizations of the physical domain, and brings together work from the present author and her collaborators in the past 10 years. A detailed description can be found in chapters 2 and 3 of this document.

It relies on two main components: a high-order node-centered finite volume solver and a nodal elliptic solver. The finite volume solver, detailed in [136], [97], and [138], evolves the vector $(h \ \mathbf{U})$ using Roe fluxes with modifications for wet/dry fronts and bathymetric source balance. Third-order accurate fluxes are obtained using quadratic polynomial reconstructions, based on either the classical MUSCL approach or a compact iterative Green-Gauss method [138]. Discontinuity capturing is achieved using limiters like van Albada or the high-order limiter from [188]. Time integration employs a third-order explicit Strong Stability Preserving Runge-Kutta method.

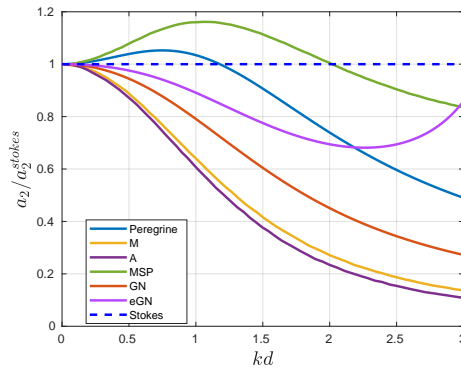
The elliptic systems are discretized with classical H^1 second order linear finite elements, stabilized by numerical dissipation in the fluxes, for the type of $Id - \text{grad div}$ PDE. Fully nonlinear models require time-dependent systems involving depth h , necessitating assembly and inversion at each time step, which is another computational overhead to account for full non-linearity. The appropriate



(a) Linear dispersion with respect to the one of the Airy theory



(b) Linear Shoaling properties



(c) Amplification of second order Stokes waves

Figure 1.3: Linear dispersion (a), linear shoaling (b), and nonlinear dispersion (c) for the models considered.

formulation of boundary condition for this step is an open research area, especially on non-straight boundaries. Usually ad-hoc techniques involving sponge layers, and internal wave generators are used in combination with simple treatments of the elliptic component. The interested reader can refer to [156], [133] and [196].

For a detailed description of the deduced numerical schemes, we refer to chapter 2 and 3 for 1HD and 2HD respectively. We would also like to stress that *unless otherwise specified, all results presented below are grid independent.*

Wet/dry transitions: In wet/dry fronts, special care needs to be taken into account to keep the well balancing of the scheme, and avoid the blow up of the velocities. This involves modifications to the states used to evaluate the numerical fluxes, as well as of the numerical gradient of the bathymetry, which are somewhat classical in the approximation of the shallow water equations. We refer to [43], [44], [136], [137], [219], [6].

For dispersive models, an important issue is related to the so-called "dispersive run-up/rundown". Weakly nonlinear models include in their dispersion operator the still water level $d(x, y)$, which is a somewhat problem dependent variable. Above the level $d = 0$, corresponding to the initial position of the shorelines, $d(x, y)$ becomes negative. In these regions the dispersive corrections do not have any meaning, so they are turned off. For cases involving moving waves interacting with shorelines, we can clearly see a different behaviour compared to the fully nonlinear GN model, for which dispersion depends on the local depth, and allows retaining the dispersive terms up to the current position of the wet/dry boundary. In contrast, the fully nonlinear GN model involves the actual depth h in the dispersive terms. These are in practice numerically limited only close to the current location of the wet/dry front, thus also computed in initially dry regions.

Wave breaking: Last but not least, an appropriate closure is required to account for the dissipation in breaking waves. There are many approaches to obtain such a closure. The interested reader is referred to [137] and [145]. Furthermore, Chapter 4 is devoted to our work on wave breaking for BT models. A wave breaking closure consists of two parts: a detection step and a dissipation mechanism. To obtain the results presented in this chapter, we use the simple, local, and robust detection criteria proposed in [137] and [97]. Concerning the dissipation mechanism, the results presented in 1.2 and 1.3 have been obtained with two approaches discussed in chapter 4 and can also be found in [145].

1.2 One dimensional benchmarks

Shoaling of a solitary wave

This is a benchmark used in two landmark papers [110, 270]. In the first the authors discuss comparisons between experimental data and a fully nonlinear/dispersive potential model. The second paper uses this benchmark to compare fully and weakly nonlinear variants of a Boussinesq

model, based on Nwogu's [198] equations, with the experimental and potential results. The benchmark setup is simple. The computational domain consists of a ramp of constant slope, whose toe is located at $x = 0$ m. The depth on the left of the ramp is $d = 0.44$ m. A solitary wave of amplitude $A = \epsilon d$ propagates and shoals on the ramp. Here, differently from [270], we compare weakly Boussinesq models with different linear and non-linear shoaling characteristics, as well as the fully nonlinear eGN code. For all the models, the usual analytical sech^2 solitary wave shape is used to initialize the computation.

We start from the case $\epsilon = 0.2$, with a slope $s = 1 : 35$, and report the wave heights measured at different wave gauges along the slope in figure 1.4. On the left we compare the experimental data to the fully nonlinear eGN results as well as to those obtained with the weakly nonlinear model of Nwogu. On the right we compare the data with the results of the fully nonlinear equations and with those obtained with the equations of Madsen and Sørensen (MS), and Nwogu-Abbott (NA). The result on the left is essentially that discussed in [270]. Note that the weakly nonlinear model provides a large overestimation of the wave heights. The right figure, however, is much different, the weakly nonlinear MS and NA models providing a small underestimation of the elevations. Similar results have been obtained in [95] using as initial data for each model its own semi-analytical soliton shape.

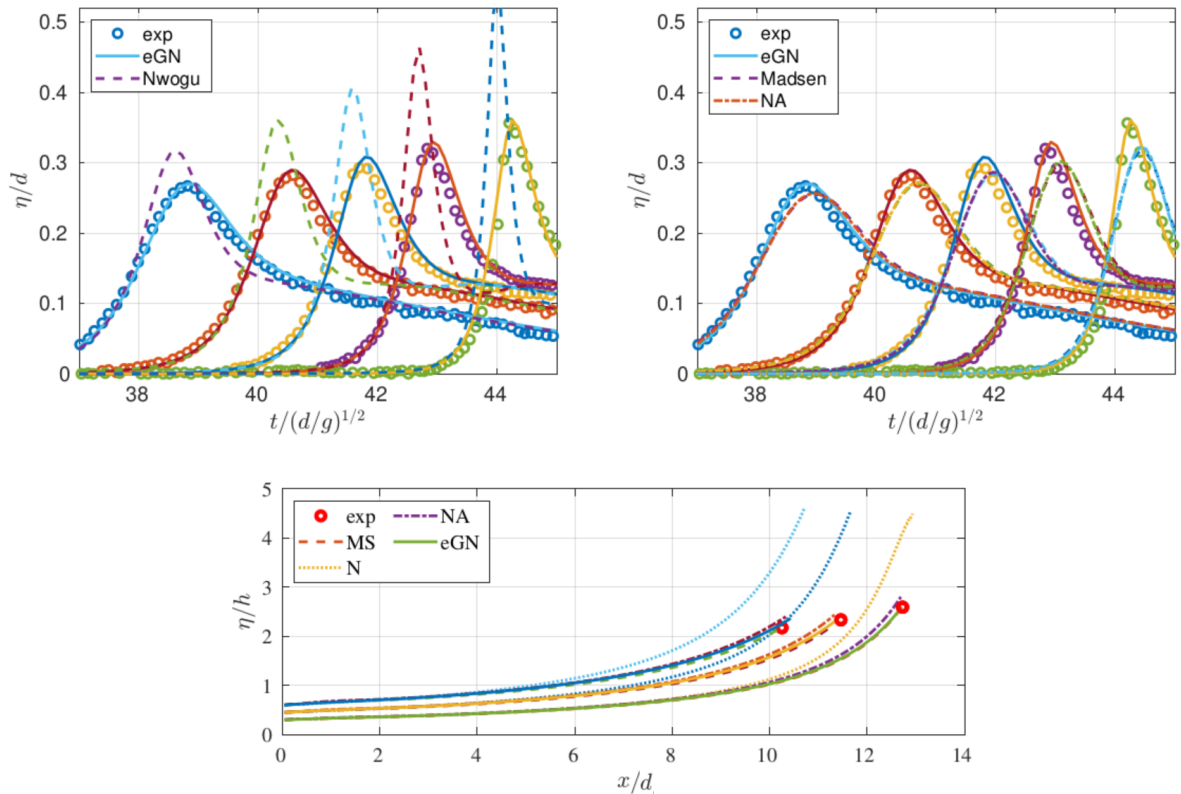


Figure 1.4: Free surface elevation on the wave gauges 1, 3, 5, 7, 9 for GN and Nwogu (up left), and for MS, NA, and GN (up right). Relative wave height computed with all the models on a 1:15 slope (down).

Next, following the test performed in [270], different solitary waves of non-linearity $\epsilon = 0.3, 0.45, 0.6$ shoal on a slope of $s = 1 : 15$, and we plot the envelopes of the wave peaks along the shoal. The results are plotted at the bottom image of figure 1.4 (soliton non-linearity increasing from left to right curves). The red circles represent the experimental breaking point of each wave. Our results confirm only partly these by [270]. Indeed, for the equations of Nwogu, the breaking point is "missed" by the model, which predict a substantial wave over-shoaling. The more nonlinear the wave, the stronger the over-prediction. However, the weakly nonlinear equations written in amplitude flux form provide results much closer to the fully nonlinear model, and a reasonable approximation of the wave peak at the breaking point. This is somewhat in contrast with the dogmatic view that all the weakly nonlinear models over predict wave heights, and that provide wrong values of the free surface elevation. In figure 1.5, we report the envelope of the wave, for all the different models and the experimental data. In addition we show the mesh independence of the solution as we refine the mesh using a grid resolution from $dx = 0.02$ m up to $dx = 0.0025$ m.

Note that in [95], it has thoroughly be shown that weakly nonlinear models written starting from Peregrine's equations, thus with linear dispersive effects expressed as space-time derivatives of the velocity, have very close nonlinear behaviour. Indeed, results similar to those of Nwogu's model can be obtained with other BT systems, e.g., Peregrine's [212], Beji-Nadaoka [15], etc., see also [95].

To conclude, despite showing important differences in the nonlinear behaviour of the models, this benchmark does not settle the question on whether full non-linearity is necessary, the models in amplitude-flux form following relatively closely the fully nonlinear model up to the breaking point as demonstrated in figure 1.4.

Undular bore propagation

The propagation of undular bores is also a classical problem, studied e.g., in [211] and [270], and for which well known experiments also exist e.g., [90], [257]. The initial setup is essentially the same as in [270]. We consider a computational domain of 300 m with wall conditions at both domain ends. A transition between uniform flow and still water is initially centered at $x = 0$ m, with velocity and surface elevation given by

$$u = \frac{1}{2}u_0 \left(1 - \tanh\left(\frac{x}{a}\right)\right), \quad \eta = u + \frac{1}{4}u^2, \quad (1.36)$$

where u_0 is the velocity of uniform flow from the left boundary and a set to 5 m as in [270]. We consider two initial states with jumps in the initial surface elevation $\eta_0 = 0.1$ and 0.3 , which also correspond to non-linearity values $\epsilon = 0.1$ and $\epsilon = 0.3$, and to Froude numbers $Fr = 1.07$ and 1.22 , respectively. Both waves evolve in undulating bores propagating through the channel. The amplitude as well as the wavelength of the oscillations depend on the initial data.

As in [270] we plot the bore profiles at different (dimensionless) times $t' = 50, 60, \text{ and } 70$, where $t' = \frac{\sqrt{gd}}{L}t$. The results are shown on figure 1.6. As one could expect, for the least nonlinear case,

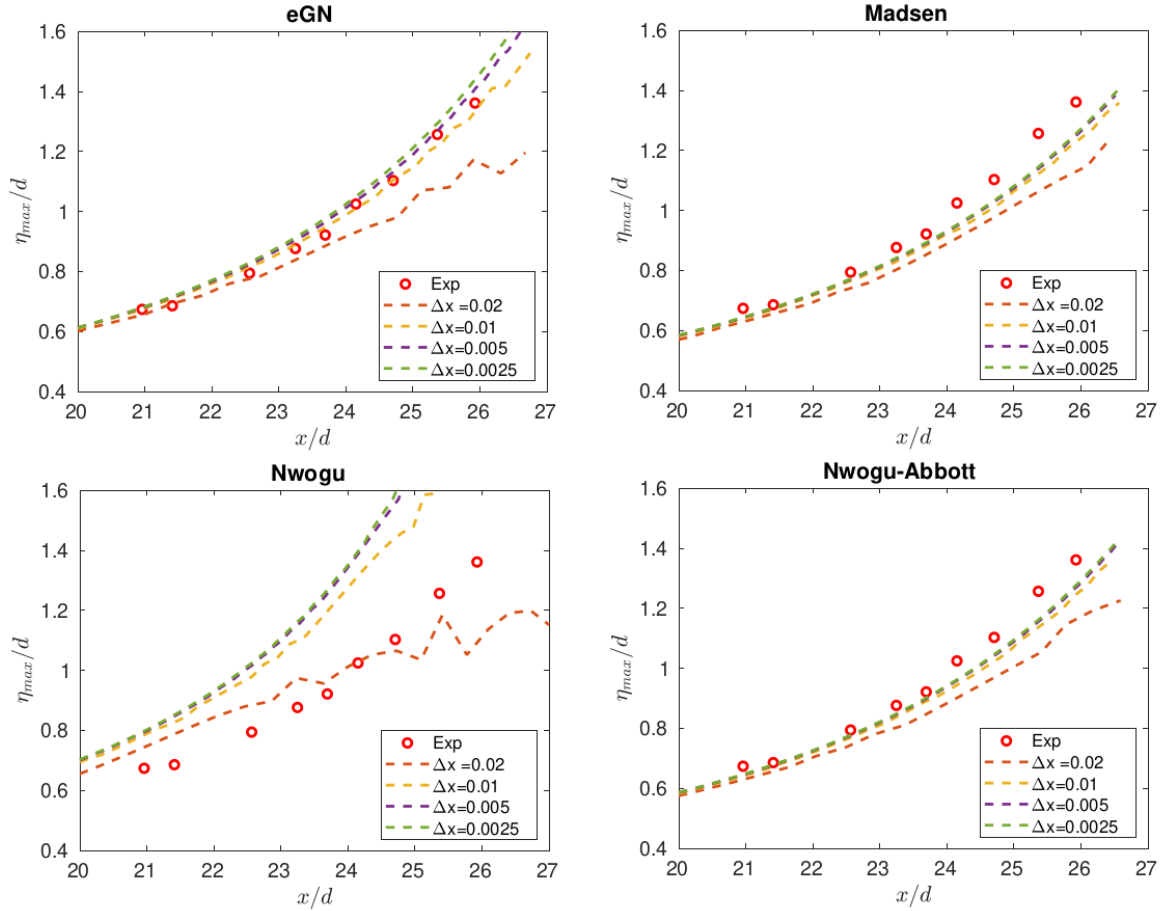


Figure 1.5: Wave envelopes for $\epsilon = 0.2$, $s = 1 : 15$. Mesh convergence of the solution for all the models.

the models provide nearly identical results, with only slight over-amplification of the oscillations by the Nwogu model, and even less visible under amplifications for the MS and NA models. As the non-linearity grows these differences become more visible. The wave heights predicted by Nwogu's model are substantially larger compared to the eGN solution. Note that the latter has been shown to provide results almost identical to a fully nonlinear potential model [49]. On the contrary, both the MS and NA models underestimate the amplitude of the oscillation. Note that this difference in behaviour is somewhat in-line with the second order analysis done in [95] showing that amplitudes of Stokes-waves are systematically under-predicted by BT models in amplitude-flux, while models in amplitude-velocity underestimate very short and over estimate longer waves (see also figure 1).

To have a more quantitative view of these differences, we look at the dependence of the amplitudes of the secondary waves on the Froude number. Experimental data are also available for this from Favre [90] and Treske [257]. So simulations are run by considering different values of u_0 corresponding to bore Froude numbers in between 1 and 1.3. Amplitudes are computed as the difference between the heights of the first peak and the first trough. On figure 1.7, in the left picture, we report the

peak/trough elevations A_{\max} and A_{\min} . The amplitude plot shows a growth with the Froude number which looks perfectly linear. For Fr roughly ≤ 1.15 all the models provide similar predictions, all close to the experimental values. For more nonlinear situations, we see three family of models: the weakly nonlinear model of Nwogu over-predicting the amplitude; the models of MS and NA under-predicting the amplitudes; the fully nonlinear eGN model in between the previous two, and somewhat closer to the experiments.

It is worth mentioning that as the Froude number increases, the difference of the result for Nwogu's equations with respect to the data (and to the eGN results), is at least twice as much as that of the other weakly nonlinear models which remain in a range of amplitudes reasonably close to the data. From the right figure, we can see that the elevation of the first trough does not change much with the Froude number, so the behaviour observed is really associated to the dynamics of the first peak which grows much faster with models in amplitude-velocity form, as Nwogu's, as remarked at the end of the previous section, see also [95].

This benchmark also does show the impact of the nonlinear behavior of the models. However, looking at the amplitudes of figure 1.7, the improvement of using the fully nonlinear eGN model is not striking, compared to the MS and NA.

Monochromatic waves on a submerged bar

We consider the laboratory experiments performed by Beji and Battjes [14] on monochromatic waves over a submerged bar. The initial conditions can be found in [146]. The experimental set up was designed to investigate both frequency dispersion characteristics of monochromatic waves, and non-linear interactions. This is possibly the most popular set of benchmarks in the literature on numerical models for dispersive free surface waves. We refer to the original reference for the setup, or to one of the numerous papers using this test, see e.g., [136], [222], [137], [95], [8].

We consider here two cases. The first is a mildly dispersive case corresponding to an incoming wave of amplitude $A = 0.01$ m. The non-linearity and dispersion parameters are $\epsilon = 0.025$ and $\mu = 0.11$, respectively. The second corresponds to a mildly nonlinear case where the amplitude of the incoming wave is $A = 0.054$ m, and non-linearity and dispersion equals to $\epsilon = 0.125$ and $\mu = 0.083$, respectively. In the second case, the breaking point is reached and wave breaking is observed above the plateau of the submerged bar. Wave breaking is modeled for this case with the hybrid approach discussed in chapter 4 for all the BT models considered.

The first case involving incoming waves with minute non-linearity, we expect all models to behave similarly. This is absolutely the case, as can be seen in the upper part of figure 1.8. The plot reports a few periods of the water elevation time series in the gauge placed at $x = 14$ m right next of the bar plateau. The results of the eGN, MS and Nwogu model are compared to the experimental data. This gauge allows to include effects of both the increased non-linearity acquired at the end of the shoaling phase, and dispersive effects during the propagation along the plateau. The numerical results obtained with the enhanced Green-Naghdi model, and those obtained with the MS and Nwogu models are extremely close to one another.

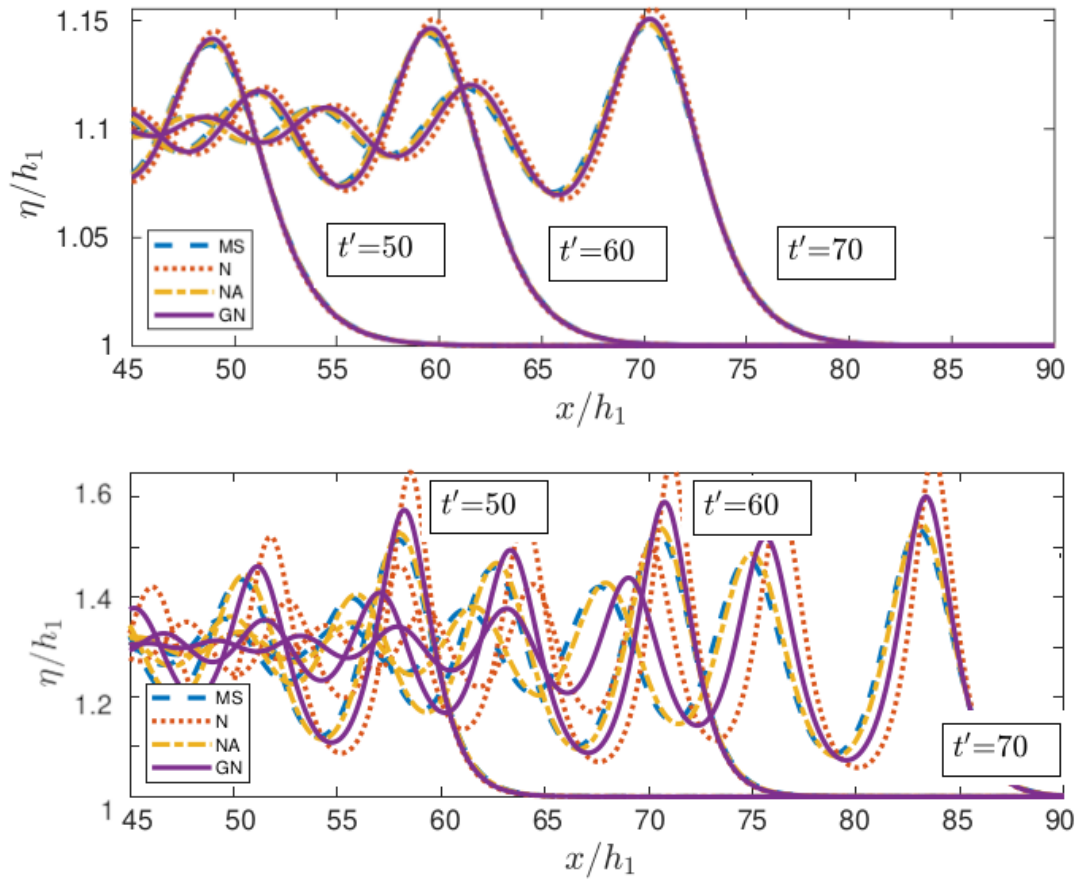


Figure 1.6: Evolution of an undular bore. Up: $\epsilon = 0.1$. Down: $\epsilon = 0.3$

For the mildly nonlinear case, with wave breaking, one might expect to see a substantial difference between different weakly nonlinear models, and with respect to the fully nonlinear one. The bottom of the picture on figure 1.8 reports the results for this case in terms of water elevation time series reported at $x = 13 \text{ m}$, in correspondence of which incipient breaking is observed. The results obtained with the enhanced Green-Naghdi model, those obtained with the MS model, and those provided by Nwogu's equations using the identical wave breaking detection, and hybrid breaking closure, and the same mesh size of 4 cm, are essentially the same.

Although it is a widely used benchmark, this test appears to have limited sensitivity to the level of linearity included in the BT models, unless of course the breaking closure is eliminated and nonphysical regimes are approximated, as demonstrated in [95].

Propagation, breaking, and over-topping of a reef

We consider now a more complex case, involving highly nonlinear waves. It consists of the propagation, breaking and reef over topping of a soliton, investigated numerically and experimentally in [226],

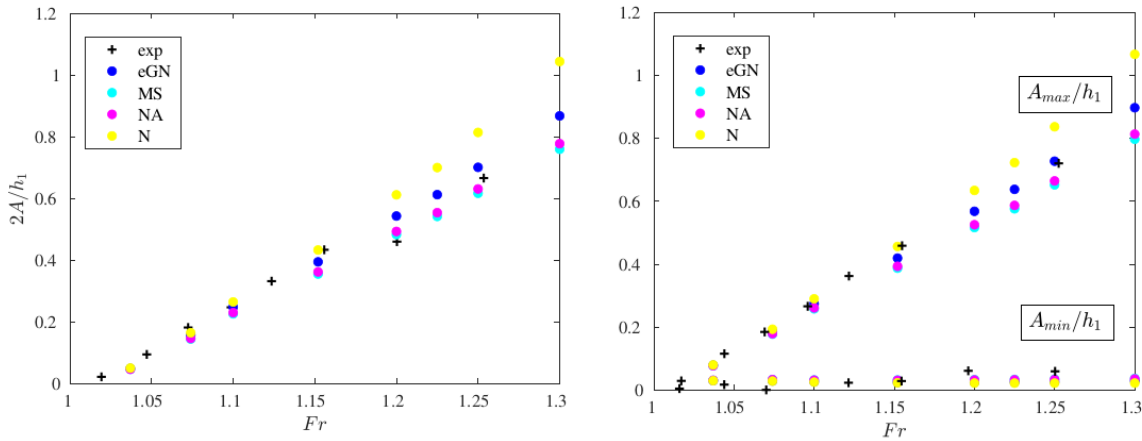


Figure 1.7: Undular bore propagation. +: Data of Treske and Favre, o: Numerical simulations. Left: Wave Amplitude for different Froude numbers. Right: Maximum and minimum wave heights for different Froude numbers.

and numerically in several other more recent works ([254, 227, 145, 141]). The geometry of the problem consists of a reef with a constant fore slope $1/10$, hiding on the lee side a shallow flat with a wall on its right end. A sketch of the geometry and the initial condition are plotted on figures 1.9 and 1.10. Water depth distributions at time series in 14 wave gauges have been measured in the flume experiments of [226]. A detailed description of the test case is provided in section 4.3.5.

A solitary wave of offshore non-linearity $\epsilon = 0.3$ propagates on the left of the reef. Simulations with all the BT models of sections 1.1.1 and 1.1.2 are discussed. Breaking is modelled using the Turbulent Kinetic Energy (TKE) closure (see chapter 4 and [145]). We visualize the results via a few snapshots of the free surface distribution and water elevation series in 4 gauges (WG4-WG8-WG10-WG14) located at $x = 21, 26, 28, 37$ m.

During propagation there is hardly any difference in the results as seen in the top left picture on figure 1.11. Minor differences are observed at the end of the shoaling phase (top right on figure 1.11), and during over topping with the MS and NA models giving almost identical water depth distributions, and Nwogu's model giving the most strongly damped wave, possibly as a result of the slight over-shoaling observed in the top left picture triggering wave breaking a little earlier. After the over topping, we see the generation of a highly nonlinear bore propagating in the shallow area, mid-left picture on figure 1.11. Here again we see differences in the nature of the bore (some dispersion still appearing in the MS and eGN results), or in its speed and magnitude (faster and stronger for Nwogu's model). In the next snapshot (mid-right picture on figure 1.11), we see the propagation of the wall reflected bore for which all models are again in phase. Perhaps a main feature to remark is the fact that the first backwash on the front side is stronger with Nwogu's model. After the reflected bore over-tops the reef (bottom-left picture on figure 1.11) we see a weak dispersive jump on the front side of the reef, and a secondary reflected more in the shallow area. On the shallow side, the results of Nwogu's model now lag phase compared to the others. This is even clearer in the wall

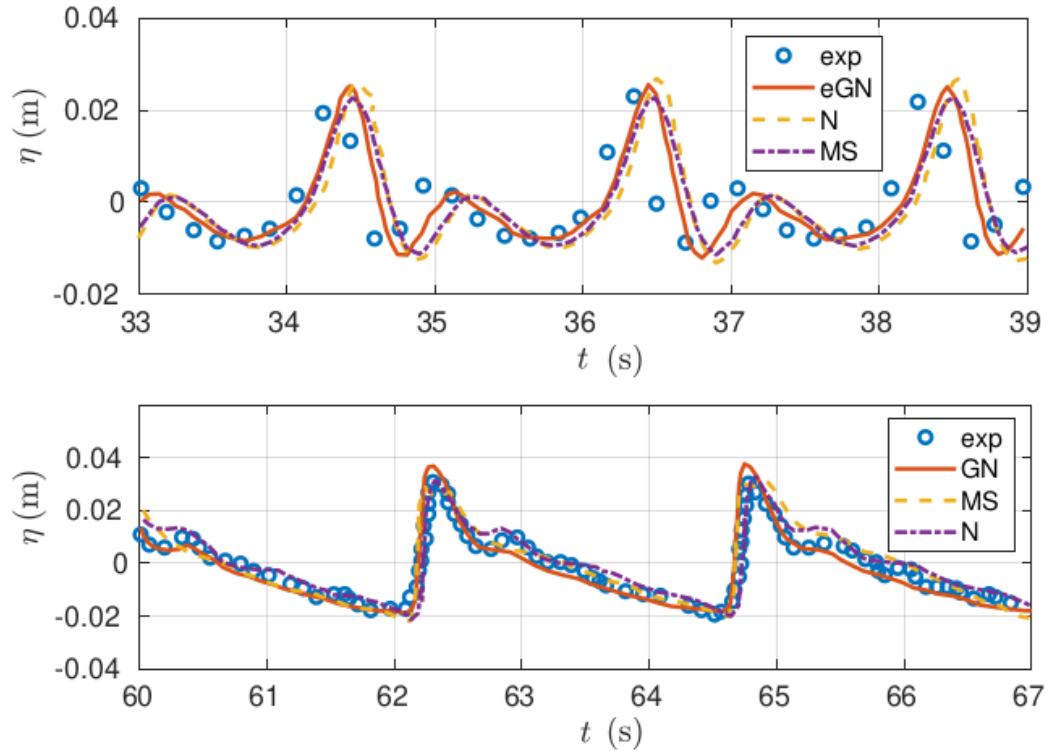


Figure 1.8: Up: Free surface elevation for eGN, MS, and Nwogu’s models for the case where initial wave’s amplitude is $A=0.01$ m (non breaking case). Down: Free surface elevation for eGN, MS and Nwogu’s models when $A=0.054$ m (breaking case).

reflection of the bore in the bottom-right picture on figure 1.11. The same figure shows the second backwash on the front side of the reef, for which all models are close to one another.

Although it is relevant for simulating the inundation process despite its non-linearity, this test does not provide a means to distinguish between the advantages of using fully nonlinear and weakly nonlinear BT models. The differences observed, when not minor, are mostly originating in shallow areas. This suggests that they may be more closely related to the parametrization of wave breaking closure and of the wet/dry treatment, than to the choice of the propagation model. A study on the sensitivity of breaking closures is presented in chapter 4. The interested reader can refer also to [129], or to [141] for a thorough study of this case using the hybrid closure. In addition, a comparison of different codes on this particular test case is performed in [141]. So far, we think to see a sort of trend, suggesting that weakly-nonlinear amplitude-flux models such as the MS and NA provide consistently results close to the fully nonlinear eGN model up to the breaking point. This will be contradicted in the following benchmarks.

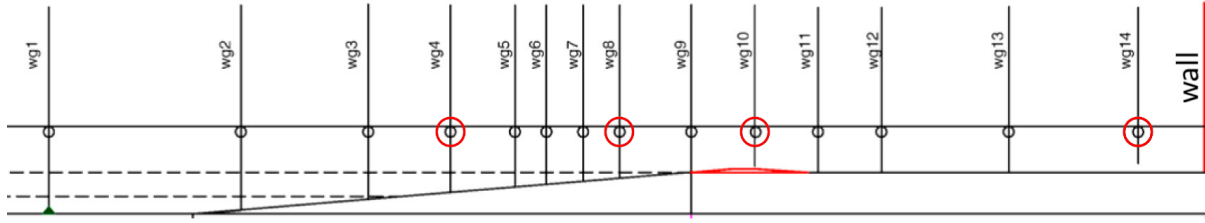


Figure 1.9: Solitary wave over topping a reef: Experimental set up.

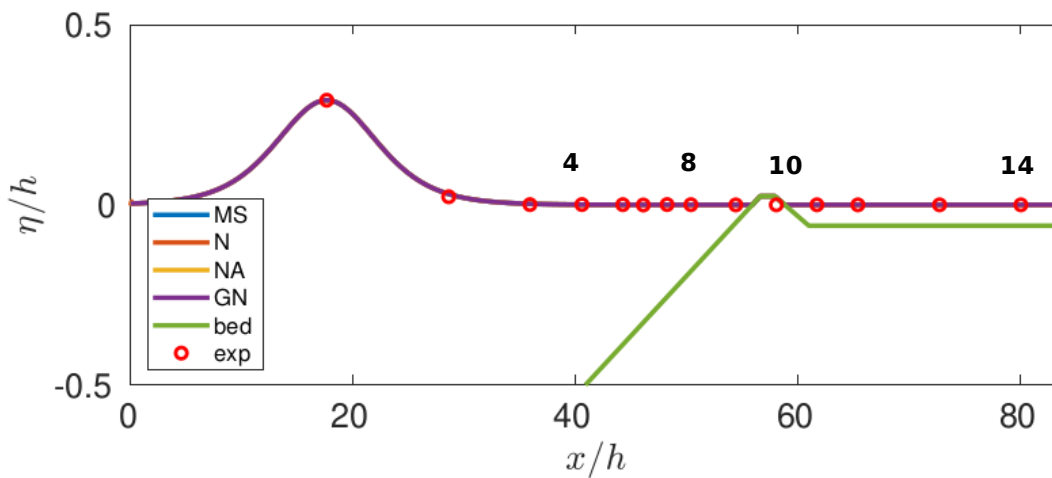


Figure 1.10: Solitary wave over topping a reef: Initial conditions.

Extreme run-up on a vertical barrier

Introduced in [260], this benchmark is relevant for wave structure applications, as e.g., the design of coastal structures like sea walls and breakwaters. The core of the problem is to correctly predict the wall run-up which can exceed six times their initial wave amplitude due to the interaction of steepening and dispersion processes. The setup involves a wave tank with flat bottom of depth $d = 10$ m and length $2L$. The actual physical domain is from 0 to L while from L to $2L$ a mirror image of the initial wave is placed. A picture of the domain is presented in figure 1.12. This symmetric arrangement allows to free the analysis of the dependence of numerical wall boundary fluxes at the point $x = L$. In [260] the problem is studied using the free surface Euler equations, and the classical (non enhanced) Green-Naghdi equations. Here we perform the study with all the BT models discussed in section 1.1.3. Both the effects of changing the non-linearity and dispersion parameters are investigated.

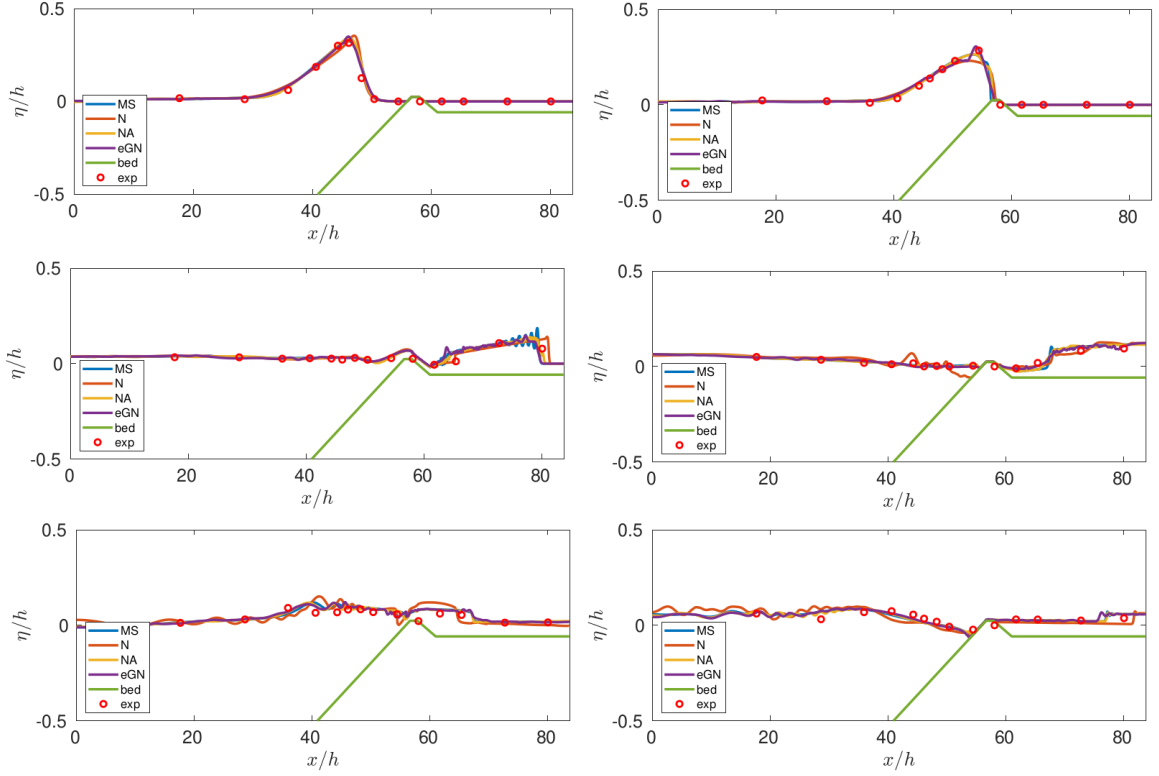


Figure 1.11: Solitary wave over topping a reef: free surface snapshots.

The initial conditions are given by a linear wave multiplied by an envelope function i.e

$$\eta(x) = W(x)\alpha_0 \sin k_0(x - x_0), \quad (1.37)$$

$$u(x) = W(x)\alpha_0 \frac{\omega_0}{dk_0} \sin k_0(x - x_0) \quad (1.38)$$

where

$$W(x) = \frac{1}{2} \tanh\left(\frac{x - x_0}{\delta}\right) - \frac{1}{2} \tanh\left(\frac{x - x_0 - N_w \lambda_0}{\delta}\right). \quad (1.39)$$

We denote $\lambda_0 = \frac{2\pi}{k}$ as the initial wavelength, and with x_0 and α_0 as the initial position and amplitude of the wave, respectively. The main parameters that characterize the initial conditions are the frequency ω_0 , which depends on the dispersion relation of the propagation model, the amplitude α_0 , and the initial wave's location x_0 or in other words, the wave's distance from the wall. The remaining parameters N_w and δ denote, respectively, the number of waves in the physical domain, set to 3 like in [260], and a thickness parameter affecting the wave dynamics set to $0.2\lambda_0$ as in the original reference.

We first examine the effect of the wavelength on the run-up. For a fixed initial wave amplitude $\alpha_0 = 0.05d$ we span the range $\lambda_0/d \in [30, 625]$, roughly corresponding to $\mu \in [0.0016, 0.033]$. In all simulations we set $L = 6\lambda_0$. The maximum run-up as a function of the initial wavelength is plotted in the left picture on figure 1.13 for all the BT models considered. The reference solution of the Euler model is taken from [260]. For this case the situation is clearly reversed compared to the

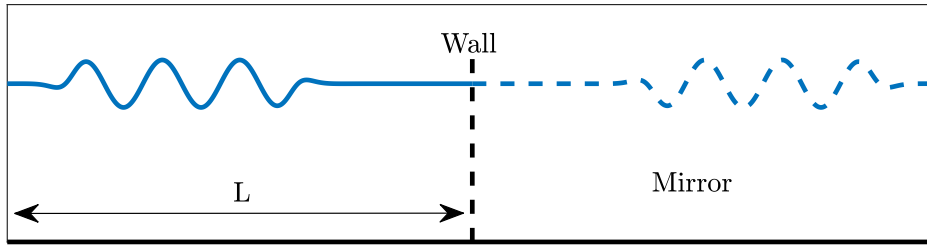


Figure 1.12: Extreme run-up on a vertical barrier: set up of the test case.

previous. The fully nonlinear models are quite close to the reference as expected, with the enhanced model providing the best results. In this case, the amplitude-flux models, namely MS and NA, provide a considerable underestimation of the run-up (up to 15%) for a wide range of wavelengths. The classical Nwogu equations instead perform quite well, as well as the eGN model, for the longest waves, reversing the trend set up from the previous benchmarks. For short waves, the Nwogu model still shows a noticeable over-prediction of the run-up, compared to the Euler equations. Only the fully nonlinear model provides a correct prediction of these waves, the weakly nonlinear equations in amplitude-flux form still underestimating the run-up.

Next, as in [260], we examine the effect of the normalized initial amplitude, for a fixed wavelength set to $\lambda_0 = 125d$, roughly corresponding to a value $\mu \approx 8 \times 10^{-3}$. We consider non-linearities in the range of $\epsilon = \alpha_0/d \in [0.01, 0.15]$. The resulting maximum run-up is plotted for all the models in the right picture on figure 1.13 (reference solution of the Euler model taken from [260]). For small non-linearity $\epsilon \leq 0.02$ all the models provide almost superimposed results, with a small underestimation of the run-up height, compared to the Euler equations. As in [260] we observe a sharp transition taking place in the range of $0.02 < \epsilon < 0.05$. This is the region in which the run-up regime changes from linear to fully nonlinear. Above $\epsilon = 0.05$, some sort of equilibrium is attained between all the processes, with the Euler equations providing run-up values all close to about $R_{max} = 6d$. Both the slopes in the second phase, as well as the run-up values and slopes in the third show significant differences between the models. For both the MS and NA models, the run-up increase in the second phase is slower, and reaches a value roughly 10% lower than all other models. In the last phase, we see a decrease in run-up, leading for the most nonlinear waves to an underestimation of the run-up of the order of 25% compared to the Euler equations. All the remaining models, including the weakly nonlinear Nwogu equations, provide a close transition in the second phase, all reaching values of R_{max}/d in between 5.5 and 5.75 for $\epsilon = 0.05$, and with values of for higher non-linearities considerably closer to the Euler model than the MS and NA equations.

Note that, for the range of kd used in this test, the difference between the weakly nonlinear models is somewhat in line with the second order analysis recalled in section 1.1.3 (cf. bottom picture in figure 1.3), and already invoked to interpret the results observed for the propagation of undular bores. Also, it is important to stress that for all the waves considered, the hypothesis $\epsilon = \mathcal{O}(\mu^2)$ underlying the weakly nonlinear models is violated systematically, the non-linearity

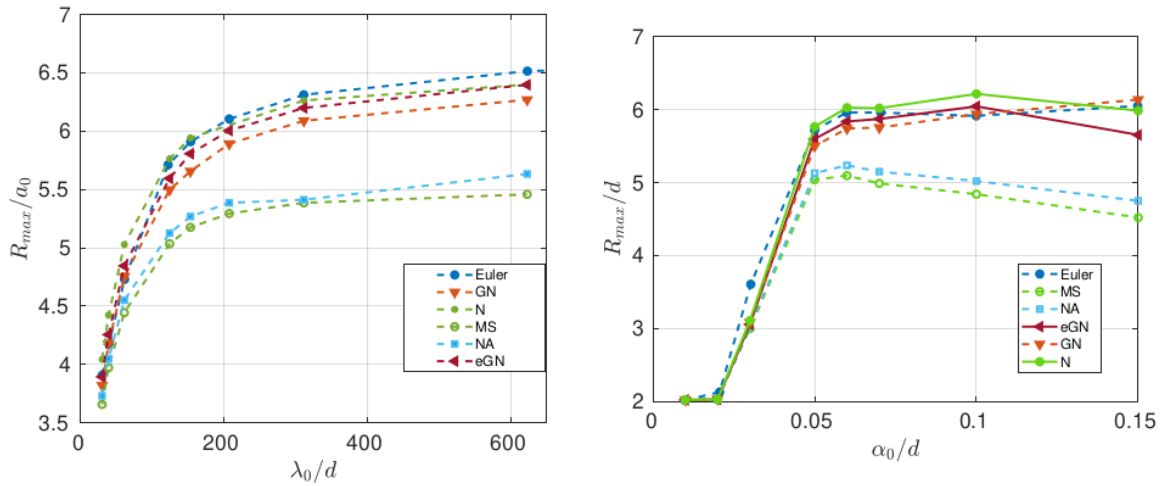


Figure 1.13: Normalized maximum run-up vs non-dimensional initial wave-length for different BT models. Left: fixed $\alpha_0 = 0.05d$. Right: fixed $\lambda_0 = 125d$.

exceeding this limit by at least one order of magnitude. Despite of this, we are far from breaking conditions (we experimentally confirmed that the breaking sensor is far from breaking onset). So all the weakly nonlinear propagation models are used well outside their initial Ansatz.

It is interesting to see in figure 1.14 the comparison of the time series of the run-up at the wall for the different BT models. We present the time series for two initial wave amplitudes, $\alpha_0 = 0.1d$ and $\alpha_0 = 0.15d$. We focus on the first dispersive wave, where $16 < \omega_0 t < 20$ in order to best appreciate the differences. All the weakly nonlinear models written in an amplitude-flux form (MS and NA) produce results with a slight phase lag and, as seen above, an under-prediction of the amplitudes of the trailing waves compared to these of the eGN equations. The later are close to the Euler equations, see [260], while Nwogu's model shows a phase advance that increases as the non-linearity of the initial wave grows.

Long distance propagation, shoaling and run-up of a rectangular wave

This test case was first proposed as a benchmark for tsunami-type surface wave simulation codes in [17], as a part of the French project TANDEM on tsunami hazard forecasting, led by the French Atomic Energy Commission. The main idea was to compare the codes based on different mathematical models, from Euler to BT and shallow water equations, regarding the dynamics of wave train propagation and run-up on the vertical walls of the domain. It involves the formation of an undular bore which propagates over a large distance, shoals on a near coastal bathymetry, and finally runs up on a vertical wall. The computational domain consists of a numerical wave tank of 30 km length and 50 m depth. The sloping bed of 1:125 is placed at the right part of the domain, where $x \in [25, 29]$ km followed by flat shelf where the water depth is constant and equals 18 m. The initial conditions of the free surface elevation are:

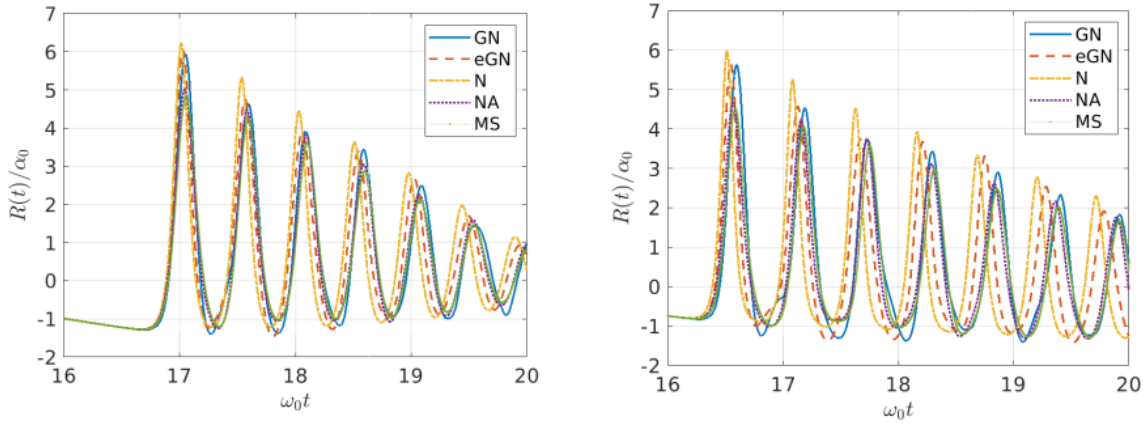


Figure 1.14: Run-up at the wall for two initial wave amplitudes $\alpha_0 = 0.1d$ (left) and $\alpha_0 = 0.15d$ (right) and fixed $\lambda_0 = 125d$.

$$\eta(x) = \begin{cases} 5 \text{ km}, & \text{if } 0 \leq x < 1900 \text{ m} \\ 2.5(1 - \tanh(229.756 \frac{x}{2000} - 1)), & \text{if } 1900 \text{ m} \leq x \leq 2100 \text{ m} \\ 0, & \text{if } 2100 \text{ m} < x \leq 30000 \text{ m} \end{cases} \quad (1.40)$$

Wall boundary conditions are imposed at both ends of the domain figure 1.15 shows the first hour of the wave's life, including its propagation, shoaling, and reflection on the right and left walls. At a large scale, the numerical solution provided by all models appear almost identical, at least up to the first reflection. However, some differences in phase and secondary wave structure can be observed after the first reflection. These differences are compensated during propagation toward the left wall, and the position and structure of the wave up to the 5th or 6th peak is quite similar for all models before and after the second reflection (middle- and bottom- right pictures on figure 1.15), except perhaps from a larger phase advance and amplitude over-prediction for the Nwogu model. A closer look of the run-up of the waves on the vertical right wall is provided in figure 1.16. This plot allows to better visualize the differences between all models. We see again a clear under-estimation of the maximum run-up from the amplitude-flux weakly nonlinear models by 15%-20% compared to the eGN equations. Note that the reference value of the maximum run-up [17] is of about 24.5 m, which means that the eGN model already provides an underestimation of roughly 18.4%, and the MS and NA models have errors of 30%-35% wrt this value. These are much worse numbers than for the previous case. We suspect that the implementation of the wall boundary conditions may affect these values and we are investigating this point. The message is, however that as for the previous case, weakly nonlinear BT models which seem to perform well in other quite nonlinear cases, under estimate substantially the run-up on vertical walls. The tendency to over-predict amplitudes somehow leads to better results for the Nwogu model for this case as for the previous.

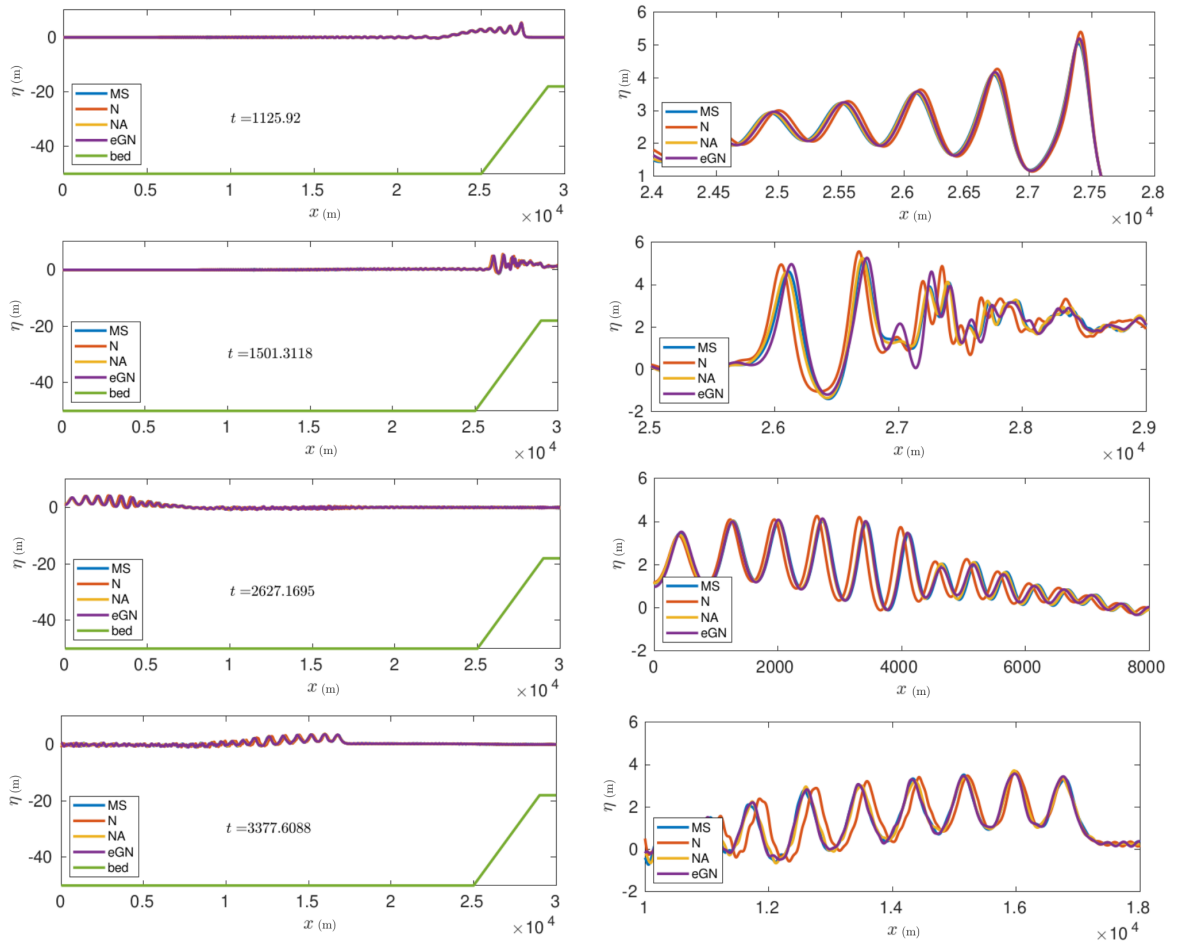


Figure 1.15: Propagation, shoaling, and wall reflection of the undular bore. A zoom on the wave trains is presented in the right column.

1.3 Two dimensional benchmarks

Bore propagation in a trapezoidal channel

We consider now a well known two dimensional variant of the bore propagation problem. The problem is similar, but involves topographic variations across the section which has a trapezoidal shape. As illustrated by the experimental work of [257], and by the numerical and theoretical study of [49], the bore dynamics are much more complex in this case. More precisely, Treske already showed that the secondary wave field has strong variations in crest height across the channel section. Additionally, variations in frequency content are observed, which depend on the Froude number. A transition occurs at a critical value of $Fr_t = 1.15$. According to [49] for Froude numbers above Fr_t , the flow is truly multi-dimensional. The waves along the centerline of the channel are similar to the Favre waves and have higher amplitudes, while much longer and less steep waves are observed on the banks. Below Fr_t the flow is quasi-one dimensional, with longer waves of higher amplitudes on the channel banks. In this regime, the same wavelength is observed all across the

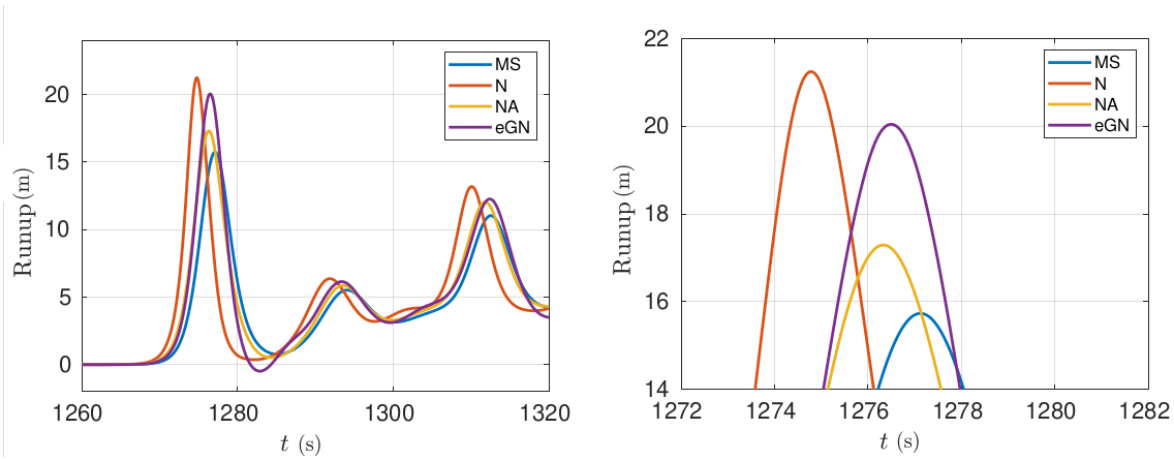


Figure 1.16: Run up of the wave on the right end. A zoom of the peak is presented in the right column.

section. This benchmark features quite nonlinear waves, with Froude numbers approaching, and locally exceeding, the breaking limit.

We performed simulations for a range of Froude numbers from 1.05 to 1.25 using the eGN, Nwogu and Nwogu-Abbott models. This range of numbers contains the transition, and remains below the transition to a fully breaking bore along the whole channel section. The computational domain of 27566 nodes, consist of a channel with $(x, y) \in [0, 25] \text{ m} \times [0, 1.5] \text{ m}$ in which half of the channel is placed. More details about the set up of the problem can be found in [49]. Free surface visualizations for Froude numbers 1.05, and 1.25, are shown in figure 1.17 . We can visually see the appearance of more oscillations along the same length of channel shown, and the presence of stronger cross-sectional waves for higher Froude numbers. To confirm these observations, the distribution of the free surface elevation along the banks and centerline are presented in the two upper illustrations of figure 1.17 for the three models.

Following [49] we post-processed the results to provide a more quantitative assessment. In particular, we have estimated the height of the first peak and trough, and the wavelength. The results of the wavelength are compared at the bottom of figure 1.18 with the experimental data of [257]. More results can be found in [146]. The main difference observed among the models is related to the wave amplitudes after the transition, i.e, for Froude numbers higher than 1.15. This is roughly the limit after which wave breaking starts taking place close to the banks. The computed wavelengths before and after the transition are almost identical for all models. The only difference observed is for the model of Nwogu in which the transition seems to take place for slightly lower Froude numbers. This is related to the over-shoal of the wave on the banks, leading to earlier breaking and possibly earlier transition.

Despite the strong non-linearities involved, and Froude numbers close to (or higher than) the breaking point, the nature of the weakly-nonlinear BT model used in the simulations does not seem to affect too much the prediction of both amplitudes, and wavelengths.

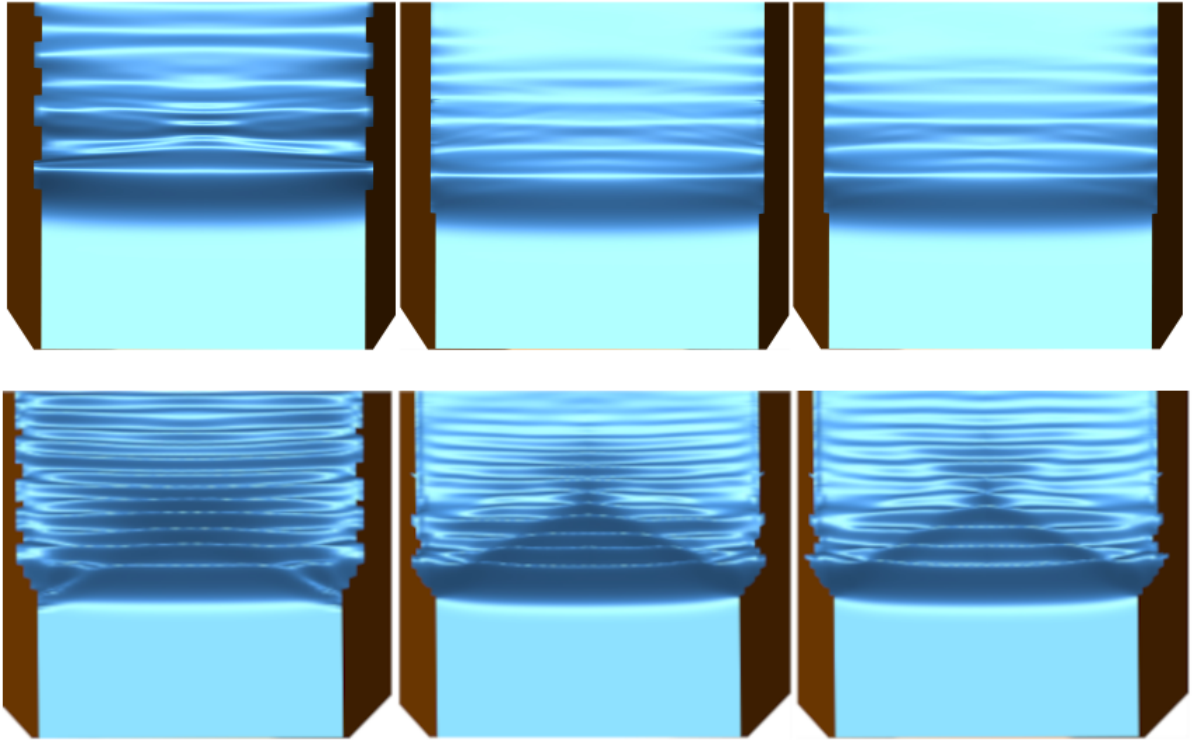


Figure 1.17: 2 dimensional free surface elevation for: eGN (left), Nwogu (centered), NA (right), at $t \approx 13.5$ s. The Froude number is 1.05 (up) and 1.25 (down).

Partial Dam Break

The dam break problem is a classical benchmark test case and has been widely studied, see e.g., [191], [6]. We will use here the partial dam failure case to test the behavior of the bore after the collapse of an asymmetric dam. We consider a square domain with dimensions of $[0, 200] \text{ m} \times [0, 200] \text{ m}$ where a dam is placed at 95 m separating two basins containing water depths of 10 m and 6 m, respectively. The dam is simulated as a rigid topography of 30 m. The sudden collapse of the dam leads to the formation of a bore that advances into the lower basin and a depression wave advancing into the left basin.

Figure 1.19 presents the numerical solution obtained using the eGN, Nwogu, and Nwogu-Abbott models at time $t = 10$ s. It shows the free surface elevation and the corresponding contours. Additionally, a cross-section of the solutions along the domain and in the dam center is provided, which can be seen in the bottom-right picture. The observations here are inline with these obtained from the 1D experiments. Nwogu's model overestimates the amplitude of the leading wave and exhibits a greater phase advance of the secondary waves compared to both the eGN and Nwogu-Abbott models.

The seaside test case

The last test case presented is the laboratory benchmark test case for tsunami inundation through an urban waterfront. The physical model was a 1:50 scale mock-up of the town Seaside, Oregon, designed to observe the complex tsunami flow around macro-roughness structure such as buildings, which are treated as impermeable rectangular blocks. The laboratory benchmark took place in the Oregon State University. It served as a blind benchmark test case for the NTHMP Mapping and Modelling Benchmarking Workshop: Tsunami Currents and as a benchmark test case for the project TANDEM [122]. Numerical predictions using fully nonlinear BT equations can be found in [209] and [138]. The numerical test setup is as follows: a rectangular domain with dimensions 42 m in the x direction and 14.5 m in the y direction is discretized using an unstructured triangulation. It consists of 172,854 nodes and is refined in the region where the buildings are located. The maximum side of the triangles is $h_{ref} \approx 0.7$ m and the minimum $h_{ref} \approx 0.03$ m. The individual structures and buildings are approximated as steep-sided topography, and a Manning coefficient of $n_M = 0.01$ is used, as suggested in the TANDEM project. The available experimental data involve the topography, the forcing signal and the time series of the waves measured at the wave gauges. The forcing signal is entering the computational domain through the left boundary and wall boundary conditions are placed elsewhere. The computational domain, including the placement of 31 wave gauges, are depicted in figure 1.20. The wave gauges are positioned between the buildings to measure the free surface.

The incoming solitary wave shoals and breaks close to the seawall and then floods an urban area which contains buildings of different heights. A detailed description of the behaviour of the free surface elevation is found in [209] and [138]. Figure 1.21 shows snapshots of the free surface elevation, for each model, at $t \approx 30$ s during the flooding of the urban area.

Figure 1.22 presents the free surface elevation for selected wave gauges, with additional results of wave gauges' available in [146]. The numerical results obtained from the Nwogu, Nwogu-Abbott, and Green-Naghdi equations are compared with experimental data. We observe that almost all the numerical results closely match the experimental data in most of the wave gauges, and that particularly for the first wave, these are almost indistinguishable. However, a difference in the arrival time of the secondary wave, occurring around 60 s, is observed at the wave gauges located in front of the buildings.

Overall, when examining the visualizations of the free surface and the time histories at the gauges for this challenging case, we do not observe significant disparities in the main flow characteristics. However, a noteworthy distinction arises in shallow areas, particularly in initially dry flooding zones, where all weakly nonlinear models do not incorporate dispersion. This distinction also impacts certain previous tests conducted. This explains in our opinion the details of the wave gauge histories for this tests which somewhat favour the fully nonlinear model, especially maybe for Locations A and B. The differences are primarily in small details; however, it is worth noting that some of these results could potentially be enhanced through the process of "tuning" the roughness parameter.

1.4 Summary

In chapter 1 we reviewed a certain number of benchmarks for dispersive wave propagation models. It is not simple to draw clear conclusions. One disappointing fact is perhaps that, when considering both amplitude-flux and amplitude-velocity weakly-nonlinear models, many well known and common test cases are not adequate to reveal differences between fully nonlinear and weakly nonlinear equations. This is the case even for quite nonlinear problems in which the breaking point is reached and exceeded.

One exception are perhaps Favre waves. Indeed, bore propagation on flat topography shows some advantage of having full non-linearity in a short window of high Froude numbers close to the breaking limit. The relatively more recent benchmarks proposed in [260] and [17] allow to highlight more clearly the need of full non-linearity at least when considering wave run-up on vertical walls, already for mild offshore non-linearity, and as long as breaking conditions are not reached.

These are however relatively academic tests. In complex physical benchmarks with bathymetric variations, wave breaking, and wet/dry transitions, both in one and two space dimensions, it seems much harder to draw clear conclusions. For models which are well known to over-estimate wave amplitudes (as Nwogu's model) we do observe some early breaking affecting the overall wave dynamics. This is however not the case with all weakly-nonlinear models. Details of the secondary waves appearing in complex problems as e.g., the Seaside case, also show some impact of not including full-non-linearity, which is certainly related to the inability of weakly nonlinear models to represent some weak dispersive propagation as soon as it takes place above the initial shoreline. However, the differences are again not striking. Some genuinely 2D extensions of the 1D cases which reveal most clearly the need of non-linearity, while being of physical and engineering relevance, with possibly openly available reference solutions or experimental data, seem still missing in the literature.

We thus draw two main conclusions. The first is that benchmarking habits need to be slightly revised. Authors, editors, and reviewers must be more careful in considering/suggesting appropriately chosen tests, so that when new models/schemes are proposed their capability for highly nonlinear propagation are clearly highlighted together with all other aspects (phase prediction, breaking location and strength, etc). Also it should be always underlined when a benchmark, although involving highly nonlinear waves, is not sensitive to the fully/weakly nonlinear nature of the model. This work by no means aims at performing this task, which is possibly to be performed with a larger set of models/codes. The second conclusion we draw from our tests is that of course fully nonlinear models allow to safely approach problems of different nature and involving highly nonlinear waves. However, as a rule of thumb, weakly nonlinear models can still be safely used in many problems of practical interest not involving planar non-breaking wave fronts reflecting on steep coastal structures in deep waters. This is true even for quite complex urban run-up of nonlinear waves, as seen in the Seaside example.

Finally, is the use of fully non-linear models a necessity or a luxury? Into the humble opinion of the author, full non-linearity is neither luxury nor necessity. There is a large class of problems for

which both appropriately chosen weakly and fully nonlinear models provide reasonable answers. Therefore, it is up to the user to be aware of the differences existing, and choose which of these models is most suited for his application.

In the following two chapters, we analytically describe the numerical procedure we derived to solve the weakly dispersive models introduced in this chapter. Specifically, we focus on the fully non-linear weakly dispersive equations of Green-Naghdi [109], but the same approach can be applied to any other Boussinesq-type model.

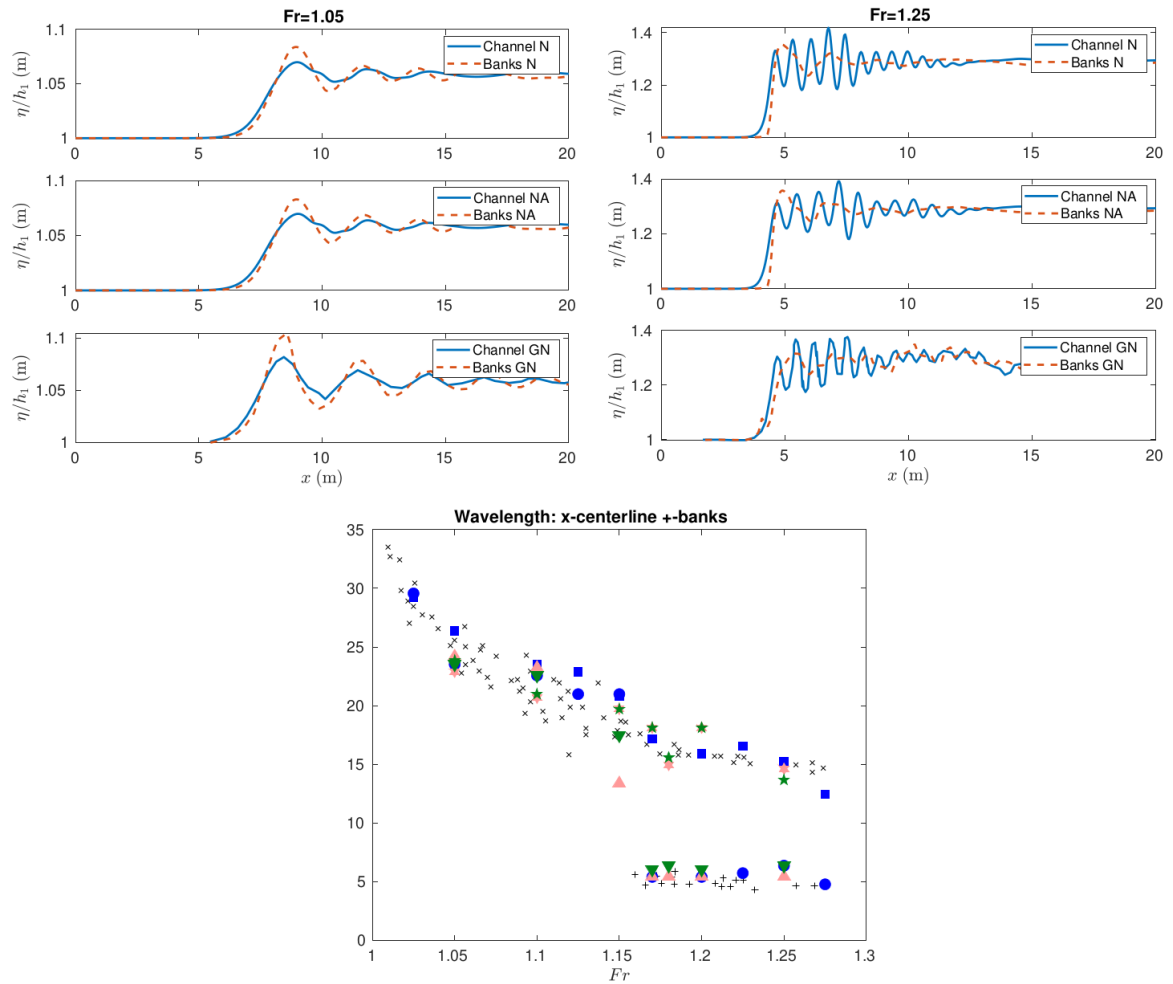


Figure 1.18: Up: Free surface profile for Froude numbers 1.05 and 1.2. Down: Wavelength vs Froude numbers x: Data of Treske (1994) axis, +: data of Treske (1994) banks, circle and triangles: simulated values on the channel axis, squares stars and hexagams: simulated values on the banks. Circle and square: eGN, upwards pointing triangle and hexagram: Nwogu, downwards pointing triangle and star : NA.

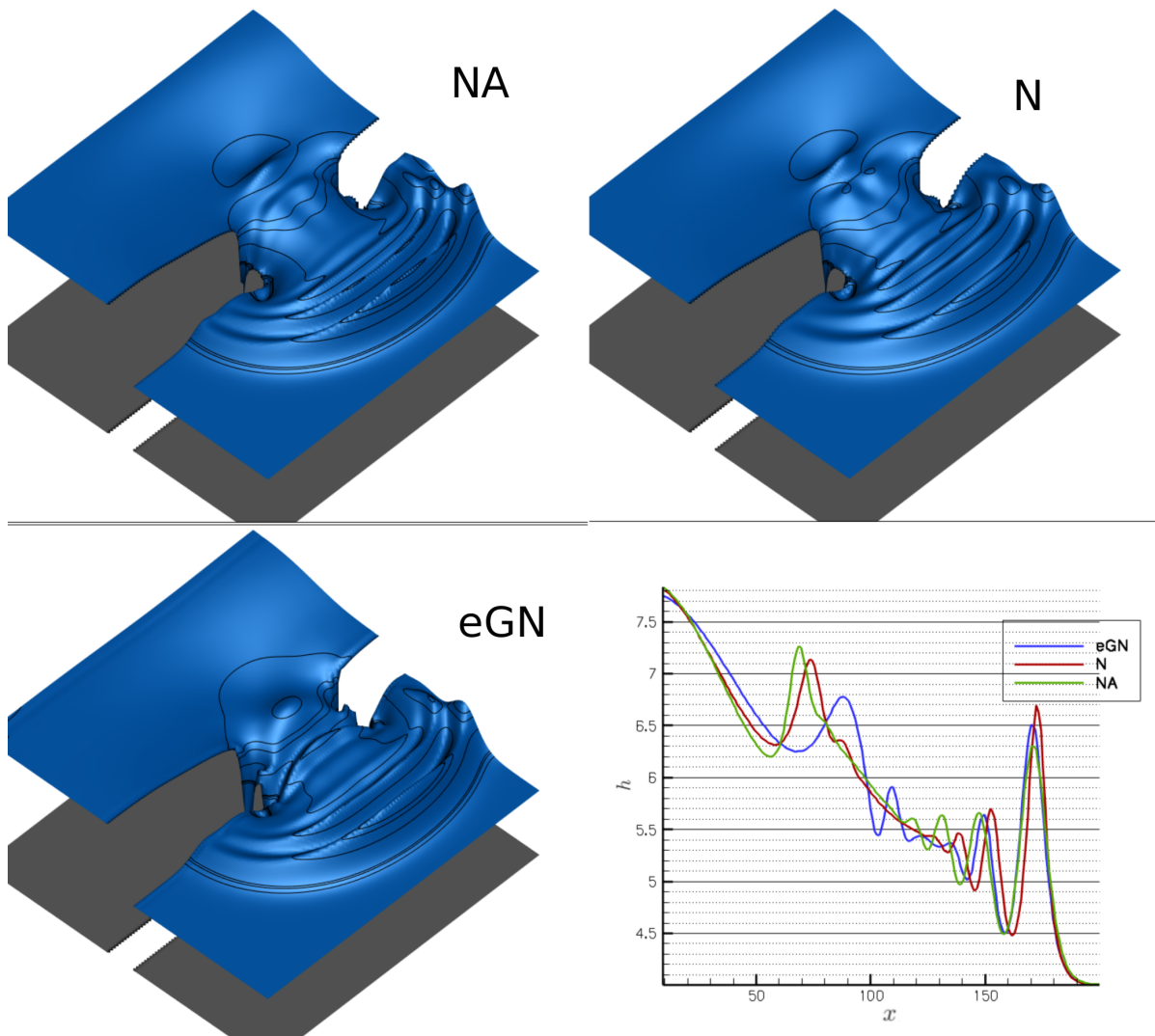


Figure 1.19: Partial dam break: free surface elevation at $t = 10$ s for NA (up left), Nwogu (up right), and eGN (down left). Cross-section along the center of the dam (down right).

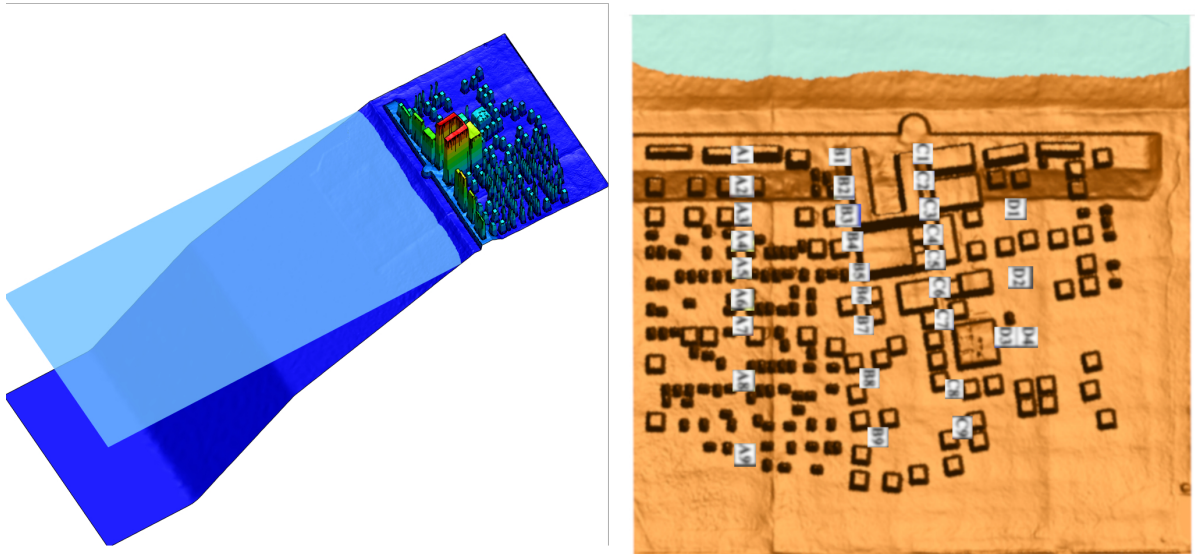


Figure 1.20: Seaside test case: Numerical set-up.

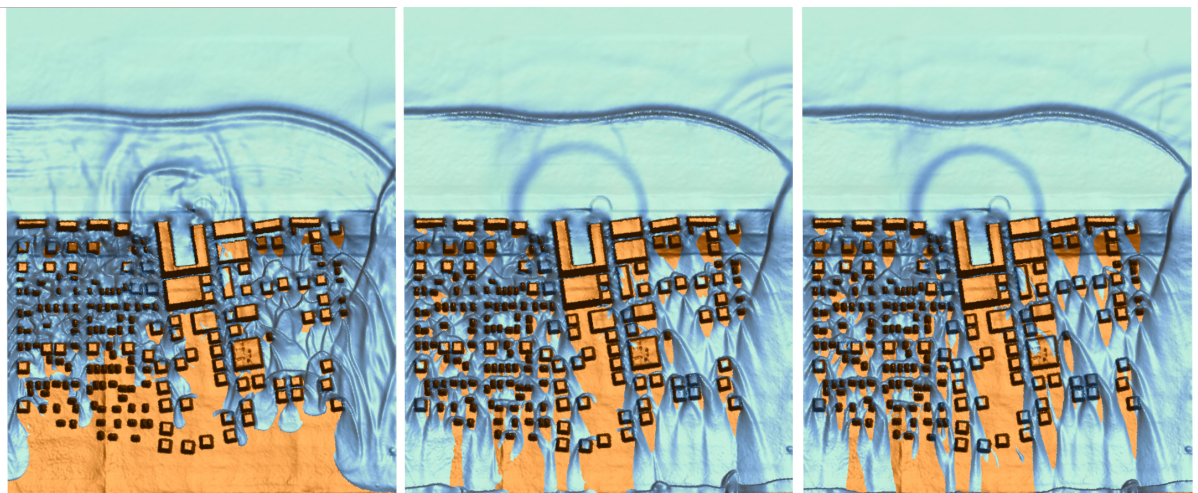


Figure 1.21: 2 dimensional free surface elevation for: eGN (left), Nwogu (centered), and NA (right) at $t \approx 30$ s.

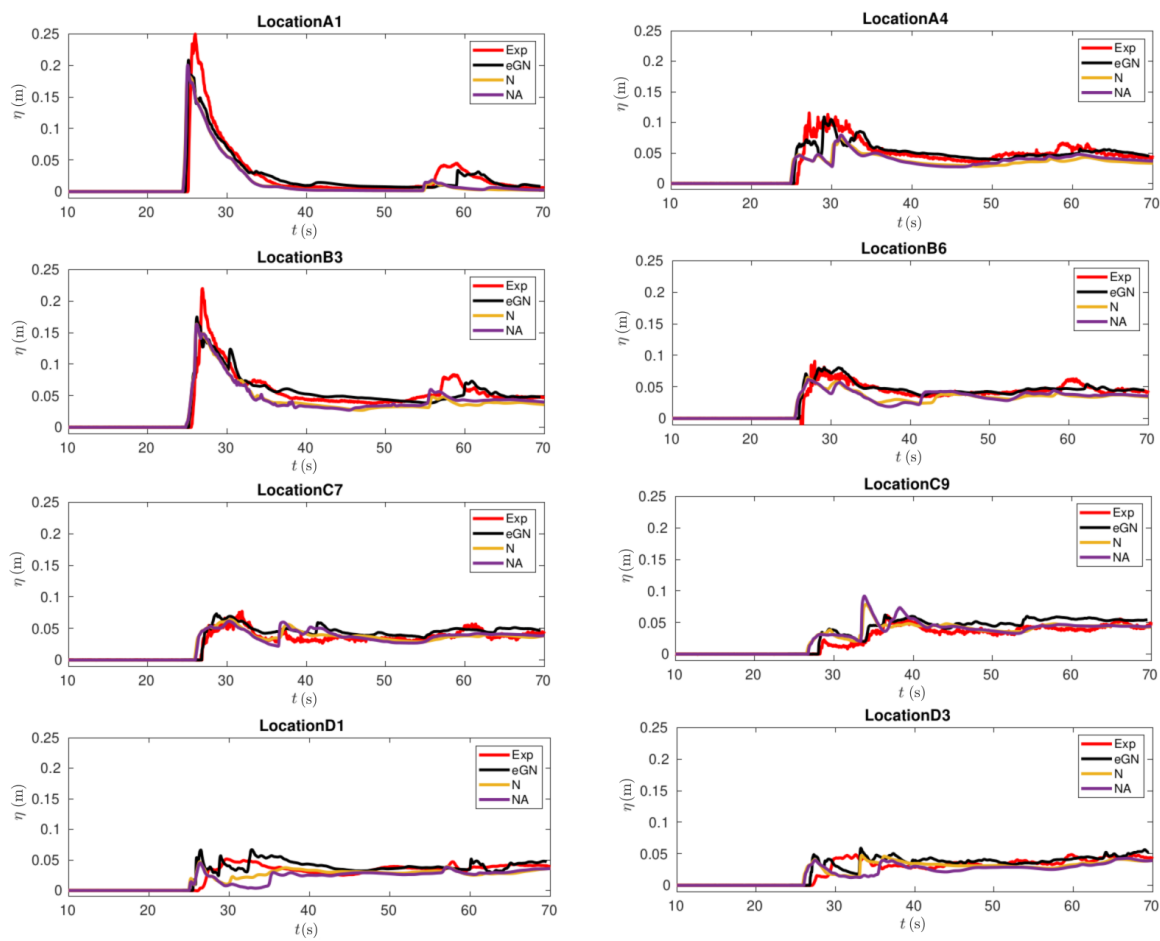


Figure 1.22: Free surface elevation measured on selected wave gauges.

Chapter 2

Numerical methods in 1D

Over the past few decades, the accurate mathematical and numerical simulation of water wave propagation in near-shore areas has garnered significant attention. These simulations have largely taken the place of laboratory experiments within the coastal engineering field. Significant efforts have been made in the development of depth averaged models or in the improvement of the existing ones, in order to give accurate description of the nonlinear and non-hydrostatic propagation over complex bathymetries. The Boussinesq-type (BT) models along with the nonlinear shallow water equations belong to the family of depth averaged models. Initially the BT models started to be discretized using the very classical Finite Difference (FD) method, see for example [16] [178], [176], [198], and [270]. The popularity of the finite difference (FD) method can be attributed to its ability to easily approximate higher-order derivatives and to the well-structured linear systems it produces, which can be efficiently solved (e.g., tri-diagonal systems). However, a significant drawback of the FD approach is that it requires structured spatial meshes for 2D simulations, even in irregular domains, which can result in a loss of accuracy.

Recently, classical finite volume (FV) schemes of the Godunov type have been adapted to solve enhanced Boussinesq-type equations in one spatial dimension. In these adaptations, the FV method is employed to handle the nonlinear shallow water components of the equations, while the dispersive terms are discretized using finite difference (FD) schemes. This results in the creation of hybrid FV/FD schemes. For 1HD the reader can refer in [168, 139, 228, 235, 236, 26]. The hybrid schemes exploit the flexibility and shock-capturing capabilities of the FV approach in the context of dispersive models. This approach proves to be particularly beneficial for interactions between short and long waves. Moreover, by eliminating the higher order Boussinesq terms, the solution can be turned to a fully FV solution of the nonlinear shallow water equations (NSWE), if required. The hybrid approach on structured meshes, has been extended also to 2HD [252, 149, 253].

The use of unstructured meshes for 2HD complex geometries favors the use of FV and Finite Element (FE) methods. While there are numerous works that use the FV method to solve the non linear shallow water equations, see for example [62, 65, 3, 256, 37], there are few that use it exclusively for solving BT equations [136, 137, 64, 81]. On the other hand, the use of FE methods, continuous/discontinuous in the solution of BT models exists since the 90's and continues to this day, see for example [84, 237, 88, 165, 262, 77, 91]. The hybrid approach (FV/FE) on unstructured

meshes has also been proposed in [138, 130].

The last decade there is an increased interest on the discretization and the use of the fully nonlinear weakly dispersive equations of Green-Naghdi (GN) [109]. The interested reader can refer to [74, 56, 57, 50, 26, 159, 164, 23, 190, 80, 182, 47, 113, 217, 105, 5, 251, 104, 206]. From the numerical point of view the GN equations have been discretized using different numerical techniques. We can distinguish them into three main categories. The first one is the classical two steps solutions procedure which is composed by a first step where the non hydrostatic source term is recovered by inverting the elliptic coersive operator associated to the dispersive effects. The second step involves the solution of the hyperbolic shallow water system with the source term computed in the previous phase, which accounts for the non-hydraustatic effects see for example [144, 80, 105, 26, 159, 251]. The second category of numerical schemes is the projection method [208] and the last one is the hyperbolic approximation [90, 41], that avoids the elliptic step in solving the GN equations.

Our work focuses on the first category of numerical schemes for the fully nonlinear and weakly dispersive equations of GN. This chapter presents and analyzes the proposed schemes in one-dimensional (1D), while the following chapter extends the analysis to two-dimensional (2D) problems.

2.1 A scheme for the fully nonlinear weakly dispersive model

2.1.1 Mathematical Formulation

In this chapter we refer to the improved Green-Naghdi (GN) system of equations in the form proposed by [26]. We recall that this formulation has been recovered by adding some terms of $O(\mu^2)$ to the momentum equation in order to improve the frequency dispersion description of the original GN model (see also 1.1.3). In the following we use the notation sketched in figure 1.1, thus we denote $h(x, t) = h_0 + \eta(x, t) - b(x)$ the total water depth and $u(x, t)$ the flow velocity (being $\eta(x, t)$ the free surface elevation with respect to the water rest state, h_0 a reference depth and $b(x)$ the topography variation).

The system of equations (1.1), (1.9)-(1.13) can be written in its one-dimensional form as:

$$\begin{aligned} h_t + (hu)_x &= 0 \\ (I + \alpha\mathcal{T}) \left[(hu)_t + (hu^2)_x + g \frac{\alpha - 1}{\alpha} h \eta_x \right] + \frac{g}{\alpha} h \eta_x + h \mathcal{Q}(u) &= 0 \end{aligned} \quad (2.1)$$

where the non-linear operator $\mathcal{Q}(\cdot)$ is defined by

$$\mathcal{Q}(\cdot) = 2hh_x(\cdot)_x^2 + \frac{4}{3}h^2(\cdot)_x(\cdot)_{xx} + b_x h(\cdot)_x^2 + b_{xx} h(\cdot)(\cdot)_x + \left[b_{xx} h_x + \frac{1}{2} h b_{xxx} + b_x b_{xx} \right] (\cdot)^2 \quad (2.2)$$

and $\mathcal{T}(\cdot)$ is

$$\mathcal{T}(\cdot) = -\frac{1}{3}h^2(\cdot)_{xx} - \frac{1}{3}hh_x(\cdot)_x + \left(\frac{h_x^2}{3} + \frac{h}{3}h_{xx} \right) (\cdot) + \left(b_x h_x + \frac{b_{xx}}{2} h + b_x^2 \right) (\cdot) \quad (2.3)$$

According to [159] the above formulation does not require the computation of third order derivatives, while this is necessary in the standard formulation of the GN system. Moreover, the presence of the operator $(I + \alpha\mathcal{T})$ makes the model very stable with respect to high frequency perturbations, which is of highest interest for numerical computations.

2.1.2 Discretization strategy : elliptic-hyperbolic decoupling

To discretize system (2.1) we first recast it in the following way:

$$\begin{aligned} h_t + (hu)_x &= 0 & (2.4) \\ (I + \alpha\mathcal{T}) [(hu)_t + (hu^2)_x + gh\eta_x] - \mathcal{T}(gh\eta_x) + h\mathcal{Q}(u) &= 0 \end{aligned}$$

This allows the operator $(I + \alpha\mathcal{T})$ to be applied to the full shallow water residual. This form suggests a possible decoupling of the elliptic part of the problem from the hyperbolic one, which is obtained as follow :

$$(I + \alpha\mathcal{T}) \phi = \mathcal{W} - \mathcal{R} \quad (2.5)$$

$$h_t + (hu)_x = 0 \quad (2.6)$$

$$(hu)_t + (hu^2)_x + gh\eta_x = \phi$$

having also defined $\mathcal{W} = g\mathcal{T}(h\eta_x)$ and $\mathcal{R} = h\mathcal{Q}(u)$. Given an initial solution, the system above can now be solved in two independent steps :

1. An elliptic step solving for the non-hydrostatic term ϕ ;
2. An hyperbolic step evolving the flow variables .

Note that our formulation differs from the ones previously proposed in literature (see e.g. [80]) as it allows the enhancement of an existing shallow water code by the addition of a purely algebraic term to the discrete momentum balance. It has the additional advantage of being a priori able to embed wave breaking effects in the elliptic phase, thus remaining completely non-intrusive w.r.t. the hyperbolic code. To evaluate this simplified and flexible strategy, we will investigate the accuracy and robustness obtainable when the two steps above are each solved with a different numerical method. Our aim is to allow the choice of the method most appropriate and efficient for each step and to provide a simple technique to enhance shallow water codes including genuinely nonlinear dispersive effects.

Note also that we purposely use here the word decoupling and not splitting. Indeed, *the elliptic phase does not involve any time derivative*, so this is not a splitting method, at least not in the sense used in [26] or in [240]. In particular, our approach provides an unpilt spatial discretisation of

$$\begin{aligned} h_t + (hu)_x &= 0 \\ (hu)_t + (hu^2)_x + gh\eta_x &= (I + \alpha\mathcal{T})^{-1} [\mathcal{T}(gh\eta_x) - h\mathcal{Q}(u)] \end{aligned}$$

This results in systems of Ordinary Differential Equations (ODEs), which can be evolved in time by any of the known high order time integration methods *without any other source of error than the truncation of the spatial discretizations involved and of the ODE integrators.*

Based on previous works like for e.g. [222], we have chosen to implement a standard C^0 Galerkin finite element method for the elliptic phase and to discretize the hyperbolic part by either a high order finite volume (FV), or by a stabilized continuous finite element (FE) method. Time integration is performed with three different methods, involving both multi-stage and multi-step approaches. The resulting hybrid algorithms are analyzed and compared. Of course, other hybrid methods can be obtained e.g. by choosing different approaches for the hyperbolic phase, as e.g. the discontinuous Galerkin method [276, 274], the residual distribution method [220], or other time discretization techniques.

Here we will study the potential of a formulation which can be easily generalised on arbitrary unstructured meshes. In particular, we will consider the method obtained by only inverting in the elliptic phase the matrices generated when considering a P^1 finite element approximation. As we will show, provided that a third order method is used in the hyperbolic phase, this choice already gives dispersion properties equivalent to those of a fourth order method. As we will see later, the additional advantage of this approach, is to allow a direct embedding of wave breaking either by simply neglecting the non-hydrostatic contribution in the hyperbolic phase, or even with a tighter coupling of the two phases using the breaking indicator to smoothly turn off ϕ in the elliptic phase.

The objective of the following sections is to discuss the proposed methods. The analysis of the dispersion error of the resulting scheme is then provided in section §2.3, while the treatment of wave breaking is discussed in chapter 4.

2.1.3 Spatial domain discretization and notation

Let $[0, L]$ be the spatial domain, we consider a tessellation composed of elements $[x_i, x_{i+1}]$. We set in general $\Delta x = \min_i(x_{i+1} - x_i)$. For simplicity we assume in the following that the points are equally spaced, so that $x_{i+1} - x_i = \Delta x \ \forall i$, but non-uniform meshes can be used with the same methods discussed here with very little modifications. For a given node i , we will denote by C_i the cell $[x_{i-1/2}, x_{i+1/2}]$, with $x_{i+1/2} - x_{i-1/2} = \Delta x$.

On this mesh, we will denote by φ_i the standard hat shaped C^0 continuous Lagrange basis functions, and we will denote by $\mathbf{U}_{\Delta x}$ the piecewise continuous polynomial obtained as

$$\mathbf{U}_{\Delta x}(x, t) = \sum_i \varphi_i(x) \mathbf{U}_i(t).$$

In this paper we consider the case of P^1 piecewise linear polynomials.

2.1.4 Elliptic phase : continuous finite element formulation

The first step for solving system (2.6) is to compute separately the value of the auxiliary variable ϕ from (2.5). In this work we discretize equation (2.5) by means of a standard C^0 Galerkin finite

element approach. This discretization strategy passes by the writing of the variational form of the equation. The actual discretization is obtained by evaluating all the integrals by a numerical quadrature over each element of the discretization, with the assumption of piecewise linear variation of all the quantities involved $h_{\Delta x}$, $\eta_{\Delta x}$, $b_{\Delta x}$, $u_{\Delta x}$, $\phi_{\Delta x}$. Defining $\Phi = [\phi_1(t), \phi_2(t), \dots, \phi_N(t)]^T$ and $U = [u_1(t), u_2(t), \dots, u_N(t)]^T$, the final form of the Galerkin approximation of the problem can be written as:

$$(\mathbf{M}^G + \alpha \mathbf{T})\Phi = \mathbf{W} - \mathbf{R} \quad (2.7)$$

$$\mathbf{W} = \mathbf{T}\delta \quad (2.8)$$

$$\mathbf{R} = \mathbf{Q}[h, U] \quad (2.9)$$

with δ an approximation of $gh\eta_x$. The matrix \mathbf{M}^G is the Galerkin mass matrix, whose entries are

$$\mathbf{M}_{i,j}^G = \int_0^L \varphi_i \varphi_j \quad (2.10)$$

The matrix $\mathbf{T}(h_{\Delta x}, b_{\Delta x})$ is deduced immediately from the variational form of (2.3), by evaluating $a_{\mathcal{T}}(\varphi_i, \varphi_j)$. All computations done, we obtain (partial derivatives now denoted by $\partial_{(\cdot)}$ for the sake of clarity)

$$\begin{aligned} \mathbf{T}_{i,j}(h_{\Delta x}, b_{\Delta x}) = & \frac{1}{3} \int_0^L \partial_x \varphi_i h_{\Delta x}^2 \partial_x \varphi_j - \frac{1}{3} \int_0^L \partial_x \varphi_i h_{\Delta x} \partial_x h_{\Delta x} \varphi_j + \\ & + \frac{1}{2} \int_0^L \varphi_i \partial_x b_{\Delta x} \partial_x h_{\Delta x} \varphi_j - \frac{1}{2} \int_0^L \partial_x \varphi_i h_{\Delta x} \partial_x b_{\Delta x} \varphi_j + \\ & - \frac{1}{2} \int_0^L \varphi_i h_{\Delta x} \partial_x b_{\Delta x} \partial_x \varphi_j + \int_0^L \varphi_i (\partial_x b_{\Delta x})^2 \varphi_j \end{aligned} \quad (2.11)$$

having developed all the derivatives of $1/h_{\Delta x}$ terms in order to to explicitly remove the singularity w.r.t. h .

Proceeding similarly, we obtain for the operator $\mathbf{Q}(h_{\Delta x}, u_{\Delta x}, b_{\Delta x}, \delta_{b\Delta x})$

$$\begin{aligned} \mathbf{Q}_{i,j}(h_{\Delta x}, u_{\Delta x}, b_{\Delta x}, \delta_{b\Delta x}) = & -\frac{2}{3} \int_0^L \partial_x \varphi_i h_{\Delta x}^3 (\partial_x u_{\Delta x})^2 + \int_0^L \varphi_i \partial_x b_{\Delta x} h_{\Delta x}^2 (\partial_x u_{\Delta x})^2 + \\ & + \int_0^L \varphi_i \delta_{b\Delta x} h_{\Delta x}^2 u_{\Delta x} \partial_x u_{\Delta x} + \int_0^L \varphi_i \delta_{b\Delta x} h_{\Delta x} \partial_x h_{\Delta x} u_{\Delta x} + \\ & + \frac{1}{2} \int_0^L \varphi_i \partial_x \delta_{b\Delta x} h_{\Delta x}^2 u_{\Delta x} + \int_0^L \varphi_i \partial_x b_{\Delta x} \delta_{b\Delta x} h_{\Delta x} u_{\Delta x} \end{aligned} \quad (2.12)$$

The arrays δ and δ_b contain nodal values of auxiliary variables introduced to handle the third order derivatives. In particular, we have

$$(\mathbf{M}^G \delta)_i = \int_0^L \varphi_i g h_{\Delta x} \partial_x \eta_{\Delta x} \quad (2.13)$$

$$(\mathbf{M}^G \delta_b)_i = - \int_0^L \partial_x \varphi_i \partial_x b_{\Delta x} \quad (2.14)$$

The linear systems (2.13) and (2.14) can be solved very efficiently, being \mathbf{M}^G symmetric, positive defined and constant. On the contrary, the properties of the matrix $(\mathbf{M}^G + \alpha \mathbf{T})$ cannot be known *a priori*. However, the continuous finite element formulation used here inherits the coercivity property of the corresponding continuous operator \mathcal{T} , for which the interested reader can refer to [4]. While ensuring the existence of an inverse for this matrix, its computation, required in the solution of the linear algebraic system (2.7), remains the most computationally demanding process of our approach. In particular, matrix inversions have been performed using the Intel® oneAPI Math Kernel Library (oneMKL). For the \mathbf{M}^G matrix, we have stored the constant LU decomposition, which, on the contrary, has to be re-computed at each time step for $(\mathbf{M}^G + \alpha \mathbf{T})$.

The kind of discretization performed allows many degrees of freedom in the management of the several Galerkin mass matrices \mathbf{M}^G which appear in it and that can be lumped (or not) always remaining second order accurate. The optimization of the linear dispersion properties of the resulting schemes (see section §2.3), together with the research of the simplest configuration possible, led us to the choice of performing the lumping only in equation (2.14). This does not affect the linear dispersion properties of the scheme, due to the fact that \mathbf{Q} is nonlinear and that b is time-independent; so δ_b can be computed once at the beginning of the calculus and kept all along the simulation.

2.1.5 Hyperbolic phase : Finite Volume Scheme

Setting $\mathbf{U} = [h, hu]^T$, we will use the FV scheme to write the equations for averages of \mathbf{U} over the cells C_i , namely for

$$\mathbf{U}_i(t) = \frac{1}{\Delta x} \int_{C_i} \mathbf{U}(x, t).$$

Using (2.5)-(2.6), and following [20, 40, 125, 195], the semi-discrete form of the equations can now be written as :

$$\frac{d}{dt} \mathbf{U}_i = - \frac{1}{\Delta x} [\mathbf{F}_{i+1/2} - \mathbf{F}_{i-1/2}] + \frac{1}{\Delta x} \Delta \mathbf{S}_{bi} + \bar{\Phi} \quad (2.15)$$

where $\mathbf{F}_{i\pm 1/2}$ and $\Delta \mathbf{S}_{bi}$ are the numerical fluxes at each cell interface and the numerical topography source respectively. The last term is where the link with the elliptic phase is made. In particular, it stands:

$$\bar{\Phi} = \frac{1}{\Delta x} \int_{C_i} \begin{pmatrix} 0 \\ \phi_{\Delta x} \end{pmatrix} = \frac{1}{8} \begin{pmatrix} 0 \\ \phi_{i-1} + 6\phi_i + \phi_{i+1} \end{pmatrix}$$

having integrated exactly over C_i the piecewise linear polynomial $\phi_{\Delta x}$ obtained from the elliptic phase discussed in the previous subsection. The numerical fluxes $\mathbf{F}_{i\pm 1/2}$ at the cell interfaces can be evaluated by means of an exact or approximate Riemann solver. In this work we used the approximate Riemann solver of Roe [225] along with an upwind discretization of the topography source. The source terms are numerical treated as to satisfy the C-property and can be easily incorporated in this solver. The numerical fluxes in (2.15) are defined as:

$$\mathbf{F}_{i+1/2} = \mathbf{F}_{i+1/2}(\mathbf{U}_{i+1/2}^L, \mathbf{U}_{i+1/2}^R) = \frac{1}{2} (\mathbf{F}(\mathbf{U}_{i+1/2}^R) + \mathbf{F}(\mathbf{U}_{i+1/2}^L)) - \frac{1}{2} |\mathbf{A}|_{i+1/2} \Delta_{i+1/2} \mathbf{U} \quad (2.16)$$

where $\Delta(\cdot)_{i+1/2} = (\cdot)_{i+1/2}^R - (\cdot)_{i+1/2}^L$. $\mathbf{A}_{i+1/2}$ is the Roe average Jacobian matrix and is equal to $[\mathbf{X}|\mathbf{\Lambda}|\mathbf{X}^{-1}]_{i+1/2}$, where $\mathbf{X}_{i+1/2}$ and $\mathbf{X}_{i+1/2}^{-1}$ are the left and right eigenvector matrices respectively and $\mathbf{\Lambda}$ is the diagonal matrix with the eigenvalues in the diagonal.

The numerical integration with the upwind scheme presented up to now lead to approximations that are only first order accurate, if a constant distribution is assumed in each computational cell C_i . To achieve higher accuracy we evaluate the left and right states using a third order MUSCL extrapolation scheme [267, 148]. The reconstruction is performed for the variables $[h, u]$ as well as for the topography b . For the $(i + 1/2)$ interface the reconstructed values of the total water depth can be written as

$$\begin{aligned} h_{i+1/2}^L &= h_i + \frac{\psi(r_i)}{4} [(1 - \kappa)\Delta h_{i-1/2} + (1 + \kappa)\Delta h_{i+1/2}] \\ h_{i+1/2}^R &= h_{i+1} - \frac{\psi(r_{i+1})}{4} [(1 - \kappa)\Delta h_{i+3/2} + (1 + \kappa)\Delta h_{i+1/2}] \end{aligned} \quad (2.17)$$

where ψ is the limiter function with $r_i = \frac{\Delta h_{i-1/2}}{\Delta h_{i+1/2}}$, and where third order of accuracy in smooth regions is obtained for $\kappa = 1/3$. In this work the widely known MIN-MODE and MC limiters are used [163].

In the numerical solution, the correct discrete balance between the numerical fluxes and the numerical topography source is very important. A scheme that respects this balance is known in the literature as a well-balanced scheme. As it has been shown in [20], an upwind discretization approach should also be used for the bed topography term \mathbf{S}_b to avoid non-physical oscillations in the solution by satisfying the C-property in hydrostatic flow conditions (flow at rest). To satisfy the exact C-property, the topography source term must be linearized in the same way and evaluated in the same state (Roe-averaged state) as the flux terms. Of course, if an other Riemann solver is employed (e.g. HLL, HLLC) for the computation of the numerical fluxes, a different technique should be used, see for example [228, 255]. In this work, following [20, 125], the source term in (2.15) contains the following two terms

$$\Delta \mathbf{S}_{b,i} = \mathbf{S}_{b,i+1/2}^-(\mathbf{U}_{i+1/2}^L, \mathbf{U}_{i+1/2}^R) + \mathbf{S}_{b,i-1/2}^+(\mathbf{U}_{i-1/2}^L, \mathbf{U}_{i-1/2}^R) \quad (2.18)$$

where

$$\begin{aligned} \mathbf{S}_{b,i+1/2}^+(\mathbf{U}_{i+1/2}^L, \mathbf{U}_{i+1/2}^R) &= \frac{1}{2} \left[\mathbf{X}(\mathbf{I} + \mathbf{\Lambda}^{-1}|\mathbf{\Lambda}|)\mathbf{X}^{-1} \right]_{i+1/2} \tilde{\mathbf{S}}_{b,i+1/2}(\mathbf{U}_{i+1/2}^L, \mathbf{U}_{i+1/2}^R) \\ \mathbf{S}_{b,i+1/2}^-(\mathbf{U}_{i+1/2}^L, \mathbf{U}_{i+1/2}^R) &= \frac{1}{2} \left[\mathbf{X}(\mathbf{I} - \mathbf{\Lambda}^{-1}|\mathbf{\Lambda}|)\mathbf{X}^{-1} \right]_{i+1/2} \tilde{\mathbf{S}}_{b,i+1/2}(\mathbf{U}_{i+1/2}^L, \mathbf{U}_{i+1/2}^R) \end{aligned} \quad (2.19)$$

and with

$$\tilde{\mathbf{S}}_{b_{i+1/2}}(\mathbf{U}_{i+1/2}^L, \mathbf{U}_{i+1/2}^R) = \begin{bmatrix} 0 \\ -g \frac{h^L + h^R}{2} (b^R - b^L) \end{bmatrix}_{i+1/2}. \quad (2.20)$$

For the first order scheme, using the relation above, the discretization of the numerical flux term balances with the one of the topography source term for hydrostatic conditions. This gives in each mesh cell: $u = 0$ and $b^R - b^L = -(h^R - h^L)$. While this holds for the first order scheme, this is not the case when using higher reconstructions as we do here. In this case, following [125, 195], we include the additional correction term \mathbf{S}_b^* for maintaining the correct balance i.e.

$$\Delta \mathbf{S}_{b_i} = \mathbf{S}_{b_{i+1/2}}^- + \mathbf{S}_{b_{i-1/2}}^+ + \mathbf{S}_b^*(\mathbf{U}_{i+1/2}^L, \mathbf{U}_{i-1/2}^R) \quad (2.21)$$

with

$$\mathbf{S}_b^*(\mathbf{U}_{i+1/2}^L, \mathbf{U}_{i-1/2}^R) = \begin{bmatrix} 0 \\ -g \frac{h_{i-1/2}^R + h_{i+1/2}^L}{2} (b_{i-1/2}^R - b_{i+1/2}^L) \end{bmatrix}.$$

2.1.6 Hyperbolic phase : Finite Element Scheme

Two FE methods are considered here. The first is a classical C^0 Galerkin approximation of the two equations (2.6). For an internal node i , the discrete continuous Galerkin equations are readily obtained by evaluating the integrals (set $q = hu$)

$$\begin{aligned} \int_0^L \varphi_i \partial_t h_{\Delta x} - \int_0^L \partial_x \varphi_i q_{\Delta x} &= 0 \\ \int_0^L \varphi_i \partial_t q_{\Delta x} - \int_0^L \partial_x \varphi_i \left[\frac{q_{\Delta x}^2}{h_{\Delta x}} + g \frac{h_{\Delta x}^2}{2} \right] - \int_0^L \varphi_i \tilde{S}_b &= \int_0^L \varphi_i \phi_{\Delta x} \end{aligned} \quad (2.22)$$

with $\tilde{S}_b = -gh \partial_x b$. With the notation of the previous section, the integrals can be approximated as [222]

$$\mathbf{M}^G \frac{d}{dt} \mathbf{U} = -\frac{1}{2} [\mathbf{F}(\mathbf{U}_{i+1}) - \mathbf{F}(\mathbf{U}_{i-1})] + \frac{1}{2} \tilde{\mathbf{S}}_{b_{i+1/2}} + \frac{1}{2} \tilde{\mathbf{S}}_{b_{i-1/2}} + \overline{\Phi}^G \quad (2.23)$$

where \mathbf{M}^G is the Galerkin mass matrix defined in (2.10).

By analogy with (2.15), we use the notation $\overline{\Phi}$ for the contribution of the non-hydrostatic terms, which in this case is given by

$$\overline{\Phi}^G = \mathbf{M}^G \Phi. \quad (2.24)$$

As shown in [262, 222], scheme (2.23) is fourth order accurate in space on regular meshes, when the shallow water limit is considered.

To obtain a discretization with some shock capturing capabilities, we consider the upwind stabilized method used in [222, 8, 7] (see also [126]). In particular, introducing the local residual

$$\mathbf{R}_{\Delta x} = \begin{pmatrix} \partial_t h_{\Delta x} + \partial_x q_{\Delta x} \\ \partial_t q_{\Delta x} + \partial_x (q_{\Delta x}^2/h_{\Delta x} + gh_{\Delta x}^2/2) - \tilde{S}_b - \phi_{\Delta x} \end{pmatrix}, \quad (2.25)$$

obtained by replacing in the continuous equations the discrete approximation of the unknowns, we consider the streamline upwind scheme :

$$\mathbf{M}^G \frac{d}{dt} \mathbf{U} = -\frac{1}{2} [\mathbf{F}(\mathbf{U}_{i+1}) - \mathbf{F}(\mathbf{U}_{i-1})] + \frac{1}{2} \tilde{\mathbf{S}}_{b_{i+1/2}} + \frac{1}{2} \tilde{\mathbf{S}}_{b_{i-1/2}} + \bar{\Phi}^G - \sum_{j=0}^1 \int_{x_{i+j-1}}^{x_{i+j}} A \partial_x \varphi_i \tau_{\text{SU}} \mathbf{R}_{\Delta x}.$$

In the last expression, the matrix τ_{SU} is a scaling parameter in practice defined as [126, 222]

$$\tau_{\text{SU}} = \frac{\Delta x}{2} |A|^{-1}.$$

With this definition, using (2.25), one easily shows that the streamline upwind scheme can be written as

$$\mathbf{M}^{\text{SU}} \frac{d}{dt} \mathbf{U} = - [\mathbf{F}_{i+1/2}(\mathbf{U}_i, \mathbf{U}_{i+1}) - \mathbf{F}_{i+1/2}(\mathbf{U}_{i-1}, \mathbf{U}_i)] + \mathbf{S}_{b_{i+1/2}}^-(\mathbf{U}_i, \mathbf{U}_{i+1}) + \mathbf{S}_{b_{i-1/2}}^+(\mathbf{U}_{i-1}, \mathbf{U}_i) \bar{\Phi}^{\text{SU}} \quad (2.26)$$

where the numerical fluxes and sources have exactly the same expression as in (2.16) and (2.19) respectively, and where the entries of the Streamline Upwind mass matrix now couple the h and q ODEs and depend on the sign of the shallow water flux Jacobian matrix A . In particular

$$[\mathbf{M}^{\text{SU}} \mathbf{V}]_i = \frac{\Delta x}{6} \mathbf{V}_{i-1} + \frac{2\Delta x}{3} \mathbf{V}_i + \frac{\Delta x}{6} \mathbf{V}_{i+1} + \frac{\Delta x}{4} \text{sign}(A_{i-1/2}) (\mathbf{V}_{i-1} + \mathbf{V}_i) - \frac{\Delta x}{4} \text{sign}(A_{i+1/2}) (\mathbf{V}_{i+1} + \mathbf{V}_i) \quad (2.27)$$

By analogy with (2.15), we have used the notation $\bar{\Phi}$ for the contribution of the non-hydrostatic terms, which in this case is given by

$$\bar{\Phi}^{\text{SU}} = \mathbf{M}^{\text{SU}} \Phi.$$

As shown in [222, 8, 7], to which we refer for all additional details, the stabilized FE method (2.26) is third order accurate in space when the shallow water limit is considered, and it preserves exactly steady state still flat free surface states.

Finally, in order to handle moving bores and dry areas, we introduce as in [7] the following nonlinear splitting of the mass matrix (sc stands for shock capturing) :

$$\begin{aligned} [\mathbf{M}^{\text{SU-sc}} \mathbf{V}]_i &= \Delta x \mathbf{V}_i + \psi_{i+1/2} \frac{\Delta x}{2} \left[\frac{1}{3} (\mathbf{V}_{i+1} - \mathbf{V}_i) - \frac{\text{sign}(A_{i+1/2})}{2} (\mathbf{V}_{i+1} + \mathbf{V}_i) \right] \\ &\quad + \psi_{i-1/2} \frac{\Delta x}{2} \left[\frac{1}{3} (\mathbf{V}_{i-1} - \mathbf{V}_i) + \frac{\text{sign}(A_{i-1/2})}{2} (\mathbf{V}_{i-1} + \mathbf{V}_i) \right] \end{aligned} \quad (2.28)$$

The final form of the scheme reads

$$\mathbf{M}^{\text{SU-sc}} \frac{d}{dt} \mathbf{U} = - [\mathbf{F}_{i+1/2}(\mathbf{U}_i, \mathbf{U}_{i+1}) - \mathbf{F}_{i+1/2}(\mathbf{U}_{i-1}, \mathbf{U}_i)] + \mathbf{S}_{b_{i+1/2}}^-(\mathbf{U}_i, \mathbf{U}_{i+1}) + \mathbf{S}_{b_{i-1/2}}^+(\mathbf{U}_{i-1}, \mathbf{U}_i) \Delta x \bar{\Phi}^{\text{SU-sc}} \quad (2.29)$$

The quantity $\psi_{i\pm 1/2}$ in (2.28) is a limiter function. For $\psi = 0$ the scheme reduces to the first order version of Roe's scheme, which is basically the first order version of (2.15). For $\psi = 1$ the third order finite element method (2.26) is recovered. Any function can be used to detect smooth areas and dry or shocked regions.

Here, we use the smoothness sensor proposed in [8, 7] and based on two different approximations of the curvature of the free surface elevation η :

$$\psi_{i+1/2} = \min(\psi_i, \psi_{i+1}), \quad \psi_i = \min\left(1, \alpha \frac{|\int_0^L \varphi_i \partial_x \eta \Delta x|}{|\int_0^L \partial_x \varphi_i \partial_x \eta \Delta x + V_i|}\right)$$

where V_i is obtained as the fourth order finite difference approximation of $\partial_{xx}\eta_i$, and with $\alpha = \frac{1}{9}$ as in [8, 7].

2.1.7 Well-balancing, wet/dry front treatment, mass conservation

In order to identify the dry cells we use the technique described in [221, 219]. In particular, we introduce two threshold parameters ϵ_h^{wd} and ϵ_u^{wd} , acting independently on the water height and the velocity respectively. So, if H on a node is less than ϵ_h^{wd} , that node is considered as dry. This parameter is very small, compared to the mesh size (typical values range are between $10^{-9} - 10^{-6} m$). The second parameter is used to avoid division by zero and is set to

$$\epsilon_u^{wd} = \frac{\Delta x^2}{L^2}$$

with L the length of the spatial domain. If on a node $h \leq \epsilon_h^{wd}$, the velocity in that node is set to zero. To avoid losing mass, and guarantee absolute mass conservation, we follow the treatments proposed in [65, 39, 166] where the total mass in nodes with $h \leq \epsilon_h^{wd}$ is redistributed uniformly to the rest of the domain.

Furthermore, the presence of dry areas should not affect the ability of the schemes to preserve steady states involving flat free surface still water. To ensure this property, we use a standard technique consisting in redefining the bed elevation at the emerging dry cell [40, 39] as:

$$\Delta b = \begin{cases} h^L & \text{if } h^L > \epsilon_h^{wd} \text{ and } h^R \leq \epsilon_h^{wd} \text{ and } b^R < (b^R - b^L) \\ (b^L - b^R) & \text{otherwise} \end{cases} \quad (2.30)$$

when a wet/dry front exists between computational cells with (reconstructed) face values L and R. For both FV and FE schemes this modification is applied in the computation of the source term \tilde{S}_b . A similar treatment holds if R is wet and L dry. Just for the FV scheme and for the flow in motion over adverse slopes, further modifications are made following [43, 135]. Finally, and as to properly detect regions in proximity of dry areas, we use an exponential filter proposed in [221, 219]. This exponential function is embedded in the limiters and activated whenever the limiter is on.

2.2 Time integration, boundary conditions, and friction

2.2.1 High order time integration methods

Similarly to the spatial domain, the temporal domain is discretized by a set of non-overlapping slabs $[t^n, t^{n+1}]$. We will denote by $\Delta t^{n+1} = t^{n+1} - t^n$. For generality, three different time discretizations are compared in this work. One is a method quite classical in the context of Boussinesq-type numerical models, while the other two have been chosen as representatives of boundedness or strong stability preserving methods. For all of these methods, the time step is computed by means of the CFL condition

$$\Delta t^{n+1} = \text{CFL} \frac{\Delta x}{\max_i (|u_i^n| + \sqrt{gh_i^n})} \quad (2.31)$$

For the shallow water equations, the stability condition for the first order methods used here is $\text{CFL}_c = 1$ when using the first order explicit Euler method. Following [108, 210], we will speak of effective CFL as the ratio CFL_c/p , with p the number of right hand side evaluations in one time step.

The first time integration scheme we consider is the Adams Bashforth-Adams Moulton (AM) predictor-corrector method, well known in the community of Boussinesq modelling [269, 228]. For the ODE

$$\mathbf{U}' = \mathcal{L}(\mathbf{U}) \quad (2.32)$$

this time integration scheme requires two stages :

1. Predictor stage (Adams-Basforth method)

$$\mathbf{U}^p = \mathbf{U}^n + \frac{\Delta t}{12} \left[23\mathcal{L}(\mathbf{U}^n) - 16\mathcal{L}(\mathbf{U}^{n-1}) + 5\mathcal{L}(\mathbf{U}^{n-2}) \right] \quad (2.33)$$

2. Corrector stage (Adams-Moulton method)

$$\mathbf{U}^{n+1} = \mathbf{U}^n + \frac{\Delta t}{24} \left[9\mathcal{L}(\mathbf{U}^p) + 19\mathcal{L}(\mathbf{U}^n) - 5\mathcal{L}(\mathbf{U}^{n-1}) + \mathcal{L}(\mathbf{U}^{n-2}) \right] \quad (2.34)$$

The Adams predictor corrector has stability properties close to those of the explicit Euler scheme, with respect to which we thus have an affective CFL of 1/2 (2 stages for the same time step magnitude). The method is obtained by a combination of Lagrange polynomial extrapolation, and polynomial interpolation to evaluate the integral of \mathcal{L} in the interval $[t^n, t^{n+1}]$. For the autonomous ODE (2.32), fourth order of accuracy can be easily shown by standard truncation error analysis. The technique used to derive the method can be generalized to include variable time step sizes, but this is way beyond the scope of this paper. A simple technique to account for variable time step sizes, while keeping constant the coefficients in the scheme, is to re-correct iteratively with the Adams-Moulton step, stopping when the relative magnitude of the correction is below a given treshold (cf. [269, 228, 85]). In practice, however, the improvement brought by this multi-corrector procedure

are very small, and a single correction is already enough to obtain accurate results also for variable step sizes (see [269]).

We also test the three stages third order SSP Runge-Kutta (RK3) scheme reading [108]

$$\begin{aligned} \mathbf{U}^p &= \mathbf{U}^n + \Delta t \mathcal{L}(\mathbf{U}^n) \\ \mathbf{U}^{2p} &= \frac{3}{4}\mathbf{U}^n + \frac{1}{4}\mathbf{U}^p + \frac{\Delta t}{4}\mathcal{L}(\mathbf{U}^p) \\ \mathbf{U}^{n+1} &= \frac{1}{3}\mathbf{U}^n + \frac{2}{3}\mathbf{U}^{2p} + \frac{2\Delta t}{3}\mathcal{L}(\mathbf{U}^{2p}) \end{aligned} \quad (2.35)$$

The RK3 belongs to the family of strong stability preserving multi-stage methods with positive coefficients, inheriting the same stability properties of the explicit Euler scheme. In particular, compared to the latter, the RK3 has a CFL condition of 1, giving an effective CFL of 1/3.

Lastly, we have tested the third order extrapolated backward differencing method (eBDF3) [154] reading

$$\alpha_{n+1}\mathbf{U}^{n+1} + \alpha_n\mathbf{U}^n + \alpha_{n-1}\mathbf{U}^{n-1} + \alpha_{n-2}\mathbf{U}^{n-2} = \beta_n \mathcal{L}(\mathbf{U}^n) + \beta_{n-1} \mathcal{L}(\mathbf{U}^{n-1}) + \beta_{n-2} \mathcal{L}(\mathbf{U}^{n-2}) \quad (2.36)$$

where the weights take the form

$$\begin{aligned} \alpha_{n+1} &= \frac{1}{\Delta t^{n+1}} + \frac{1}{\Delta t^{n+1} + \Delta t^n} + \frac{1}{\Delta t^{n+1} + \Delta t^n + \Delta t^{n-1}}, \\ \alpha_n &= -\frac{(\Delta t^{n+1} + \Delta t^n)(\Delta t^{n+1} + \Delta t^n + \Delta t^{n-1})}{\Delta t^{n+1}\Delta t^n(\Delta t^n + \Delta t^{n-1})}, \\ \alpha_{n-1} &= \frac{\Delta t^{n+1}(\Delta t^{n+1} + \Delta t^n + \Delta t^{n-1})}{(\Delta t^{n+1} + \Delta t^n)\Delta t^n\Delta t^{n-1}}, \\ \alpha_{n-2} &= -\frac{\Delta t^{n+1}(\Delta t^{n+1} + \Delta t^n)}{(\Delta t^{n+1} + \Delta t^n + \Delta t^{n-1})(\Delta t^n + \Delta t^{n-1})\Delta t^{n-1}} \end{aligned}$$

and

$$\begin{aligned} \beta_n &= \frac{(\Delta t^{n+1} + \Delta t^n)(\Delta t^{n+1} + \Delta t^n + \Delta t^{n-1})}{\Delta t^n(\Delta t^n + \Delta t^{n-1})}, \quad \beta_{n-1} = -\frac{\Delta t^{n+1}(\Delta t^{n+1} + \Delta t^n + \Delta t^{n-1})}{\Delta t^n\Delta t^{n-1}}, \\ \beta_{n-2} &= \frac{\Delta t^{n+1}(\Delta t^{n+1} + \Delta t^n)}{(\Delta t^n + \Delta t^{n-1})\Delta t^{n-1}} \end{aligned}$$

The eBDF3 is part of a family of high order explicit multi step methods verifying, under a time step restriction, the same boundedness preserving property of the explicit Euler scheme. Compared to the latter, the eBDF3 has a stability condition of CFL= 1/3 [127], which gives the same effective CFL of the RK3 method.

2.2.2 Boundary conditions and internal source function

To define differential problems, boundary conditions must be introduced. In this work we use two types of boundary conditions, depending on the examined test case: solid (reflective) wall and absorbing boundary conditions. For the FV scheme with third-order MUSCL reconstruction,

the reconstructed values on the first and last cell of the computational domain are computed using neighbouring ghost cells. More informations can be found at [135]. For the FE schemes, ghost cells are in no need since it is a node centered scheme and the degrees of freedom are located directly on the physical boundary.

Absorbing boundaries are also applied in order to dissipate completely the energy of the incoming waves, trying at the same time to eliminate any non physical reflection. This kind of boundaries require the definition of a sponge layer in which the surface elevation and the momentum are damped by multiplying their values by a coefficient $m(x)$ defined as [137]

$$m(x) = \sqrt{1 - \left(\frac{x - d(x)}{L_s}\right)^2}. \quad (2.37)$$

L_s is the sponge layer width and $d(x)$ is the normal distance between the cell center with coordinates x and the absorbing boundary. Typical values for the sponge layer width are related to the wavelength of the incoming wave: $L \leq L_s \leq 1.5L$. Thus, longer wavelengths require longer sponge layers.

Wave generation in the model is achieved by using the internal wave generator of Wei et al. [268]. In [268] the wave generator of free surface waves is introduced as a source function added to the mass equation. It is derived using the equations of Nwogu [198], but it can be used for many types of Boussinesq-type equations by changing the dispersion relation used in the generator. In this work, as to be compatible with the equations of GN, we use the dispersion relation (1.24).

2.2.3 Friction terms discretization

An explicit treatment of the friction can produce numerical oscillations [39, 194, 193] when the roughness coefficient is high. For this reason, we use the technique proposed by [39, 193]. More precisely, for all schemes, at the end of each time step, we have :

$$(hu)_i^{n+1} = (hu)_i^* - g(hS_f)_i^{n+1} \Delta t^n \quad (2.38)$$

where all the values signed with $*$ are the values computed without the friction. Using $(S_f)_i = (uR_f)_i = u_i \frac{N_m^2 \|u_i\|}{h_i^{4/3}}$ and substituting in the above equation, we have :

$$(hu)_i^{n+1} = (hu)_i^* - g(huR_f)_i^{n+1} \Delta t^n = (hu)_i^* - g(hu)_i^{n+1} [(1 - \theta)(R_f)_i^{n+1} + \theta(R_f)_i^n] \Delta t^n \quad (2.39)$$

with N_m being the Manning roughness coefficient. Now, by separating explicit and implicit part and by assuming that $R_f^{n+1} = R_f^*$, we can write:

$$(hu)_i^{n+1} = \frac{(hu)_i^* - \theta g(hu)_i^n (R_f)_i^n \Delta t^n}{1 + (1 - \theta)g(R_f)_i^* \Delta t^n} \quad (2.40)$$

When the implicitness parameter θ is set to zero, the friction source term is computed in a completely implicit manner, while it is computed in a totally explicit point wise manner when $\theta = 1$. In all the computations shown in this work the value $\theta = 0$ has been used. This modification, albeit very robust, makes the scheme locally first order in time when friction is dominating. This is especially the case in wet-dry fronts. Techniques to construct high order variants for the eBFD and Runge-Kutta methods are discussed in [128, 52], and will be exploited in the future.

2.3 Semi-discrete error analyses

2.3.1 Time continuous analysis

The analytical expression of the linear dispersion relation for the present model has been already given in chapter 1 and will be here rewritten (with $d = h_0$ since the bottom is flat):

$$\omega_{\text{GN}}^2 = gh_0k^2 \frac{1 + \frac{\alpha-1}{3}k^2h_0^2}{1 + \frac{\alpha}{3}k^2h_0^2}. \quad (2.41)$$

As already explained, this relation can be recovered by means of a Fourier analysis on a horizontal bottom performed on the linearized system of equations:

$$(I + \alpha T_{LIN})\phi = T_{LIN}(gh_0\eta_x) \quad (2.42)$$

$$\eta_t + h_0u_x = 0 \quad (2.43)$$

$$h_0u_t + gh_0\eta_x = \phi$$

where h_0 represents the constant water depth and $T_{LIN}(\cdot) = -\frac{1}{3}h_0^2(\cdot)_{xx}$.

Having a low dispersion error w.r.t. the model, is of paramount importance for any numerical scheme that wants to be applied to the study of near-shore wave propagation. In this section we will perform an analysis on the discrete dispersion relations of the several schemes here implemented: continuous finite element (with and without the upwind stabilization) and finite volume; comparing them and finding the best possible configuration of the discretization which minimizes the dispersion error.

We performe our analysis replacing the nodal values of η and u in each discretized scheme by a propagating Fourier mode $W_i = W_0e^{\nu_{\Delta x}t + jkx_i}$; where $\nu_{\Delta x} = \xi_{\Delta x} + j\omega_{\Delta x}$ and $\xi_{\Delta x}$ and $\omega_{\Delta x}$ represents respectively the amplification rate and the phase speed, while k is the wave number of the Fourier mode. The algebraic expression obtained in such a way can be easily rewritten in terms of the nodal value W_i , using relations of the type $W_{i\pm 1} = e^{\pm jk\Delta x}$. The resulting system of equations constitutes a complex eigenvalue problem, whose solution is the dispersion factor $\nu_{\Delta x}$.

The dispersion formula obtained are hard to interpret, so we choose to present the results in the form of comparison plots, in which the dispersion error curves of the model are compared among them and w.r.t. the ones given by second (FD2) and fourth (FD4) order finite different discretization schemes. For the sake of brevity and clarity, in the following, we will just present the concluding remarks. The reader can refer to [97] for more details.

Finite element

When also the hyperbolic part is discretized with the centered Galerkin FE scheme described in (2.23), the system obtained for the nodal values of a Fourier mode is

$$\left(\tilde{\mathbf{M}}^G - \frac{\alpha h_0^2}{3} \tilde{\mathbf{S}}^G\right) \phi_i = -\frac{g h_0^3}{3} \tilde{\mathbf{T}}^G \left(\tilde{\mathbf{M}}^G\right)^{-1} \eta_i \quad (2.44)$$

$$\tilde{\mathbf{M}}^G \nu_{\Delta x} \eta_i + h_0 \tilde{\mathbf{F}}^G u_i = 0 \quad (2.45)$$

$$\tilde{\mathbf{M}}^G \nu_{\Delta x} u_i + g \tilde{\mathbf{F}}^G \eta_i = \frac{1}{h_0} \tilde{\mathbf{M}}^G \phi_i$$

While different expressions are obtained for the second and third equations when other schemes are used in the hyperbolic phase, note that the first one remains the same in all the cases considered. The discrete phase $\omega_{\Delta x}$ is computed by imposing that the above linear system admits a non-trivial solution, and hence that the associated matrix has zero determinant.

The results obtained from (1.24) are summarized in figure 2.1 in terms of the relative dispersion error w.r.t. the exact phase (2.41). The curves are obtained for the two values $kh_0 = 0.5$ and $kh_0 = 2.5$, corresponding to a long and to a short(er) wave (or equivalently to shallow and deep waters) respectively, and plotted against the inverse of the number of nodes per wavelength N . The relative errors of the FD2 and FD4 finite difference schemes are also reported as a reference (see [97] for detailed expressions). The pictures show that the centered Galerkin scheme provides a dispersion error which is comparable or better than the fourth order finite difference method.

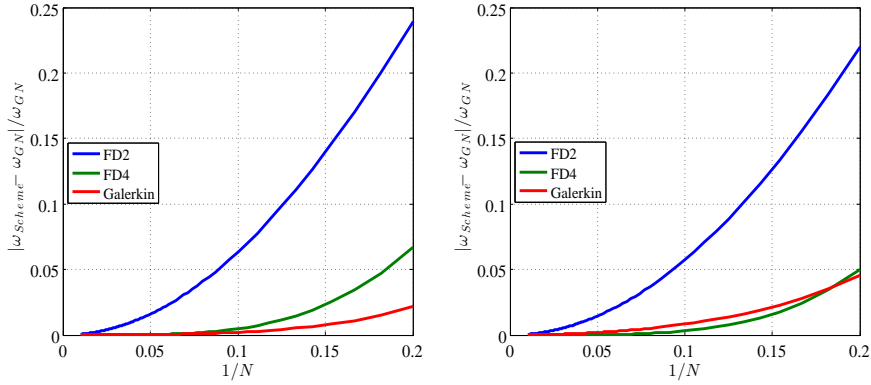


Figure 2.1: Dispersion error for the centered Galerkin FE scheme for $kh_0 = 0.5$ (left) and $kh_0 = 2.5$ (right): comparison w.r.t. the FD2 and FD4 schemes.

In section §2.1.4 we mentioned some implementation choices associated to the finite element solution of the elliptic problem (2.5). These boil down to the type of quadrature used to evaluate some of the integrals, or, in other words, to the use of mass lumping for the mass matrices appearing in equations (2.7), (2.13) and (2.14). The first two, in particular, influence the form of the $\tilde{\Phi}_{LIN}$ injected in the hyperbolic component. We have studied the impact of this choice with interesting results. Four possibilities exist, for which explicit calculations are provided in our work [97]:

1. mass lumping is performed in both (2.7) and (2.13), in which case the elliptic solver is exactly the same obtained with the FD2 method ;
2. mass lumping is only performed in the computation of the auxiliary variable (2.13), and not in (2.7). In this case, the elliptic system is not identical to the FD2 one, however the third order derivative formula obtained is exactly the same as the one used in FD2 ;
3. no mass lumping is performed for the auxiliary variable (2.13), while (2.7) is lumped. In this case, the elliptic system is the same as the FD2 one, however, its right hand side contains an approximation of the third order derivatives obtained starting from an L^2 projection of the gradients of the free surface ;
4. no mass lumping is performed, leading to the first in (2.44) ;

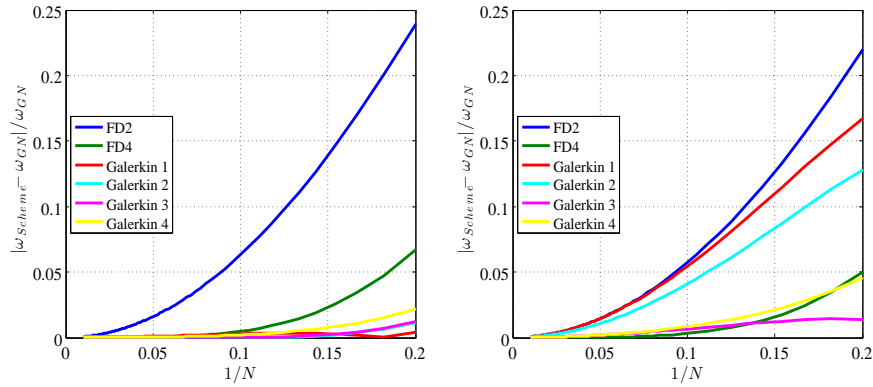


Figure 2.2: Dispersion error of the Galerkin scheme for $kh_0 = 0.5$ (left) and $kh_0 = 2.5$ (right): impact of lumping strategy.

The differences between these four cases are visualized in figure 2.2 for the continuous Galerkin scheme, showing that in deep waters the first and second configurations provide a considerable increase in error. This clearly means that the most relevant parameter is the approximation of the third order derivative. It appears from the results that the use of an improved approximation of the free surface gradient in the third order derivatives is the key element to reduce the dispersion error. In particular, the configurations 1 and 2 provide errors of the same magnitudes as the FD2 scheme, despite the fact that the hyperbolic phase, and part of the elliptic phase, are not the same. These are precisely the cases in which the approximation of the third order operator is the same as in FD2.

SUPG scheme

We repeat the analysis for the upwind stabilized finite element scheme (SUPG). We refer to [97] for details and analytical expressions. Please, note that a system similar to (2.44)-(2.45) has to be analyzed and, in particular, that the first equation of this system is exactly the equation (2.44) itself.

In figure 2.3, we visualize the impact of the mass lumping strategy on the dispersion error, as done for the un-stabilized method . Also in this case, for short waves/deep waters the largest errors

are obtained whenever the third order derivatives are approximated with the simple FD2 formula (cases 1 and 2). In the other two cases, involving an improved treatment of this term, we obtain errors comparable or even smaller than those of the non-stabilized method, confirming the results already obtained in [222].

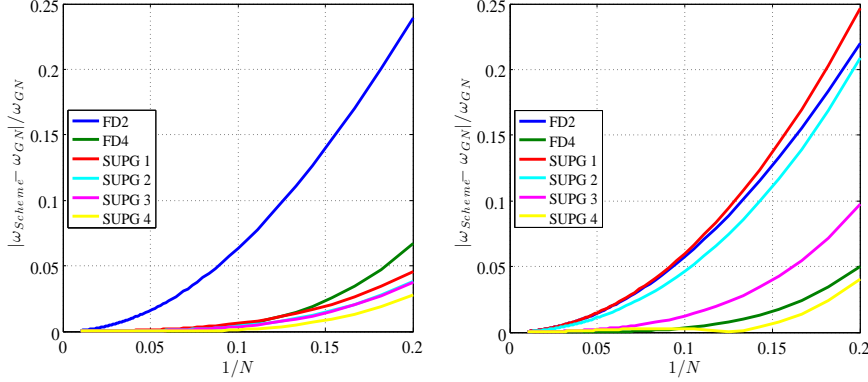


Figure 2.3: Dispersion error of the SUPG scheme for $kh_0 = 0.5$ (left) and the $kh_0 = 2.5$ (right): impact of lumping strategy.

Finite volume

We repeat the same exercise for the finite volume scheme. Here we have, of course to be more careful since the evolving quantities are the averaged values in a cell and not the nodal values like in the finite element. Again, we need to replace a Fourier mode into our scheme. So we assume that for a wavenumber k , the solution has the form $\mathbf{U} = \mathbf{U}_0 e^{\nu_h t + j k x}$, with j the imaginary unit, and where $\nu_h = \xi_h + j \omega_h$ and ξ_h , ω_h represent the discrete amplification rate and phase respectively. We can indeed find that

$$\bar{\mathbf{U}}_i = \int_{x_{i-1/2}}^{x_{i+1/2}} \mathbf{U}_0 e^{\nu_h t + j k x} = \frac{\mathbf{U}_i}{j \mu_h} (e^{j \frac{\mu_h}{2}} - e^{-j \frac{\mu_h}{2}}) = \frac{\mathbf{U}_i}{j \mu_h} 2 \sin\left(\frac{\mu_h}{2}\right) \quad (2.46)$$

with $\mathbf{U}_i = \mathbf{U}_0 e^{\nu_h t + j k x_i}$, and $\mu_h = kh$. Using this relation consistently, and replacing in the one-dimensional version of the scheme we obtain

$$\begin{aligned} j(\nu_h C - B) \eta_i + h_0 A u_i &= 0 \\ g A \eta_i + j(\nu_h C - B) u_i &= -\mu_h \frac{1}{h_0} M^{FV} D \eta_i. \end{aligned} \quad (2.47)$$

The right hand side of the second equation is the inverse of the Fourier symbol of the finite element discretization of the elliptic equation reducing in 1D to a Poisson equation (cf. e.g. [97]). The coefficients A , B , C , D are reported in [138]. The impact of the definition of the matrix M^{FV} arising depending on the quadrature of Φ is also provided. Only the most significant results are left here for clarity. These are obtained when all matrices are evaluated exactly as we can see also in

figure 2.6. Straightforward computations show that the phase speed provided by the discrete scheme is :

$$\omega_h^2 = (ghA^2 + \mu M^{FV} AD)/C^2. \quad (2.48)$$

Figure 2.4 plots the relative dispersion errors (rde) $|\omega_s - \omega_{gn}|/\omega_{gn}$ with respect to the dispersion relation of the eGN equations (2.41). For comparison and sake of reference, we also plot in the same pictures the relative dispersion errors provided by a second and fourth order finite difference schemes (see [97, 222] for the full expressions). The pictures show that dispersion error of our scheme is smaller or close to the one of FD4 depending on the number of nodes per wavelength. For completeness, we also plot on figure 2.5 the error $|\omega_s - \omega_{airy}|/\omega_{airy}$ with respect to the exact dispersion relation $\omega_{airy}^2 = gk^2 \tanh(kh_0)$. We observe there a kind of compensation between the discretization and modeling errors, so that for $N = 15$ and $kh > 1.5$ the scheme has a lower error w.r.t the exact dispersion relation than it has wrt the Green-Naghdi one. This is related to the interaction of the phase advance/lag error of the scheme and the form of the phase of the Boussinesq model. This finding may be used in the future as a design criterion for low order (second and third) schemes in the context of Boussinesq models.

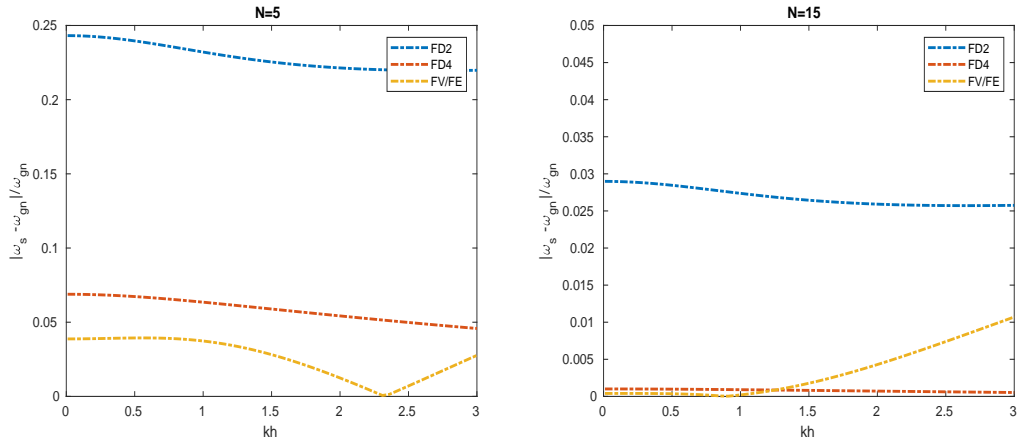


Figure 2.4: Dispersion error with respect to ω_{gn} for nodes per wave length $N = 5$ and $N = 15$

For completeness, figure 2.6 reports the main findings for the hybrid Galerkin-FV scheme of section §2.1.5. Once more, the critical element to obtain low errors in deeper waters is the approximation of the third order derivative. The use of the FD2 approximation for this term (cases 1 and 2) provides error levels comparable to those of the FD2 scheme. The improvement in the approximation of the nodal gradient (2.13) leads to a reduction of the error of a factor three or four, providing errors close to those of the FD4 method. The best results are obtained in this case when no mass lumping is performed.

Time continuous analysis: summary

This analysis has allowed to highlight the following results. First, the behaviour of the schemes is quite similar, despite the different treatment of the hyperbolic part. It appears that the treatment of

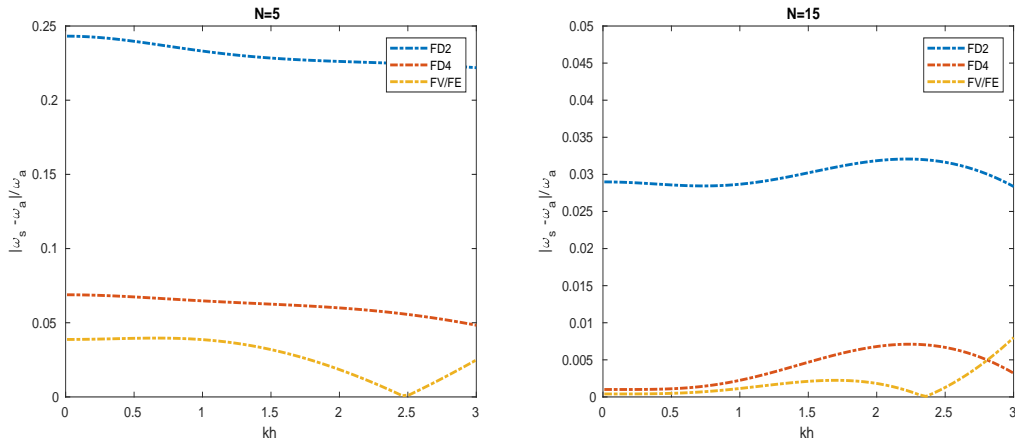


Figure 2.5: Dispersion error with respect to ω_{airy} for nodes per wave length $N = 5$ and $N = 15$

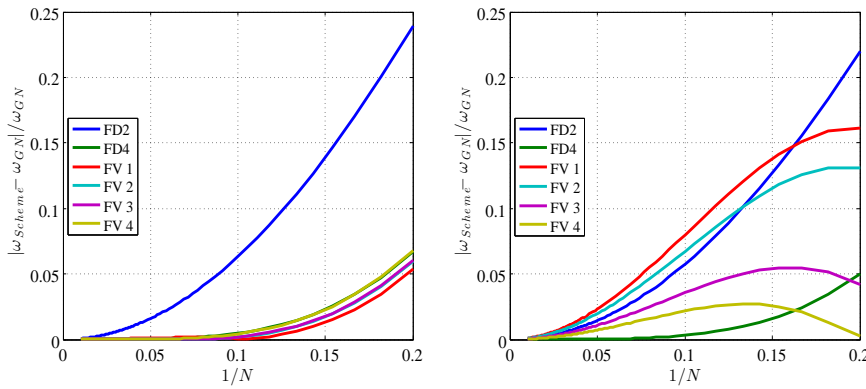


Figure 2.6: Dispersion error for the FV scheme for $kh_0 = 0.5$ (left) and the $kh_0 = 2.5$ (right): impact of lumping strategy.

the third order derivatives is very important, and in particular that the use of exact quadrature in the L^2 projection defining the auxiliary variable (2.13), is fundamental to reduce the error for deeper water/shorter waves. When no lumping is performed, the errors are similar or smaller than those provided by fourth order finite differences.

Finally, these similarities allow to provide a general recipe for the elliptic solver, as, for all the methods involved, the choice of the approach 4 allows to reduce the dispersion errors to those of the FD4 scheme or below. A summary of the resulting error curves is reported on figure 2.7 confirming the above observations.

2.4 Numerical tests and results

Since most of the standard numerical tests were presented in the previous chapter, we will only present three test cases here to confirm the performance of our scheme

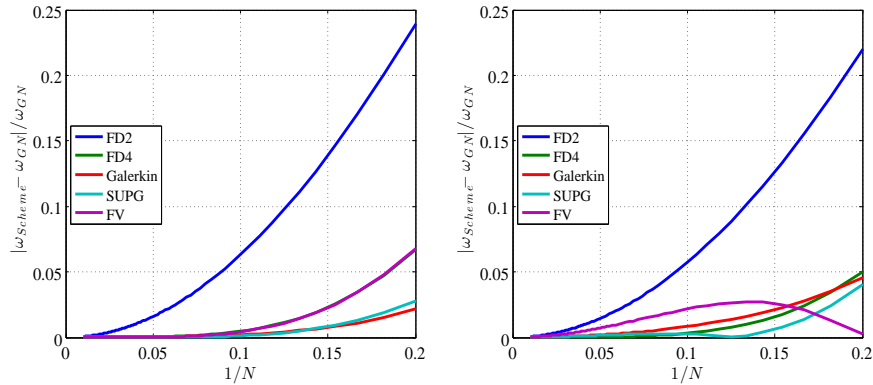


Figure 2.7: Dispersion error of FD2, FD4, Galerkin, SUPG, and FV schemes. Left: $kh_0 = 0.5$. Right: $kh_0 = 2.5$.

2.4.1 Space-time grid convergence

We perform a convergence analysis w.r.t to space and time step size. The physical case considered is the propagation of a solitary wave over a flat bed, with depth $h_0 = 10m$, and with $\epsilon = 0.2$. The domain is of $2000m$, $[0, 2000]$ and the initial wave was placed in $x_0 = 1000m$. For this case, an analytical solution is available. The test case is performed on a set of six meshes with $dx = 5, 2.5, 1.25, 0.625, 0.3125, 0.1562m$, and with corresponding time step sizes refined according to (2.31), with $CFL \approx 0.2$. At $T = 1sec$ the relative error $E_{L_2}(h) = \|h_{num} - h_{ex}\|_2 / \|h_{ex}\|_2$ on the total water depth is computed, where h_{num} is the numerical solution and h_{ex} is the analytical one.

The convergence of the L^2 error is plotted in Figure 2.8, where the slopes 2.5 and 3 are also plotted for reference. Similar behaviours are observed with other norms. The slopes obtained from the error reveal convergence rates in between 2.5 and 3 for all the combinations, showing that the dominant component of the error is the one related to the spatial discretization.

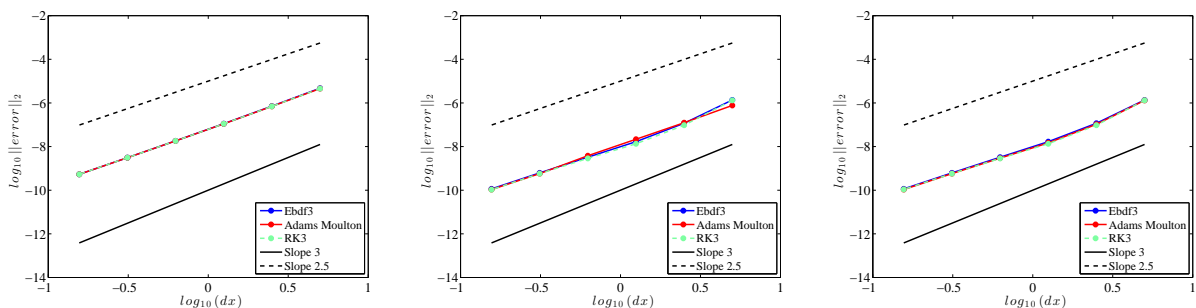


Figure 2.8: Convergence rates for the FV scheme (left) the SUPG scheme (center) and the Galerkin scheme (right)

2.4.2 Influence of mesh regularity

In order to assess the influence of mesh regularity on the results, we present some examples of computations on perturbed point distributions, obtained from uniform ones by displacing all the points by a factor of $\rho_i \Delta x$ (with ρ_i a random number such that $|\rho_i| \leq 0.2$, and with Δx the initial mesh size). For completeness we consider both a smooth case, and a non smooth one.

The first test involves the interaction of two symmetric solitary waves in a flat frictionless channel. This head-on collision is characterized by the change of shape, along with a small phase-shift of the waves as a consequence of the nonlinearity and dispersion. We consider a channel 200m long with $h_0 = 1\text{m}$, and two solitary waves with an equal initial height of $A/h_0 = 0.3$, initially centered at $x = 60\text{ m}$ and $x = 140\text{ m}$. The computational parameters used are CFL value 0.2, number of nodes 4000 and domain $x \in [0, 200\text{m}]$.

Figure 2.9 shows the surface profiles of the solitary waves in time $t = 5, 11$ and 17sec for the SUPG (up) and the FV model (down) respectively (virtually identical results are obtained with the Galerkin method). Each subfigure compares the numerical solutions obtained from the uniform and the non-uniform meshes. The waves initially propagate undisturbed until they collide. After the collision, as expected, the waves are transformed and a dispersive tail appears. The influence of mesh irregularity is clearly negligible.

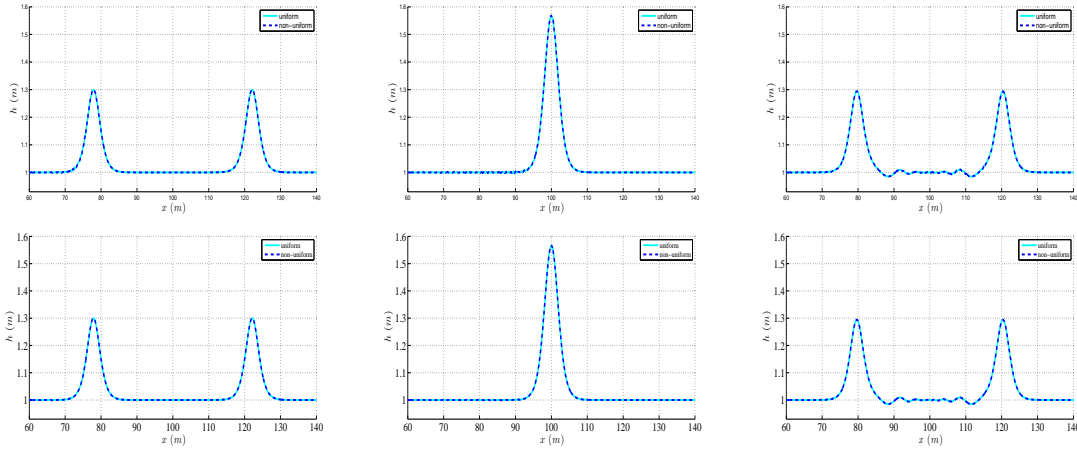


Figure 2.9: Surface profiles of solitary waves at times $t = 5, 11, 17\text{sec}$ with A/h_0 propagate in opposite directions for SUPG (up) and FV (down) schemes.

As a non-smooth example, we repeat on a perturbed mesh the computation of a solitary wave run-up on a plane beach. The results obtained are shown on figure 2.10 for both the hybrid FV and SUPG methods, using the Adams-Moulton time integration. Comparing to the results of the previous section, we can again see that the influence of mesh regularity is very small, and perhaps the main impact of the irregularity is on the efficiency of the limiters implemented in detecting the shocks, especially for the SUPG scheme. This is clearly a topic for future improvement.

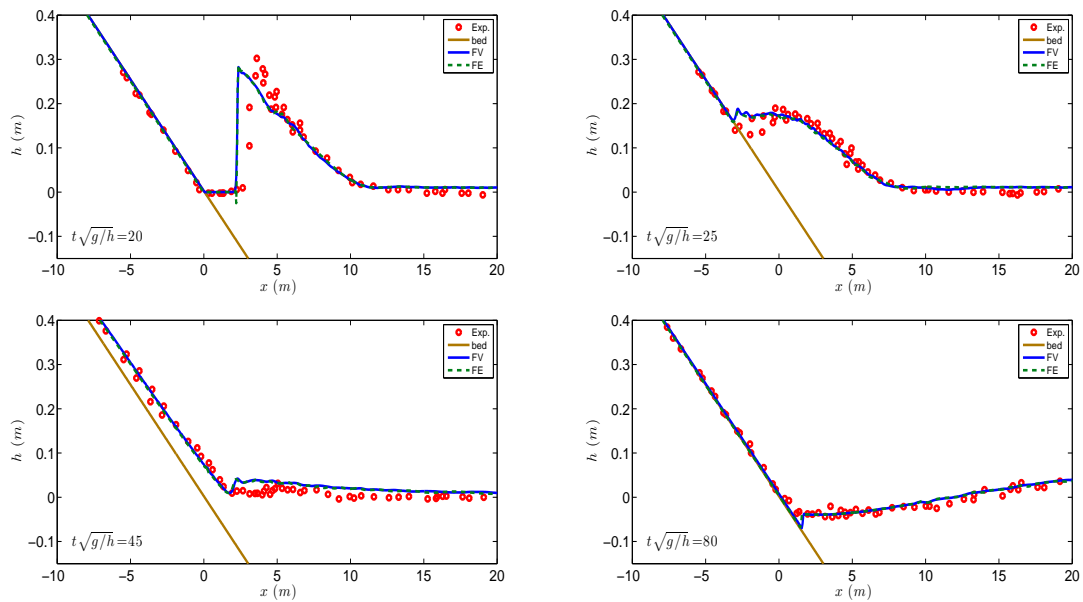


Figure 2.10: Comparison on a solitary wave run-up on a plane beach, for the FV scheme and the SUPG scheme using a non-uniform mesh

2.4.3 Solitary wave on a composite beach

One of the benchmark methods for tsunami model validation and verification according to the NOAA center for tsunami research is the problem the propagation of a solitary wave over a composite beach which simulates the Revere beach in Massachusetts. A physical model was constructed at the Coastal Engineering Research Center in Vicksburg, Mississippi by the U.S. Army Corps of Engineers. The configuration of the problem can be found in [159]. The setup of the problem is shown in figure 2.11. The wave gauges, where the time series of the surface elevation is examined, are placed at $x = 15.04, 17.22, 19.04, 20.86, 22.33, 22.80m$. Two cases are implemented and tested in this work. The first one is the propagation and breaking of a solitary wave of $\epsilon = 0.3$ and the second one involves a solitary wave of higher non-linearity of $\epsilon = 0.7$. The computational domain used is of $27.23m$, $x \in [-5, 23.23]$, with the initial solitary placed at $x = 0m$ and $h_0 = 0.218m$. The CFL number is set to 0.2 and $dx = 0.046m$. A sponge layer of $2m$ is placed at the left boundary while a vertical wall is placed at the right boundary. For the surface variation criterion, γ is set equal to 0.6.

Figure 2.12 shows the comparison between the experimental data (red circles) and the numerical results. Again, blue line denotes the numerical results produced by the FV scheme while green dotted line denotes the results given by the SUPG scheme. The solitary travels down the domain, shoals and break between the second and the third wave gauges. After breaking it continues to travel onshore until it hits the wall, reflects and starts to propagate offshore. We observe a very good match between the experimental data and the numerical results for almost all the wave gauges.

In figure 2.13 the numerical results along with the experimental data for the second case ($\epsilon = 0.7$) are presented. The solitary wave is highly non-linear and presents the same behavior. It

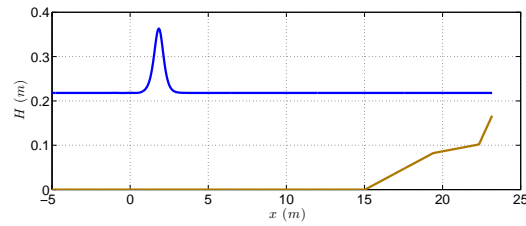
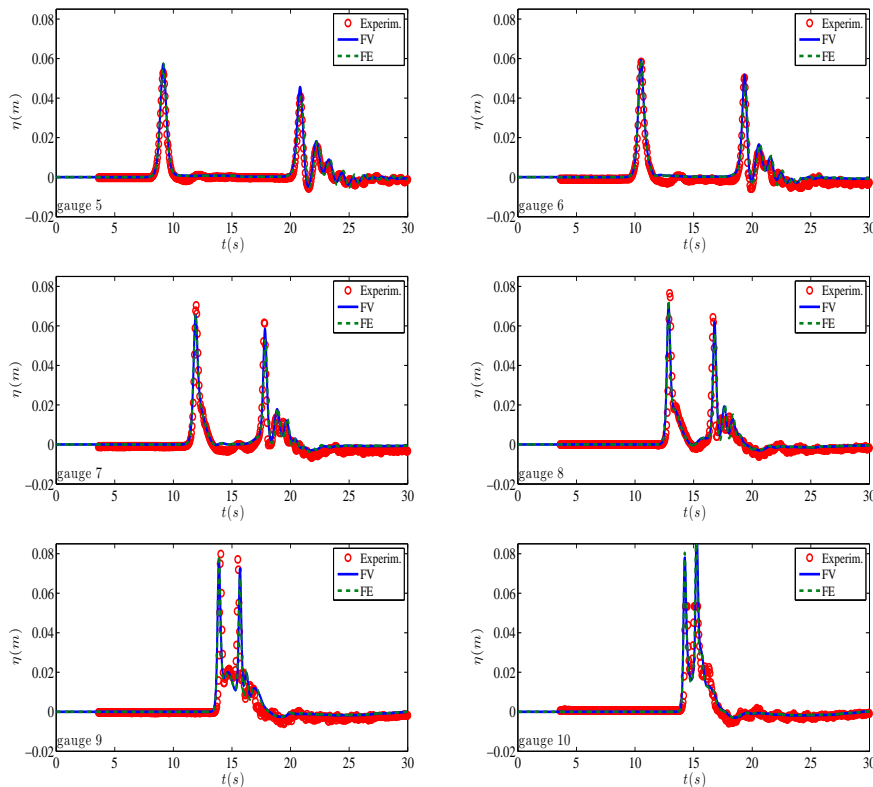


Figure 2.11: Initial conditions of the solitary wave on a composite beach

Figure 2.12: Time series of the free surface elevation at the wave gauges for the solitary of non-linearity $\epsilon = 0.3$

breaks between the second and the third wave gauges, reflects on the wall and travels offshore. The numerical results are in agreement with the experimental data. We must notice that after the reflection of the solitary, the numerical results produced by the FV scheme are slightly ahead compared to the ones produced by the SUPG scheme and the experimental data.

2.5 Summary

In this chapter we proposed and studied a flexible and unsplit strategy to enhance a shallow water code to embed the fully-nonlinear weakly dispersive effects of the Green–Naghdi equations. We

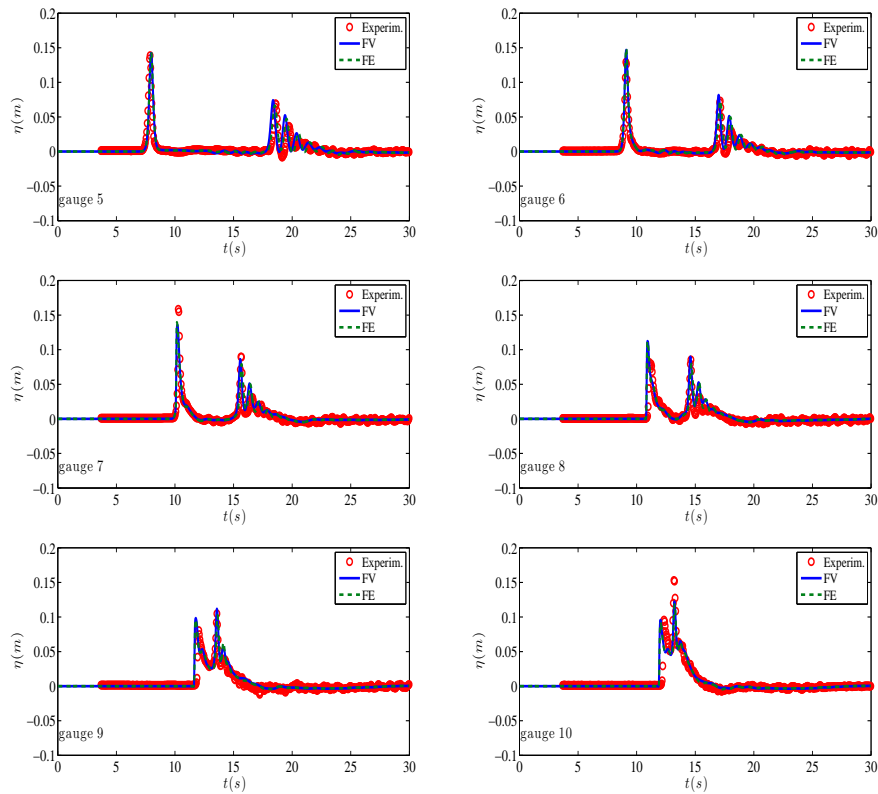


Figure 2.13: Time series of the free surface elevation at the wave gauges for the solitary of non-linearity $\epsilon = 0.7$

have proposed a decoupled unsplit formulation which allows to enhance a (hyperbolic) shallow water code by a purely algebraic correction to the discrete momentum equation. This correction can be computed from the solution of a stationary elliptic problem to embed both the fully-nonlinear weakly dispersive effects, and wave breaking. We investigated different discretization techniques for the two different phases and we derived both a time and space continuous dispersion analysis to compute the discrete dispersion relationship of our schemes. Our results show that the proposed method has enormous potential as a non-intrusive enhancement technique for the existing shallow water models. Indeed, the next chapter presents it's extension into two spatial dimensions.

Chapter 3

A numerical method in 2D

This chapter describes the extension of our 1HD hybrid scheme in 2HD on unstructured meshes. More precisely, and like before, we re-write the standard form of the equations by splitting the original system in its elliptic and hyperbolic parts, through the definition of a new variable, accounting for the dispersive effects and having the role of a non-hydrostatic pressure gradient in the shallow water equations. We consider a two-step solution procedure. In the first step we compute a source term by inverting the elliptic coercive operator associated to the dispersive effects; then in a hyperbolic step we evolve the flow variables by using the non-linear shallow water equations, with all non-hydrostatic effects accounted by the source computed in the elliptic phase. The advantages of this procedure are firstly that the GN equations are used for propagation and shoaling, while locally reverting to the non-linear shallow water equations to model energy dissipation in breaking regions. Secondly and from the numerical point of view, this strategy allows each step to be solved with an appropriate numerical method on arbitrary unstructured meshes. We propose a hybrid finite element (FE) finite volume (FV) scheme, where the elliptic part of the system is discretized by means of the continuous Galerkin FE method and the hyperbolic part is discretized using a third-order node-centred finite volume (FV) technique. Furthermore a number of issues are addressed. For example the issue of the compatible data representation, in the hyperbolic and the elliptic phase, the well-posedness of the solution which is highly affected by the choice of the numerical fluxes used in the hyperbolic step, and the accuracy of the model which is affected by the non-consistent reconstruction of the derivatives on the unstructured meshes. The performance of the numerical model obtained is extensively validated against experimental measurements from a series of relevant benchmark problems.

3.1 Solution strategy and geometrical notation

To numerically solve (1.1), (1.9)-(1.13) we rewrite the system of two dimensional enhanced GN equations as:

$$h_t + \nabla \cdot \mathbf{q} = 0, \quad (3.1)$$

$$\mathbf{q}_t + \nabla \cdot \left(\frac{\mathbf{q} \otimes \mathbf{q}}{h} \right) + gh \nabla \eta = \Phi \quad (3.2)$$

$$(I + \alpha T) \Psi = W - R, \quad (3.3)$$

$$\Phi = \Psi + \frac{gh}{\alpha} \nabla \eta \quad (3.4)$$

by splitting the original system in its elliptic and hyperbolic parts, through the definition of the new variable $\Phi = [\phi_x, \phi_y]^T$. Φ accounts for the dispersive effects and has the role of a non-hydrostatic pressure gradient in the Shallow water equations. We define

$$\begin{aligned} W &= -\frac{gh}{\alpha} \nabla \eta \\ R &= hQ \left(\frac{\mathbf{q}}{h} \right) \end{aligned} \quad (3.5)$$

where the operators $T(\cdot)$ and $Q(\cdot)$ are (1.12) and (1.13) respectively. In this work we solve (3.1)-(3.4) using a hybrid Finite Element (FE)- Finite volume (FV) scheme where the elliptic part of the system is discretized by means of the continuous Galerkin FE method. The hyperbolic part of the system is discretized by the two dimensional formulation of the finite volume scheme inspired by the works [136, 137]. We refer to the work [136], which has been proven to be a robust scheme, capable of simulating wave transformations providing accurate results in complex scenarios and over two dimensional unstructured triangular meshes.

So we consider a triangulation of the spatial domain which we denote by Ω_h , with the roman h denoting the largest element diameter. In the approach developed here, we will both make use of elements defined by each of the non-overlapping triangles of the mesh, as well as of a *median-dual* partition in order to generate non-overlapping nodal control volumes. Let us denote by K the generic triangular element, and by K_i the set of elements sharing node i . We then denote by C_i the median dual cell obtained by joining the gravity centers of the triangles in K_i with the midpoints of the edges meeting in i . Simple geometry shows that $|C_i| = \sum_{K \in K_i} \frac{|K|}{3}$. We also define D_i as the set of nodes connected to i . For any $j \in D_i$, the shared portion of boundary of C_i and C_j is named ∂C_{ij} , and it is composed by the union of two segments connecting the barycenters of the two triangles sharing the edge ij with the edge midpoint (see figure 3.1). The boundary of the median dual cell of i can thus be defined as: $\partial C_i = \sum_{j \in K_i} \partial C_{ij}$. Moreover, we define \mathbf{r}_{ij} the vector connecting nodes i and j . Note finally, that the intersection of C_i intersects each element $K \in K_i$ can be split into two half cells associated to the two edges stemming from i . The half cell containing node j is denoted by C_{ij}^K , and we set $C_{ij} = \bigcup_{K \in K_i \cap K_j} C_{ij}^K$ so that $C_i = \bigcup_{j \in D_i} C_{ij}$.

3.2 Hyperbolic step: third order FV scheme and derivatives recovery via successive corrections

For simplicity we rewrite the system of conservation laws (3.1)-(3.2) as

$$\mathbf{U}_t + \nabla \cdot \mathbf{F}(\mathbf{U}) = \mathbf{S}_b + \Phi_i. \quad (3.6)$$

with $\mathbf{U} = [h, \mathbf{q}]^T$, $\mathbf{F} = [\mathbf{q}, \mathbf{q} \otimes \mathbf{q}/h + gh^2\mathbf{I}_2]^T$, with \mathbf{I}_2 the rank 2 identity matrix, and with $\mathbf{S}_b = -[0, gh\nabla b]^T$. The FV integration over each computational cell C_i leads to the semi-discrete form of the scheme as:

$$\frac{\partial \bar{\mathbf{U}}_i}{\partial t} + \frac{1}{|C_i|} \sum_{j \in D_i} \int_{\partial C_{ij}} \hat{\mathbf{F}} \cdot \mathbf{n} = \frac{1}{|C_i|} \sum_{j \in D_i} \int_{C_{ij}} \mathbf{S}_b + \bar{\Phi}_i, \quad (3.7)$$

where $\bar{\mathbf{U}}_i$ is the volume averaged value of \mathbf{U} over C_i , \mathbf{n} is the unitary outward vector normal to ∂C_i , and with $\bar{\Phi}_i = \int_{C_i} \Phi$ evaluated using numerical quadrature (cf. section §5). In the above expression, $\hat{\mathbf{F}}$ is the numerical flux defined here using the approximate Riemann solver of [225]. The method used here is relatively standard and we will not provide much details. It is based on a well balanced formulation of the integrals of the fluxes and of the bathymetry source, as well as a robust modification of the reconstruction and numerical flux to cope with the wet/dry transition. We refer the interested reader to e.g. [19, 39, 45], and to [136, 140] for some details on our implementation.

To reach high-order spatial accuracy, we have to reconstruct each component of the physical variables and bed topography. Following the classical strategy by [269] (cf also [234, 136] and [97]), to reduce the introduction of spurious numerical dispersion we avoid second order approximations for the hyperbolic terms, and look into the design of a fully third order method. This is achieved in this work by means of a successive correction method which iteratively improves derivatives computed by means of the standard Green-Gauss formula. This allows to construct k-exact polynomials with all local operations, requiring only the exchange of information between adjacent cells. In particular for a third order method we need a quadratic polynomial requiring the knowledge of gradient and Hessian of the variables in the dual cell. The standard Green-Gauss formula is unfortunately not well suited for general unstructured meshes on which it provides first order derivatives which are at most consistent (1st order accurate), and second derivatives which may event be inconsistent. There are many methods to overcome this: from the classical least square method used in k-exact method by Barth in [11, 9, 10], to more recent ones used in [263, 264, 278] and [53]. The basic limitation of most of the above methods is the computational cost, related to the need of solving a more or less large linear system, and the complexity of the implementation, related to the need of assembling and using an enlarged stencil.

We follow here the method first proposed by [30, 119, 118] and more recently in [215]. In the references the authors constructed a generalized hybridization of Green-Gauss and Least square methods, called quasi-Green method, which results in a first-order accurate gradient on unstructured meshes. A successive correction method allows the construction of consistent gradient and Hessian

on unstructured meshes. The idea of the corrections is to impose exact consistency with the monomials of appropriate degree. A thorough discussion and the general derivation of the method can be found in [215, 186] to which we refer for details. All the above works are using cell centered methods. In our work we have extended the approach to node centered finite volumes. Very recently (and independently on this work) [233] and [232] also provided a similar re-formulation for the linear advection equation and of the incompressible Euler equations.

In our work, we develop a node centered successive correction method for the hyperbolic nonlinear shallow water system, and appropriately combine it with a slope limiter to handle bores and hydraulic jumps. To our knowledge this is the first time that a nodal variant of the successive reconstruction technique is used for a hyperbolic system and combined with a limiter. We recall hereafter the basic steps to obtain a third order reconstruction. Most of the formulas allowing the implementation are provided in [146].

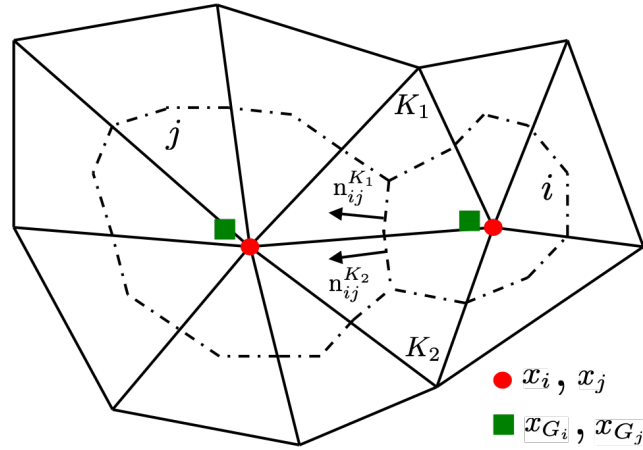


Figure 3.1: Notation and volume area used in the successive correction method

3.2.1 Polynomial expansion and derivative reconstruction via successive corrections

The reconstruction problem consists in defining a piece-wise polynomial of degree k that approximates $f(\mathbf{x})$ to the $(k+1)^{\text{th}}$ order of accuracy. Our aim is to calculate approximations of the solution to the faces of the cells. To do this, we use high order polynomials obtained by Taylor expansions. Let us introduce the vector and tensor moments

$$\begin{aligned}\delta_{G_i}^{(1)}(\mathbf{x}) &= (\mathbf{x} - \mathbf{x}_{G_i}), \\ \delta_{G_i}^{(2)}(\mathbf{x}) &= \delta_{G_i}^{(1)} \otimes \delta_{G_i}^{(1)} = (\mathbf{x} - \mathbf{x}_{G_i}) \otimes (\mathbf{x} - \mathbf{x}_{G_i})\end{aligned}\quad (3.8)$$

For a third order scheme ($k = 2$) a conservative approximation is of the form [12, 201]

$$f_i(\mathbf{x}) = \bar{f}|_{G_i} + \mathbf{D}_f^{(1)}|_{G_i} \cdot (\mathbf{x} - \mathbf{x}_{G_i}) + \frac{1}{2} \mathbf{D}_f^{(2)}|_{G_i} : \left(\delta_{G_i}^{(2)}(\mathbf{x}) - M_i^{(2)} \right), \quad (3.9)$$

3.2. HYPERBOLIC STEP: THIRD ORDER FV SCHEME AND DERIVATIVES RECOVERY VIA SUCCESSIVE

where where $\mathbf{D}_f^k|_{G_i}$ represents the order k spatial derivative of f (gradient, Hessian, etc) at the gravity center \mathbf{x}_{G_i} , and where the $A : B$ operator denotes the element by element lumped matrix product

$$A : B = \sum_{i,j} A_{ij} B_{ij}.$$

The matrix M_i contains the geometric moments:

$$M_i^{(2)} = \int_{C_i} \delta_{G_i}^{(2)}$$

Note that these geometric moments are mesh dependent quantities that can be pre-computed via numerical quadrature and stored (cf. [146] for mode details). The cell polynomials thus defined guarantee the conservation property

$$\frac{1}{|C_i|} \int_{C_i} f_i(\mathbf{x}) dS = \bar{f}|_{G_i}.$$

The crucial step is to computation of the spatial derivatives with the desired accuracy.

First derivatives

To get the first derivative at the gravity center of C_i , we apply the quasi-Green gradient approximation. This consists in a Green-Gauss reconstruction with a correction restoring the consistency of the operator on general meshes [186]. We end up with an operator approximating the gradient to first order accuracy on general meshes as (cf again figure 3.1 for the notation):

$$\mathbf{D}_f^{(1,o1)}|_{G_i} = M_1^{-1} \sum_{j \in D_i} [w_{ij}^{K_2} \bar{f}_i + (1 - w_{ij}^{K_1}) \bar{f}_j] \mathbf{n}_{ij}^{K_1}. \quad (3.10)$$

where the superscript $o1$ denotes that the approximation is first order accurate, and with the weights w_{ij} computed based on the relative distance of the cell center's \mathbf{x}_i to its face:

$$w_{ij}^{K_1} = \frac{\mathbf{s}_{ij}^{K_1} \cdot \mathbf{n}_{ij}^{K_1}}{\mathbf{r}_{ij} \cdot \mathbf{n}_{ij}^{K_1}}, \quad \mathbf{s}_{ij}^{K_1} = \frac{1}{2} \mathbf{x}_G^{K_1} + \frac{1}{4} (\mathbf{x}_i + \mathbf{x}_j) \quad (3.11)$$

and similarly for $w_{ij}^{K_2}$. The 2×2 matrix $(M_1)_i$ corrects the gradient to ensure its consistency. It is computed by imposing that for $f = x$ we have $\mathbf{D}_x^{(1,o1)}|_{G_i} = (1, 0)$, and similarly for $f = y$ we have $\mathbf{D}_y^{(1,o1)}|_{G_i} = (0, 1)$. This leads to:

$$M_{1i} = \left[\sum_{j \in D_i} w_{ij}^{K_1} (\mathbf{x}_{G_j} - \mathbf{x}_{G_i}) \otimes \mathbf{n}_{ij}^{K_1} + w_{ij}^{K_2} (\mathbf{x}_{G_j} - \mathbf{x}_{G_i}) \otimes \mathbf{n}_{ij}^{K_2} \right]^T \quad (3.12)$$

As the geometrical moments, this correction matrix is mesh dependent, but can be pre-computed and stored before the simulations. The first order gradient $\mathbf{D}_f^{(1,o1)}|_{G_i}$ allows to construct polynomials with second order of accuracy at most.

Second derivatives and second order corrected gradients

Once consistent first derivatives are available in all cells, we can proceed to a second iteration which will provide consistent second derivatives and improved gradients. As previously stated, a first order approximation of the second derivatives is enough to guarantee third order of accuracy for the overall polynomial (3.9). Unfortunately, unless the mesh presents special symmetries, applying (3.10) twice results in an inconsistent approximation of $\mathbf{D}_f^{(2)}|_{G_i}$. We denote hereafter this approximation as

$$\mathbf{D}_f^{(2,o0)}|_{G_i} = \mathbf{D}^{(1,o1)}(\mathbf{D}_f^{(1,o1)})|_{G_i}$$

The idea is to correct this quantity as done for the gradient

$$\mathbf{D}_f^{(2,o1)}|_{G_i} = M_{2_i}^{-1} \mathbf{D}_f^{(2,o0)}|_{G_i} = M_{2_i}^{-1} \mathbf{D}^{(1,o1)}(\mathbf{D}_f^{(1,o1)})|_{G_i} \quad (3.13)$$

As for the gradient, the correction matrix M_{2_i} can be computed component by component by requiring the approximation to be consistent when applied to $\mathbf{x} \otimes \mathbf{x}$, so that for example $(\mathbf{D}_{x^2}^{(2,o1)}|_{G_i})_{11} = 2$, $(\mathbf{D}_{y^2}^{(2,o1)}|_{G_i})_{22} = 2$, $(\mathbf{D}_{yx}^{(2,o1)}|_{G_i})_{12} = 1$, etc. It can be shown [117] that M_{2_i} can be obtained by a double application of the first derivative of first order derivative to $(\mathbf{x} - \mathbf{x}_{G_i}) \otimes (\mathbf{x} - \mathbf{x}_{G_i})$. For brevity we omit here the expressions obtained, which are reported in detail in [146].

The computation of a first order accurate second order derivative is not enough to achieve third order accuracy in the reconstruction. We also have to correct the approximation of the first derivative for it to be at least second order. To obtain a correction strategy, we can compare the Taylor series development of the exact gradient with the one obtained using the available reconstructed derivatives:

$$\begin{aligned} \nabla f^{\text{exact}} &= \nabla f|_{G_i} + \nabla(\nabla f)|_{G_i} \cdot (\mathbf{x} - \mathbf{x}_{G_i}) + \mathcal{O}(h^2) \\ &= \mathbf{D}_x^{(1),(o1)}|_{G_i} + \mathcal{O}(h) + \mathbf{D}_f^{(2),(o1)}|_{G_i} \cdot (\mathbf{x} - \mathbf{x}_{G_i}) + \mathcal{O}(h^2) \end{aligned} \quad (3.14)$$

The first order remainder on the second line, is due to the poor accuracy of the available gradient. For the gradient to be second order the second line should provide an exact answer for $f = (\mathbf{x} - \mathbf{x}_{G_i}) \otimes (\mathbf{x} - \mathbf{x}_{G_i})$. This is precisely the strategy suggested in [186, 215] to correct the gradient. So in practice we set

$$\mathbf{D}^{(1,o2)}|_{G_i} = \mathbf{D}^{(1,fo)}|_{G_i} + M_{1_i}^{o2} \mathbf{D}^{(2,o1)}|_{G_i}, \quad (3.15)$$

where $M_{1_i}^{o2}$ is obtained by requiring the errors in the second line of (3.14) to vanish when $f = (\mathbf{x} - \mathbf{x}_{G_i}) \otimes (\mathbf{x} - \mathbf{x}_{G_i})$. For our 2D case $M_{1_i}^{o2}$ is a 2×3 matrix of the form (full expressions available in [146]):

$$M_1^{o2} = - \begin{bmatrix} (\alpha_i)_x - x_{G_i} & (\beta_i)_x & (\gamma_i)_x - y_{G_i} \\ (\alpha_i)_y & (\beta_i)_y - y_{G_i} & (\gamma_i)_y - x_{G_i} \end{bmatrix}.$$

Note that all of the above matrices are only involved in local operations (involving nearest neighbors), they can all be pre-computed and stored during a pre-processing step, and then used to

3.2. HYPERBOLIC STEP: THIRD ORDER FV SCHEME AND DERIVATIVES RECOVERY VIA SUCCESSIVE

update the gradients by simple matrix-vector multiplications. There is no need of solving multiple linear systems. These are the main advantages of this method.

Unfortunately, the correction matrices seem to have no theoretical property guaranteeing their irreversibility. However, in all the cases that we examined here and in the references using the same approach, no problem was ever observed even in quite irregular meshes. Another issue is how to preserve the accuracy near boundaries. In this work we have been only concerned with two conditions: symmetry or periodic conditions along straight lines. In both cases we have used ghost cells. For the symmetry/slip wall conditions we have defined the ghost values on a locally mirrored mesh on which scalar quantities (depth and bathymetry) have been copied, and vectors rotated by 180° wrt normal. In this framework, third order of accuracy can be obtained easily only for straight boundaries for which two layers of elements are mirrored in order to have enough stencil to compute the successive correction derivatives. Periodic conditions are imposed simply by extending the connectivity of the mesh to include the correspondence of the periodic boundaries so that all the geometrical quantities, as well as the residuals account for periodicity.

Capturing of non-smooth solutions and limiting

In order to prevent oscillations from developing in the numerical solution we use the slope limiter proposed by Michalak and Ollivier-Gooch in [188], for higher order MUSCL numerical schemes on unstructured meshes using a cell centered fv scheme for the Euler equations. Following the spirit of the above work we write the limited form of the higher order reconstruction in the middle point M of an edge connecting the nodes i and j , as

$$f_i(\mathbf{x}_M) = \bar{f}|_{G_i} + Lim_M \left(\mathbf{D}_f^{(1)}|_{G_i} \cdot (\mathbf{x}_M - \mathbf{x}_{G_i}) + \frac{1}{2} \mathbf{D}_f^{(2)}|_{G_i} : \left(\delta_{G_i}^{(2)}(\mathbf{x}_M) - M_i^{(2)} \right) \right). \quad (3.16)$$

The design of the slope limiter requires three steps. First we have to find the minimum $(\delta f)_{min}^i$ and the maximum values $(\delta f)_{max}^i$ of the difference $\bar{f}|_{G_j} - \bar{f}|_{G_i}$ in the stencil formed by the cell i and all the direct neighbors j . Then we compute the unlimited reconstructed value $f(\mathbf{x})_M$ and finally we compute the maximum allowable value for Lim_i as:

$$Lim_M = \begin{cases} g((\delta f)_{min}^i) & \text{if } f(\mathbf{x})_M - \bar{f}_i > 0, \\ g((\delta f)_{max}^i) & \text{if } f(\mathbf{x})_M - \bar{f}_i < 0, \\ 1 & \text{if } f(\mathbf{x})_M - \bar{f}_i = 0 \end{cases} \quad (3.17)$$

where $g(x) = \frac{x^2+2x}{x^2+x+2}$.

3.2.2 Numerical verification for smooth and non-smooth flows

We provide here a quick verification of the hyperbolic step. First we consider the smooth traveling vortex solution proposed by [221], and widely used in literature to measure the accuracy of discretizations for the shallow water equations. Please refer to [221] for the precise definition of the test. We compute the solution at a specific time, as prescribed in the reference, on a series of regular and

irregular unstructured grids. The reference size of the coarsest mesh is $h = 0.107573$, which is reduced to half at each refinement step. The convergence of the depth error is reported on figure 3.2. Following the discussion in section 4 we performed the test in both structured and unstructured meshes confirming that the Green-Gauss reconstruction on unstructured meshes, spoils the convergence since is not able to produce consistent gradients. The picture confirms that the nominal accuracy is measured in practice in third order case when the derivatives are recovered via the successive correction approach. For the second order case the Green-Gauss is consistent with the gradient so the order of convergence is 2 interdependently of the mesh. The results are omitted for brevity.

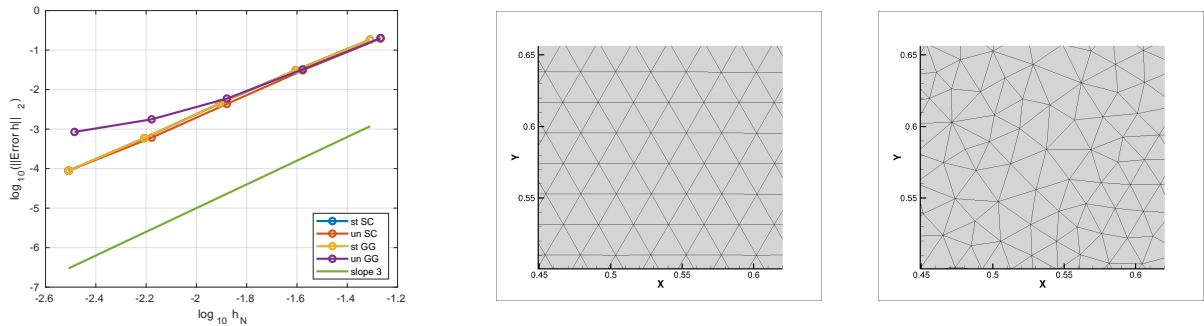


Figure 3.2: Error decay for the third order scheme. Representative structure (center) and unstructure meshes (right).

We then consider the Monai valley benchmark [167], a classical test inspired by a flume experiment reproducing a scaled version of the 1993 the Hokkaido-Nansei-Oki tsunami impact on the Monai valley. The test involves bore formation, propagation, and reflection, as well runup. Following [220], we have run the experiment on an unstructured grid adapted to the bathymetry variations, and we show the wave patterns obtained at time $16.5s$ (see figure 3.3) with the second and third order schemes, as well as the water height times series in two of the gauges of the experiment (figure 3.4).

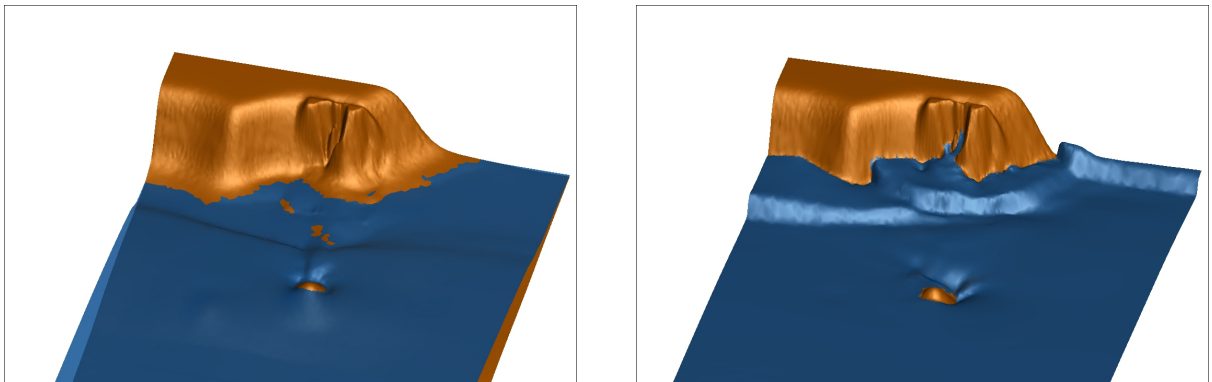


Figure 3.3: Monai valley: 3D view at time $t=14.5$ and $t=16.5$ s using the third order scheme.

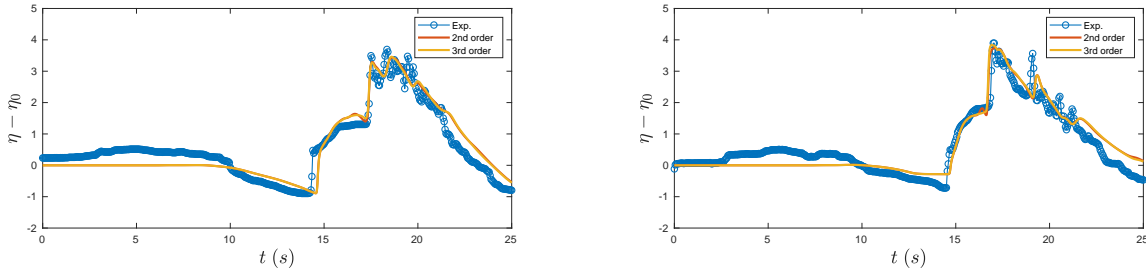


Figure 3.4: Monai valley: Free surface elevation at gauges 5 and 7.

3.3 Finite element solver for dispersive effects

Following the classical strategy [269], we now couple the non-dispersive hyperbolic solver to a second order solver for the physical weakly-dispersive effects. To this end, we propose to compute the auxiliary variable Ψ in (3.3) by means of a standard nodal P^1 (continuous) finite element (FE) method. Note that there is a notable change now in the meaning of the data associated to a mesh node i . The FV method evolves median dual cell averages which are in general different from the values of the variables at the nodes, used in the FE method. Similarly, we need to transfer from one representation to the other the derivatives of the depth and of the velocity appearing both in the coefficients in the operator T (equation (1.12) and equations (1.14)-(1.15)), and the right hand side where derivatives appear both in the definition of W and of R (cf. (3.5) and (1.13)). We will get back to this point in the next subsection.

The definitions of the operator T , $S_1(\cdot)$ and $S_2(\cdot)$, from (1.14) and (1.15) respectively, lead to the following variational form of the elliptic equation (3.3)

$$\int_{\Omega} \nu \cdot \Psi + \alpha \int_{\Omega} S_1(\nu) h S_1\left(\frac{\Psi}{h}\right) + \alpha \int_{\Omega} S_2(\nu) h S_2\left(\frac{\Psi}{h}\right) = \text{RHS} + \text{BCs}, \quad (3.18)$$

or equivalently using (1.15)

$$\int_{\Omega} \left\{ \frac{1}{3} \left(h \nabla \cdot \nu - \frac{3}{2} \nabla b \cdot \nu \right) \left(h^2 \nabla \cdot \left(\frac{\Psi}{h} \right) - \frac{3}{2} \nabla b \cdot \Psi \right) + \frac{1}{4} (\nabla b \cdot \nu) (\nabla b \cdot \Psi) \right\} = \text{RHS} + \text{BCs}, \quad (3.19)$$

with RHS a variational approximation of the term $W - R$. BCs are the boundary condition terms which we briefly discuss below. The value of Φ , required in the hyperbolic step, is recovered nodally from (3.4).

To obtain a fully discrete approximation of (3.19) we now consider the finite element approximation

$$\Psi_h = \sum_{K \in \Omega_h} \sum_{j \in K} \varphi_j \Psi_j \quad (3.20)$$

where $\text{span}\{\varphi_j\}_{j \in \Omega_h}$ is the classical continuous P^1 finite element space. We similarly introduce discrete approximations h_h , b_h , η_h , and \mathbf{u}_h for the elevations and velocity, as well as elemental discrete approximations of their first and second derivatives. Some options to provide these definitions

and the solution we propose are discussed in the next subsection. The fully discrete variational form is expressed in terms of the array of the nodal values $\{\Psi_j\}_{j \in \Omega_h}$, which by abuse of notation we also label Ψ .

$$(\mathbb{M} + \alpha \mathbb{T}(h_h, b_h)) \Psi = \mathbb{W}(h_h, b_h) - \mathbb{R}(h_h, b_h, \mathbf{u}_h) \quad (3.21)$$

where the matrices on the left hand side are sparse 2×2 block matrices. In particular, \mathbb{M} is the mass matrix with entries

$$[\mathbb{M}]_{ij}^{mn} = \delta_{mn} \sum_{K \in K_i \cap K_j} \int_K \varphi_i \varphi_j, \quad (3.22)$$

while the entries of $\mathbb{T}(h_h, b_h)$ are evaluated using the relation $h^2 \nabla \cdot (\Psi/h) = h \nabla \cdot \Psi - \Psi \cdot \nabla h$ as

$$\begin{aligned} [\mathbb{T}(h_h, b_h)]_{ij}^{mn} = & \sum_{K \in K_i \cap K_j} \int_K \left\{ \frac{1}{3} \left(h_h \partial_{X_m} \varphi_i - \frac{3}{2} \varphi_i (\partial_{X_m} b)_h \right) \left(h_h \partial_{X_n} \varphi_j - \frac{3}{2} \varphi_j (\partial_{X_n} b)_h - \varphi_j (\partial_{X_n} h)_h \right) \right. \\ & \left. + \frac{1}{4} \varphi_i (\partial_{X_m} b)_h \varphi_j (\partial_{X_n} b)_h \right\} \end{aligned} \quad (3.23)$$

Note that in the above expression the mn indices run over the spatial components of the unknown, while ij run over the mesh nodes.

Finally the right hand side terms are defined as

$$\mathbb{W}(h_h, b_h) = -\frac{g}{\alpha} \sum_{K \in K_i} \int_K \varphi_i h_h (\nabla \eta)_h \quad (3.24)$$

and

$$\begin{aligned} \mathbb{R}(h_h, b_h, \mathbf{u}_h) = & \sum_{K \in K_i} \mathbb{R}^K \\ \mathbb{R}^K = & -\frac{2}{3} \int_{\Omega_h} \nabla \varphi_i h_h^3 \left((\nabla u)_h \cdot (\nabla^\perp v)_h + (\nabla \cdot \mathbf{u}_h)_h^2 \right) + \int_{\Omega_h} \varphi_i h_h^2 \left((\nabla u)_h \cdot (\nabla^\perp v)_h + (\nabla \cdot \mathbf{u}_h)_h^2 \right) (\nabla b)_h \\ & - \frac{1}{2} \int_{\Omega_h} \nabla \varphi_i h_h^2 \left((\mathbf{D}_b^{(2)})_h : (\mathbf{u}_h \otimes \mathbf{u}_h) \right) + \int_{\Omega_h} \varphi_i h_h \left((\mathbf{D}_b^{(2)})_h : (\mathbf{u}_h \otimes \mathbf{u}_h) \right) (\nabla b)_h. \end{aligned} \quad (3.25)$$

having used the notation of section §4.1.1 for the Hessian of the bathymetry $\mathbf{D}_b^{(2)}$, and for its term product with the tensorised velocity.

Once the local polynomials representing h , b , \mathbf{u} and their derivatives are defined over the element, all the above formulas can be evaluated by means of a sufficiently accurate quadrature formula. In practice we have used here a 6 points symmetric formula exact for polynomials of degree 4 taken from [76]. This definition is the objective of the next section.

3.4 Finite element/volume coupling: consistency and well-posedness considerations

This section provides some additional constraints on some of the numerical choices possible with the method proposed. These are justified by means of some theoretical (albeit heuristic) arguments, as well as by strong numerical evidence. We consider first the issue of ensuring a compatible data representation in the two phases of the computation. This will give an indication on how to use FV data in the FE solver (and vice-versa). We then provide a few comments on the well-posedness of the overall procedure which show the importance of using dissipative numerical fluxes.

3.4.1 Consistency: using FV data in the FE solver and vice-versa

We start by recalling that the two approaches being used to solve the equations are based on different representation of the data. The FV scheme evolves the solution averages \bar{U}_i over the dual cells C_i , and local polynomials within the cells are reconstructed using essentially all the neighboring information. The FE method uses a collocated nodal representation, and within each element the polynomial variation is obtained by interpolating the data available at the nodes.

Although both methods used unknowns associated to the mesh nodes, their meaning is substantially different. More importantly, the approximation of the derivatives has an impact on the accuracy of the right hand sides of the elliptic problem. For this reason we have chosen here to proceed as follows:

- when passing the FV solution to the elliptic solver we sample the reconstructed polynomials and their derivatives at the nodes:

$$\begin{aligned} f_i &= \bar{f}|_{G_i} + \mathbf{D}_f^{(1)}|_{G_i} \cdot (\mathbf{x}_i - \mathbf{x}_{G_i}) + \frac{1}{2} \mathbf{D}_f^{(2)}|_{G_i} : \left(\delta_{G_i}^{(2)}(\mathbf{x}_i) - M_i^{(2)} \right). \\ (\nabla f)_i &= \mathbf{D}_f^{(1,o2)}|_{G_i} + \mathbf{D}_f^{(2,o1)}|_{G_i} \cdot (\mathbf{x}_i - \mathbf{x}_{G_i}) \\ (\mathbf{D}_f^{(2)})_i &= \mathbf{D}_f^{(2,o1)}|_{G_i} \end{aligned} \quad (3.26)$$

We then use these nodal values as a basis for a linear finite element approximation, so within any element $K \in \Omega_h$ we set:

$$f_h = \sum_{j \in K} \varphi_j f_j, \quad (\nabla f)_h = \sum_{j \in K} \varphi_j (\nabla f)_j, \quad (\mathbf{D}_f^{(2)})_h = \sum_{j \in K} \varphi_j (\mathbf{D}_f^{(2)})_j.$$

This, combined with the successive corrections method, allows to ensure on general meshes the second order of accuracy of all the first derivative terms (of h , b , and \mathbf{u}) appearing in (3.24), (3.25), and (3.23), and at least first order for the second derivatives of the bathymetry in (3.25). For configurations with high curvature in the topography, this is not enough and this value should be improved. A possible solution in relative simple cases, as those considered here, is to use the point-wise analytical value.

- The nodal finite element values Ψ_i are used to compute the post-processed average non-hydrostatic term

$$\bar{\Phi}_i := \int_{C_i} \Psi_h + \frac{g}{\alpha} \int_{C_i} h_h(\nabla\eta)_h$$

this formula are evaluated by splitting the integral in local contributions over the quadrangular shapes $C_i \cap K$, then further splitting the quadrangles in triangles by joining the node i to the the gravity center of K , and then by using numerical quadrature on each sub-triangle.

Note that these choices have a direct impact on the theoretical accuracy attainable by the method. To see this, let us write an estimate on the local truncation error, for simplicity in the case of flat bathymetry.

We start by recasting (1.1), (1.9)-(1.13) in dimensionless form. Using the standard fully nonlinear scaling leading to the Green-Naghdi system (see e.g.[155, 159] as well as [73] section §5) one easily shows that (3.1)-(3.4) can be written in dimensionless form as

$$\begin{aligned} \partial_t h + \nabla \cdot \mathbf{q} &= 0 \\ \partial_t \mathbf{q} + \nabla \cdot \left(\frac{\mathbf{q} \otimes \mathbf{q}}{h} \right) + h \nabla h &= \mu \left(\Psi + \frac{h}{\alpha} \nabla h \right) \\ (I + \mu \alpha T) \Psi &= -\frac{h}{\alpha} \nabla h + h Q(\mathbf{u}) \end{aligned} \quad (3.27)$$

where we recall that $\mu = h_0^2/\lambda^2$ is the ratio of the reference depth on reference wavelength, and measures the shallowness and magnitude of dispersion. More importantly, as already recalled in the introduction, the above model is an approximation of the full non-linear free surface potential equations within an asymptotic error of $\mathcal{O}(\mu^2)$ [155]. We now consider an exact smooth solution, and combine (3.27) with (3.6) to write the following local error:

$$\begin{aligned} TE_i &= \frac{1}{|C_i|} \int_{C_i} (\mathbf{U}_i^{\text{ex}}(\mathbf{x}) - \mathbf{U}^{\text{ex}}(\mathbf{x})) + \frac{1}{|C_i|} \int_{C_i} \sum_{j \in D_i \partial C_{ij}} \int_{\partial C_{ij}} \left(\hat{\mathbf{F}}(\mathbf{U}_i^{\text{ex}}(\mathbf{x}), \mathbf{U}_j^{\text{ex}}(\mathbf{x})) - \mathbf{F}(\mathbf{U}^{\text{ex}}(\mathbf{x})) \right) \\ &\quad + \frac{\mu}{|C_i|} \int_{C_i} \left(\Psi_h^{\text{ex}} + \frac{h_h^{\text{ex}}}{\alpha} \nabla h_h^{\text{ex}} - \Psi^{\text{ex}} - \frac{h^{\text{ex}}}{\alpha} \nabla h^{\text{ex}} \right) \end{aligned} \quad (3.28)$$

having denoted by $\mathbf{U}_i^{\text{ex}}(\mathbf{x})$ the reconstructed polynomial obtained starting from the averages of a smooth exact solution $\mathbf{U}^{\text{ex}}(\mathbf{x})$, and similarly by h_h^{ex} the finite element approximation of exact nodal data. We can now proceed to a term by term estimation of the right hand side. The first one is, by construction, equal to zero for quadratic polynomials, giving a rest of order $\mathcal{O}(h^3)$, and a similar result is easily proven for the second term too (see e.g. [265] §2). The last one requires an evaluation of the error of the solution of the elliptic step. Standard finite element error estimates for elliptic equations (see e.g. [55, 87, 31]) rely firstly on a consistency assessment involving two main components: an estimate of the interpolation error for the solution, an estimate of the residual error, related to the approximation of the right hand side of the problem. For linear finite elements, the approximation error in L^2 norm is of an order $\mathcal{O}(h^2)$. Concerning the right hand side,

3.4. FINITE ELEMENT/VOLUME COUPLING: CONSISTENCY AND WELL-POSEDNESS CONSIDERATION

an inspection of (3.25) reveals that the limiting factor, for constant bathymetry, is the accuracy in the approximation of the derivatives of the velocity. This indicates that, *provided that the gradient approximation is second order accurate on general meshes, the consistency of the scheme is of order $\mathcal{O}(\mu h^2)$, which is within the modeling error as soon as $h = \mathcal{O}(\mu)$* . The scheme is thus second order accurate wrt the mesh size. However, when the shallow water sub-system is approximated to third order, we gain a factor μ in error without any increase in the cost of approximation of the elliptic problem which is the most computational intensive part of the model. Since μ is small in all applications for which the model is relevant, this gain is in principle non-negligible. This is essentially the same rationale behind the method of [269], extended to unstructured grids.

To confirm numerically the impact of these choices, we consider a traveling solitary wave which is an exact solution of the GN equations for $\alpha = 1$. Depth and velocity are known analytically and given by:

$$h(x, y, t) = h_0 + \alpha_0 \operatorname{sech}^2(k(x - c * t)), \quad u(x, y, t) = c \left(1 - \frac{h_0}{h(x, y)} \right) \quad (3.29)$$

with h_0 the still water depth, α_0 the wave's amplitude, and with $k = \sqrt{3\alpha_0/4h_0^2(h_0 + \alpha_0)}$, and $c = \sqrt{g(h_0 + \alpha_0)}$. Although this is essentially a 1D solution, we have run it on 2D unstructured triangulations (rightmost picture on figure 3.2) to perform a grid convergence. In figure 3.5 (left), we compare the results obtained by using the correctly sampled values of the solution and of its derivatives at the nodes, as discussed above (orange curve), against the result (blue curve) obtained by passing the nodal average as it is, and using it to construct the finite element approximation, including the elemental derivatives computed on each element as $(\nabla u)_h = \sum_{j \in K} \nabla \varphi_j u_j$. The result shows the importance of accounting for the meaning of the data in the FE/FV coupling to attain the proper convergence rate with mesh size. Concerning the impact of using the extra correction in the polynomial reconstruction in the hyperbolic phase, from comparing curves in figure 3.5 (left) and (right), we see that this relatively inexpensive extra iteration allows an error reduction roughly of a factor 5.

3.4.2 A comment on well-posedness

The choice of the numerical fluxes plays a fundamental for the robustness of the hyperbolic step in the presence of irregular solutions, for which the use of dissipative/upwind fluxes is necessary (cf. sections §4.1.3 and §4.2). When considering the propagation of smooth dispersive waves one may think that non-dissipative fluxes could be more appropriate. It turns out that for the method proposed here this is not case, and numerical dissipation plays a major role also in the propagation region. To show this, we will consider the simplified setting of the linearized dimensionless equations without

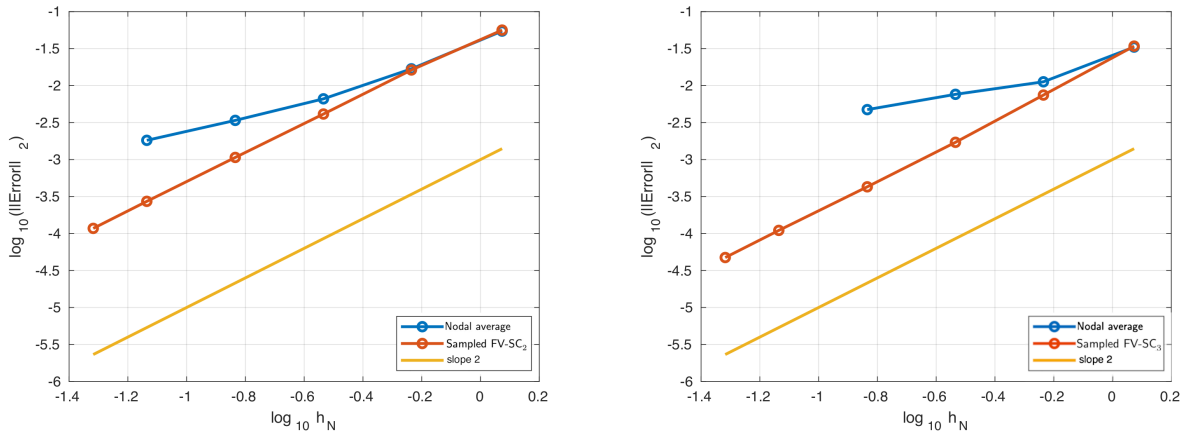


Figure 3.5: Error decay for the solitary wave. Left: hyperbolic step with second order successive correction. Right: hyperbolic step with third order successive correction. Orange: consistently sampled FV data used in the FE step. Blue: nodal averages in the FE step.

bathymetry, which can be written as

$$\begin{aligned}
 (I - \alpha\mu(\nabla\nabla\cdot))\Psi &= -\frac{\nabla\eta}{\alpha} \\
 \partial_t\eta + \nabla \cdot \mathbf{u} &= 0 \\
 \partial_t\mathbf{u} + \nabla\eta &= \mu\Psi + \mu\frac{\nabla\eta}{\alpha}
 \end{aligned} \tag{3.30}$$

Despite the scheme having been derived and coded for the above form, for the discussion of this section it is more appropriate to start from the more classical formulation

$$\begin{aligned}
 \partial_t\eta &= -\nabla \cdot \mathbf{u} \\
 (I - \alpha\mu(\nabla\nabla\cdot))\partial_t\mathbf{u} &= -(I - (1 - \alpha)\mu(\nabla\nabla\cdot))\nabla\eta
 \end{aligned} \tag{3.31}$$

The operator to be inverted to evolve the velocity \mathbf{u} (as well as to pre-compute Ψ) is a grad-div operator, quite common in the modelling of e.g. electromagnetic waves. The important aspect of this type of equation is that it is naturally formulated in the functional space of vectors $H(\text{div})$, as its variational form involves the scalar product

$$(\mathbf{v}, \mathbf{u})_\Omega := \int_\Omega \mathbf{v} \cdot \mathbf{u} + \alpha\mu \int_\Omega \nabla \cdot \mathbf{v} \cdot \nabla \cdot \mathbf{u} \tag{3.32}$$

which readily generates the equivalent squared $H(\text{div})$ norm $\mathbf{u}^2 + \alpha\mu(\nabla \cdot \mathbf{u})^2$. It is well known that, despite the symmetry of the bilinear form induced by the equation, H^1 finite elements, as the one used here to solve the elliptic problem, are not well posed as prone to spurious modes related to the rotational of the solution. For electromagnetic waves this is a long time known fact [61, 60, 115]. Divergence conforming elements allow of course to side-step this issue.

3.4. FINITE ELEMENT/VOLUME COUPLING: CONSISTENCY AND WELL-POSEDNESS CONSIDERATION

To use H^1 elements, which are easier to implement, and better suited to be coupled with a hyperbolic solver something needs to be done. Usually, this is achieved by introducing, at the PDE level or in the scheme, a regularizing operator that stabilizes the spurious modes otherwise not controlled by the incomplete norm generated by the variational formulation (or equivalently (3.32)). In our method this is essentially the case. However, we do not modify the elliptic solver. The stabilization is embedded in the hyperbolic evolution step, and associated to the form of the upwind finite volume numerical fluxes which embed a discrete Laplacian which plays a crucial role.

To provide some heuristics into this mechanism, we consider the following regularized explicit discrete in time linear equivalent of the GN system

$$\begin{aligned} \frac{\eta^{n+1} - \eta^n}{\Delta t} - \nabla \cdot (\epsilon_h^\eta \nabla \eta)^n &= - \nabla \cdot \mathbf{u}^n \\ (I - \alpha \mu(\nabla \nabla \cdot)) \frac{\mathbf{u}^{n+1} - \mathbf{u}^n}{\Delta t} - \nabla \cdot (\epsilon_h^{\mathbf{u}} \nabla \mathbf{u})^n &= - (I - (1 - \alpha) \mu(\nabla \nabla \cdot)) \nabla \eta^n \end{aligned} \quad (3.33)$$

The regularization here is explicitly added in the form of an artificial diffusion terms, which in reality stems from the use of upwind numerical fluxes. The above system can be seen as some space continuous equivalent of the fully discrete scheme, somewhat similarly to the modified equation in finite difference methods [266]. In particular, the coefficients ϵ_h^η and $\epsilon_h^{\mathbf{u}}$ depend on the numerical flux. For the dimensionless linearized problem under consideration, these can be both approximated by $\epsilon_h^\eta = \epsilon_h^{\mathbf{u}} \approx \mathbb{C} h$ for some mesh dependent constant \mathbb{C} , which we assume for simplicity to be diagonal. Note that this implies that the divergence acting in the second term in each equation is applied line by line.

To show the impact of numerical dissipation we proceed as follows. We start by introducing at each time step the Helmholtz/Hodge decomposition of the velocity vector [123, 124, 22]

$$\mathbf{u}^n = \nabla \phi_1^n + \nabla^\perp \phi_2^n \quad (3.34)$$

where the orthogonal nabla operator $\nabla^\perp = (\partial_y, -\partial_x)$ being the equivalent of the rotational in the 2D plane. We then introduce this decomposition into the second in (3.33), and look for closure equations for the two potentials. Using the div-free property of the second component of the decomposition, the first relation we can write is that

$$\frac{\nabla^\perp \phi_2^{n+1} - \nabla^\perp \phi_2^n}{\Delta t} + (I - \alpha \mu(\nabla \nabla \cdot)) \frac{\nabla \phi_1^{n+1} - \nabla \phi_1^n}{\Delta t} - \nabla \cdot (\epsilon_h^{\mathbf{u}} \nabla \mathbf{u})^n = - (I - (1 - \alpha) \mu(\nabla \nabla \cdot)) \nabla \eta^n \quad (3.35)$$

We now apply the $-\nabla^\perp \cdot$ operator, and use the identity $\nabla^\perp \cdot \nabla = 0$. This allows to write

$$-\nabla^\perp \cdot \frac{\nabla^\perp \phi_2^{n+1} - \nabla^\perp \phi_2^n}{\Delta t} + \nabla^\perp \nabla \cdot (\epsilon_h^{\mathbf{u}} \nabla \mathbf{u})^n = 0 \quad (3.36)$$

The first conclusion we can draw is that for $\epsilon_h^{\mathbf{u}} = 0$ then an admissible solution is that ϕ_2 is constant in time. In other words, at any time step *the velocity field is defined up to an arbitrary rotational component $\nabla^\perp \phi_2$ not seen by the scheme. This is essentially a spurious mode, which is*

not controlled and may prevent the discrete solution to converge.

We now consider the case in which the numerical dissipation is present. With the hypothesis that ϵ_h^u is diagonal and that the $\nabla \cdot$ is applied line by line, simple manipulations show that

$$\begin{aligned} -\nabla^\perp \cdot \nabla^\perp \phi_2 &= -\Delta \phi_2 \\ \nabla^\perp \nabla \cdot (\epsilon_h^u \nabla \mathbf{u})^n &= -\Delta^2 \phi_2 \end{aligned} \quad (3.37)$$

with Δ the usual Laplace operator. This allows to write (3.35) as

$$-\Delta \left(\frac{\phi_2^{n+1} - \phi_2^n}{\Delta t} - \epsilon_h^u \Delta \phi_2^n \right) = 0 \quad (3.38)$$

For uniform and homogeneous boundary conditions, we may deduce that

$$\frac{\phi_2^{n+1} - \phi_2^n}{\Delta t} - \epsilon_h^u \Delta \phi_2^n = 0. \quad (3.39)$$

This shows that *in presence of numerical dissipation, spurious rotational effects are smoothed according to a parabolic operator with a smoothing rate proportional to the numerical dissipation.*

We propose some numerical evidence to confirm the above observations by studying again the grid convergence of the solitary wave solution (3.29). We perform the following experiment. On one hand, we solve the nonlinear shallow water equations forced with $\Phi = \Phi^{\text{exact}}$ obtained by replacing (3.29) in the momentum equation. This corresponds to imposing the solitary wave as a manufactured solution (cf [224]). On the other, we solve the full system including the dispersive terms for which (3.29) is an exact solution if $\alpha = 1$. In both cases, we perform a grid convergence with centered numerical fluxes, as well as with the full upwind flux.

We perform the computations up to time $t = 0.1$ on 7 unstructured meshes starting with a triangulation with 328 triangles, and then halving the mesh size. The results are reported in figure 3.6 for the second order (left), and third order (right) polynomial reconstruction in the hyperbolic fluxes. For the shallow water equations with manufactured solution all configurations converge. The centered fluxes fail to provide third order of accuracy, at least on the meshes considered however, full second order is observed. For the GN system, the error obtained with centered fluxes quickly stalls, and error or even solution blow-up is observed on the last meshes for the final time considered. Full convergence is restored with the upwind fluxes, confirming our heuristics that numerical dissipation is sufficient to control the growth of spurious modes.

3.5 Stability and dissipation

While the well-posedness in 2D can be justified with the arguments of section 3.4.2, in one dimension the Fourier analysis (see section 2.3) provides a characterization of the linear stability of monochromatic waves in terms of the discrete wave amplification rate ξ_h . We recall here the system that we obtained after we replace the Fourier mode into our scheme:

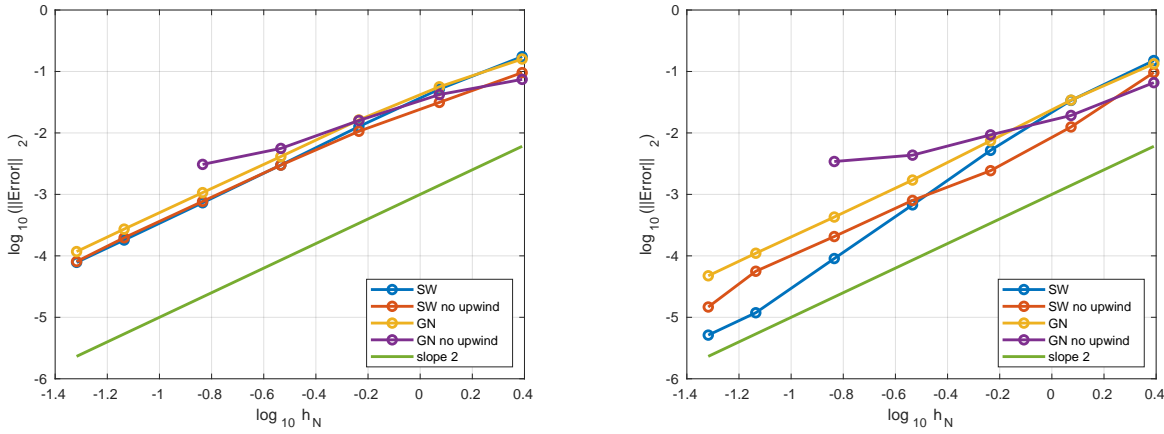


Figure 3.6: Solitary wave. Left: second order successive correction. Right: third order successive correction. Blue: shallow water with upwind fluxes and manufactured solution. Orange: shallow water with centered fluxes and manufactured solution. Yellow: Green-Naghdi with upwind fluxes. Magenta: Green-Naghdi with centered fluxes.

$$\begin{aligned}
 j(\nu_h C - B)\eta_i + h_0 A u_i &= 0 \\
 g A \eta_i + j(\nu_h C - B)u_i &= -\mu_h \frac{1}{h_0} M^{FV} D \eta_i.
 \end{aligned} \tag{3.40}$$

For the upwind schemes we can obtain from the above system, the relation:

$$\xi_h = \frac{B}{C} \tag{3.41}$$

where the coefficients B and C are

$$B = \frac{ck}{\mu} \left(-\frac{115}{48} \sin\left(\frac{\mu}{2}\right) + \frac{61}{48} \sin\left(\frac{3\mu}{2}\right) - \frac{15}{48} \sin\left(\frac{5\mu}{2}\right) + \frac{1}{48} \sin\left(\frac{7\mu}{2}\right) \right) \tag{3.42}$$

$$C = 2 \sin\left(\frac{\mu}{2}\right). \tag{3.43}$$

for the case of third order successive reconstructions, and

$$B = \frac{ck}{\mu} \left(-\frac{10}{4} \sin\left(\frac{\mu}{2}\right) + \frac{5}{4} \sin\left(\frac{3\mu}{2}\right) - \frac{1}{4} \sin\left(\frac{5\mu}{2}\right) \right) \tag{3.44}$$

and C is the same as before, for the second order successive reconstruction.

Figure 3.7 plots the numerical wave amplification for three different choices of number of points per wavelength. We can see that the amplification rate is negative, which means the schemes are stable. Of course the presence of damping constrains somewhat the number of nodes per wavelength required to resolve long time/distance propagation, although considerably less for the third order scheme, as the plot suggests. For the fully centered discretizations, the spectral analysis provides systematically $\xi_h = 0$.

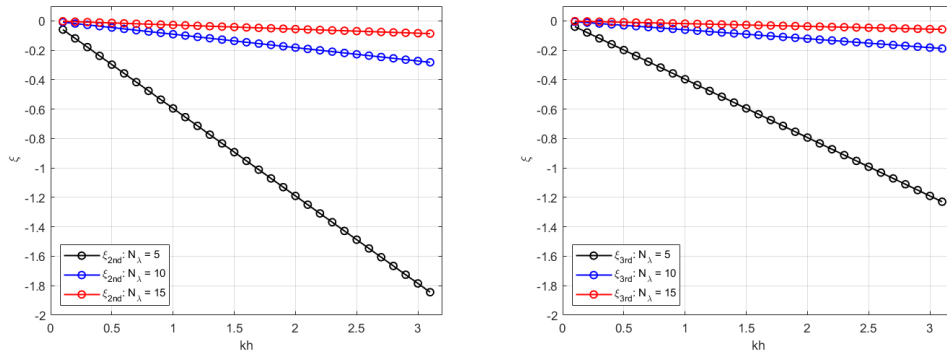


Figure 3.7: Numerical amplification rate as a function of the reduced wavenumber kh when using the second (left) and the third (right) order reconstruction in the hyperbolic part, for different choices of the number of points per wavelength N_λ

3.6 Boundary conditions and wave generation

In this work, we have implemented periodic, fully reflective/wall and absorbing boundary conditions. In the case of wall boundary conditions, the elliptic solver is modified in boundary nodes to set the conditions

$$\begin{aligned}\Phi \cdot \mathbf{n} = 0 &\Rightarrow \Psi \cdot \mathbf{n} = -h \frac{\nabla \eta \cdot \mathbf{n}}{\alpha} \\ \partial_{\mathbf{n}} \Phi \cdot \boldsymbol{\tau} = 0 &\Rightarrow \partial_{\mathbf{n}} (\Psi \cdot \boldsymbol{\tau} + h \frac{\nabla \eta \cdot \boldsymbol{\tau}}{\alpha}) = 0\end{aligned}$$

For straight walls the first condition is a consequence of $\mathbf{u} \cdot \mathbf{n} = 0$, while the second forces the rotational components of Φ to zero at the walls. This latter condition is consistent with $\nabla \wedge \Phi = 0$, which can be easily proved for the continuous equation used in the bulk. In practice we modify both the RHS and matrix of the elliptic system to account for these conditions. In the hyperbolic solver we also make sure that $\mathbf{u} \cdot \mathbf{n} = 0$ by modifying the hyperbolic fluxes and source and removing the normal component.

Absorbing boundaries are applied in order to dissipate completely the energy of the incoming waves, trying at the same time to eliminate any non-physical reflection. This kind of boundaries requires the definition of a sponge layer in which the surface elevation and the momentum are damped by multiplying their values by the coefficient:

$$m(\mathbf{x}) = \sqrt{1 - \left(\frac{\mathbf{x} - d(\mathbf{x})}{L_s} \right)^2}.$$

where L_s is the sponge layer width and $d(\mathbf{x})$ is the normal distance between the cell center with coordinates \mathbf{x} and the absorbing boundary. Typical values of the sponge width are related to the wave length λ of the incoming wave and usually are: $\lambda \leq L_s \leq 1.5\lambda$.

Finally, a large number of numerical tests demand the generation of monochromatic waves. One very common approach is to use an internal wave generator. This means, generating the waves

inside the computational domain avoiding issues that may arise from boundaries. In this work we make use of the internal wave generator, firstly described in [270]. In our scheme this is obtained by adding a source term to the mass equation, as described in [222] and references therein.

3.7 Numerical validation and benchmarking

3.7.1 Grid convergence for the solitary wave

We return to the exact solitary wave to compare on figure 3.8 the errors obtained when using the second (blue lines) and third order (orange lines) reconstructions. Convergence plots are reported for the free surface, and for Φ . We observe that using the third order scheme in the hyperbolic step, thus passing from $\mathcal{O}(h^2)$ to $\mathcal{O}(\mu h^2)$, allows an increasing slope and a more or less consistent reduction of the error by a factor between 3 and 5.

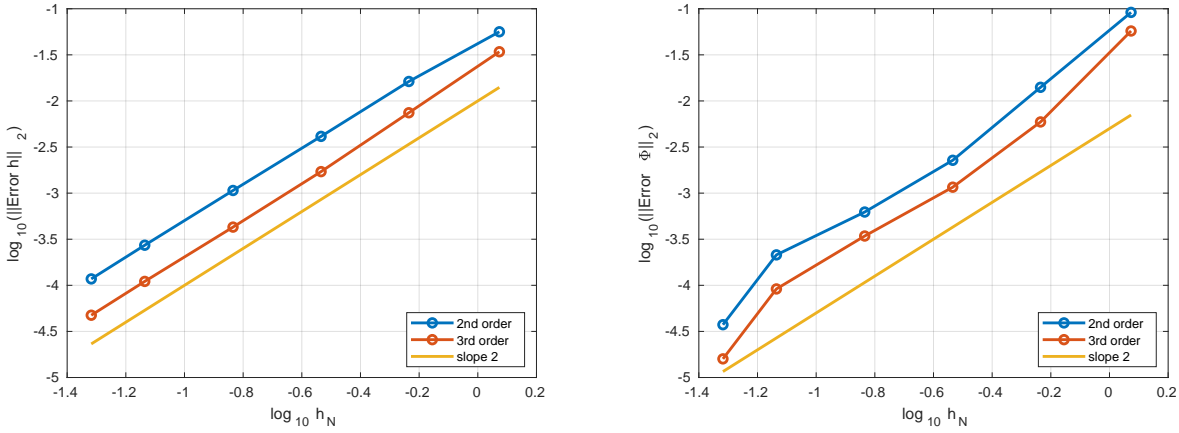


Figure 3.8: Error decay for second and third order schemes for h and Φ .

3.7.2 Circular shoal

Whalin [272] studied the focusing effected induced by a semi-circular shoal on wave trains of different periods. The wave tank used is of $6.096m$ wide and $25.6m$ long. A semi-circular shoal was placed at the middle portion of the tank leading the water depth to decrease from $0.4572m$ at the wave maker region to $0.1524m$ to the end of the tank. This test case has been used by many authors in order to test the dispersive properties of their models, see for example [178, 16, 262, 88, 252, 136, 222] in which a detailed description of the set up of the case can be found. The three test cases that have been reproduced here are:

- (a) $T = 1s$, $A = 0.039m$, $h_0/\lambda=0.306$ and $\epsilon = 0.085$
- (b) $T = 2s$, $A = 0.015m$, $h_0/\lambda=0.117$ and $\epsilon = 0.033$
- (c) $T = 3s$, $A = 0.0136m$, $h_0/\lambda=0.075$ and $\epsilon = 0.030$

where T is the wave period, A the wave height and λ the wave length. Wave gauges are placed along the center line to record the time series of the free surface elevation, which are analyzed in the frequency domain using a Discrete Fourier Transform (DFT) to obtain the first three harmonic amplitudes. The computational domain used is $[-10, 36] \times [0, 6.096]m$. Periodic waves are generated using the internal generator placed at $x = 4m$ and sponge layers of $6m$ are placed at the left and right end of the domain. Reflective boundary conditions are imposed at the remaining boundaries. For the computation of the first case a triangular grid was used, consisting of triangles with side lengths $h_x = 0.05m$ and $h_y = 0.1m$ leading to a mesh of $N = 56211$ nodes. For the last two cases the grid consists of equilateral triangles, with $h_N = 0.01m$ leading to a mesh of $N = 28151$ nodes. The CFL value used was 0.5.

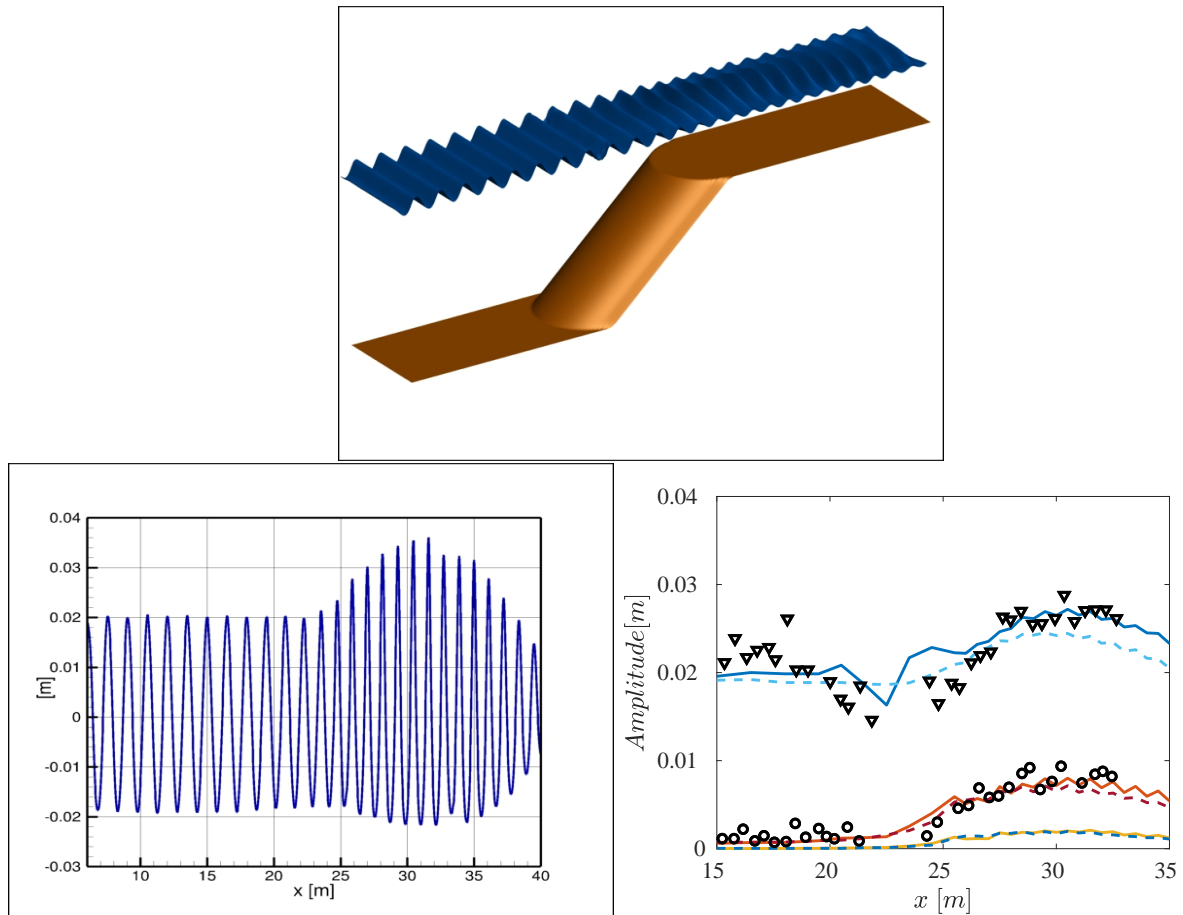


Figure 3.9: Wave diffraction over a semi-circular shoal. Case (a): Left: Computed free surface data along the centerline of the domain. Right: comparison of the DFT of the numerical data over the centerline with experimental data. Dashed line second order scheme, continuous line third order scheme.

For all the test cases, the incoming waves are linear in the deeper portion of the tank and they are steepening due to the wave shoaling. Wave energy gradually spreads out to higher harmonics, which increase in amplitude in the shoaling region. For both case (a) and (b) the agreement between

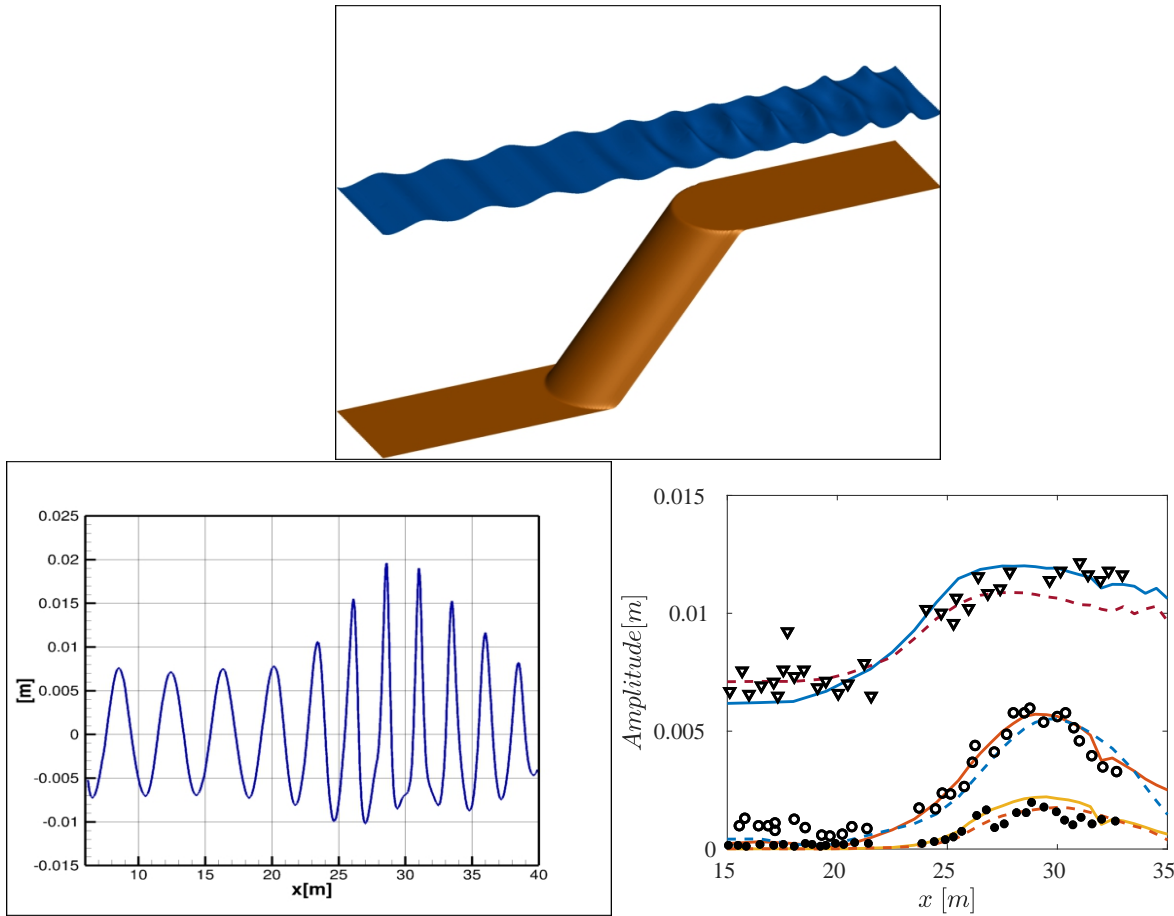


Figure 3.10: Wave diffraction over a semi-circular shoal. Case (b): Left: Computed free surface elevation at time $t = 40\text{sec}$. Right: comparison of the DFT of numerical data over the center-line with experimental data. Dashed line second order scheme, continuous line third order scheme.

the numerical and experimental data is quite satisfactory for all the harmonics, while in the last test case (c) the numerical results overestimate the first harmonic and underestimate the other two. This behavior has also been observed by other authors [178, 16, 252, 165] and the discrepancies are attributed to the shorter evolution distance of this test case or to the presence of free reflected waves. We compare the numerical solution obtained using the third order scheme (continuous line) and the second order scheme (dashed line) in the hyperbolic part. The difference, as expected, is more pronounced in the first two cases where the waves are shorter.

3.7.3 Elliptic shoal

This test case studies the refraction and diffraction of a regular wave over a complex bathymetry and it is a reproduction of the experiment of [18]. It is mainly used to verify models based on mild-slope equations but also the extended Boussinesq-type equations. The numerical domain is 20m wide and 22m long, with $x \in [-10, 10]$ and $y \in [-17, 15]$. The bathymetry consists of an elliptic shoal placed on a ramp of constant slope forming a 20° angle with the x -axis. The maximum water depth

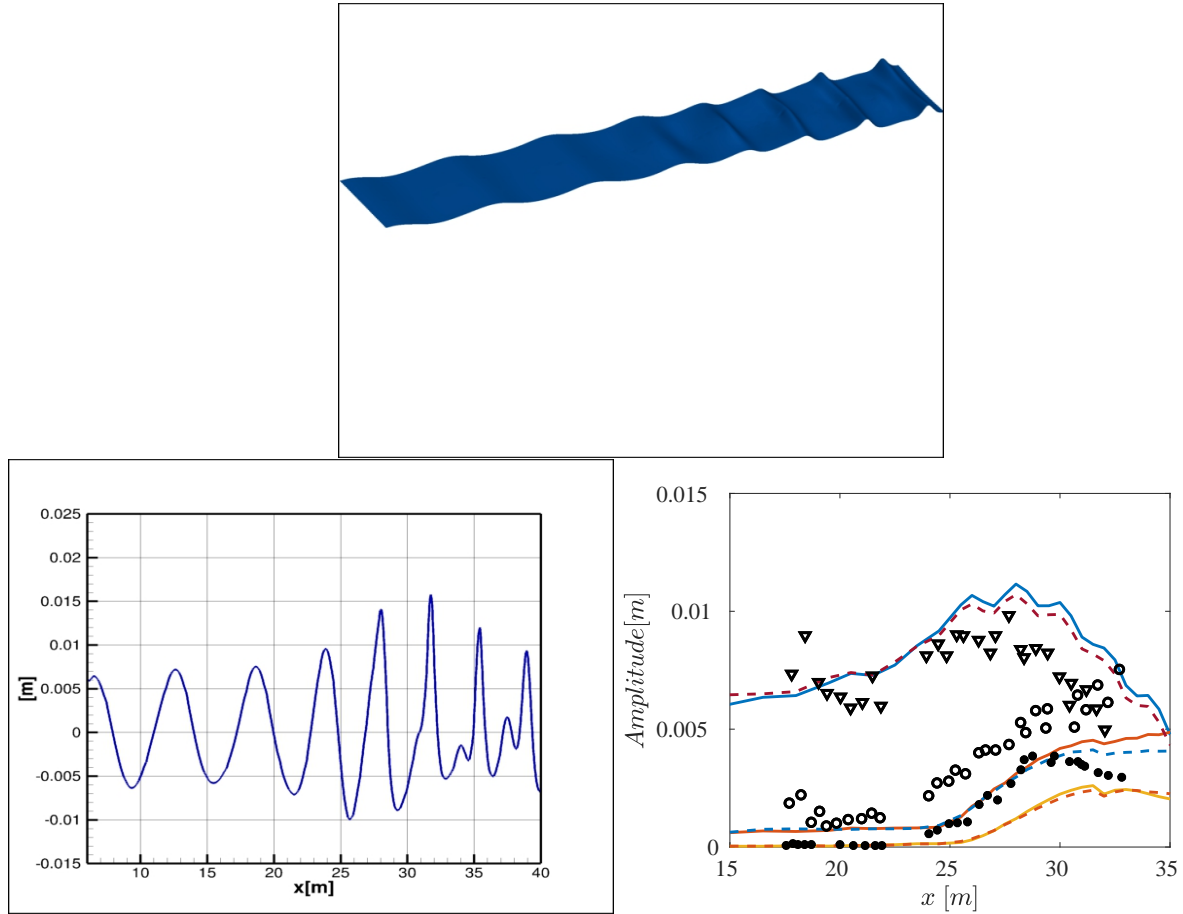


Figure 3.11: Wave diffraction over a semi-circular shoal. Case (b): Left: Computed free surface elevation at time $t = 40\text{sec}$. Right: comparison of the DFT of the numerical data over the center-line with experimental data. Dashed line second order scheme, continuous line third order scheme.

is $h_0 = 0.45\text{m}$ at the wave maker's position, which is placed at $y = -13\text{m}$. The bathymetry set up can be found in [136, 222] and references therein. The monochromatic wave's characteristics are: period $T = 1\text{s}$ and amplitude $a = 0.0232\text{m}$ corresponding to a non linearity degree $\epsilon = a/h = 0.3$. The normalized time average wave height was measured in eight different sections (see figure). Wall boundary conditions are imposed on the left and right boundaries, while sponge layers of 4m are placed at the bottom and top ends of the domain. In this test case, we used an unstructured grid refined in the region of the shoal. In particular the grid size in the y -direction varies from $h_y \approx 0.1\text{m}$ on the top and bottom boundaries, to $h_y = 0.05\text{m}$ in the region around the shoal. The simulation period is 50sec and the CLF used is 0.5 . A three dimensional view of the water elevation at the final time is reported on figure 3.12. In order to compare the numerical results with the experimental data [18], time series of the water elevation have been extracted in sections 1-8 during the last 25sec of the simulation. The time series are analyzed using the zero-up crossing technique to isolate single waves and to compute the averaged wave height. The results are normalized by the incoming wave height $2a = 0.0464\text{m}$ and are reported on figures 3.13 and 3.14. The agreement between the

numerical results and the experimental data are satisfactory and comparable to the results given by the literature ([222],[252], [262]).

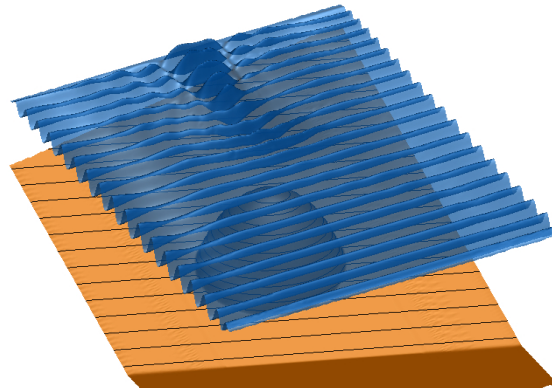


Figure 3.12: Wave diffraction over an elliptic shoal: 3D view of the free surface elevation at time $t = 50\text{sec}$.

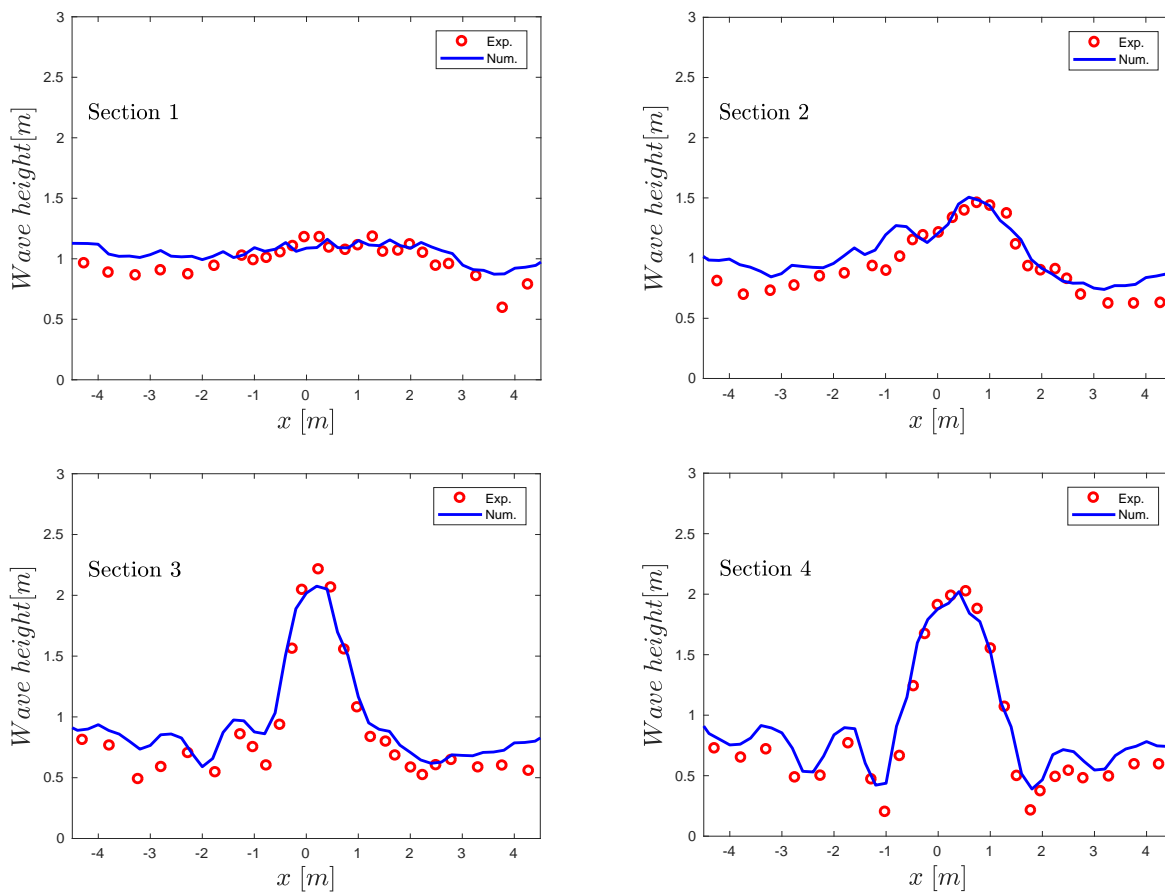


Figure 3.13: Wave diffraction over an elliptic shoal: Normalized wave height from sections 1 to 4.

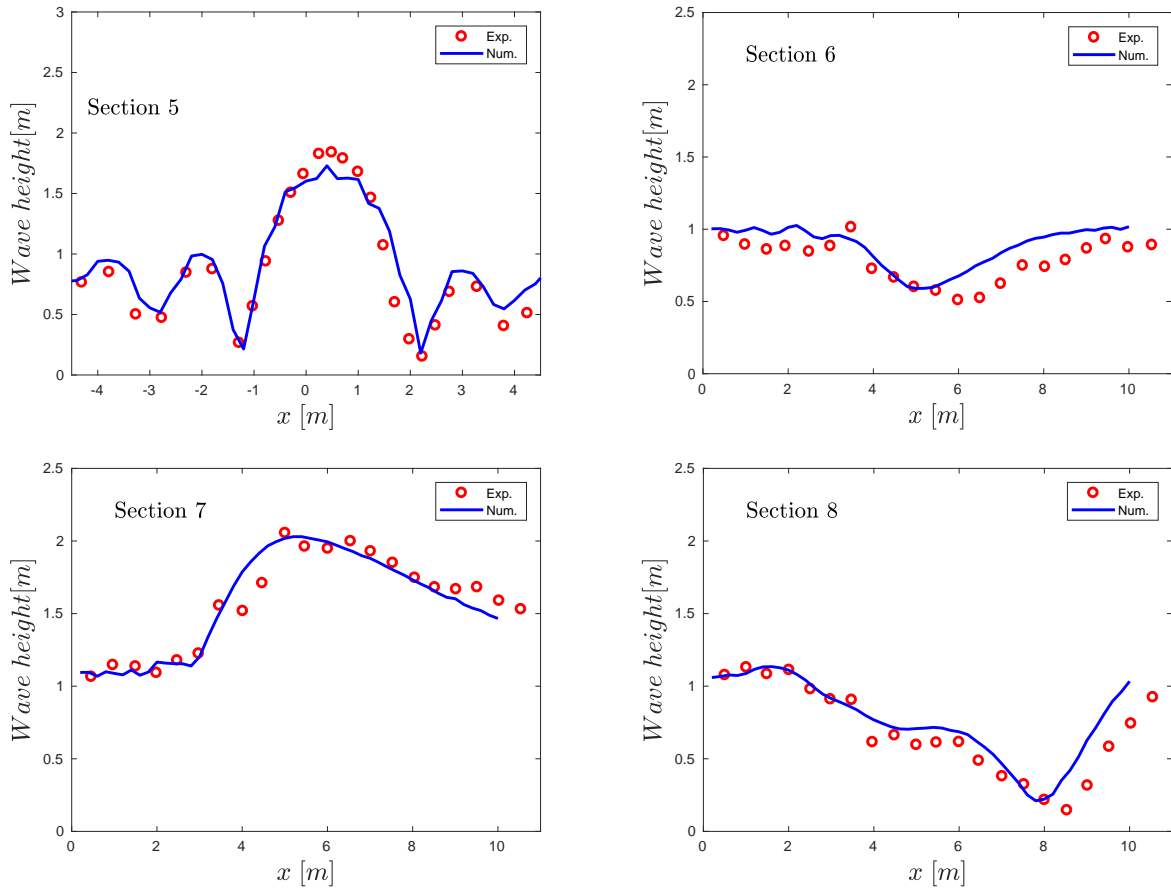


Figure 3.14: Wave diffraction over an elliptic shoal: Normalised wave height from sections 5 to 8.

3.7.4 Solitary interacting with a cylinder

In this test case we examine numerically the propagation and scattering of a solitary wave with a vertical cylinder. The laboratory experiment [75] investigates the interaction of the wave with the cylinder and it has been used by [132, 136] and references therein to validate their numerical models. The numerical domain used here is $x \times y \in [0, 14m] \times [0, 0.55m]$. A vertical cylinder of diameter $0.16m$ was placed at $(x_0, y_0) = (8.5, 0.275)$. The solitary has amplitude $A = 0.0375m$ and it is placed at $x = 4m$. The undisturbed water depth is $h_0 = 0.15m$, so the nonlinearity of the wave is $\epsilon = 0.25$. Six wave gauges were recording the free surface elevation and were located at: $wg1 = (8.4, 0.275)$, $wg2 = (8.5, 0.170)$, $wg3 = (8.5, 0.045)$, $wg4 = (8.6, 0.275)$, $wg5 = (8.975, 0.275)$, $wg6 = (9.375, 0.275)$. The mesh has 11345 nodes and it is refined around the cylinder. Figure 3.15 presents the 3d view of the free surface elevation after 4 sec, when the solitary interacts with the cylinder. This interaction causes the generation of scattering waves that propagate downstream while the rest of the wave recovers to a solitary wave and propagates upstream. The first wave that interacts with the cylinder and propagates upstream is computed quite accurately compared to the experimental data as seen in figures 3.16-3.18. The reflected waves, even though are better resolved compared to the ones that can be found in the bibliography [132, 136], still presents some discrepancies compared to the experimental data. This may indicate that a fully

dispersive model is needed for this case.

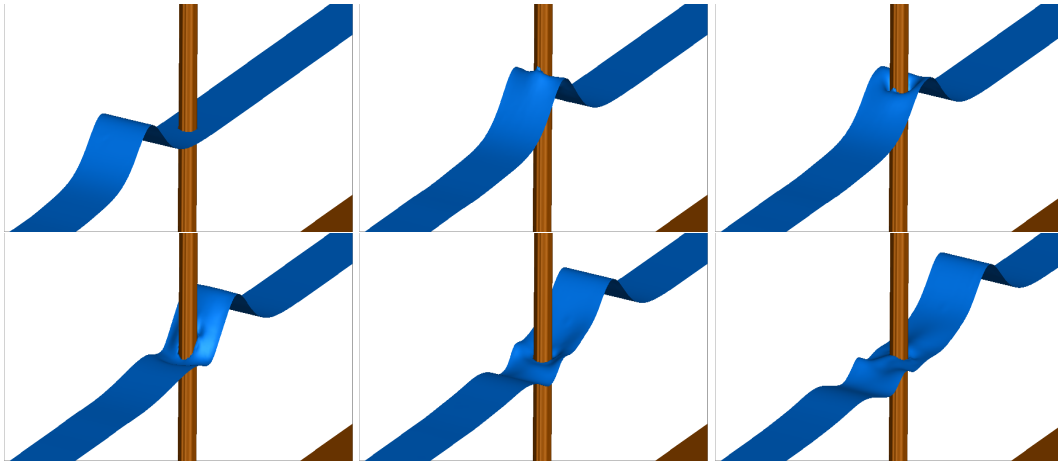


Figure 3.15: 3D view of the free surface elevation. Interaction of the solitary wave with the vertical cylinder.

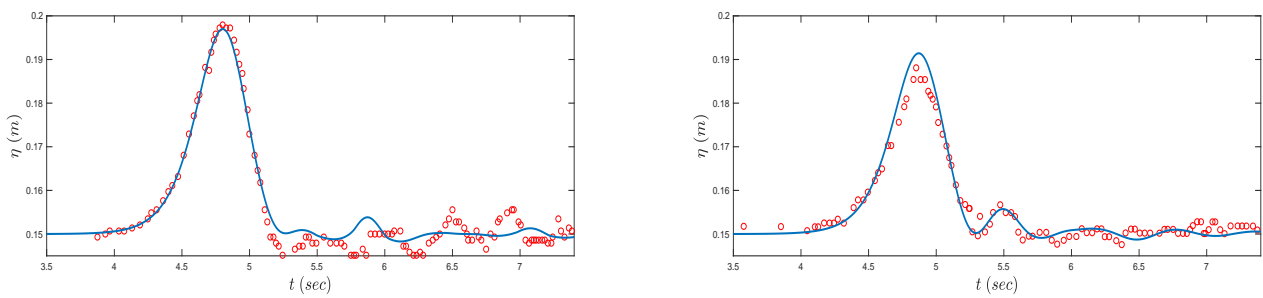


Figure 3.16: Free surface elevation at wave gauges 1 and 2

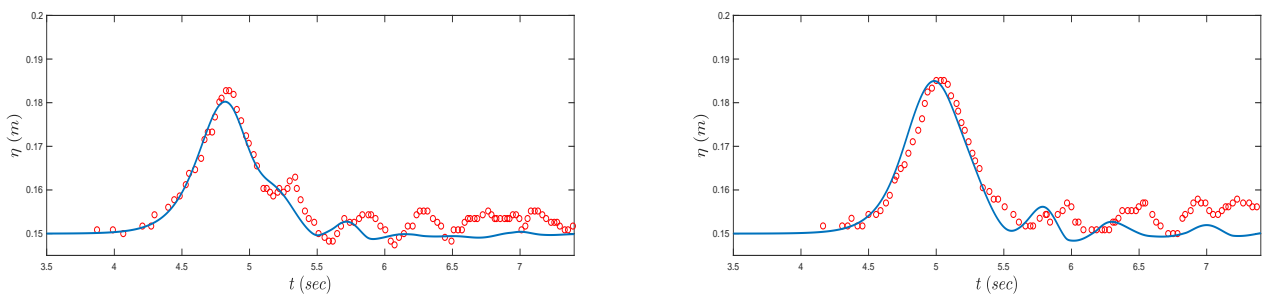


Figure 3.17: Free surface elevation at wave gauges 3 and 4

3.7.5 Solitary wave breaking on a 3D reef

Swigler et Lynett (2011) performed laboratory experiments at the O.H. Hinsdale Wave Research Laboratory of Oregon State University to study the specific phenomena which occurs when a

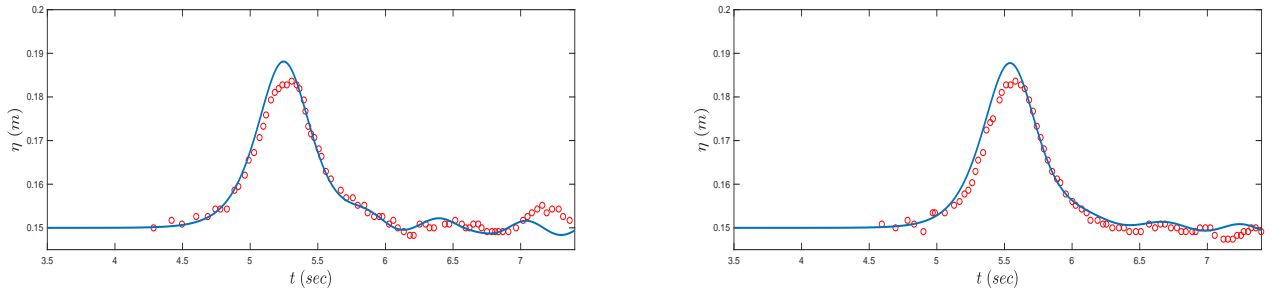


Figure 3.18: Free surface elevation at wave gauges 5 and 6

tsunami like wave approaches the coast: namely the shoaling, refraction, breaking and run-up of the wave. Many authors have used this case to validate their codes, since it is quite demanding and involves multiple physical phenomena correct representation. The computational domain is $48.8m$ long and $26.5m$ wide. Figure 3.19 shows the test set up along with the position of the wave gauges. The topography is determined from a laser scan and it consists of a slope of 1:30 connected with a triangular reef flat submerged between $0.75m$ and $0.9m$ below the still water level. The offshore shelf edge has an elevation of $0.71m$ with the apex located at $x=12.6m$. The steepest slope of the shelf is at the apex and becomes milder moving along the shelf edge toward the basin side walls. A concrete cone is also placed at the apex of the reef between $x=14m$ and $20m$. It has a diameter of $6m$ and a height of $0.45m$. The planar beach continues up to $x=31m$ and then becomes level until the back of the basin. Nine wave gauges were placed into the basin in order to measure the variation of the free surface elevation: gauges 1, 2, 3, 7 were located at $y = 0m$ and $x = 7.5, 13, 21, 25m$ gauges 4, 5, 6, 8 were located at $y = 5m$ and $x = 7.5, 13, 21, 25m$, while gauge 10 have been set at $y = 10m$ and $x = 25m$.

A hybrid strategy is implemented in the scheme as to account for the wave breaking that occurs after the wave's shoaling. The strategy is analytically explained in chapter 5. Compared to the experimental case, the computational domain has been extended from $x = 0m$ to $x = -5m$ in order to be able to completely contain the initial solitary wave. It has been discretized by means of two different unstructured grids. The first one is adapted to the bed curvature, as shown in 3.19, and characterized by reference maximum and minimum size respectively: $\max(h_K) = 0.3m$ and $\min(h_K) = 0.125m$. The second one is a triangular, non-refined grid of $h_k = 0.3$. A solitary wave of amplitude $A = 0.39m$, corresponding to $\epsilon = 0.5$, is initially placed in $x = 0$ and wall reflecting boundary conditions are imposed in each boundary of the domain. We used a Manning coefficient $N_m = 0.014$ for representing bed roughness. A CFL number of 0.5 was used, together with $\gamma = 0.6$ for the breaking detection criterion.

Figure 3.20 shows the computed free water surface at different time instants, using the refined mesh. With white color we denote the time evolution of the breaking regions detected by the criteria of the breaking mechanism. As the solitary wave propagates towards the beach it shoals, increases its steepness and nonlinearity, up to a breaking point at $t = 5s$ on the center line of the domain,

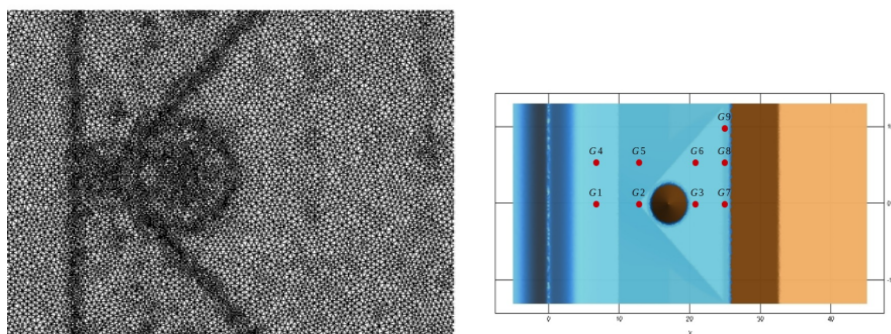


Figure 3.19: Solitary wave propagation over a three dimensional reef: Close up view of the adapted mesh used for the computation(right) and positioning of wave gauges (left)

when it reaches the apex of the triangular shelf. At $t = 6.5s$ the central part of the wave has completely overtopped the concrete cone, while on the two sides, the surge continues to shoal, diffracting around the base of the cone. By $t = 8.5s$, the refracted and diffracted waves collide on the lee side of the shelf. After $t = 9s$, the water starts to withdraw from the con top and a bore-front forms, from the combined waves after the diffraction, and propagates on the shelf behind the cone and then onshore. After $t = 15s$, a new bore is created from the the drawn-down of the water and collides with the refracted waves.

The next figure 3.21 plots the computed free surface time series on the wave gauges 1- 9 against the experimental data using the two grids. Green color represents the numerical results obtained using the coarser mesh and blue color the ones obtained using the refined mesh. Both cases show the same behavior, although the results obtained with the coarser mesh are more diffusive in the secondary waves, as expected. The arrival of the first incoming wave is correctly captured in gauges 1 and 2, as it is for the refracted and diffracted waves at the lee side of the cone, as can be seen from gauge 3. The signal at the gauges located at the north side of the cone indicates that wave shoaling, breaking and propagation on the shelf is accurately predicted, together with the complex nonlinear interaction between diffracted and refracted waves.

3.8 Summary

In this chapter we presented a hybrid numerical approach for the solution of the Green-Naghdi equations on unstructured meshes. We split the original system in a hyperbolic and an elliptic part. For the hyperbolic part, we used a third order, in space, node centered FV scheme. We achieve a third order reconstruction of the physical variables by means of a successive correction method which iteratively improves derivatives computed by means of the standard Green-Gauss formula. This approach guarantees global third order accuracy even on unstructured meshes. In order to prevent oscillations on non smooth solutions, we used a slope limiter [188] applied for a first time

on a node centered scheme using the derivative reconstruction via the successive correction. We coupled the non-dispersive hyperbolic solver to a second order solver for the physical weakly dispersive effects. We used the standard P1 FE method for this part. We ensured compatible data representation in the two phases of the computations, since both methods evolve unknowns associated to the mesh nodes, but with a totally different meaning.

We examined the impact of this different data representation on the theoretical accuracy, by writing an estimate of the local truncation error for constant bathymetry, concluding that, providing a second order accurate gradient on general meshes, the consistency of the scheme is of order $O(\mu h^2)$. The importance of accounting for the meaning of the data in the FE/FV coupling has also been confirmed by performing a convergence test.

An other conclusion of this work is related to the choice of the numerical fluxes in the hyperbolic step. It turns out that we have to use dissipative/upwind fluxes in order to stabilize the incomplete norm generated by the variational formulation, since we use H^1 finite elements, in the elliptic step. We provided numerical evidences to confirm this fact by studying again grid convergence.

Finally we showed that, using the third order scheme in the hyperbolic step, it allows a consistent reduction of the error by a factor between 3 and 5.

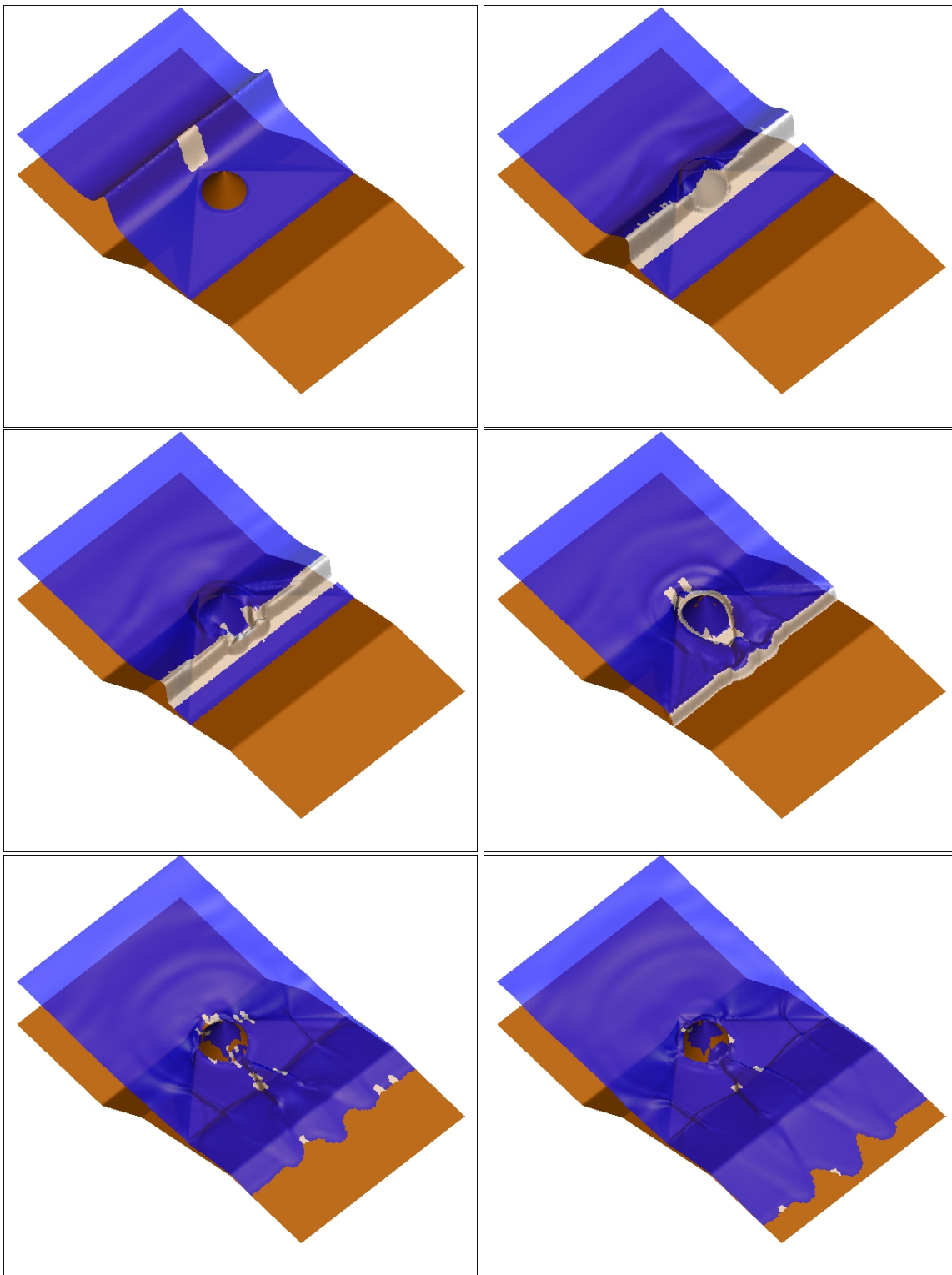


Figure 3.20: Solitary wave propagation over a three dimensional reef: evolution of free surface solution. The white area represents the region where wave breaking is detected and the NLSW equations are solved.

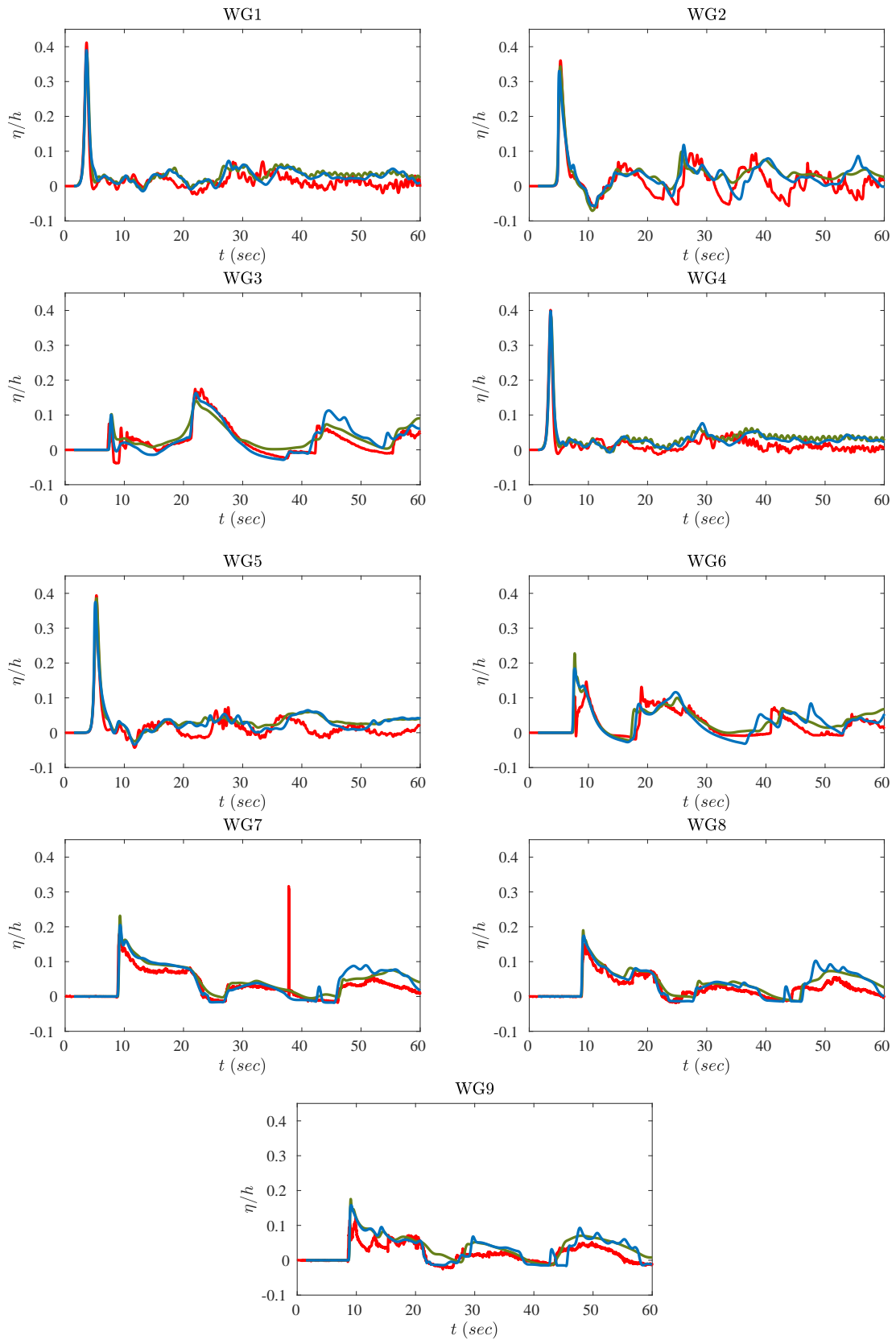


Figure 3.21: Solitary wave propagation over a three dimensional reef: computed time series of the free surface elevation on gauges positions (green : coarse uniform mesh; blue : refined mesh; red : experiments).

Chapter 4

Wave breaking closures for BT models

4.1 Wave breaking closures: a summary

One of the most important physical mechanisms that plays a significant role in on near-shore dynamics is the wave breaking. For this reason is crucial to incorporate dissipation mechanisms to the relevant wave propagation models. These equations are obtained under the hypotheses of ideal, and most often irrotational flow, and cannot account for the transformation processes taking place in breaking regions. In time-dependent Boussinesq-type models, such as those examined in the previous chapters, three distinct methods, hereafter wave breaking closures, have been applied separate or in combinations. The three main wave breaking closures are *the surface roller*, *the eddy viscosity approach* and *the hybrid model*. Detailed reviews on the topic can be found in [46, 137, 99].

A wave breaking closure typically consists of two components. The first part includes the criteria used to identify and initiate wave breaking, sometimes also determining when it ends. The second part involves the dissipation mechanism that simulates how the energy from wave breaking is dispersed. Based on the review by [213] onset breaking criteria can be categorized as geometric, dynamic and kinematic. The geometric criteria encompass aspects such as wave steepness, wave asymmetry and skewness, and wave crest-front face steepness. In phase-averaged models, breaking criteria mainly fall within the geometric category. For instance, the critical front slope introduced by Schaffer et al [230], or the velocity gradient limit proposed by Zelt [275] and used also by [151, 51]. Additionally, there have been proposals for combining geometric criteria, as discussed by [137] in their numerical implementation. A similar approach of the later is used by Kennedy et al. [147] where they replace the spatial velocity gradient by the time derivative of the free surface elevation. Papoutselis et al. [203] have employed analogous strategies more recently. Other approaches are based on factors like the acceleration of the free surface [46], the critical surface Froude criterion [8], the Froude number at the wave trough position [200], or the criterion introduced by [252] that uses the similarity between spilling breakers and moving hydraulic jumps. Considerable effort has also been made on the kinematic criteria which are often based on the relationship between the crest particle velocity and the wave phase speed with wave breaking occurs when the ratio of the particle velocity over celerity is greater than one. Recently [13] proposed a different ratio for the triggering

of breaking on indeterminate and deep water and [69] verified this ratio for all water depths using a large eddy simulation/volume of fluid model [68] and a fully nonlinear potential flow solver using a boundary element method [111, 112]. An extensive review on the criteria of wave breaking can be found in [99].

Wave breaking has been incorporated into BT models by means of different artificial techniques. The surface roller model, the vorticity model and the eddy viscosity model are three types of additional momentum dissipation methods. The first attempt to simulate wave breaking using a Lagrangian Boussinesq model, was proposed by Zelt [275] introducing a dissipation term in the momentum equation. This term controls the dissipation of energy produced by the wave breaking and it is governed by the value of an eddy viscosity coefficient which must be calibrated with experimental data. Of course, different calibration is needed for different sets of equations. The same approach has been followed from Wei and Kirby [271]. Karambas and Koutitas [131] used also an eddy viscosity mechanism with the limitation that the formulation was not momentum preserving and the setup prediction in the inner surf zone (in the investigation of the performance for periodic waves) was very poor. Kennedy et al. [147] followed [275] but with extensions to provide a more realistic description of the initiation and cessation of wave breaking resulting in a more accurate portrayal of wave height and setup when regular waves break on planar beaches. Many researchers through the years have used this approach, or simple modifications of this see for e.g [228, 171, 58]. Although, the eddy viscosity model is a very successful one and intensively used, we have shown in some previous works [137, 139] that the largest disadvantage in the classical formulation [147] is that, in some special cases, such as stationary hydraulic jumps, wave breaking initiation is not recognized and that even modifying the inception mechanism, the amount of the viscosity obtained is not enough for this type of breakers. Additionally, [58] showed that Kennedy et al.'s eddy viscosity breaking model could hardly predict simultaneously accurate wave height and asymmetry along the surf zone. Another criticism to this approach is that, while simple, no direct physical meaning can be attributed to the scaling coefficients involved in the definition of the viscosity [58]. For this reason we have looked at an extended approach involving partial differential equations to describe the key physical quantities like the turbulent kinetic energy, the energy dissipation, eddy viscosity, and so on. We will delve into this in the next section. More precisely, in this approach, the definition of the eddy viscosity involves its computation over the breaking event by solving the turbulent kinetic energy equation (TKE) after the breaking onset. This approach has been introduced by Nwogu [199] and followed by many others [83, 277, 67, 223, 106, 145]. Very recently it has also been used by [99] in order to improve Kennedy's [147] model. Last but not least, very recently a new fully non linear model, for coast waves, capable of describing also breaking has been derived by [134]. The model's variables are the fluid depth, the average velocity and the enstrophy, which includes the large-scale turbulence effects. Breaking is detected when a sudden increase of enstrophy occurs and it is the impact of the enstrophy that is handling the dissipation due to breaking. There is no additional dissipation source in the model.

A more relevant physical definition of the effects of breaking on the large scale flow has been attempted using the so-called roller models see for example [241, 238, 180, 58, 246]. While

based on a better physical background, these models still require some ad-hoc definition of a momentum dissipation, and require some calibration [192]. A more advanced version of these roller models has been proposed in [33], and more recently extended in [261]. These models attempt at accounting for variations along the depth of some of the physical quantities (eddy viscosity, horizontal velocity), thus going beyond the irrotational hypothesis when computing the vorticity and/or dissipation generated in breaking regions. While promising in principle, these models are more complex to implement, require an additional vertical discretization, and have so far been applied only to simple configurations.

An other option and possibly the most used in this time [252, 137, 234, 97, 138, 159, 46] is the hybrid wave breaking closure approach. It is based on the local coupling of the dispersive propagation model with the nonlinear shallow water equations. The rationale behind this is that the energy dissipation of broken waves are well characterized by the shocks produced by the NSW [38, 26] while the rest of the flow can accurately be described by dispersive equations. It is a simple method in which one first detects breaking regions, and in these the dispersive terms are suppressed. In these breaking regions thus one solves the non-linear shallow water (NSW) equations which allow to model a breaker as a shock. Through this discontinuity mass and momentum are conserved, while total energy is dissipated, thus modelling the energy dissipation due to breaking. The idea was first introduced in [252] in order to exploit the Finite Volume (FV) technique as to simulate discontinuous phenomena such as wave breaking and run-up. As pointed out in some works like [252, 234, 97], this approach has a major limitation in the stability of the coupling which introduces spurious oscillations at the interface between the breaking and non-breaking region. This phenomenon has been observed by many [77, 152] but is unfortunately poorly documented in the literature. Recently we tried to formulate the problem and reveal its sensitivity to mesh refining [145]. The problem described falls within a broader category of research involving the coupling of dispersive and non-dispersive models. This area of study is indeed quite active and has gained significant attention in recent years [102, 160, 207].

Going back to the hybrid wave breaking closure, one of the issues not fully addressed is the role of numerical dissipation in curing the flow of oscillations. Some researchers advocate for the use of more robust limiting procedures, as demonstrated by [103] and [77], to stabilize numerical solutions. For instance, Duran [77] proposes degrading the accuracy of numerical discretization near the shallow water-Boussinesq interface. This adjustment effectively increases numerical dissipation, thereby mitigating numerical perturbations on relatively coarse meshes. However, the sensitivity of this closure to grid size remains uncertain.

To demonstrate this point we consider the following motivational example involving the shoaling and breaking of a solitary wave on a slope. This example is part of a set of very classical benchmarks by [242]. Here, we present results for a breaking case (wave nonlinearity equal to 0.28), in which we set manually the transition region according to its known position from the experiments. Compared to actual simulations with the hybrid method, note that this eliminates one of the causes of instability: the intermittency of the detection. We then perform simulations degrading the numerical scheme at the interface between the Boussinesq and shallow water regions, and in all the shallow water

region. In these areas we use the most non-oscillatory and robust possible choice: the first order upwind finite volume method. We consider in 4.1 results in two very close time instants, on three meshes. The red line shows the detection flag separating the Boussinesq and shallow water regions (one indicates the breaking region, and zero the Boussinesq region). The figures show that: no instabilities whatsoever are observed in the largest gradient region (which will become the bore). An oscillation is instead triggered at the interface, and its blow up is almost instantaneous on the finest mesh, despite the fact that the most dissipative approach available has been used.

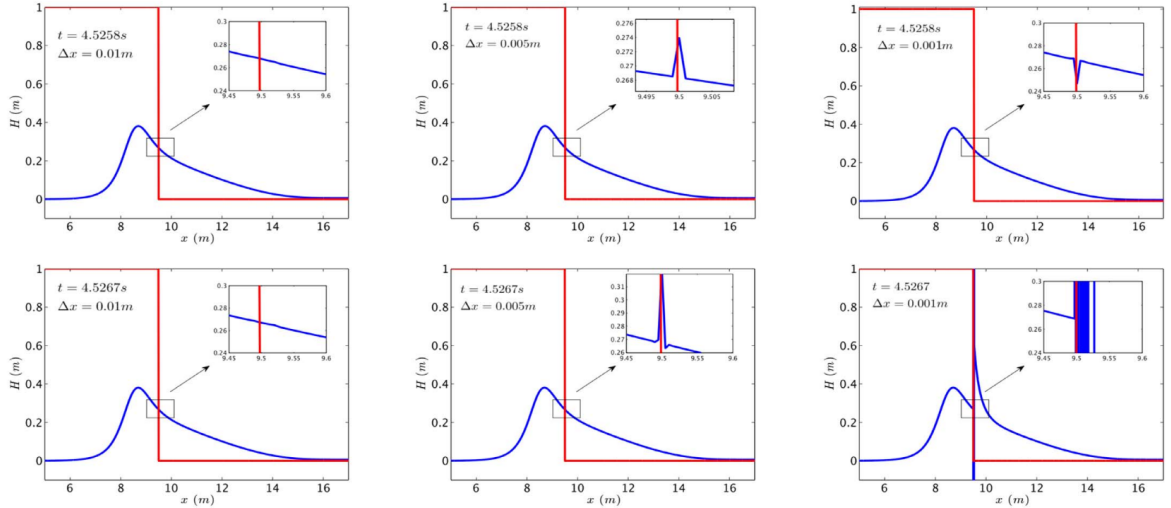


Figure 4.1: Solitary wave breaking on a slope: hybrid treatment with order reduction at the coupling interface. Wave height at times $t = 4.5258$ s, 4.5267 s (top and bottom rows), on mesh sizes (from left to right) $\Delta x = 0.01$ m, 0.005 m, 0.001 m .

Grid convergence analysis for breaking cases are quite rare in literature. The only exception we are aware of is the single computation shown in [235] in which the authors observe convergence in time averaged quantities, but report the appearance of increasing oscillations in the point-wise values of the solution without further notice. Clarifying these aspects is of paramount importance. Indeed if one cannot be sure that the mesh size allows the numerical dissipation to be sufficiently large, the initiation of the numerical instabilities may be confused with physical/dispersive effects. A control of this flaw is of course also needed if one wishes for example to use mesh adaptation in breaking regions.

Our work in [145] investigates the above issues for choices of propagation models and wave breaking closures representative of classical and well known models such as BOUSS-2D [67], FunWave [270, 235], Coulwave [171], BOSZ [226, 228], MIKE21, TUCWave [136, 137], Uhaina [94] and others. We thus used two enhanced weakly dispersive Boussinesq models: the weakly nonlinear model of Nwogu (used e.g. in BOUSS-2D, BOSZ, and TUCWave), and a frequency enhanced variant of the fully nonlinear Green–Naghdi equations (with similar properties to those used in Funwave and Coulwave). We compared the hybrid approach to an eddy viscosity model. Note that with the eddy viscosity closure the breaking wave fronts are smoother than those obtained

with the hybrid method which relies on the approximation of these fronts as shocks. For this reason when using the hybrid approach one has to carefully choose the conservative form used to solve the model, which is essential to recover the right jump conditions, and some form of limiting to avoid the creation of additional spurious numerical oscillations in correspondence of the shock [135, 137, 136]. The original definition of an eddy viscosity model [147] has been previously shown to have difficulties in handling steady hydraulic jumps [137]. For this reason we have chosen to use an approach based on the solution of a partial differential equation for the turbulent kinetic energy, similar to the one studied with BOUSS-2D [67].

The representative wave propagation models that we used, as we mentioned earlier, are the one of Nwogu's and the enhanced Green-Naghdi (see chapter 1 for details). The numerical treatment of both systems, is done using an implicit treatment of the dissipative components (friction and/or turbulent dissipation). In particular, the kernel of both models is the hyperbolic component which rules the evolution of the water level and flux variables. Consider then non-overlapping temporal slabs $[t^n, t^{n+1}]$, with $\Delta t^{n+1} = t^{n+1} - t^n$. The hyperbolic evolution is performed with the two-stages Adams Bashforth-Adams Moulton predictor-corrector method. For the models' numerical discretization in space, the reader can refer to chapter 3 of this document. Concerning the dispersive terms, the \mathbf{D}_q contribution in (1.6) is discretized using finite differences. While for the hyperbolic component the minimization of the dispersion error requires at least a third order approximation, this is not the case for the higher derivatives in the dispersive terms (see [269, 97] and chapter 3 for more details on this issue). Here, following our previous work [135], the second and third order derivatives in (1.6) are treated by means of second order central differencing. We have to highlight that the only difference with the work described in chapter 3 is the treatment of the friction and the turbulent dissipation (if present). They are embedded in an implicit manner, by appropriately correcting the velocity values. The reader can refer to [145] for more information.

4.1.1 Trigger mechanism

As already stated, Boussinesq equations are unable to describe both the overturning of waves, and the dissipation of kinetic energy originated during wave breaking. A physical closure is necessary. Generally, this closure consists of two main steps. The first one is a trigger mechanism allowing to localize in space and time the initiation and the termination of breaking. The second one is a mechanism introducing a dissipation of total energy in the model. This paper focuses on two techniques to define the second element, which are discussed in some detail in the following sections. In both cases, the triggering of wave breaking is done following the criteria proposed in [137, 97] which have been found simple and robust. The idea is to introduce a flagging strategy based on the following conditions:

- the surface variation criterion: a cell is flagged if $|\eta_t| \geq \gamma\sqrt{gH}$, with $\gamma \in [0.3, 0.65]$ depending on the type of breaker;
- the local slope angle criterion: a cell is flagged if $\|\nabla\eta\| \geq \tan\varphi_c$, with critical angle $\varphi_c \in [15^\circ, 30^\circ]$ depending on the flow configuration.

The first criterion is usually active in correspondence of moving waves and has the advantage of being completely local. The second criterion acts in a complementary manner, and allows to detect stationary or slow-moving hydraulic jumps [228, 137]. Flagged cells are grouped to form a breaking region. This region is either enlarged to account for the typical roller length, as suggested in [137, 249], or deactivated, depending on the value of the Froude number $Fr^2 = H_{\max}(H_{\max} + H_{\min})/(2H_{\min}^2)$, defined starting from the minimum and maximum wave height in the flagged zone. The interested reader can refer to [249, 137, 8] and references therein for more details regarding the implementation of these detection criteria.

4.1.2 Hybrid wave breaking model

This closure attempts to exploit the properties of hyperbolic conservation laws embedded with an entropy inequality. For the shallow water equations, in particular, the mathematical entropy coincides with the total energy [245, 121, 243, 244, 98, 273]. At the continuous level, while conserved in smooth regions, entropy/total energy is dissipated in discontinuous weak solutions. Provided that the numerical scheme introduces the correct amount of dissipation in shocks [245, 244, 98, 273], this lends itself naturally for the wave breaking closure. This approach is in itself neat and simple. It has the limitation that the form of the dissipation is, at best, fixed by that determined by the shallow-water Rankine-Hugoniot jump conditions. This quantity can be analytically computed and it is given by (see e.g. [218] chapter 1.6, and [24])

$$\mathcal{D}_{sw} = g \sqrt{g \frac{H_{\max} + H_{\min}}{2H_{\max}H_{\min}} \frac{(H_{\max} - H_{\min})^3}{4}} \quad (4.1)$$

This is however a parameter free definition of the dissipation which has been proved to reproduce quite well the large scale decay of the total energy in for several types of breaking waves, and with several different underlying propagation models and relative numerical discretizations [252, 253, 235, 137, 159, 8, 95]. The implementation of this closure is somewhat trivial once the wave detection algorithm discussed earlier has been properly set up. For the Nwogu's equations, it boils down to locally turning off in the whole flagged region the dispersive source \mathbf{D}_q and D_h , in (1.5) and (1.4) respectively. Similarly, for the GN system, the nodal values of \mathbf{D}_q in (1.9) are set to zero in the breaking region.

The most limiting aspect of this approach is the switch between the non-hydrostatic and the hydrostatic equations. What has been reported by many authors in a more or less marked way, is the difficulty of performing this switch in a stable manner. Unless coarse grids are considered, with eventually the addition of local regularization numerical dissipation terms, several authors have reported the appearance of strong oscillations [235, 137, 97, 78]. These artifacts tend to become stronger and stronger as the mesh is refined. To our knowledge, there are no studies in literature reporting fully grid converged solutions with this approach due to this problem. An exception to this is perhaps one result reported in [235] showing some convergence (on only 3 grids) of the time averaged wave heights and setup, even though increasing oscillations in the local profiles are reported for the same test. This behaviour clearly poses a limitation in terms of potential for local automatic adaptation of the mesh, and its investigation is one of the objectives of this article.

4.1.3 Eddy viscosity closure via a PDE based TKE model

The use of an eddy viscosity model to provide the dissipation required for the breaking closure is one of the earliest approaches [275]. The definition of this artificial viscosity is the key of this approach, as well as the way in which it enters the Boussinesq equations. One of the most common approaches, due to Kennedy and collaborators [147] (see also [228, 137, 139, 170] and references therein), involves a definition of the eddy viscosity based essentially on the variation in time of the free surface elevation. This term is then embedded in a viscous flux in the momentum equation. There exist improved variants of this idea, allowing to embed a richer physical description of the vertical kinematics and of the effects of turbulence (e.g. the so-called roller models). Some approaches explicitly embed the effects of the dynamics of vorticity (roller-models) [34, 261], others include partial differential equations for an average turbulent kinetic energy [199, 277], and others introduce a multi-layer description embedding PDEs for a turbulent layer flowing on top and interacting with the bulk of the wave, well representative of spilling flows [35, 173, 189, 223, 106]. Simpler methods have attempted at improving the behaviour of the total energy dissipation by also including a water elevation viscosity [58]. In this work, we have chosen to adopt a model of intermediate complexity based on the solution of an additional PDE, weakly coupled to the main Boussinesq system of equations. In particular consider the approach initially proposed by Nwogu [199] who used a standard TKE (turbulent kinetic energy) equation coupled to the fully non-linear equations of Wei et al. [270]. A highly non-linear Boussinesq model with the same turbulence wave breaking model of Nwogu has been used by Elnaggar and Watanabe [82]. More recent work on the same model is discussed in [277] where the TKE equation is manipulated to obtain a PDE for the eddy viscosity which is coupled to a fully nonlinear fully dispersive Green-Naghdi model. Here we propose a variant of the model proposed by Nwogu modified according to some of the definitions proposed in [277], as well as some definition which improve the consistency of the model with the wave breaking detection criteria we adopt.

Following [216, 277], the eddy viscosity is determined from the amount of the turbulent kinetic energy k , produced by the wave breaking, and a turbulent length scale ℓ_t :

$$v_t = C_\nu \sqrt{k} \ell_t \quad (4.2)$$

In $k - L$ turbulence models [187, 2] (see also [277]), the constant C_ν is usually set to $C_\nu = (0.09)^{1/4} \approx 0.55$ which is the value used here. We now need a model for the computation of k and ℓ_t . Differently from the models discussed in [187, 2], here we adopt a one equation approach in which only one PDE is solved for k , while the for ℓ_t , inspired by the definition used in [277], we use a vertical average mixing length defined as

$$\ell_t = \kappa H$$

where κ is a constant controlling the width and intensity of the breaking. The length ℓ_t is expected to be of the order of the wave height [199], so κ is a case dependent constant. Concerning turbulent

kinetic energy, it can be shown that in three space dimensions the following transport equations holds [216]

$$k_t + \mathbf{u} \cdot \nabla k = \mathcal{D} + \mathcal{P} - \mathcal{E} \quad (4.3)$$

with \mathcal{D} , \mathcal{P} , and \mathcal{E} , diffusion, production and dissipation (or destruction) terms respectively. Definitions and possible expressions of these quantities in terms of mean flow quantities can be found e.g. in the book [216]. When coupling (4.3) with a depth averaged Boussinesq model, several approximations are possible. Here we will combine some of the elements suggested in [199] and in [277] in order to obtain a model simple to implement, to be compared to the hybrid approach. First of all, we will assume that both k (and hence ν_t) and its transport dynamics are constant along the depth, so that (4.3) can be replaced by a zero-th order approximation involving only depth averaged quantities, namely

$$(Hk)_t + (Huk)_x = H\overline{\mathcal{D}} + H\overline{\mathcal{P}} + H\overline{\mathcal{E}}. \quad (4.4)$$

For the definition of the terms on the right hand side of (4.4) we have followed [199]. In particular, we have for the diffusion and destruction terms

$$H\overline{\mathcal{D}} = H\sigma\nu_t k_{xx}, \quad H\overline{\mathcal{E}} = -HC_D \frac{k^{3/2}}{\ell_t} \quad (4.5)$$

where, following [199, 277], we have set $C_D = C_\nu^3$. The constant σ allows to control the smoothness of the TKE, and hence of the breaking viscosity, in the breaking region. Concerning the production term, the model used is again the one suggested in [199] assuming this quantity to depend on the vertical gradient of the velocity at the free surface. Following the notation of (4.3), and denoting the velocity at the free surface by $\mathbf{u}^s = \mathbf{u}(t, x, y, z = \eta)$, we have

$$H\overline{\mathcal{P}} = HB(t, x) \mu_{\mathcal{P}} \mathbf{u}_z^s \cdot \mathbf{u}_z^s$$

As in [199], the turbulent viscosity $\mu_{\mathcal{P}}$ appearing in the production term is defined based on a mixing length hypothesis assuming a balance between production and dissipation, namely

$$\mu_{\mathcal{P}} = \frac{\ell_t^2}{\sqrt{C_D}} \sqrt{\mathbf{u}_z^s \cdot \mathbf{u}_z^s}$$

so that we end with

$$H\overline{\mathcal{P}} = HB(t, x) \frac{\ell_t^2}{\sqrt{C_D}} (\mathbf{u}_z^s \cdot \mathbf{u}_z^s)^{3/2}. \quad (4.6)$$

In [199] the parameter B is equal to 0 or 1 depending on a wave breaking criterion. In the reference the criterion used is based on the ratio between the free surface velocity and the wave celerity being larger than one. Here, for simplicity B is set to one in the breaking regions detected exactly as discussed in the beginning of section §4.1. This also allows to detect wave breaking in the same way for the TKE and hybrid approach. Having fixed the values of C_ν and C_D , the only “tunable” parameters are κ and σ .

Lastly, we need to be able to evaluate the depth averaged and free surface velocities for both Boussinesq models, as well as the value of the vertical gradient of the velocity at the free surface. For this we use the vertical asymptotic development underlying the two models. In the weakly nonlinear case, this development can be used to write the following relations [198, 157]

$$u(z) = u^a - \left(\frac{z^2}{2} - \frac{d^2}{6} \right) u_{xx}^a - \left(z + \frac{d}{2} \right) (du^a)_{xx}$$

giving the free surface vertical gradient

$$u_z^s = -\eta u_{xx}^a - (du^a)_{xx}. \quad (4.7)$$

and the depth averaged (within the asymptotic accuracy) velocity required for the transport term in (4.4)

$$u = u^a + \left(\frac{(z^a)^2}{2} - \frac{d^2}{6} \right) u_{xx}^a + \left(z^a + \frac{d}{2} \right) (du^a)_{xx} \quad (4.8)$$

The GN equations directly provide a value of the depth averaged speed, while the fully nonlinear asymptotic development allows to write

$$u(z) = u - \left[\frac{z^2}{2} - \left(\frac{H^2}{6} - \frac{H(H-d)}{2} \right) \right] u_{xx} - \left[z - \left(\frac{H}{2} - d \right) \right] (du)_{xx}$$

which yields a similar expression for the vertical gradient of the free surface velocity, this time in function of the depth averaged velocity u :

$$u_z^s = -\eta u_{xx} - (du)_{xx}. \quad (4.9)$$

The fully discrete distribution of the nodal values of the TKE is obtained by integrating equation (4.4) with a semi implicit approach. Before the predictor step (2.33) is applied to the Boussinesq models, the nodal TKEs are evolved by first applying an explicit Euler update involving a third order MUSCL upwind discretisation of the transport operator $(Huk)_x$, essentially the same presented in section chapter 1 for the shallow water equations. To avoid spurious negative values in this phase, the min-mod limiter is applied [157]. The predicted values k_i^* are then corrected by means of diagonally semi-implicit relaxation iterations similar to those used for the breaking dissipation and reading

$$\begin{aligned} \left(\frac{\Delta x}{\Delta t} + \frac{2\sigma v_{t,i}^n}{\Delta x} \right) (k_i^{m+1} - k_i^m) &= \Delta x \frac{k_i^m - k_i^*}{\Delta t} + \sigma v_{t,i}^n \frac{k_{i+1}^m - 2k_i^m + k_{i-1}^m}{\Delta x} \\ &+ \left(\frac{B\ell_{t,i}^2}{\sqrt{C_D}} (u_z^s)_i^{3/2} \right)^n - C_D \left(\frac{k_i^{3/2}}{\ell_{t,i}} \right)^n \end{aligned}$$

with an initial condition, $k^0 = k^*$. For the benchmarks discussed in this chapter, 4 or 5 relaxation iterations are used unless otherwise stated. Where necessary, depth averaged velocity (for the Nwogu model) and velocity gradient at the free surface (for both Boussinesq models) are obtained by a second order central finite difference approximation of (4.8), (4.7), and (4.9).

As a final note, we will keep in the following the notation TKE when referring to this closure, as this eddy viscosity method clearly relies on the solution of the PDE for the turbulent kinetic energy.

4.2 Discussion on the dissipation mechanisms

One of the key aspects concerning the numerical modelling of wave breaking is the notion of dissipation. As discussed in the introduction, the mechanisms related to the transformation of potential energy into mechanical energy, and its subsequent dissipation, are not embedded in Boussinesq models that we study which stem from a potential description of the flow. The role of the closure model is thus to mimic these mechanisms. Clearly the main interest in the closure is to be able to predict correctly the dynamics of wave heights and (in the multidimensional case) currents. It is however interesting to understand what is the underlying dissipation mechanism active during the numerical breaking process. The main question we want to contribute to answer to in this paper is how much the numerical method is involved in this process, and if it is at all. We provide here a short discussion of this aspect, and suggest quantities which we will use in the numerical applications to quantify the contributions to the breaking process of the numerics, as well as of the PDE model itself. A proper formulation of this analysis requires a formal definition of what is the energy to be dissipated for the propagation models under consideration. This has to be done at the continuous level, but of course we must be able to provide an appropriate discrete translation of this energy conservation/dissipation statement.

When looking at the discrete models, even for the GN equations it is still a matter of research how to devise a numerical method with a clear associated discrete energy conservation statement. For hyperbolic systems, including the shallow water equations, there is a clear and well established theory now allowing to construct methods which are exactly entropy-conservative or entropy stable see [145] and references therein. Unfortunately, the construction of exactly energy preserving schemes for dispersive equations is still a subject of research citations.

In order to be able to provide some quantitative information on the sources of dissipation, we had to make some choices, and some hypotheses. We start by recasting our PDE models as the shallow water system plus a dispersive source

$$\partial_t \mathbf{U} + \partial_x \mathbf{F}(\mathbf{U}) - \mathbf{S}_b - \mathbf{S}_f - \mathbf{R}_{wb} = \mathcal{D}$$

This is a form similar to (1.1), except that in the above equation the left hand side only contains the shallow water terms and the eddy viscosity model \mathbf{R}_{wb} , if present. All the dispersive terms are included in \mathcal{D} . We then look at the contributions to the balance of the shallow water total energy, whose time variation can be expressed as (see e.g. [243, 245, 244])

$$\partial_t E = \mathbf{V}^t \partial_t \mathbf{U} = -\mathbf{V}^t (\partial_x \mathbf{F}(\mathbf{U}) - \mathbf{S}_b - \mathbf{S}_f - \mathbf{R}_{wb} - \mathcal{D})$$

with $E = H(gH + u^2)/2 + gHb$, and having denoted by \mathbf{V}^t the transpose of the array of the so-called energy (or entropy, or symmetrizing) variables $\mathbf{V}^t = [g\eta - u^2/2, u]$. For both numerical models tested, we can easily provide a nodal discrete analog of the last expression which, using the notation of (2.16), reads

$$\partial_t E_i = \mathbf{V}_i^t \partial_t \mathbf{U}_i = -\mathbf{V}_i^t (-\mathcal{L}_i^{SW} - \mathbf{S}_{f_i} - \mathbf{R}_{wbi} - \mathcal{D}_i)$$

Neglecting the boundary conditions (or assuming periodic or null the boundary fluxes), the total variation of the shallow water energy can be deduced using the explicit form \mathcal{L}_i^{SW} and of the central and upwind contributions in the bathymetry terms [20, 135, 79, 43, 6]. The final result can be recast as

$$\sum_{i \geq 1} \Delta x \partial_t E_i = \sum_{i \geq 1} \Delta x \mathbf{V}_i^t \partial_t \mathbf{U}_i = \sum_{i \geq 1} \Delta \mathcal{F}_i^E - D_{upwind} - D_{friction} - D_{vis} + \Delta E_{\mathcal{D}}.$$

We can now try to say more on the terms on the right hand side. It seems quite reasonable to assume that wave breaking is not associated to the dispersive contributions. This means that we will leave out of the analysis the contributions of the dispersive source $\Delta E_{\mathcal{D}} = \sum_i \mathbf{V}_i^t \mathcal{D}_i$. Another term which in principle one would expect not to contribute to the analysis, is the centered part of the flux which enters the above expression via the terms

$$\Delta \mathcal{F}_i^E = -\mathbf{V}_i^t \left(\mathbf{F}_{i+1/2}^C - \mathbf{F}_{i+1/2}^C + \frac{gH_{i+1/2}}{2} \Delta_{i+1/2} [0, b]^t + \frac{gH_{i-1/2}}{2} \Delta_{i-1/2} [0, b]^t \right).$$

This is where the analysis provided in e.g. [244, 98] is most useful. Without going into much detail, the references provide a very simple rule to define the centered flux for which one can show that $\Delta \mathcal{F}_i^E = \mathcal{H}_{i+1/2} - \mathcal{H}_{i-1/2}$, with $\mathcal{H}_{i \pm 1/2}$ consistent numerical approximations of the total energy flux. This algebraic relation leads to the conclusion $\sum_{i \geq 1} \Delta \mathcal{F}_i^E = 0$ exactly, whether the solution is continuous or not. This means that, even if slightly different implementations of the central flux are used, this quantity is in principle not relevant for our analysis.

This leaves three quantities to be monitored, associated to the numerical (upwind) dissipation

$$D_{upwind} = \sum_{i \geq 1} \left\{ \Delta \mathbf{V}_{i+1/2}^t \left(\frac{1}{2} |\mathbf{A}|_{i+1/2} \Delta_{i+1/2} \mathbf{U} + \frac{gH_{i+1/2}}{2} \text{sign}(\mathbf{A})_{i+1/2} \Delta_{i+1/2} [0, b]^t \right) \right\},$$

and to the friction and wave breaking (eddy viscosity) model

$$D_{friction} = \sum_{i \geq 1} gH_i S_{fi} u_i^2 \quad \text{and} \quad D_{vis} = \sum_{i \geq 1} \nu_{t,i+1/2} H_{i+1/2} (\Delta_{i+1/2} u)^2.$$

Note that with the spatial discretization choices made both $D_{friction}$ and D_{vis} are clearly positive definite. The same cannot be said a-priori about the upwind dissipation D_{upwind} . To be sure of the positivity of this term, indeed one should have implemented the dissipation in terms of variations of the entropy variables [244, 98, 273], instead of using in the numerical flux variations at cell interfaces of the conservative variables, as done in standard implementations of the upwind flux. Furthermore, this term involves both the reconstruction and the limiter, the latter only in the shallow water regions associated to wave breaking when using the hybrid approach of section §4.1. This makes it a perfect candidate to monitor the impact of the numerical choices and their contribution to the wave breaking process, and when possible compare these contributions to those of the eddy viscosity and friction terms. This analysis has been performed for three of the benchmarks proposed, involving both periodic and non periodic waves, dry areas, as well as pure propagating bores. Note that in practice the above expressions have to be evaluated in post-processing, by saving the different

terms evaluated during the computations. The time stepping of course also plays a role in this analysis. The interested reader can refer to [245] for a discussion on this. To minimize these effects, while keeping as much as possible of the actual terms computed in the code and used to obtain the numerical solutions, in all the cases presented we have used $t^{n+1/2}$ half time-step evaluations of these terms by averaging values at t^n and t^{n+1} .

4.3 Numerical results

4.3.1 Wave breaking over a bar

This test case of Beji and Battjes [14] examines the sinusoidal wave propagation over a submerged bar. The scope of this test case is to investigate the frequency dispersion characteristic and non-linear interaction of complex wave propagation phenomena. A sketch of the problem is provided in figure 4.2. The computational domain is $x \in [0, 35m]$, with sponge layers placed at both ends. Periodic waves were generated at $x = 10m$ over a mean water depth of $0.4m$. Wave height and period are set to $a = 0.054m$, and $T = 2.5s$, corresponding to a dispersion parameter $kh \approx 0.52$. Waves propagate over submerged trapezoidal bar with a toe at $x = 15m$, a front slope of 1 : 20, a $2m$ long plateau of $0.3m$ height, and a lee slope of 1 : 10. More informations on the experiment can be found in [14] and in the references using this test case for model validation [97, 137, 153, 249].

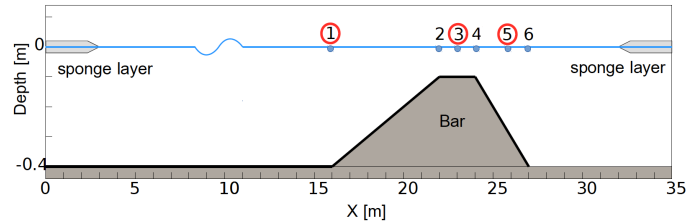


Figure 4.2: Wave breaking over a bar: problem sketch, and position of the gauges

Concerning the model parameters, for this highly unsteady problem the surface variation detection parameter γ (cf. section §4) is the one more sensitive to the onset of breaking. For the computations performed here we have set $\gamma = 0.3$. The parameters used for the TKE are not the same for the two Boussinesq propagation models. In particular, we have set $\kappa_{GN} = 2.8$ and $\sigma_{GN} = 1.2$ for the GN equations, while $\kappa_N = 3.2$ and $\sigma_N = 1.2$ for the Nwogu system.

Experimental data are available in several wave gauges placed before, on top, and after the bar. Here we focus on three gauges (cf. figure 4.2) placed before the toe of the bar, gauge 1 at $x = 16m$, on top of the plateau, gauge 3 at $x = 23m$, and on the lee slope, gauge 5 at $x = 26m$. We will discuss numerical results obtained on three different meshes of size $4cm$, $2cm$, and $1cm$. For the Nwogu model, we could not run the hybrid breaking simulations on the last mesh due to instabilities at the Boussinesq-shallow water interface. Similarly, when using the hybrid approach we could not go below $\Delta x = 1cm$ when using the GN model for propagation. Note also that the

results discussed here are those obtained after a transient of 36 seconds, differently from what is done e.g. in [97, 137], where the four first waves are analyzed. The results are presented in figures 4.3, 4.5 and 4.6, for gauges 1,3, and 5, respectively.

Figure 4.3 allows to visualize the behaviour of the models at the toe of the bar, right at the end of the wave propagation region. This gauge allows to highlight the initial asymmetry of the waves, essentially due to the interaction with the submerged bar. Some preliminary observations can be made. Firstly, the fully nonlinear model (left column) seems to capture better the shape of the waves, the weakly nonlinear one providing a signal which is slightly too peaky. Secondly, we see already at this stage that while the TKE model (blue curves) shows little sensitivity to the mesh size, the signals obtained with the hybrid approach (green curves) depend strongly on this parameter. We can clearly see on the intermediate and fine mesh (in the GN case) higher frequency components absent in the TKE results. These components are generated in correspondence of the boundary of the wave breaking region, as it can be clearly seen in the snapshots of figure 4.4. These instabilities become stronger as the mesh is refined, and may ultimately lead to the blow up of the solution, as it is the case for the Nwogu model on the fines mesh, and of the GN model on finer meshes.

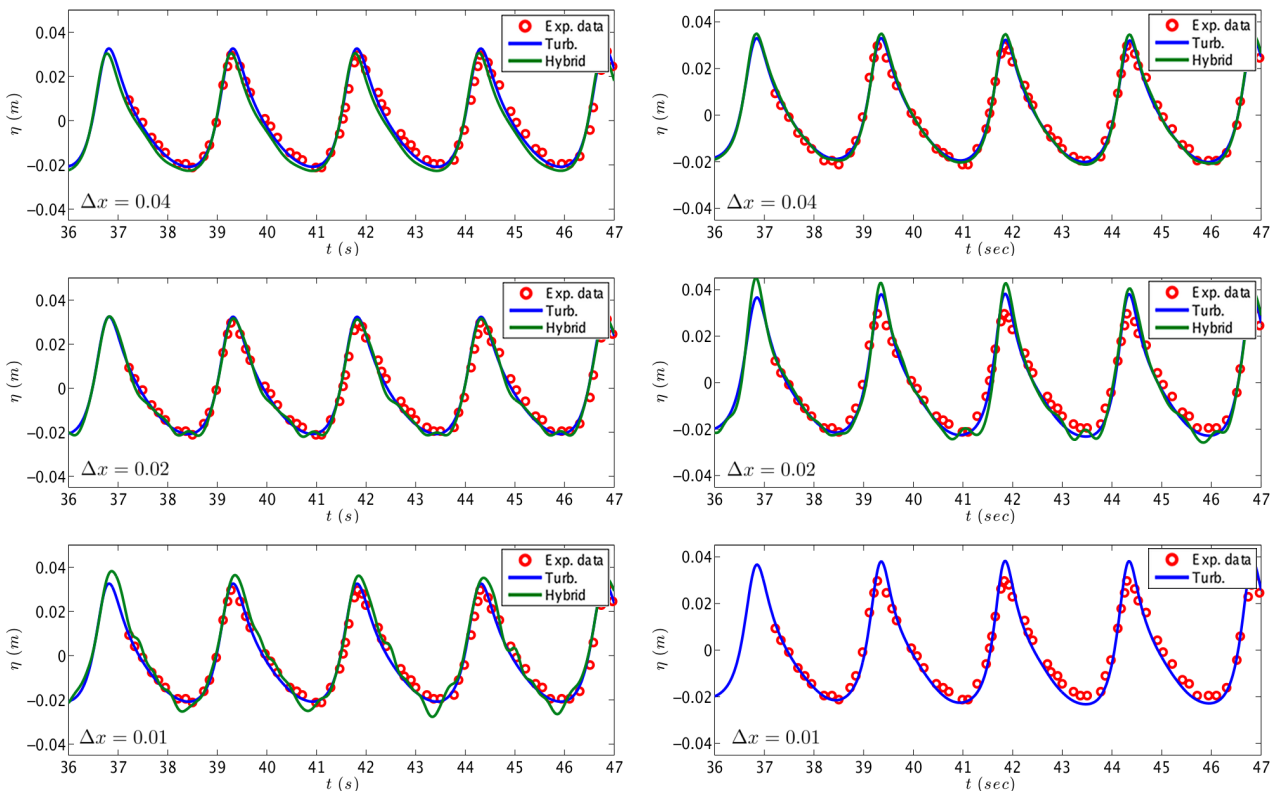


Figure 4.3: Time series of surface elevation at wave gauge 1 for the GN (left) and Nwogu (right) models using the TKE (blue) and Hybrid (green) wave breaking closure. Mesh size is 0.04, 0.02, 0.01m from top to bottom.

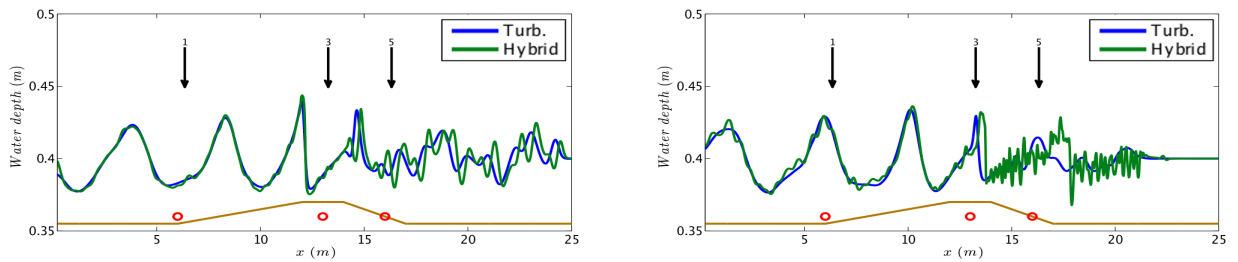


Figure 4.4: Snapshots of the flow for the GN (left) and Nwogu (right) models using the TKE (blue) and Hybrid (green) wave breaking closure. Mesh size is 0.02m

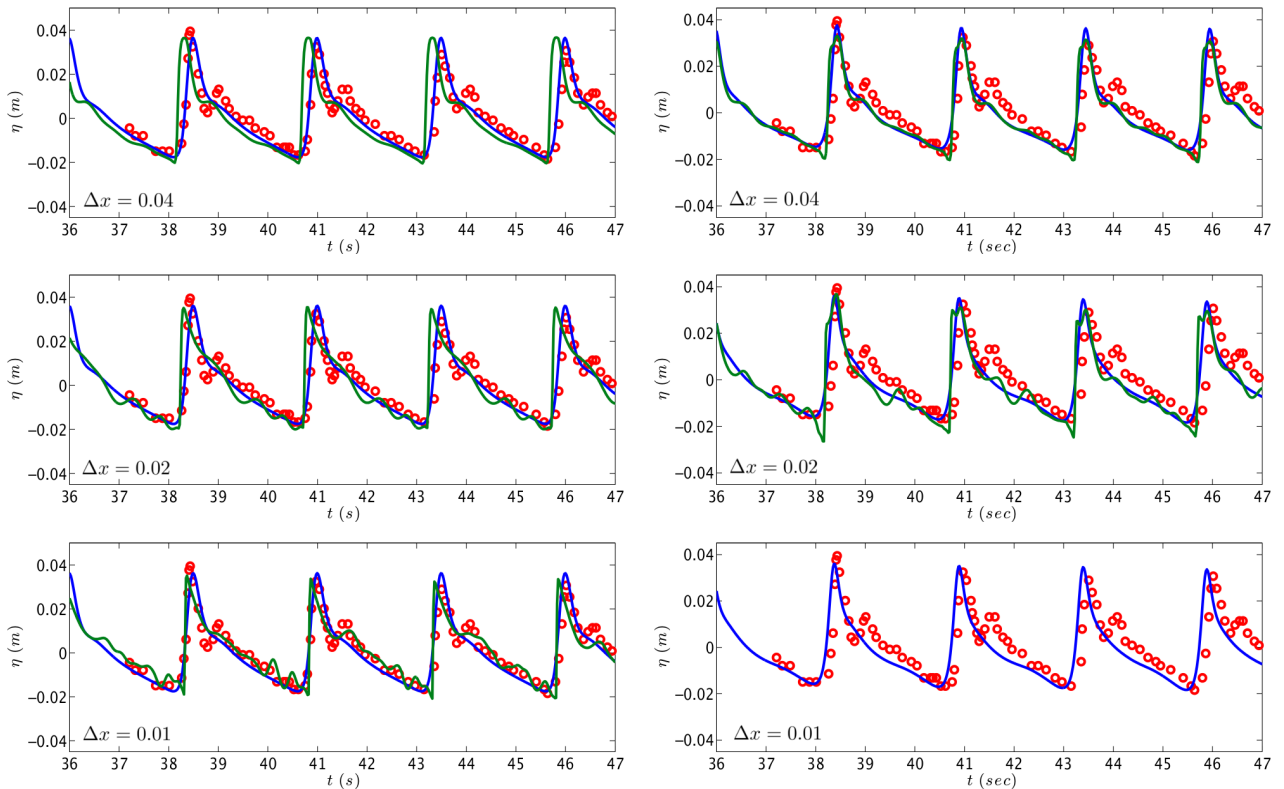


Figure 4.5: Time series of surface elevation at wave gauge 3 for the GN (left) and Nwogu (right) models using the TKE (blue) and Hybrid (green) wave breaking closure. Mesh size is 0.04, 0.02, 0.01m from top to bottom.

Figures 4.5 and 4.6 confirm the preliminary observations made for the first gauge. In particular we can clearly see the strong dependence of the results of the hybrid model on the mesh size. For this approach we can also see how the breaking waves are represented as very sharp fronts. For the GN model, on the coarse mesh breaking stops early enough for the signal in these two gauges to be smooth. This however leads to a noticeable phase lag. As the mesh is refined, the waves break more strongly. This leads clearly to an improvement on the phase. This behaviour curiously is not observed for the Nwogu model which shows strong and sharp breaking fronts already on the coarsest mesh level, with a correct phase. This allows to highlight the need of tailoring the choice

of the breaking detection criterion to the propagation model. Here the same parameters have been used for both. Nevertheless, both set of results allow to visually see the appearance of spurious higher frequencies in the signal. These are the result of the coupling between the dispersive and non-dispersive regions. For the weakly non-linear model (right column) we can see the inception of the instability already on the medium resolution used here in figure 4.6. This is less evident for the GN model, which still provides numerical solutions on the finer level used. We were however unable to refine once more the mesh without solution blow up.

The TKE approach is clearly less sensitive, at least for this test, to both the choice of the model parametrization, and the mesh size. This is summarized in figure 4.7, showing a grid convergence for the gauge 3. We also would like to remark that, for Nwogu's equations and for plunging breakers, Demirblik and Nwogu in [66] resorted to a more complex TKE closure with a PDE for the B coefficient in the production term (4.6). We found out that the simplified formulation adopted here, combined with the physical criteria for the initiation and termination of the process discussed in the beginning of section §4 can simulate reasonably well plunging wave breakers.

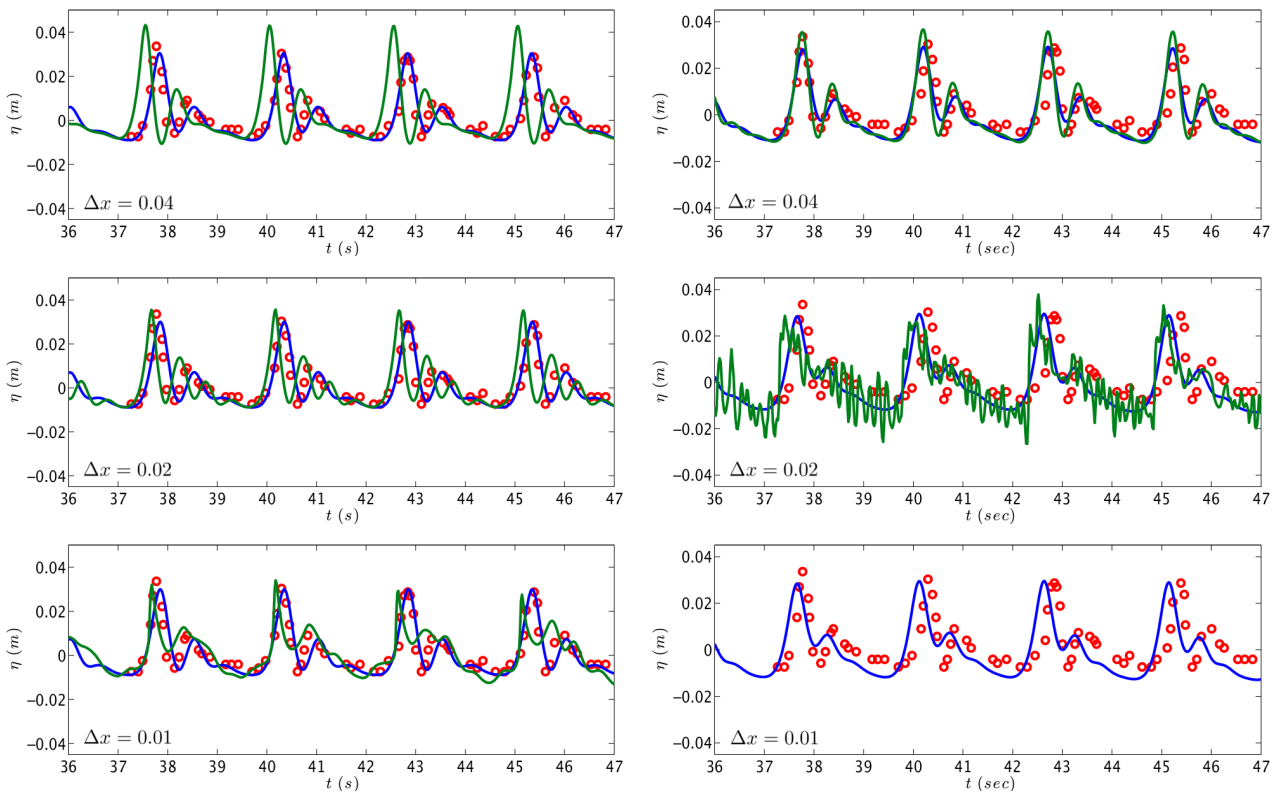


Figure 4.6: Time series of surface elevation at wave gauge 5 for the GN (left) and Nwogu (right) models using the TKE (blue) and Hybrid (green) wave breaking closure. Mesh size is 0.04, 0.02, 0.01m from top to bottom.

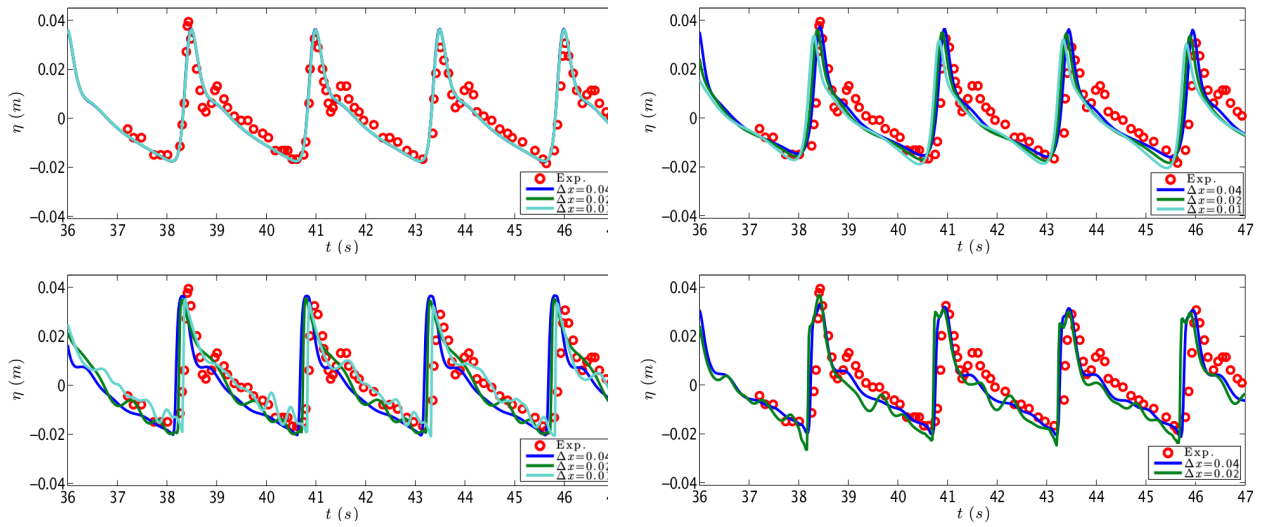


Figure 4.7: Time series of surface elevation at wave gauge 3: grid convergence for the GN (left) and Nwogu (right) models using the TKE (up) and Hybrid (down) wave breaking closure. Mesh size: 0.04m (blue), 0.02m (green), 0.01m (cyan).

Dissipation mechanisms

We report in figures 4.8 and 4.9 the time evolution of the dissipation terms active for this test: D_{upwind} (in blue) and D_{vis} (in green). The flow is periodic so we focused on 5 periods from time 12s to time 14s. The results show the dissipation *flashing* when the tallest wave approaches the bar, and then reducing as the breaking process continues on top of the bar. Also, the inception of breaking for the Nwogu model has a phase advance of about one second which can be explained by the over-shoaling characteristics of this model [95, 110]. The results for the GN model, figure 4.8, allow the following remarks. The role of numerical dissipation D_{upwind} when using the eddy viscosity closure (left column) is extremely small. This term definitely does not contribute at all to the breaking process. On the second mesh, its values approach machine zero. On the contrary, in the case of the hybrid closure, D_{upwind} is doing all the job. We can also see that on the coarser mesh the area under the dissipation bells is larger, which means that the overall contribution in time to the energy dissipation is more important. When using the model of Nwogu, figures 4.9, we can see again, from the left column, that the numerical dissipation plays no role in the breaking process, and it quickly reaches very low values. The right column allows to visualize the inception of the numerical instabilities (top figure) and their blow up (bottom figure). Note that for the finer meshes used in figure 8 the behaviour observed for the GN and in general for the TKE closure are the same. Also, we stress once more that further halving the mesh size was not possible for the GN. The finest computation we could perform until the final time is for $\Delta x = 0.008$.

The behaviour observed allows to clearly demonstrate that the numerical dissipation has no impact on the computations performed with the TKE closure. This means that with this closure one could (or should) in principle use a non-dissipative numerical method to discretize the PDEs. The results, at least those for the GN equations, also show that the overall numerical dissipation when

using the hybrid approach is larger on coarser meshes.

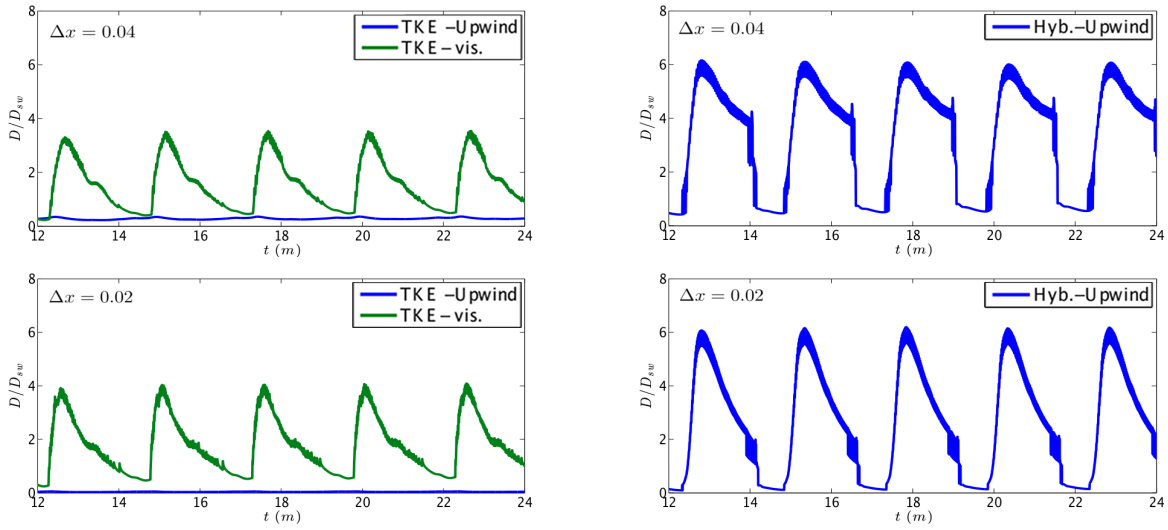


Figure 4.8: Energy dissipation profile for GN model using the TKE (left) and the Hybrid (right) closures for $\Delta x = 0.04$ (top) and $\Delta x = 0.02$ (bottom)

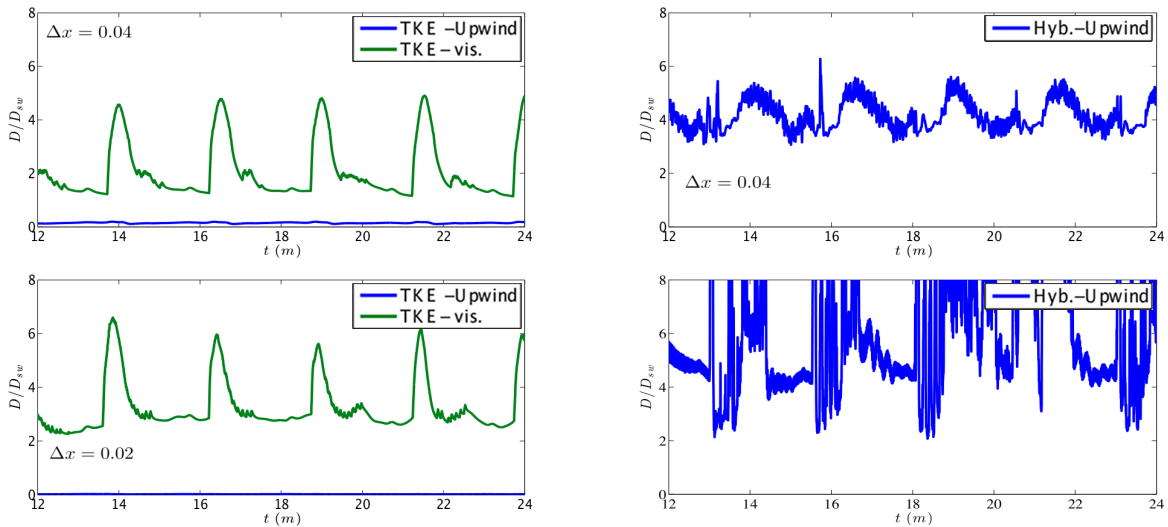


Figure 4.9: Energy dissipation profile for Nwogu model using the TKE (left) and the Hybrid (right) closures for $\Delta x = 0.04$ (top) and $\Delta x = 0.02$ (bottom)

4.3.2 Solitary waves breaking on a slope

One of the most intensively studied problems in long wave modelling is the solitary wave run-up on a plane beach, see for example [242, 80, 137, 253, 275, 226, 56] among others. In this test case we want to study propagation, breaking and run-up of a solitary wave over a planar beach with a slope 1 : 19.85. With this famous test case we assess the ability of our model to describe shoreline motions

and wave breaking when it occurs. The incident wave height considered in this case is $A/d = 0.28$ with $d = 1$, so according to Synolakis [242] the wave breaks strongly both in the run-up and in the rundown phase of the motion. The GN and Nwogu's equations are tested and compared, using for each one the turbulent kinetic energy wave breaking model and the hybrid wave breaking model. The same holds for all the test cases that follows.

The computation domain is of $120m$, where $x \in [-20, 100]$. The CFL used is 0.3 and sponge layer was applied off-shore with length $L_s = 5m$. A Manning coefficient of $n_m = 0.01$ was used to define the glass surface roughness used in the experiments. As before, computations have been run on three different meshes with size $\Delta x = [0.025, 0.0125, 0.0063m]$. The parameters of the wave breaking criteria used in this test case are $\gamma = 0.6$ and $\phi_c = 30^\circ$ for both models. To properly capture the hydraulic jump generated at during backwash, the TKE parameters depend here both on the propagation model and on the type of breaking criterion satisfied. In particular, for unsteady waves the surface time variation criterion is the one activated. In this case we use $\kappa_{GN} = 0.75$, $\sigma_{GN} = 0.9$ for the GN model and $\kappa_N = 0.8$, $\sigma_N = 1.5$ for Nwogu's model. If the slope criterion is activated, we use instead higher values, namely we set $\kappa_{GN} = 1.5$, $\sigma_{GN} = 15.5$ and $\kappa_N = 1.5$, $\sigma_N = 1.5$.

Figure 4.10 compares the numerical surface profiles for the GN equations and the experimental measurements. The same is plotted for Nwogu's equations in figure 4.11. The numerical solution was obtained using $\Delta x = 0.05m$. As expected, both mathematical models produced similar behaviour. Until time $t\sqrt{g/h} = 10$ the solitary propagates to the shore and the two wave breaking models produce, as expected, identical results since wave breaking hasn't started yet. As expected the Nwogu's model gives a wave which overshoots and breaks slightly earlier compared to the one produced by the GN equations. The experimental wave breaks around $t\sqrt{g/h} = 20$. The numerical solution for the hybrid model is represented like a bore storing the water spilled from the breaking wave behind the front. At time $t\sqrt{g/h} = 20$ the turbulence model represents the solution as a triangular bore considerably closer to the experimental data than the hybrid one. Similar behaviour has been observed by other researchers that used eddy viscosity models [147, 226, 275]. At time $t\sqrt{g/h} = 25$ the bore collapses at the shore, and both approaches show good qualitative agreement with the data. After that the wave starts to run-up, with a maximum run-up occurring at $t\sqrt{g/h} = 45$. As the water recedes, a breaking wave is created near the still water level. The numerical solution is approximated as a hydraulic jump for both numerical models. It is fully resolved using both breaking models, since the breaking criterion recognizes the hydraulic jump and the NSW equations are used for the hybrid model while the proper amount of viscosity is added by the turbulent kinetic energy model.

Figures 4.12 and 4.13 show the numerical results for both breaking phases (at time $t\sqrt{g/h} = 20$ and $t\sqrt{g/h} = 60$ respectively) while refining the mesh. Up to the authors knowledge it is the first time that such a study is performed for a (quasi-)steady hydraulic jump for an eddy viscosity type model. The first set of figures depict the breaking of the wave which travels on-shore for both GN (left column) and Nwogus equations (right column). We can clearly see the oscillatory nature of the hybrid wave breaking mechanism. The profiles obtained indicate some sort of convergence of

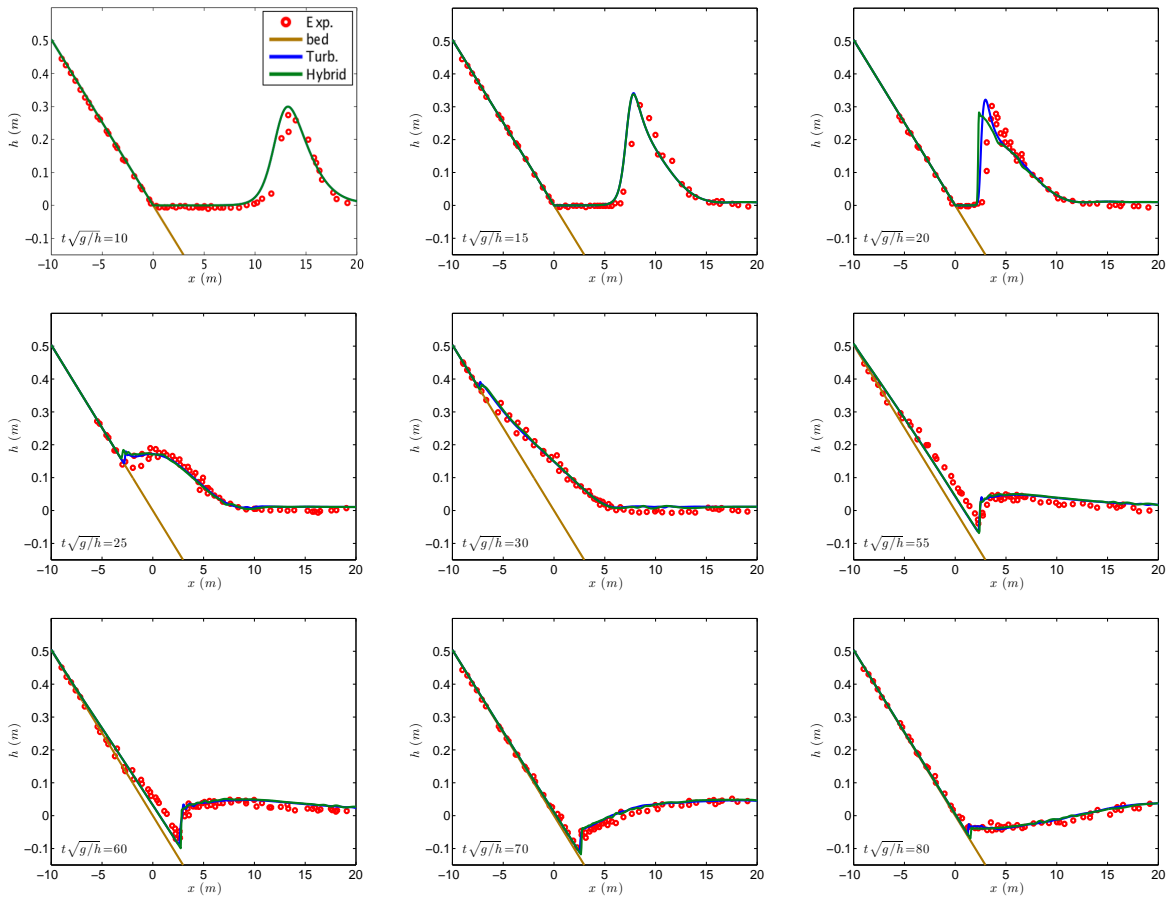


Figure 4.10: Free surface elevation of solitary wave run-up on a plane beach for the GN model.

the mean. However this is completely spoiled by the oscillations produced due to the switching between the two sets of equations. On the contrary the turbulent kinetic energy wave breaking mechanism remains stable and gives a convergent solution for both sets of equations. The second set of figures plot the same for the hydraulic jump formed at backwash. The difference between the two approaches is more accentuated here. It is quite hard to see a convergence for the hybrid results, while this is clearly the case for the TKE ones. We must mention that the GN equations combined with the hybrid model is blowing up after $t\sqrt{g/h} = 60$ for $\Delta x = 0.0063$, while Nwogu's equations are more sensitive to the hybrid formulation since numerical solution is obtained only for the first two meshes.

We have repeated this test for a more non-linear initial wave with $\epsilon = 0.5$, on the mesh with $\Delta x = 0.025m$. The results obtained at incipient breaking before the runup and during backwash are reported on figure 4.14. As before the hybrid mechanism produces oscillations, in both breakers, and it is very unstable for Nwogu model. Oscillations are clearly visible for the GN results with the hybrid breaking. Smooth capturing of the breakers is obtained also in this case with the TKE model. Figures 4.15 and 4.16 show again, the numerical results for both breaking phases while refining the meshes for the turbulent kinetic energy mechanism. The Hybrid closure is not converging since the

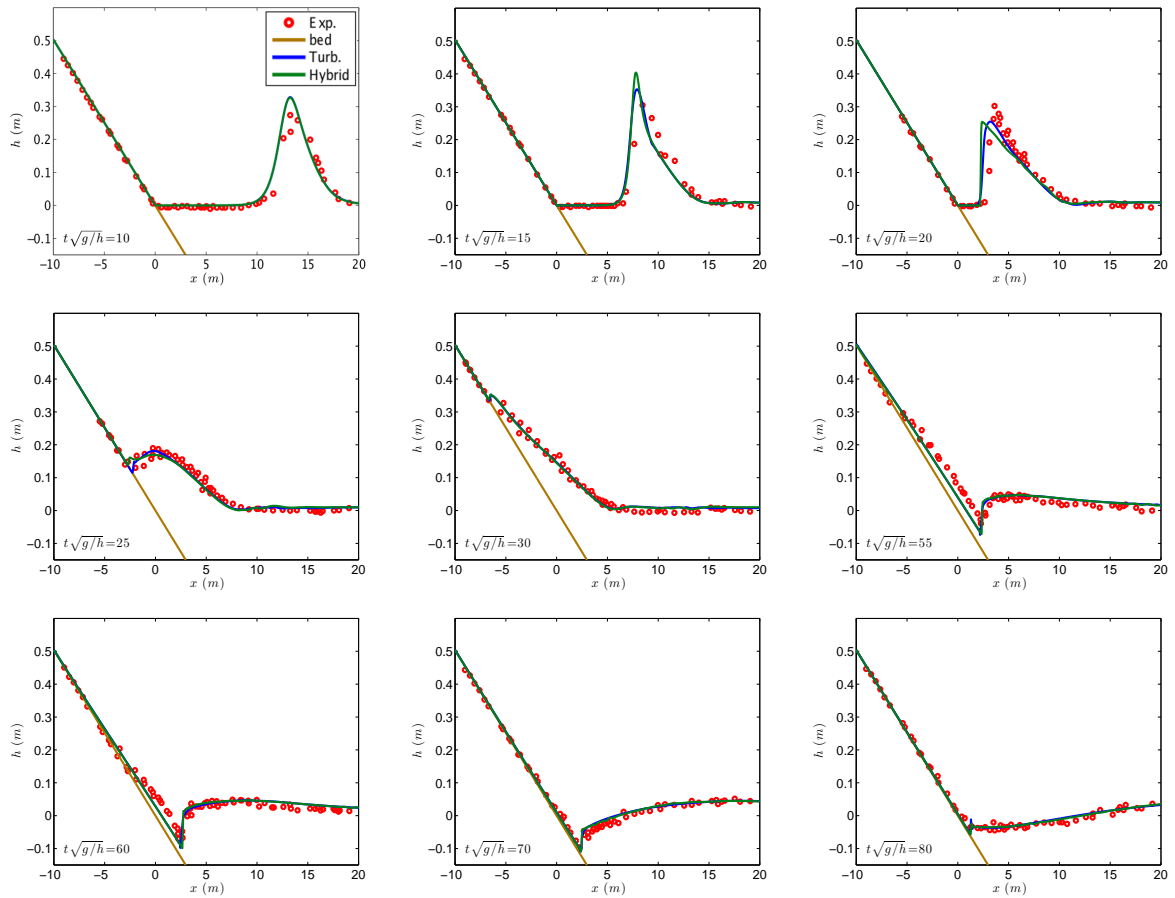


Figure 4.11: Free surface elevation of solitary wave run-up on a plane beach for Nwogu's model.

oscillatory nature of the mechanism is more pronounced in this case.

Dissipation mechanisms

For both cases we now look at the contributions to the dissipation of energy. In this case, all three sources of dissipation are active: numerical dissipation D_{upwind} , dissipation due to friction $D_{friction}$, and the dissipation due to the eddy viscosity D_{vis} when using the TKE closure. Let us first focus on the results for a nonlinearity of 0.28 reported in figures 4.17- 4.18 for the GN and Nwogu models. The results with the Nwogu model are on coarser meshes to allow some comparison on the behaviour of the hybrid closure on different meshes. The figures allow to see the dynamics of dissipation associated to the different phases of the flow. The first breaking of the incoming wave is seen in all figures around time 5s, with the Nwogu model again showing earlier breaking certainly due to its over-shoaling characteristics. As the wave reaches higher bathymetries and the runup process starts, the friction takes over and dominates the flow, with no or very little contributions from the other terms. Dissipation is reduced to zero at the end of the runup, and if increases again during backwash, with again the friction dominating, and the other terms providing again non negligible contributions around time 17s – 20s when the hydraulic jump is formed. Note

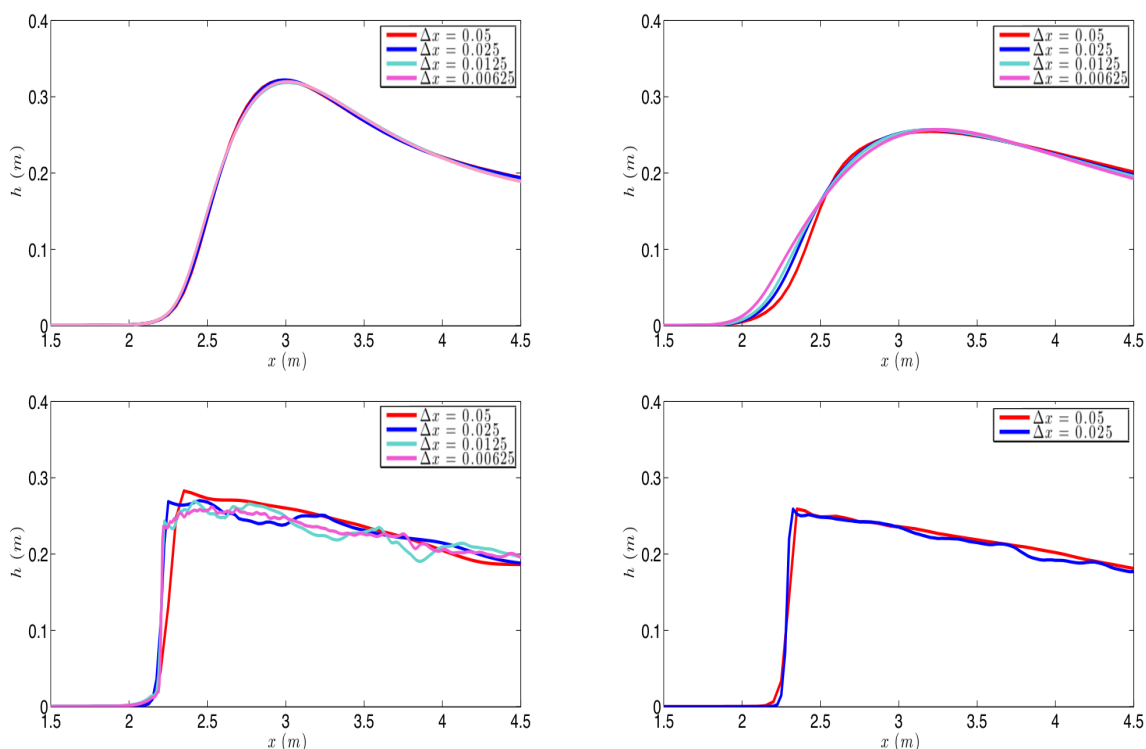


Figure 4.12: Breaking bore on different meshes for the GN (left) and Nwogu's (right) models, using the TKE (up) and the hybrid (down) wave breaking closure.

that these contributions arise from integrals in space. So the plot may lead to confusion as to which mechanism allows to capture the hydraulic jump. Indeed, the friction contributions are localized in the region very close to the wet/dry interface, and they would not allow to capture the hydraulic jump.

Looking at the behaviour of the different terms on the meshes considered, we can remark again that when using the TKE closure the numerical dissipation D_{upwind} is not contributing, or providing very small contributions, throughout the flow. In the case of the hybrid closure, we can again see that it is indeed D_{upwind} that provides dissipation during breaking. We can also see from figure 4.17 that this contribution is slightly larger on the coarser mesh, even though it is less clear that in the previous case. The oscillations observed during backwash in both the viscous contribution and numerical dissipation are associated to the intermittency of the breaking detection criterion, which is certainly something to be improved in the future. Finally, we remark that the behaviour for finer meshes is exactly the same, and that the finest meshes on which we managed to run this case until the final time with the hybrid closure are those mentioned earlier, namely $\Delta x = 0.0063m$ for the GN model, and $\Delta x = 0.025$ for the Nwogu model.

We perform the same analysis for the case with a nonlinearity of 0.5. The results are reported on figures 4.19- 4.20. As mentioned already, in this case we could only run the Nwogu model with hybrid closure on the coarsest resolution of $\Delta x = 0.1m$. The dynamics observed in the figures are

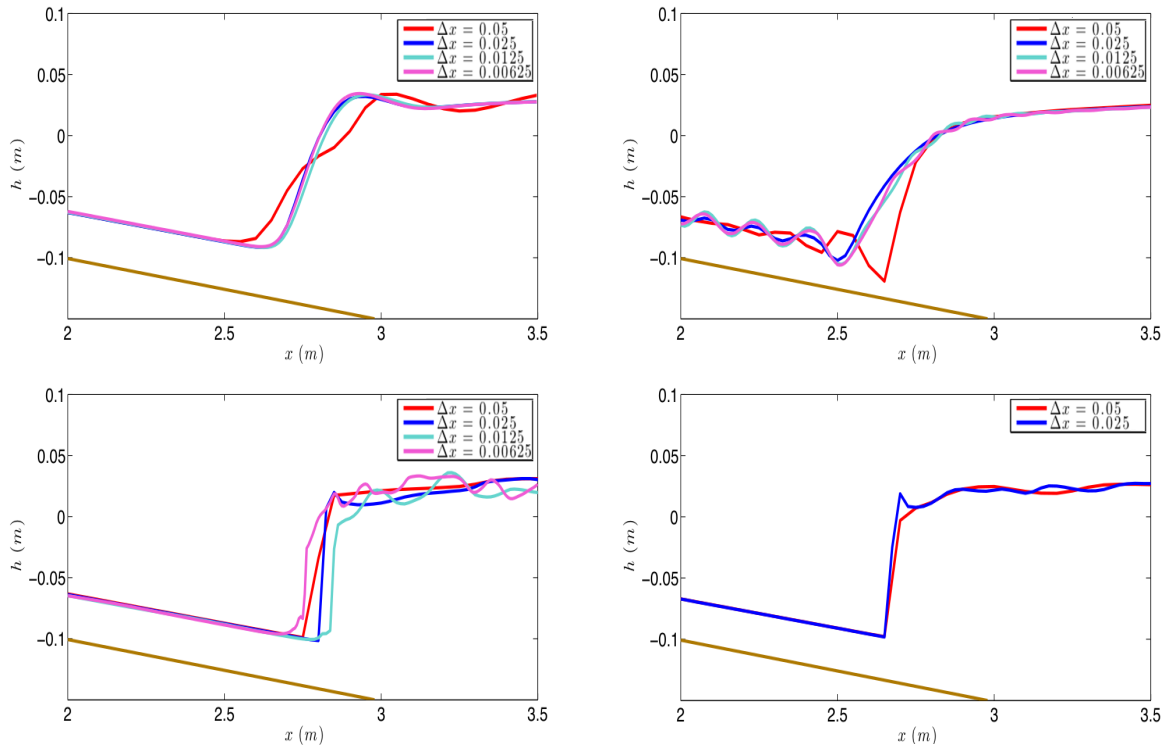


Figure 4.13: Hydraulic jump on different meshes for the GN (left) and Nwogu's (right) models, using the TKE (up) and the hybrid (down) wave breaking closure.

very similar to those of the previous case. Of course in this case the first breaking occurs earlier (around $2s$) with the Nwogu model again providing an earlier breaking. We can again see the friction dissipation taking over during the runup process, then decreasing, and increasing again during backwash. As before, breaking is re-activated to capture the hydraulic jump forming during backwash. We can again remark that when using the TKE closure the numerical dissipation is not contributing to the process, which is dominated by the terms embedded in the PDE. On the contrary, it is the numerical dissipation term that rules the dynamics of breaking. We can also see quite clearly that a considerable reduction of this contribution is obtained with mesh refinement. Again, the contributions of D_{vis} and of D_{upwind} are quite oscillatory during the backwash, and this is related to the intermittency of the detection mechanism. The meshes shown here are the finest we could run this case on until the final time with the hybrid closure.

As for the previous case, this analysis shows that when using the eddy viscosity closure the numerical dissipation plays very little or no role. This is motivation to look for non-dissipative/energy conserving schemes in this context. The mesh size seems to have an impact on the magnitude of the overall dissipation introduced during breaking. Finer meshes providing overall less dissipation. The TKE closure is very little sensitive to the mesh. This analysis also shows a very interesting interplay between the breaking and friction dynamics.

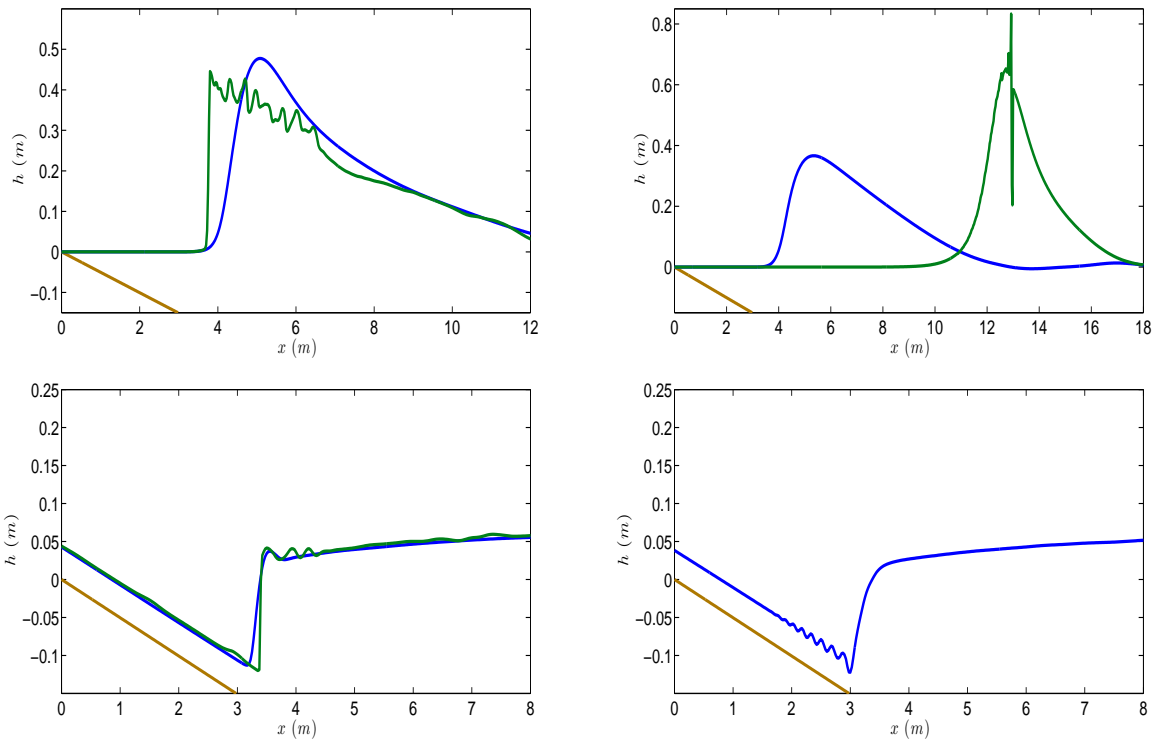


Figure 4.14: Breaking in the run-up (up) and the run-down (down) phase for GN (left) and Nwogu's equations (right) for $\epsilon = 0.5$, using the TKE (blue) and the hybrid (green) wave breaking closure. Mesh size is 0.025m.

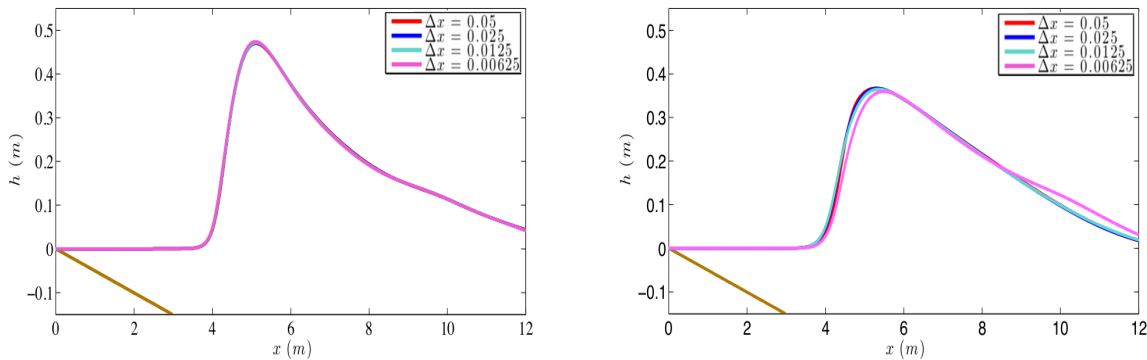


Figure 4.15: Breaking bore on different meshes for the GN (left) and Nwogu's (right) models for $\epsilon = 0.5$, using the TKE wave breaking closure. Mesh size is 0.025m.

4.3.3 Bore propagation and dissipation in function of the Froude number

We consider in this test case the propagation of a breaking bore over a flat bottom. We have chosen this benchmark as its simple setting allows to perform some quantitative comparison between the discrete energy dissipation terms analyzed in the paper, and the exact theoretical shallow water dissipation, equation (4.1), for different values of the Froude number. The test is defined by an

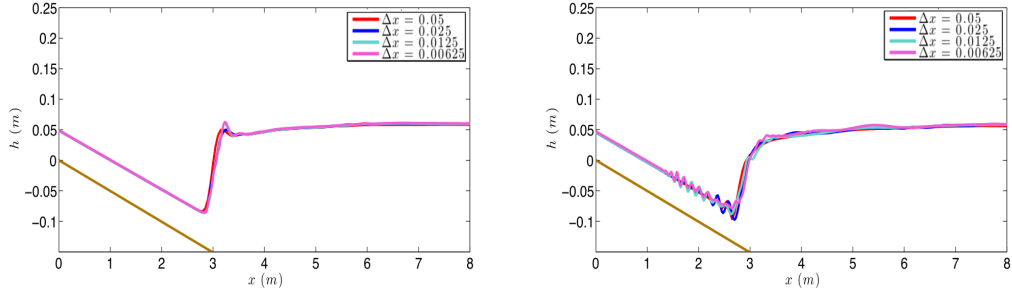


Figure 4.16: Hydraulic jump on different meshes for the GN (left) and Nwogu's (right) models for $\epsilon = 0.5$, using the TKE wave breaking closure. Mesh size is 0.025m.

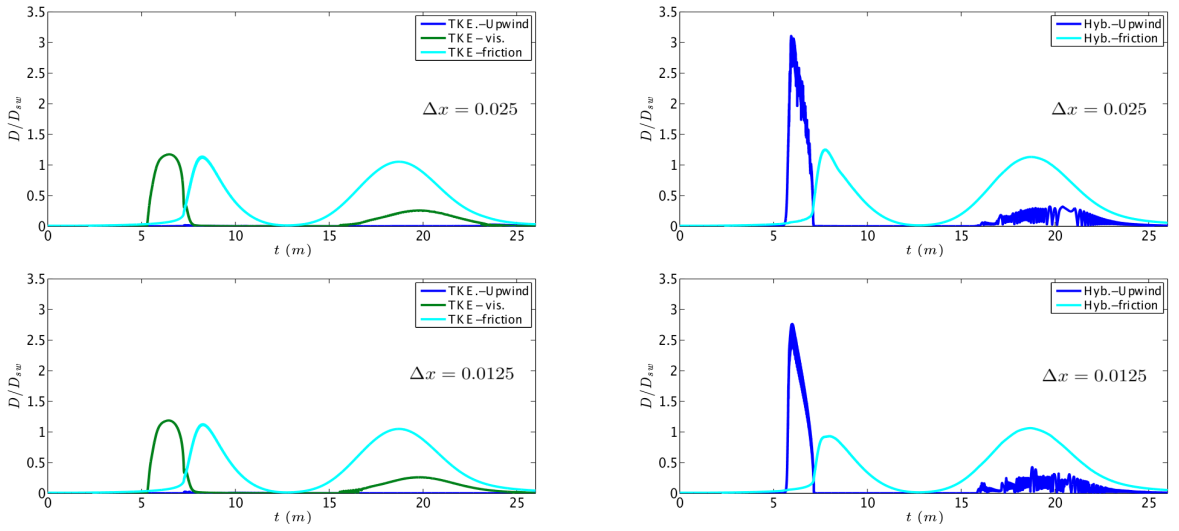


Figure 4.17: Energy dissipation profile for GN model using the TKE (left) and the Hybrid (right) closures on three different meshes: $\Delta x = 0.025, 0.0125m$ from top to bottom. The nonlinearity of the wave is 0.28.

initial step which transforms to a bore. The initial solution is defined by

$$\begin{cases} h(x, 0) = \frac{1}{2}(d_b - d_a)(1 - \tanh \frac{x}{a}) + d_a \\ u(x, 0) = \frac{1}{2}(u_b - u_a)(1 - \tanh \frac{x}{a}) + u_a, \end{cases} \quad (4.10)$$

where d_a and d_b are the water depth in front and behind the bore, u_a and u_b the corresponding depth-averaged velocities. In our case $u_a = 0$, $d_a = 1m$ and $a = 2m$. For each Froude number (F_r), u_b and d_b are computed, solving the mass and momentum conservation conditions across the bore. For $F_r > 1.4$ the initial step evolves into a breaking bore. More informations on the test case can be found in [249] and references therein.

The computational domain used is $x \in [-150, 150] m$, $CFL = 0.2$ and $\Delta x = 0.1 m$. For this type of wave the parameter most sensitive to the onset of breaking is the time derivative of the elevation γ , which we have set here to $\gamma = 0.4$. For the turbulence model we have used

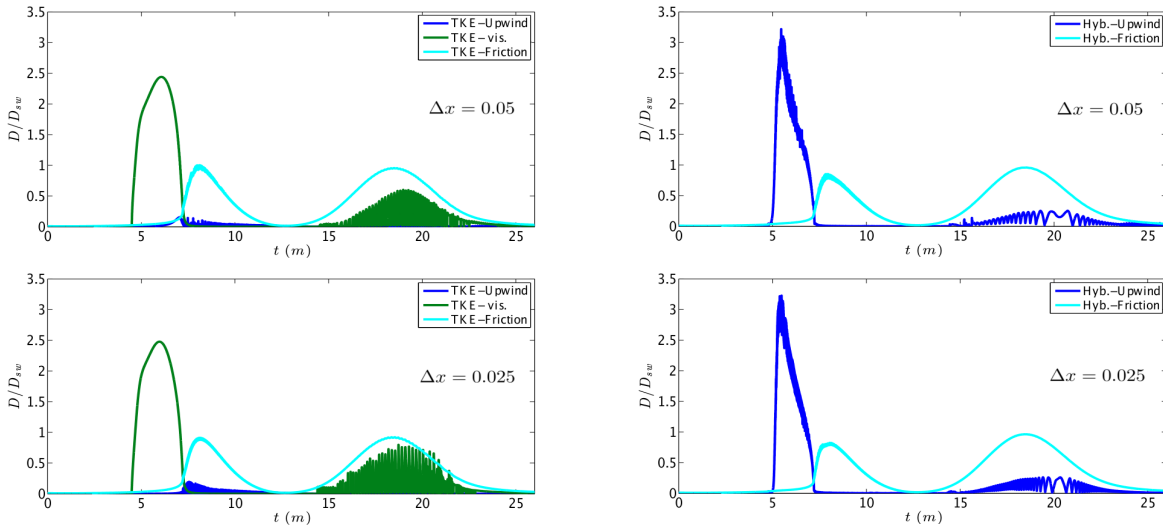


Figure 4.18: Energy dissipation profile for Nwogu model using the TKE (left) and the Hybrid (right) closures on three different meshes: $\Delta x = 0.05, 0.025m$ from top to bottom. The nonlinearity of the wave is 0.28.

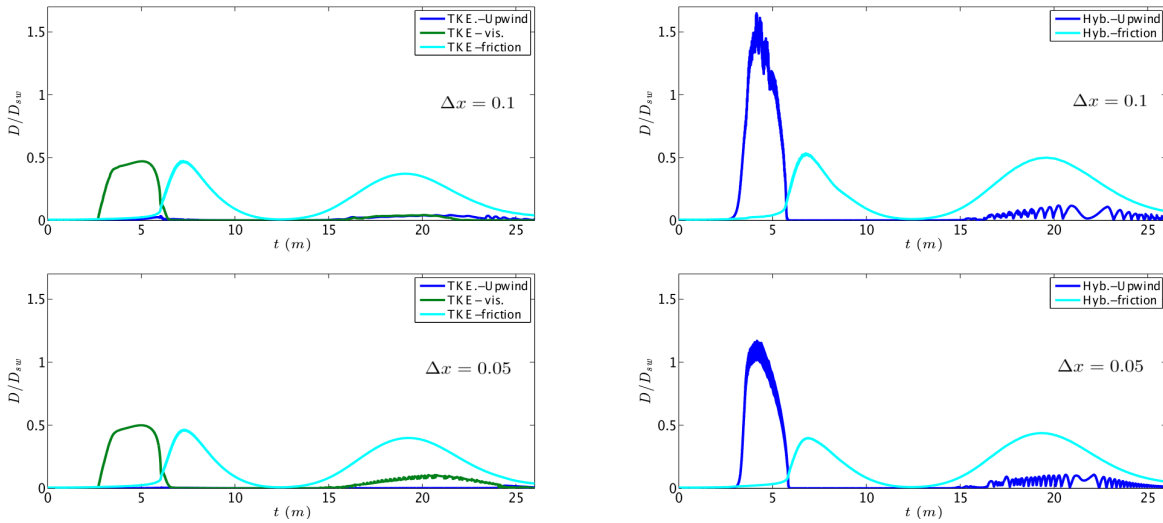


Figure 4.19: Energy dissipation profile for GN model using the TKE (left) and the Hybrid (right) closures on two different meshes: $\Delta x = 0.1, 0.05m$ from top to bottom. The nonlinearity of the wave is 0.5.

$\kappa_{GN} = \kappa_N = 1.5$, $\sigma_{GN} = \sigma_N = 0.8$ for the GN and Nwogu equations respectively. Figure 4.21 shows the propagated bore at $t = 0, 1, 15s$ for the two models for a Froude number $F_r = 2$. The bore is breaking as it propagates through the channel, and a slightly different behaviour is observed for the two breaking closures. Hybrid breaking provides a travelling shock, for both propagation models, while the turbulent closure presents a more diffusive behaviour, with a small overshoot before the bore for the GN model.

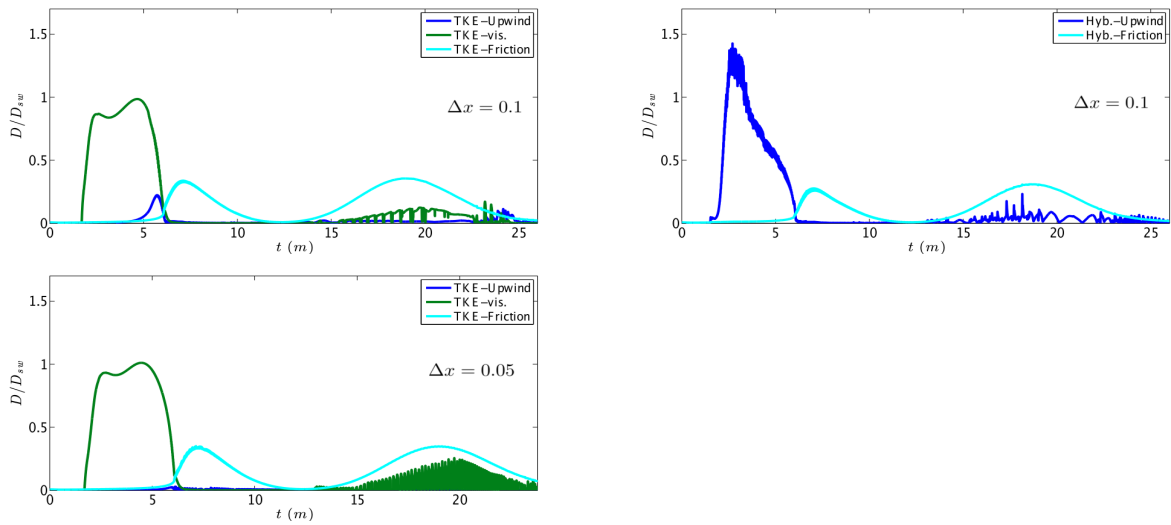


Figure 4.20: Energy dissipation profile for Nwogu model using the TKE (left) and the Hybrid (right) closures on three different meshes: $\Delta x = 0.1, 0.05m$ from top to bottom. The nonlinearity of the wave is 0.5.

The terms related to the upwind dissipation and to eddy viscosity evolve during the transformation of the solution into a bore, as shown on figure 4.21, and quickly converge to a steady (in time) value, which is plotted in figures 4.22 and 4.23 against the shallow water dissipation (4.1), for different Froude numbers and on different meshes. Note that in this case, the wave breaking interface is located in correspondence of a constant solution region. This makes this case easier compared to the previous ones. This also reduces a lot the impact of mesh size on the final value of the dissipation, essentially dictated by the jump in water height. Nevertheless, exactly as the previous cases with the hybrid approach the initial development of the solution shows instabilities, for meshes finer than those reported in the figures, solution blow up. For the GN model, and for the range of Froude numbers tested, the TKE dissipation is within 10-15% of the value predicted by (4.1), while the upwind terms basically provide a negligible contribution. Conversely, these terms are, when using the hybrid approach, within 6% of (4.1). As in the previous tests, this allows to demonstrate that the numerical dissipation does not contribute to the dynamics of wave breaking when using the TKE eddy viscosity closure. It also shows that the particular choice of eddy viscosity we performed allows to reproduce with some accuracy the behaviour with Froude number predicted by the classical formula (4.1). Similar conclusions can be drawn for the Nwogu model by looking at figure 4.23.

4.3.4 Wave height and setup prediction

The analysis of [24] shows that wave setup is very sensitive to the dissipation mechanism in wave breaking. So this is an interesting parameter to study for our purposes. To investigate this aspect we consider two of the experiments performed by Hansen and Svendsen [120]. These experimental studies consider several different regular waves shoaling and breaking on a sloping beach. Many

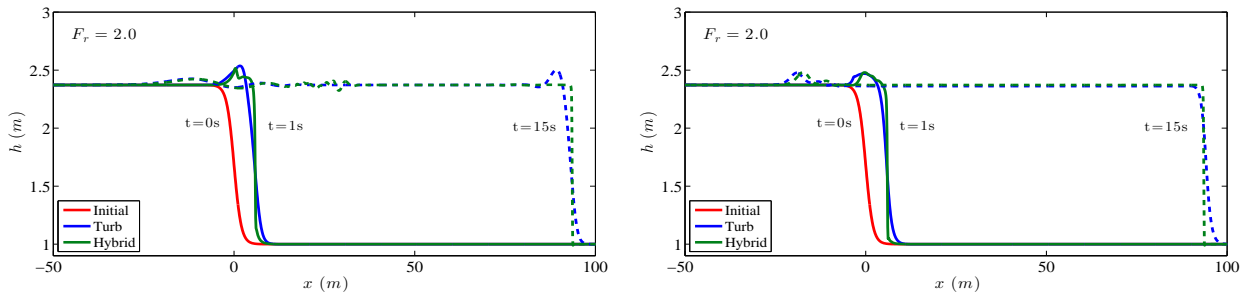


Figure 4.21: Free surface profiles at $t = 0, 1, 15s$ of hydraulic bores with $Fr = 2.0$. Left: GN model. Right: Nwogu model.

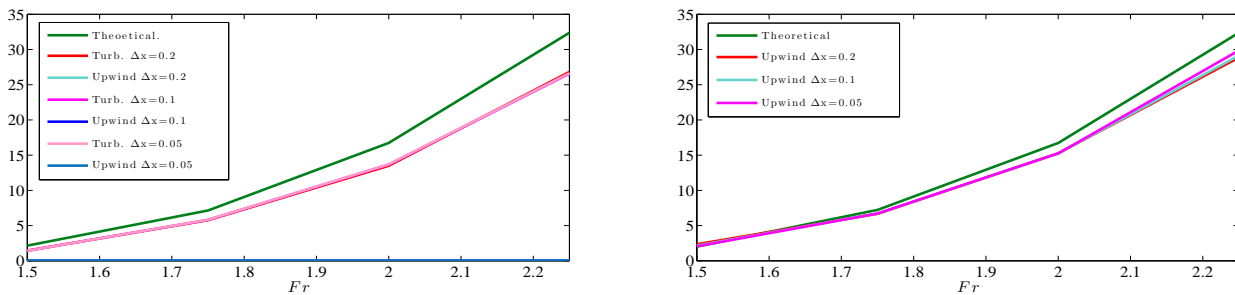


Figure 4.22: Energy dissipation profile for GN model using turbulent closure (left) and hybrid closure (right).

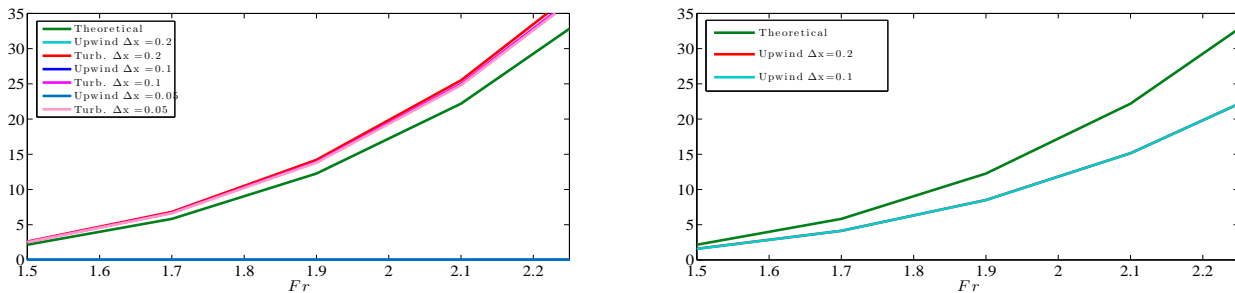


Figure 4.23: Energy dissipation profile for Nwogu model using turbulent closure (left) and hybrid closure (right).

authors have used these tests to validate their models and the associated breaking closures [147, 253, 137, 235, 58].

We consider here two cases, one involving a spilling breaker, the second involving a plunging breaker. Regular waves are generated over a 0.36 m horizontal bottom, propagated shoaled and broke over a slope of $1 : 32.26$. In the spilling breaking case (test number 05041) the regular wave's period T is $2.0s$, and the wave's height H is 0.036 m . The second test case (test number 03041) is a strong plunging breaking case with $T = 3.33s$ and $H = 0.043m$. The tests have been run on a 52 m long domain $x \in [-26\ 26]\text{ m}$, discretized with cells of $\Delta x = 0.02\text{ m}$, and with $CFL = 0.3$. A sponge layer is applied offshore with length $L_s = 5\text{ m}$. The wave making internal

source was placed 14.78 m offshore from the toe of the beach, and bottom friction is neglected. The free surface elevation, recorded at wave gauges which placed every 0.1 m., is analysed to compute the mean wave height, and the position of the mean water level (MWL). The value of γ in the surface variation criterion equals to 0.5 for both models. Concerning the wave breaking closures, we have set $\kappa_{GN} = 0.8$, $\sigma_{GN} = 0.05$ and $\kappa_N = 0.8$, $\sigma_N = 0.4$, for the two GN and Nwogu models respectively.

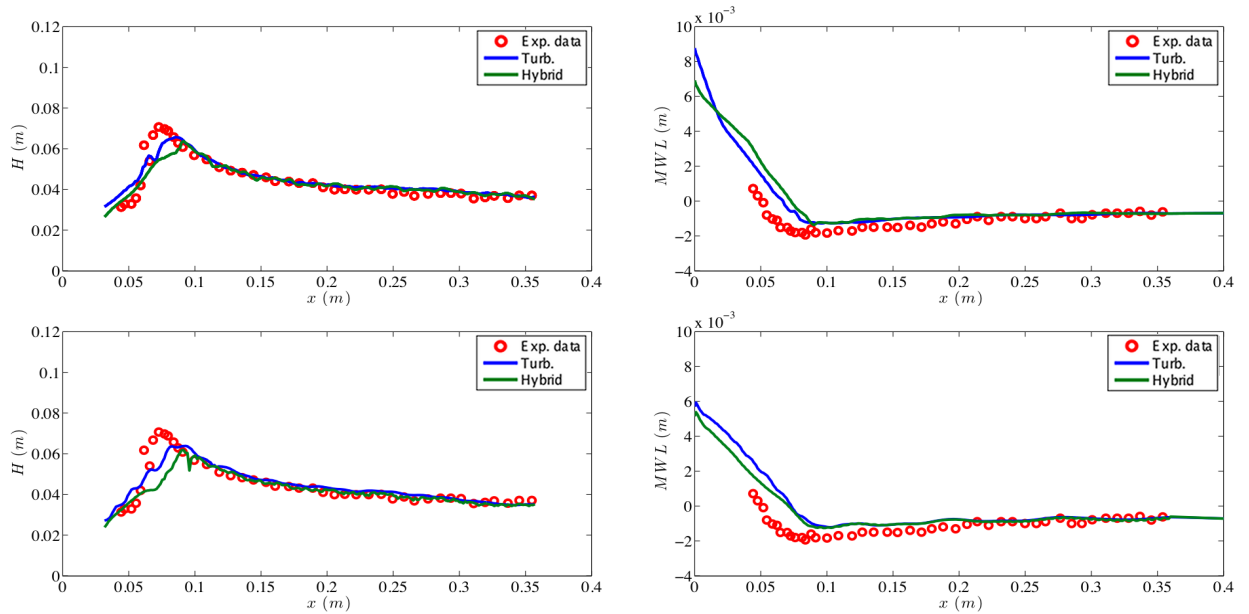


Figure 4.24: Computed and measured wave heights (left) and set-up (right) using two different equations. Test number 05041 (spilling breaking). Top: GN equations. Bottom: Nwogu equations. Blue line- TKE closure, green line- Hybrid closure.

The numerical results obtained for the two cases considered are reported on figures 4.24 and 4.25, in terms of wave height (left) and mean water level (right). As before, the blue lines in the figures refer to the TKE results, while the green ones to the hybrid wave breaking, and the top row report the computations of the GN model, while the bottom ones the results of the Nwogu equations.

For the spilling case, figure 4.24 seems to indicate that in all cases the detection criterion provides an early breaking. This of course alters the strength of the numerical breaking, which is less intense. This translates in a wave height decrease slower than the experimental one. Even so, the computations compare reasonably well with the experiments, especially when compared with results in the published literature [147, 253, 137, 235, 58]. This is confirmed by the mean water level plots. Although we can clearly observe the early start of setup, due to the early breaking, the slopes of the numerical signals are quite close to those of the experimental ones. According to the analysis of [24] this shows that the amount of dissipation introduced is correct. We stress that the differences between the TKE and hybrid approach are minor, even though we tend to consider the results obtained with the turbulence model slightly better in terms of both wave height and slope of the setup.

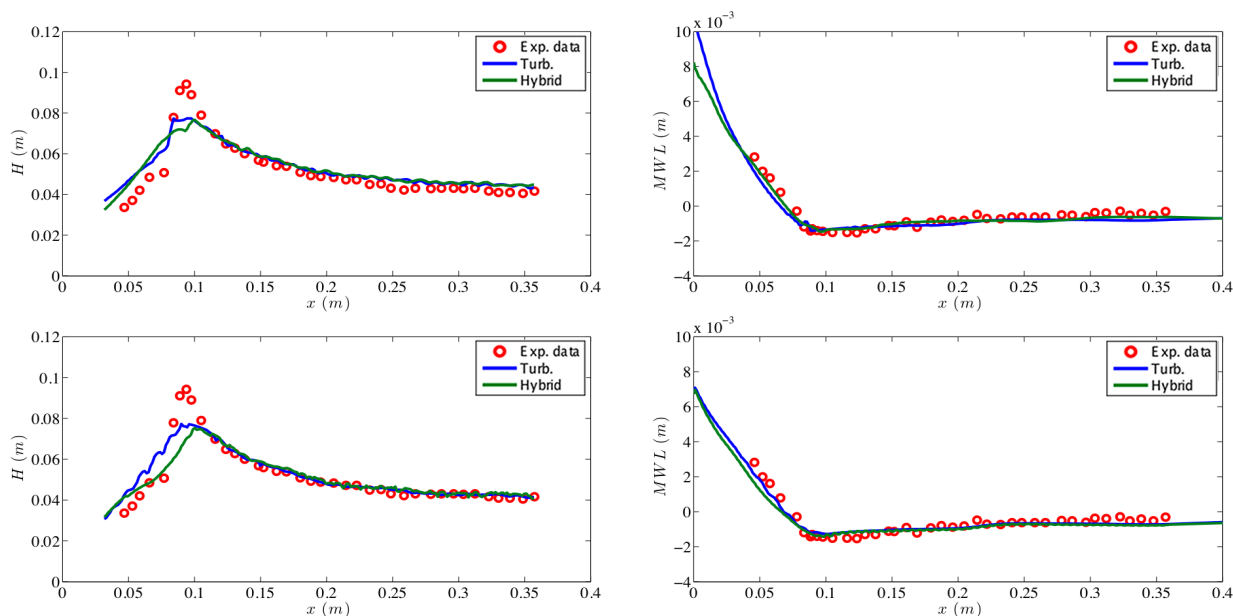


Figure 4.25: Computed and measured wave heights (left) and set-up (right). Test number 03041 (plunging breaking). Top: GN equations. Bottom: Nwogu equations. Blue line- TKE closure, green line- Hybrid closure.

For the plunging case, figure 4.25, the agreement with the experimental values is even better. We can see that the breaking location is detected correctly in this case, even though both the GN and the Nwogu model provide an underestimation of the shoaling with both breaking closures. The wave height decrease is predicted with a slightly smaller slope, but the agreement with the data is quite satisfactory. The setup prediction is very good, with both location of the breaker and slope reproduced correctly by all models.

Some conclusions can be drawn from the implementation of this numerical test case. The first one is that both wave breaking closures allow to detect and handle both spilling and plunging breaking of regular waves. We stress that the parametrisation used for TKE closure is the same for the two cases considered. This shows the potential of this type of approach to provide a robust accurate energy dissipation rate, independently on the number of nodal points per wavelength, and on the nonlinearity of the problem.

4.3.5 Application: propagation, breaking, and overtopping of a 2D reef

This next test case is reported as a complex application in order to show the potential of the modelling choices evaluated here to handle the interaction of the whole range of phenomena: dispersive propagation, shoaling, breaking, overtopping, reflection. The benchmark considered was initially proposed in [226, 226], and later used by several authors for validation [254, 95, 141]. The problem involves a bathymetry consisting of a reef with a fore slope of $1/12$ and a crest of $0.2m$ reef crest and an offshore water depth of $2.5m$. The reef crest is exposed by $0.06m$ and hides on the lee side a flat with a depth of $0.14m$. Water height distributions at several time instants and water

height time series in 14 wave gauges have been measured in the flume experiments at Oregon State University within the PhD work of V. Roeber [226] (see also [226]). A sketch of the reef geometry, showing the positioning of the wave gauges, is reported in figure 4.26. The initial state consists of a solitary wave of amplitude $a = 0.75m$ which propagates onshore, shoals and breaks in front of the reef crest. Walls are present at both ends of the domain. We refer to [226, 228] for a more detailed description of the experimental and computational setup. Our results have been computed on a mesh with size $\Delta x = 0.05$, and setting $CFL = 0.3$. Manning friction has been used, with a Manning coefficient $n_m = 0.012$. Both wave breaking detection criteria are used with $\gamma = 0.6$ and $\phi_c = 30^\circ$. Concerning the TKE closure $\kappa_{GN} = 0.75$, $\sigma_{GN} = 0.8$ and $\kappa_N = 1.2$, $\sigma_N = 1.5$ but when a hydraulic jump is detected the values are set to $\kappa_{GN} = 1.5$, $\sigma_{GN} = 15.5$ and $\kappa_N = 3.5$, $\sigma_N = 16$.

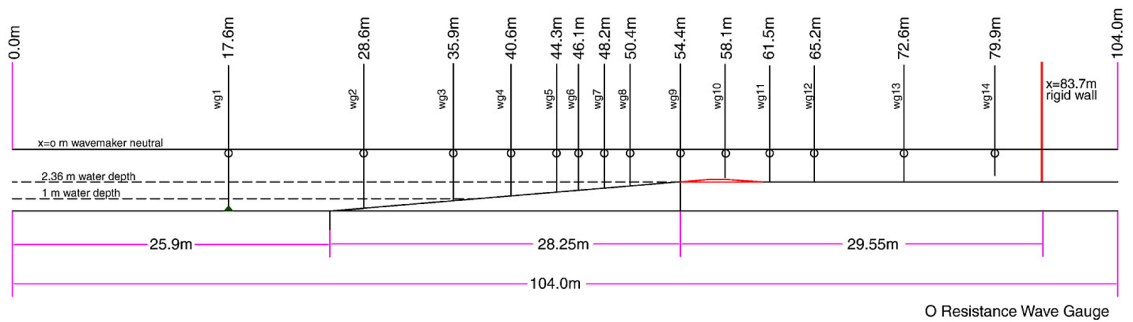


Figure 4.26: 2D reef geometry and wave gauge locations. Adapted from [228].

To visualise the results we group snapshots of the free surface in three phases : propagation and shoaling of the initial soliton (figure 4.27); overtopping and formation, propagation and reflection of a bores on the lee side of the reef (figure 4.28); secondary overtopping, with formation of a quasi-steady hydraulic jump and of an undular bore (figure 4.29). In all the figures, the top rows report the results obtained with the GN model, the bottom rows refer to the results of the Nwogu model, the blue lines are those obtained with the TKE breaking model, and the green lines are those of the hybrid breaking treatment. Symbols refer to the experimental values provided in [226].

The figures show that all models allow, on this mesh resolution, a quite satisfactory prediction of the water height. The differences between different choices appear to be minor. We can mention that, at least in our implementation both the fully and the weakly nonlinear models tend to predict the moving bores on the lee side with some phase advance. This, at least in our implementation, is more pronounced for the fully nonlinear GN mode, as we can see e.g. on figure 4.28 (central and right column). This behaviour is independent on the breaking closure adopted. We can also remark that when using the hybrid wave breaking with the Nwogu equations some over-prediction of the amplitude of the undulating bores is observed.

To have some more insight in the capabilities of the models, we analyze the water height time series in gauges WG5, WG9, WG10, and WG12. The plots are reported on figures 4.30 and 4.31. The dispersive propagation of the waves is visible in WG5 and, at for the fore side undulating bores, in WG9. We can see that all the models capture correctly the shoaling of the initial solitary, and that

despite a visible phase lag, provide a quite reasonable amplitude and frequency of the undulating bores on the fore side, as it can be seen e.g. in the WG5 series on figure 4.30, for times larger than 70s, and in WG9 after 80s. In WG5 we can see again the over-amplification of the amplitude of the undular bores for the Nwogu's model with hybrid wave breaking.

Concerning breaking, we can see the first breaker approximation very well reproduced from the WG9 series at time around 34.5s. The hydraulic jump forming at 55s is also well reproduced in amplitude, albeit with a phase advance. Similar observations can be made when looking at figure 4.31. The WG12 results, in particular, show an excellent agreement for the first four bores. All the models give an under-prediction of the water level behind the slowly moving hydraulic jump which forms behind the main right-going bore (time 38s). The first reflected bore at time roughly 50s, as well as the second hydraulic jump forming after the second overtopping (time 60s) are also very well captured by the models. The later reflections present instead a visible phase error, albeit correct in amplitude. Lastly, the WG10 results in the same figure show a nice capturing of the first two overtopping phases, although an over-prediction of the water height is also observed. The later overtoppings are affected by a phase advance already mentioned for the bores responsible for them.

Overall we consider the results quite good for all the models. Some of the differences w.r.t. the experimental water heights we are convinced that are also due to the definition of this quantity in presence of air entrainment at the free surface, as it was the case for the experimental breakers. We stress very strongly that with the current implementation the simple TKE breaking closure can handle without any problem simultaneous breakers of different types, and of different intensities. For this test, as for all the others analyzed in the paper, the fully nonlinear GN model with TKE closure provides the most robust combination.

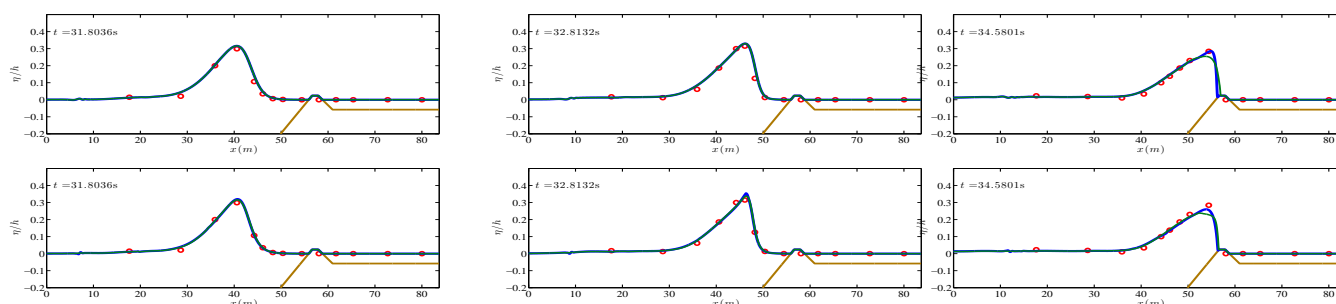


Figure 4.27: Overtopping of a 2D reef. Propagation, shoaling, and overtopping phases. Top row: GN model. Bottom row: Nwogu model. Blue lines: TKE breaking closure. Green Lines: hybrid wave breaking closure. Left: $t = 31.8036s$. Middle: $t = 32.8132s$. Right: $t = 34.5801s$.

4.4 Parameter sensitivity analysis of selected wave breaking closures

Another part of our work on wave breaking for Boussinesq-type modes has been on the understanding of this mechanism. In this work, that has been published in [129], we systematically analyze the

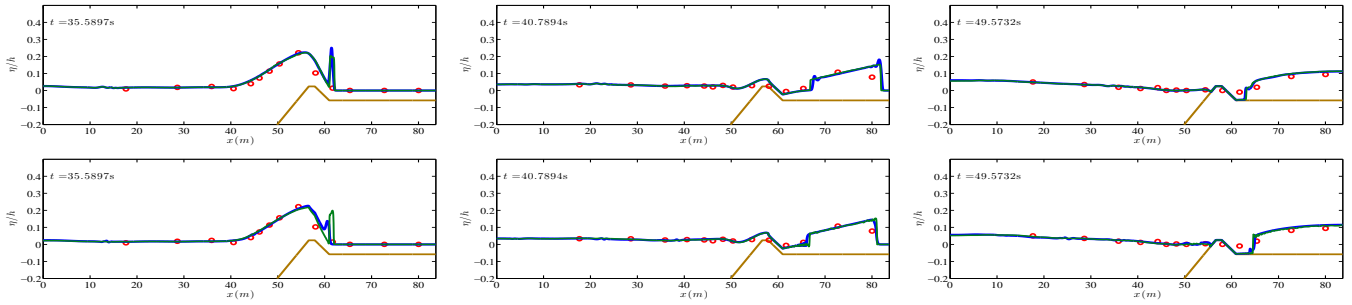


Figure 4.28: Overtopping of a 2D reef. Bore formation and propagation behind the reef. Top row: GN model. Bottom row: Nwogu model. Blue lines: TKE breaking closure. Green Lines: hybrid wave breaking closure. Left: $t = 35.5897s$. Middle: $t = 40.7894s$. Right: $t = 49.5732s$.

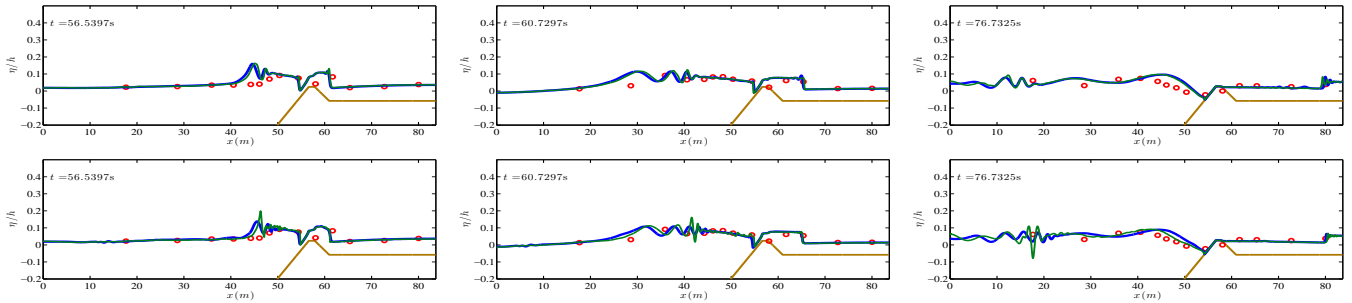


Figure 4.29: Overtopping of a 2D reef. Second overtopping and undular bore formation. Top row: GN model. Bottom row: Nwogu model. Blue lines: TKE breaking closure. Green Lines: hybrid wave breaking closure. Left: $t = 56.5397s$. Middle: $t = 60.7297s$. Right: $t = 76.7325s$.

effect of various parameters on the performance of two models for wave breaking. The hybrid and the TKE wave breaking model. In particular, we performed the Analysis of Variance (ANOVA) which gives First and Total-order Sobol's indices, quantifying the sensitivities of specified output metrics to the input parameters. Prior to performing the ANOVA analysis, we first obtain a Gaussian Process Regression metamodel of the high-fidelity CFD model. We quantify the sensitivities using several deterministic metrics such as the maximum height of the wave, the location of the breaking of the wave, the maximum run-up, the time-series values at several gauges, as well as stochastic metrics such as the skewness, asymmetry, and kurtosis of the time-series of the wave at several gauge locations. We study various configurations of the classical problem involving the run-up of solitary waves on a slope. Additionally, we investigate the time-evolution of the Sobol indices at specific gauge locations. The importance of this analysis is twofold. First, this analysis helps us gain insights into the physics of nonlinear and dispersive waves, specifically during the breaking and run-up phases. Secondly, our analysis quantitatively distinguishes between the two prominent approaches for modeling wave breaking, namely the hybrid method and the TKE model.

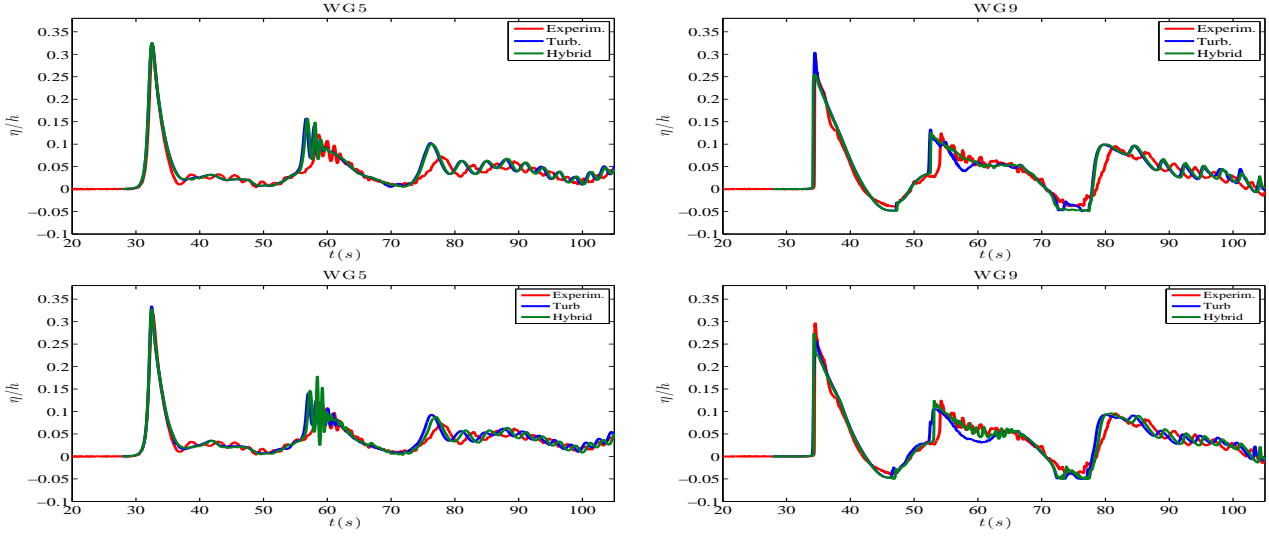


Figure 4.30: Overtopping of a 2D reef. Free surface time series in wave gauges WG5 (left) and WG9 (right). Top row: GN model. Bottom row: Nwogu model. Blue lines: TKE breaking closure. Green Lines: hybrid wave breaking closure.

4.4.1 Sensitivity Analysis Model

The Analysis of Variance (ANOVA), first proposed by Sobol et. al. [174, 175], is a powerful technique for global sensitivity analysis. Later, an improved algorithm was proposed by Saltelli et. al. to reduce the computational cost of ANOVA [229]. A comprehensive review of the global sensitivity analysis methods, including the ANOVA technique, is given by Iooss and Lemaître in [21]. Here, we briefly describe the ANOVA method to find out Sobol indices, that characterize the sensitivity of the model output with respect to contribution of each of the input parameters. Consider $\mathbf{X} \in \Omega \subset \mathbb{R}^d$, $d \in \mathbb{N}$ to be a random variable and let $f(\mathbf{X}) \in L^2(\Omega)$ be a square integrable function on domain $\Omega = [0, 1]^d$. ANOVA decomposition of f quantifies the variance of the function output in terms of the input parameters (or a combination of the input parameters), and is given as follows (see [21, 174] and the references therein).

$$f(\mathbf{X}) = f_0 + \sum_{1 \leq i \leq d} f_i(X_i) + \sum_{1 \leq i < j \leq d} f_{ij}(X_i, X_j) + \dots + f_{12\dots d}(\mathbf{X}) \quad (4.11)$$

under the condition imposed by the following equation:

$$\int_0^1 f_{i_1, i_2, \dots, i_s}(x_{i_1}, \dots, x_{i_s}) dx_{i_k} = 0, \quad 1 \leq k \leq s, \quad \{i_1, \dots, i_s\} \subseteq \{1, \dots, d\}. \quad (4.12)$$

Here, f_0 is the expected value of the function f , which is quantified by $\mathbb{E}[Y]$ for each random variable $Y = f(\mathbf{X})$. The univariate function $f_i(X_i) = \mathbb{E}[Y|X_i] - \mathbb{E}[Y]$ quantifies contribution due to each random variable $Y = f(\mathbf{X})$. The bivariate function $f_{ij}(X_i, X_j) = \mathbb{E}(Y|x_i, x_j) - F_0 - F_i - F_j$ quantifies the joint contribution of each pair of input parameters covering all possible combinations. Similarly, the rest of the terms quantify the higher-order effects. It is possible to get a similar decomposition of the variance of the function $f(\cdot)$ as follows [21],

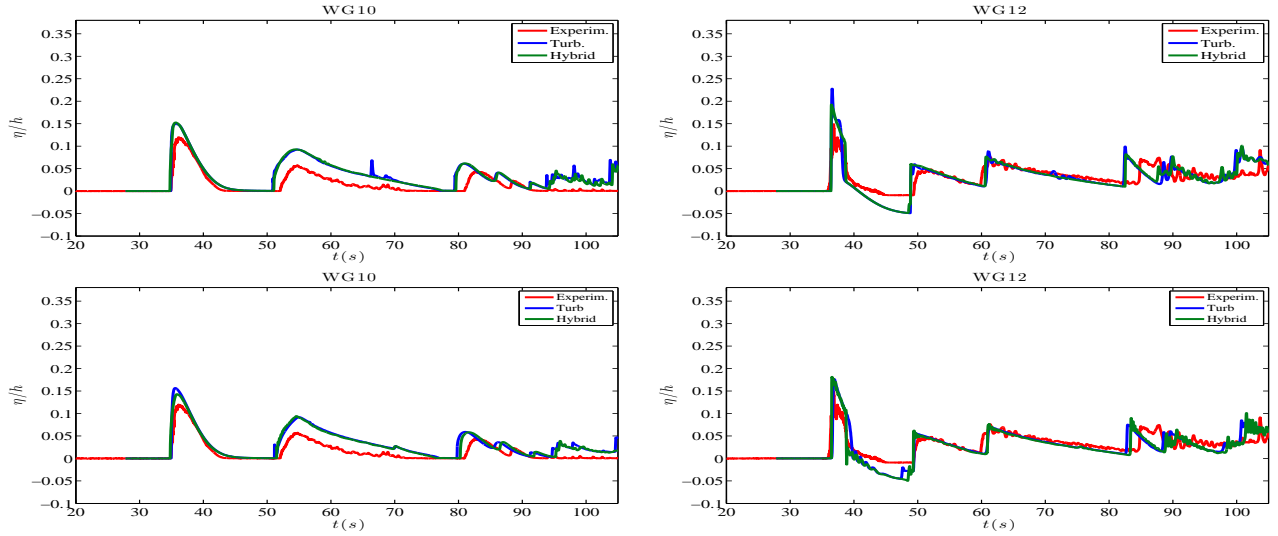


Figure 4.31: Overtopping of a 2D reef. Free surface time series in wave gauges WG10 (left) and WG12 (right). Top row: GN model. Bottom row: Nwogu model. Blue lines: TKE breaking closure. Green Lines: hybrid wave breaking closure.

$$Var(Y) = \sum_{i=1}^d D_i(Y) + \sum_{i<j}^d D_{ij}(Y) + \dots + D_{12\dots d}(Y), \quad (4.13)$$

where, $D_i(Y) = Var[\mathbb{E}(Y|X_i)]$, $D_{ij}(Y) = Var[\mathbb{E}(Y|X_i, X_j)] - (D_i(Y) + D_j(Y))$ and so on for the higher order terms. This decomposition is known as ANOVA decomposition. Finally, the Sobol' indices are given as (refer [21, 174]),

$$S_i = \frac{D_i(Y)}{Var(Y)}, \quad S_{ij} = \frac{D_{ij}(Y)}{Var(Y)}, \quad \text{Higher Order Terms} \quad (4.14)$$

Further, the Total Order (TO) Sobol' indices combine the lower-order and higher-order terms and are given by:

$$S_{T_i} = S_i + \sum_{i<j} S_{ij} + \sum_{j \neq i, k \neq i, j < k} S_{ijk} + \text{Higher Order Terms} \quad (4.15)$$

Note that two-parameters (as well as three-, four- etc.) interactions involving x_i are already accounted in S_i , the same way that three-parameters contributions to the variance are also hidden in the two-parameters contributions, and so on. For this reason, the sum of all the total indices usually larger than 1.

To perform the sensitivity analysis in this work we used the UQlab-The framework for Uncertainty Quantification [183]. More precisely, we use the sensitivity analysis module which contains the methods for global sensitivity analysis that quantitatively measure the importance of each input parameter. We construct a surrogate model (meta-model) of our computational model prior to the Sobol sensitivity analysis. The surrogate model is a functional approximation of our computational model and is faster to evaluate. It is constructed using a relatively small number of input parameters

and corresponding output results from our computational model. This way, we reduce the total computational cost to a great extent. In this work we use the Kriging (or Gaussian process regression) metamodel. A review on Kriging metamodeling can be found in [162, 86].

4.4.2 Case study: propagation, breaking and runup of a solitary wave

We study, once again, the very well known solitary wave over a slope test case [242] (see section 4.3.2 for the setup). It is based on the work of Synolakis [242], where solitary waves with various nonlinearities $\epsilon = A/h_0$ were studied experimentally and numerically. For simplicity, we only investigate the breaking and runup processes and their sensitivity to the different physical and model parameters. This already will provide a quite large spectrum of results and information related to the closure models. The computational domain is $[-20, 80]m$ and the numerical parameters are constant and set to $\Delta x = 0.05$, $cfl = 0.1$. They are intentionally kept relatively small as to limit the numerical diffusion in the results. Figure 4.32 confirms that the computed solution, presented at time $6.4sec$ (i.e. already breaking), does not change as Δx is refined and that we are still far from the fine mesh instabilities highlighted for the hybrid closure in [145] and analysed in the previous section. We record time series of the surface elevation in 10 wave gauges every $0.5m$ from $x = 0$ to $x = 3.5$, plus two additional at $x = 4.0$, and $5.0m$. In this spatial window, we have observed wave-breaking occurs for all the examined waves.

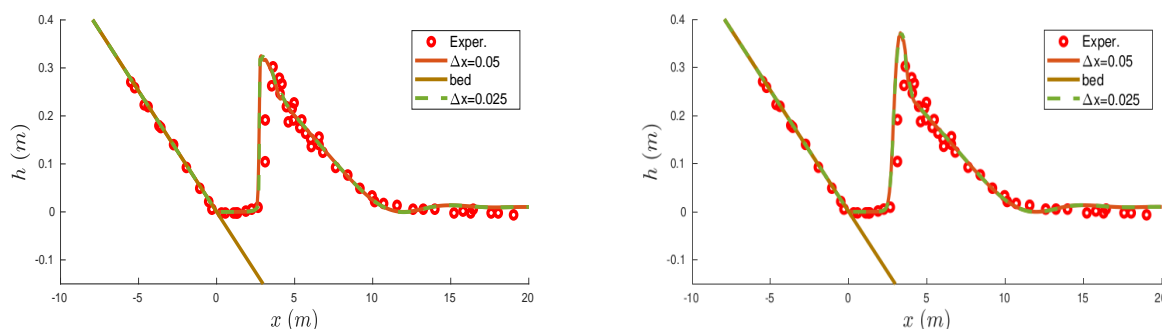


Figure 4.32: Computed solution, at early breaking for the hybrid(left) and the TKE (right) closures using $\Delta x = 0.05m$ and $\Delta x = 0.025m$.

We introduced uncertainties in both the model set up and the model parameters. In particular, wave amplitude, slope of the beach, and Manning friction coefficient are assumed to vary uniformly in the ranges $A \in [0.1, 0.6]$, $\text{slope} \in [-1/15, -1/25]$, $Nm \in [0.009, 0.075]$ respectively. All of the possible combinations of these parameters cover most of the practical scenarios. Uncertainty is introduced also in all the parameters of the breaking models.

For completeness, Figure 4.33 shows the evolution of the free surface, compared to the experimental data of [242], computed in the deterministic setting: $\text{slope} = -1/19.85$, $A = 0.28$, $Nm = 0.01$. For these computations, the wave breaking closure models have been parametrized using values proposed in literature [145, 97, 252]: $\gamma = 0.6$, $\theta = 0.53$ and $C_v = 10$, $\kappa_b = 2.5$ and $\sigma_b = 20$ for the TKE model. As the wave approximates the shore and shoals it is clear that the two models,

as expected, give identical results since wave-breaking has not started yet. The breaking procedure starts around $t = 4.79\text{sec}$. Both the hybrid closure and the TKE model represent the solution as a triangular bore, albeit with a different resolution of the peak which is kept smoother and higher by the TKE approach. At time $t \sim 7.9\text{sec}$ the bore collapses on the shore and the wave starts to run-up. For this particular case both numerical solutions provide a good qualitative agreement with the data. We highlight here that the objective of this work is not so much related to which method best predicts the available data, but to provide some quantitative measures of the variability of the outputs wrt changes in the input parameters. In the current study, the variations of the flow quantities with numerical parameters, and more particularly mesh size, is not included. As already said, the interested reader is referred to the previous work [145, 8] for a detailed analysis of this aspect.

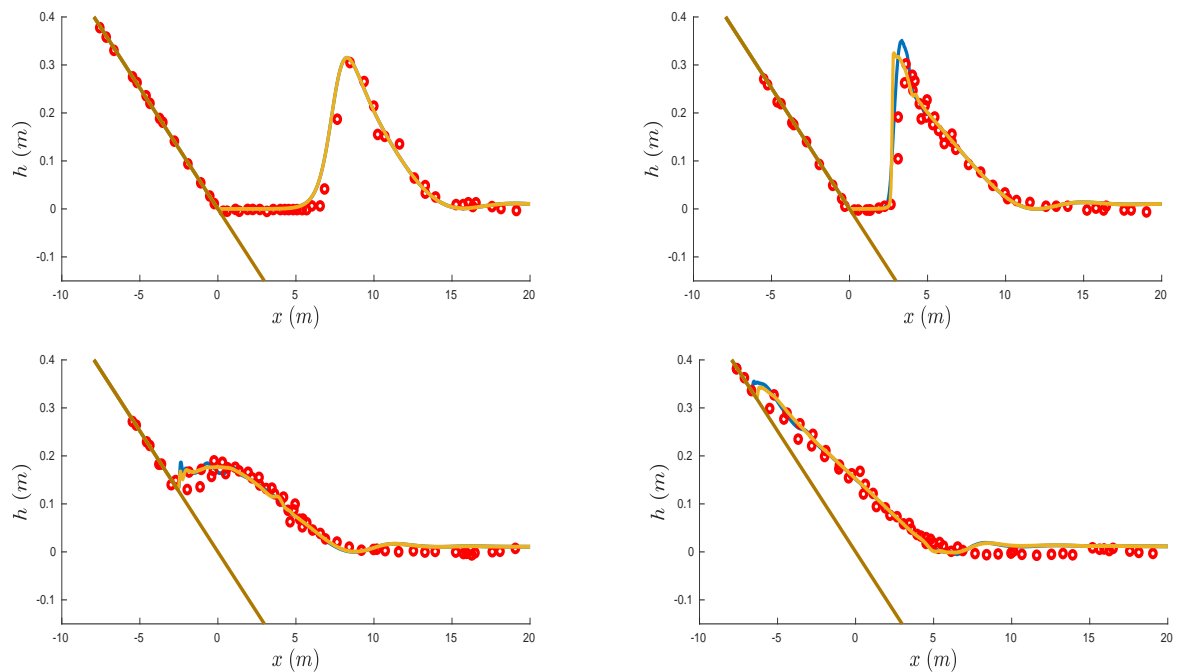


Figure 4.33: Time evolution of the free surface (deterministic). Yellow line: Hybrid wbc, blue line: TKE wbc.

Model outputs and post-processing

An important point is the definition of the output observables to be used in the analysis. We will start by considering the sensitivities of the location of the breaking point, the wave height at the breaking point, the maximum wave height at the wave gauges and the maximum run-up.

To have a more detailed picture of the evolution of the wave as it shoals and breaks, we will also consider a set of statistical outputs. There exist several works that examine them in the context of BT models, see for example [147, 255]. A measure to examine the left-right differences in a wave

is the wave asymmetry which is defines as

$$As = \frac{\langle H(\eta^3) \rangle}{\langle \eta^2 \rangle^{3/2}} \quad (4.16)$$

where H is the Hilbert transformation and $\langle \cdot \rangle$ denotes the mean operator. A similar information is provided by wave skewness, which is a measure of crest-trough shape. It is defined as

$$Sk = \frac{\langle \eta^3 \rangle}{\langle \eta^2 \rangle^{3/2}}. \quad (4.17)$$

Finally, the kurtosis will allow to estimate whether the wave is heavy tailed or light tailed with respect to the normal distribution. It is defined as

$$Ks = \frac{\frac{1}{n} \sum (\eta_i - \langle \eta \rangle)^4}{\left(\frac{1}{n} \sum (\eta_i - \langle \eta \rangle)^2\right)^2} \quad (4.18)$$

where n is the length of the time series data in the wave gauge.

4.4.3 Parameter sensitivity analysis

Besides the variations in the physical parameters already discussed, we consider uncertainties in the parameters of the models, involved in the detection (γ and θ) for both models and the energy dissipation for the TKE model (κ , C_v , σ). In particular we assume the the uniform distributions $\gamma \in [0.3, 0.8]$, $\theta \in [0.32, 0.6]$ and $\kappa \in [0.5, 2.5]$, $C_v \in [5, 15]$, and $\sigma \in [10, 25]$. Note that the last three parameters appear only in the TKE model.

Figure 4.34 presents the First and Total order Sobol indices for the physical outputs, including the results in wave gauges. The results indicate that the amplitude of the wave is mainly the dominant parameter for the maximum wave height at the wave gauges and on the location of the breaking point for the hybrid model while for the TKE, κ plays also a significant role in the formation of the maximum wave height at the wave gauges offshore. As expected, and for both models, friction affects the maximum wave height at $x = 0m$, which is located on the initially dry slope. The parameter γ affects the location of the breaking point in the hybrid wbc but surprisingly plays no role in the TKE. An interesting outcome is the one of the runup process. Only the physical parameters are those who affect the maximum runup with the slope of the topography affecting only the hybrid wbc. We have to highlight here that all the second order Sobol indices are less that 0.1 (not shown). This indicates a small correlation between input parameters.

So, as a general conclusion we can say that the model parameters have a significantly smaller impact on the outputs than the problem setup parameters, with the exception of γ that does affect the breaking point location when using the hybrid wbc and κ that affects the maximum wave hight on the wave gauges. Among the problem parameters, the amplitude turns out to be the dominating one, followed by the friction. The slope has a somewhat smaller impact on the runup and that too only for the hybrid closure. To go further we look at the statistical parameters of the water elevation signals in the gauges. The results are summarized in figures 4.35 and 4.36 for the hybrid and the

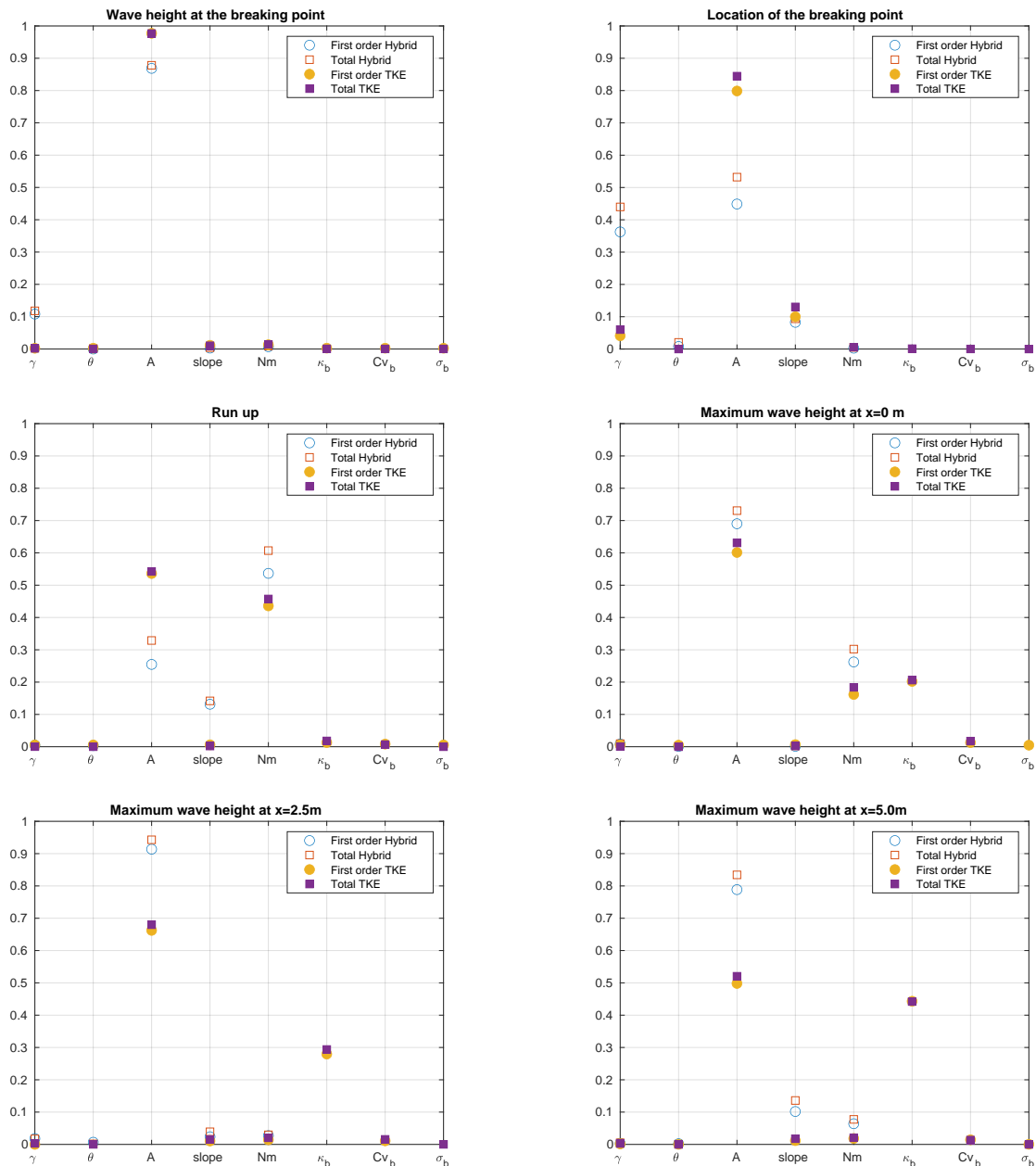


Figure 4.34: First (circles) and Total (squares) Sobol Indices for the output parameters using the hybrid and TKE (squares) wbc's.

TKE wave breaking closures respectively. Wave amplitude, slope, and friction coefficient have the largest impact, while the indices of γ and θ are close to zero and they are not presented. When using the TKE model the only model parameter that shows sensitivity is κ and this only for the kurtosis. The asymmetry is largely controlled by the amplitude. This is especially true in the first gauges, close to the collapse of the wave (impact of amplitude), and to the runup/backwash (slope). The slope shows bigger sensitivity when the TKE closure is used.

Skewness and kurtosis present a different sensitivity profile for the two models revealing the different way of simulating propagating bores since the hybrid model represents the solution as a triangular

bore with a sharp front and TKE as a bore with a smother and higher peak. When we use the hybrid wbc the skewness is highly affected by the amplitude as the wave breaks and collapses on the slope (first gauges). The impact of the slope and the amplitude are equally dominating the shoaling phase, with friction playing a smaller but not a negligible role. For the TKE wbc the behavior of the parameters are more clear since only the wave's amplitude and friction are dominating the process. The impact of the slope is only visible as the wave collapses on the slope.

The thickness of the wave tails, measured by the kurtosis, is controlled mainly by slope and friction as shown in figure 4.35 on the right. The first has a much higher sensitivity in the intermediate gauges suggesting that its impact is related to the propagation, while the impact of the friction more to the backwash. The results show that for the hybrid closure model the wave-breaking parameters have considerably smaller contributions to the shape of the wave. Finally the kurtosis, when we use the TKE wbc, is dominated by the wave's amplitude and the slope but also κ shows some sensitivity. We recall that κ controls both the magnitude of the eddy viscosity as well as the dissipation of turbulent kinetic energy. The latter may affect the rate at which the eddy viscosity is reduced in space, thus affecting the wave tail

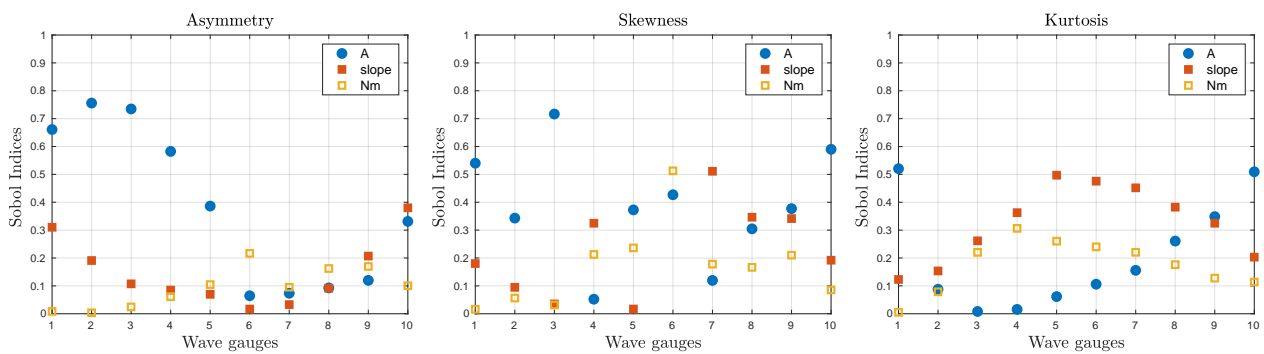


Figure 4.35: First order Sobol indices for Asymmetry, Kurtosis and Skewness measured on the wave gauges using the hybrid closure.

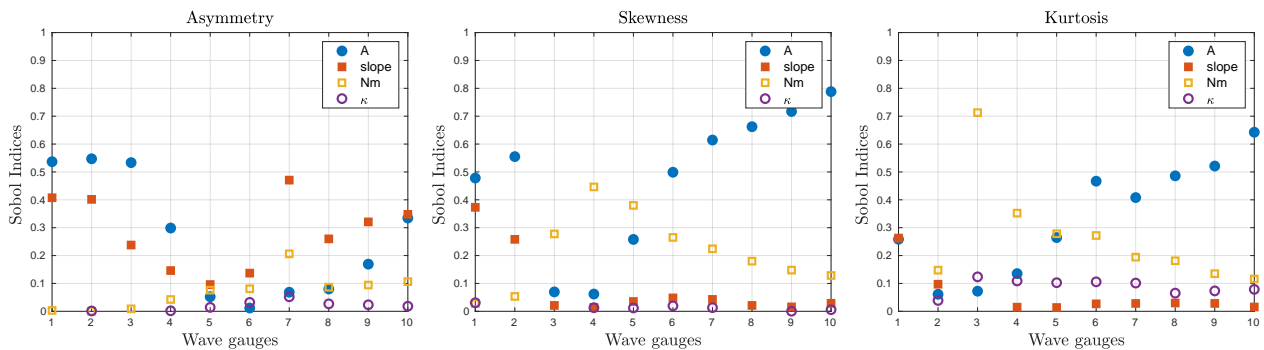


Figure 4.36: First order Sobol indices for Asymmetry, Kurtosis and Skewness measured on the wave gauges using the TKE closure.

Discussion on the convergence of the sensitivity indices

One of the main questions that can arise in this study is how the results are changing with respect to the numerical resolution. The answer to this question is twofold. The first aspect concerns the change of the physical output as the mesh is refined and is largely covered in [145]. We briefly report that the study performed in [145] has involved a systematic analysis of the behavior of the two closures for different mesh sizes, the study of dynamics of breaking through dissipation monitors. Thorough evidence of the equivalent capabilities of the two approaches to provide satisfactory results has been given. The results indicate that both closure approaches allow to describe correctly wave breaking at large scales and when we use the TKE the numerical dissipation plays a negligible role. The results also showed a reduced sensitivity to the mesh of this approach compared to the hybrid one.

The second issue that arises is the convergence of the statistical outputs as the mesh is refined. We investigate here this aspect by considering the variations of the statistics on four different meshes of sizes $\Delta x \in [0.05, 0.025, 0.0125, 0.00625m]$. Note that in this analysis we made sure that on each mesh the metamodel built for the sensitivity analysis has converged in terms of number of samples for each output value and for each mesh.

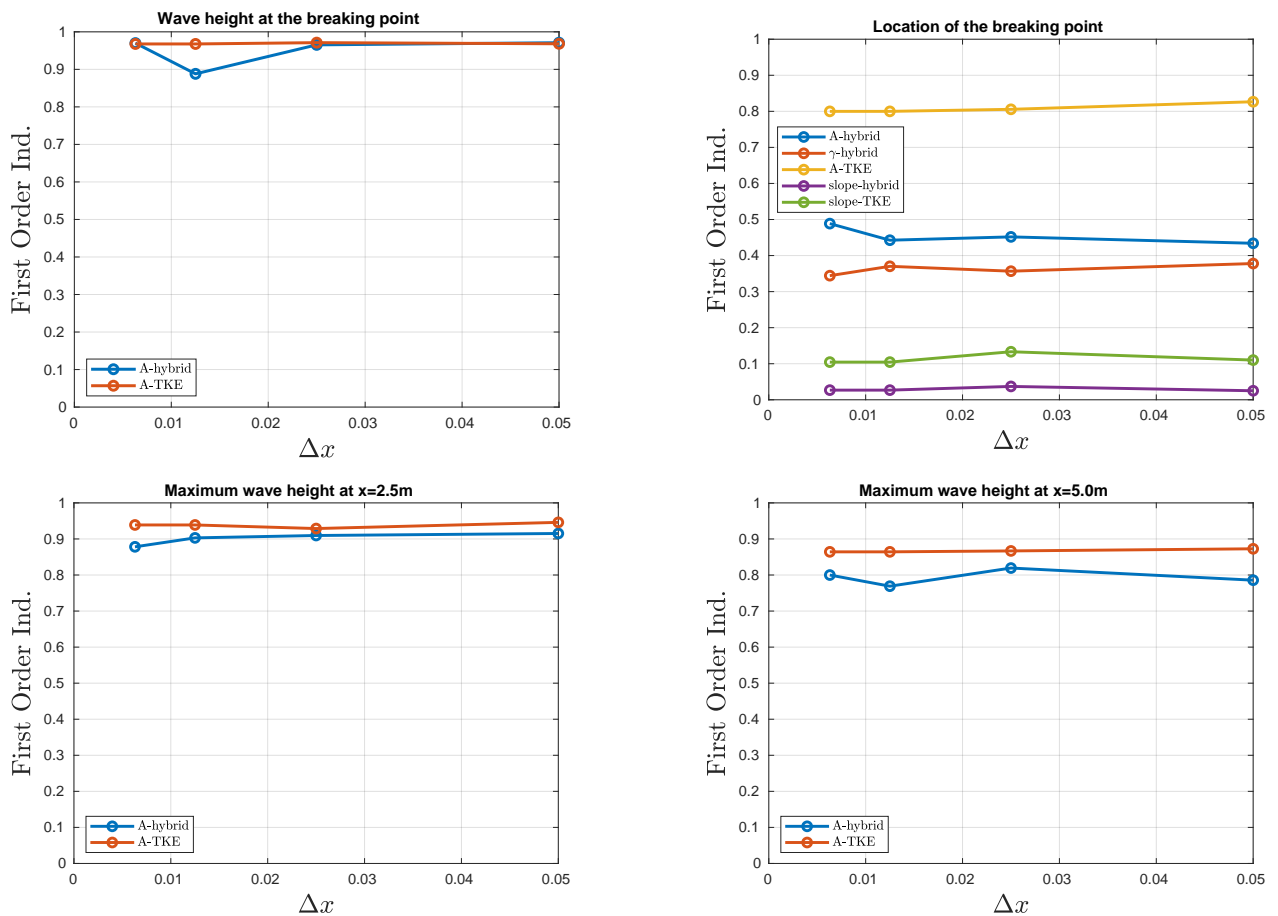


Figure 4.37: Sensitivity indices using different meshes for both closures.

Figure 4.37 presents the sensitivity indices for the four output parameters, the wave height and the location on the breaking point, and the maximum wave height at the wave gauges at $x = 2.5m$ and $x = 5.0m$. The input parameters of the closures are varied within 50% of their initial value. We plot only the indices that are more than 0.1. As expected, for the hybrid wbc the indices are almost constant for the coarser meshes while they start to diverge when the mesh is finer. As explained in [145] for finer meshes, and when we use the hybrid model, abrupt and spurious oscillations are introduced at the interface between the breaking and the nonbreaking region. This of course spoils the solution and consequently affects the sensitivity analysis. On the other hand when using the TKE wbc, the indices are almost the same for all the different discretizations proving that the solution is not changing when we vary the input parameters of the closure.

Sensitivity analysis with respect to runup

One of the most relevant outputs for risk assessment is the maximum runup. It is well understood that waves with higher amplitudes have higher impact on the coast, or in other words higher maximum runup. To investigate this, we look at the variability of the latter with respect to physical parameters. The maximum run-up as a function of the wave's amplitudes (for fixed slope=1/19.85, $Nm = 0.01$) is reported in the leftmost pictures in Figure 4.38 for both wave breaking closures. For comparison, the experimental data [242] are also plotted. We also report in the figure the dependence of the maximum runup on the slope (for fixed $A = 0.28$ and $Nm = 0.01$), and on the Manning coefficient (for fixed slope=1/19.85 and $A = 0.28$). The metamodel predictions for different values of the wave breaking parameter γ are plotted.

Above the amplitude ~ 0.15 the maximum run-up increases almost linearly with A . The metamodel predictions are quite close to the data. For the hybrid wbc, the impact of the wave breaking parameter γ is not uniform over the range of amplitudes. Relevant variations of runup are only observed for intermediate values of A , when sensibly reducing γ (early breaking), and for the highest amplitudes when delaying too much the detection (highest values of γ). The local maximum variations of runup observed are of the order of $\sim 5-7\%$, the predictions remaining relatively close to the experimental data.

In the same spirit we fix the TKE closure by setting $\kappa = 0.5$, $C_v = 5.0$, $\sigma = 10.0$, and evaluate the impact of γ , of the slope and of the friction coefficient. The plots obtained are reported at the bottom of figure 4.38. For the amplitude dependence, we see that the match with the data in the plot against the dependence is very good. We also note a behavior much different than the one of the hybrid closure. In accordance to the sobol indices presented in the previous section we confirm that, for the present closure the wave breaking detection has virtually no effect.

The variability of the runup with the slope and the Manning has however a different behavior, for the hybrid closure. When lowering the value of the detection parameter (early breaking), we see a systematic impact of the order of $\sim 9-10\%$ over the entire range of slopes. A weaker dependence on the slope is observed when using the TKE closure.

A similar, to the variability of the runup with the slope, trend is observed, for the hybrid model, when looking at the dependence with the Manning coefficient. The lowest value of the parameter γ

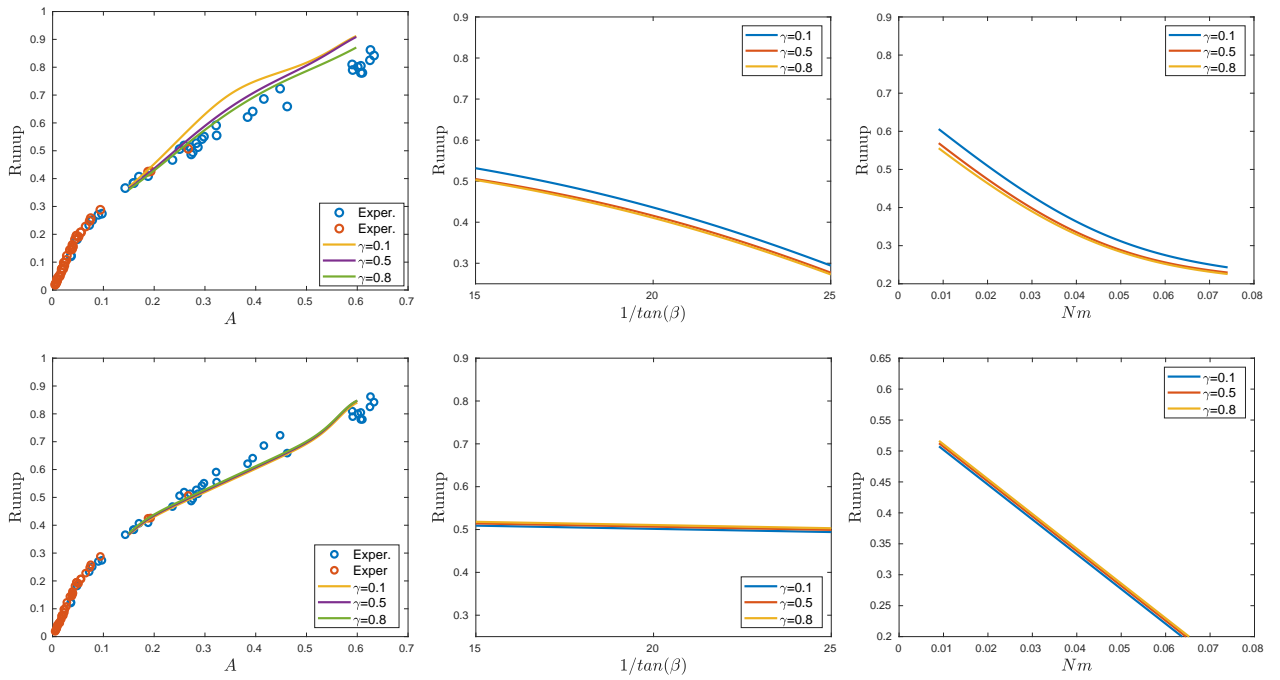


Figure 4.38: Run up as a function of wave’s amplitude were slope= $1/19.85$, $Nm = 0.01$ (left), of slope were $A = 0.28$, $Nm = 0.01$ (center) and of the Nm number were slope= $1/19.85$, $A = 0.28$ (right). Using the hybrid (up) and the TKE (down) wave breaking closures.

leading consistently to variations of the runup of the order of the maximum observed when changing the amplitude. This suggests that the runup may be more tolerant to some input error on the wave amplitude, while the correct parametrization of the breaking detection for the hybrid closure is more crucial when we have uncertainties in the slope and friction. The runup dependence on the Manning coefficient for the two closures is very similar.

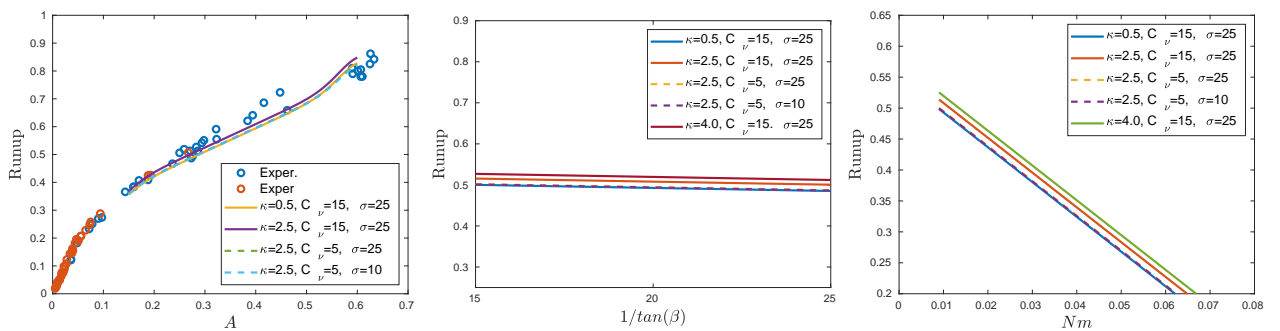


Figure 4.39: Run up as a function of wave’s amplitude were slope= $1/19.85$, $Nm = 0.01$ (left), of slope were $A = 0.28$, $Nm = 0.01$ (center) and of the Nm number were slope= $1/19.85$, $A = 0.28$ (right).

Finally and for the TKE, we fix $\gamma = 0.6$ and vary the other input parameters. The resulting behavior is the one reported on Figure 4.39. Again we see a secondary and almost negligible impact

of the model parameters on the runup. This is quite interesting as it means that the value predicted is quite robust with respect to the parametrization of the wave breaking, and mostly controlled by the problem setup.

A solitary wave of $\epsilon = 0.28$ over a slope

For completeness we now focus on the impact of the model parameters alone, for the fixed nominal values of the physical parameters: $A = 0.28$, $\text{slope} = -1/19.85$ and $Nm = 0.01$. For the hybrid closure, we are left only with the γ and θ parameters controlling wave breaking detection, and we have seen already that the first has a dominant contribution to output variations in the general case. As usual for the second wave breaking closure we have both the initiation and diffusive parameters that control the analysis. Figure 4.40 shows the first and total Sobol indices for some of the examined outputs. We can see that breaking detection, and in particular γ , has a major impact on the maximum wave heights. Large contributions to the variance also come from κ and C_ν , which in particular are the only dominating parameters for the run-up. We see here also a non-negligible difference between some first and Total indices, indicating the presence of some important interactions on the maximum wave's height. More precisely at WG 1 ($x = 0m$) and WG 6 ($x = 2.5m$) the second order index for γ and κ is 0.17 and 0.109 respectively.

Pointwise spatial distributions and temporal evolutions of sensitivities

For fixed values of the problem parameters, we see a similar behaviour of the Sobol indices in Figure 4.41 for the wave moments in the wave gauges. The γ parameter is responsible for almost 100% of the variance, except in the intermediate regions (breaking area), and in the last gauge. For the TKE, in Figure 4.42, wave's asymmetry and kurtosis are affected mainly by the parameters κ and C_ν , i.e. from the dissipation and production term in the transport equation (4.4). On the other hand, skewness, i.e the crest to trough shape, is mainly affected by C_ν which probably controls the kinetic energy cutoff before and after the breaking front.

To try to understand how θ still affects the solution, we report on Figure 4.43 the variance of dimensionless outputs for fixed values of γ for the hybrid closure. More precisely, the wave height at the breaking point (whbp) and the maximum height for the wave (mwh) at $x = 0, 2.5, \text{ and } 3m$ are scaled by the initial amplitude of the wave, and the location of the breaking point (bp) is scaled by the initial position of the solitary. Finally, the run-up values are scaled by the experimental values for the specific case. We see that variations above 1% are only observed for the position of the breaking point, and for the maximum wave height at breaking point and at $x = 2.5$, corresponding to the initial shoreline. In particular, for all these outputs we see a clear increase variance above a certain threshold of γ . This is the sign that above this value breaking detection is related to the second criterion. This is visualized in the right picture on the figure showing the variation of the position of the breaking point with γ for different samples of the metamodel. Above a critical value of γ this position only depends on θ .

To have a better insight we study the evolution of the water depth in the whole domain in space

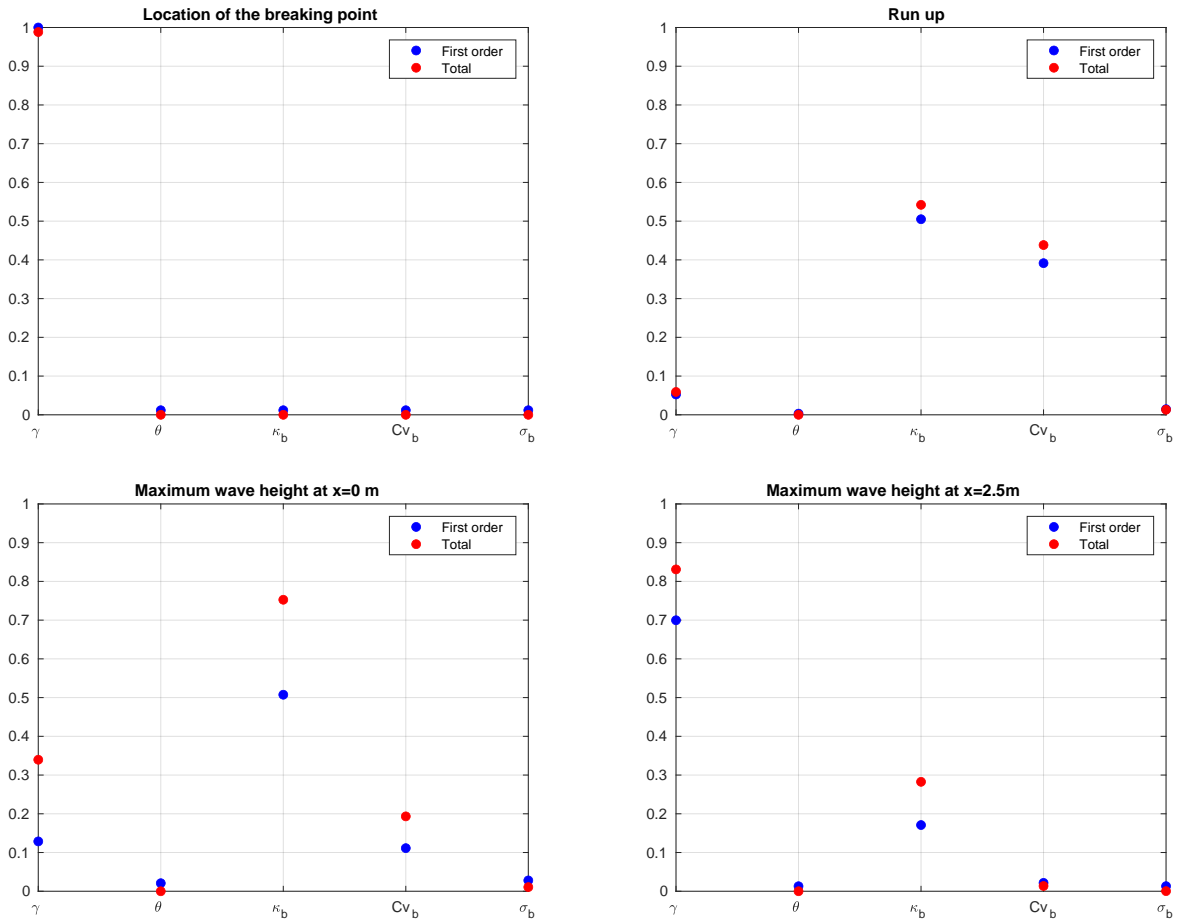


Figure 4.40: First (blue) and Total (red) Sobol Indices for the run-up and the maximum wave height at WG1 and WG6 using the TKE wbc.

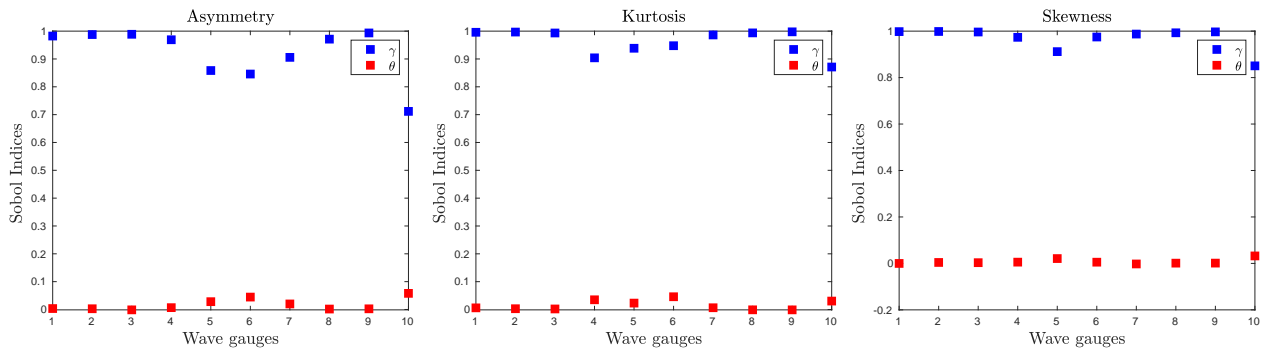


Figure 4.41: First order Sobol indices for Asymmetry, Kurtosis and Skewness measured on the wave gauges, when $A = 0.28m$.

by freezing the time in specific characteristic time spots. This means that we look at the spatial evolution of the sensitivity indices of the free surface elevation, shown in the left plot in Figure 4.45. The spatial distribution is computed at $t = 6.0sec$, i.e. during the breaking process. Red line denotes the location of the closest wave gauge, i.e. WG 10. Since γ is the dominant parameter

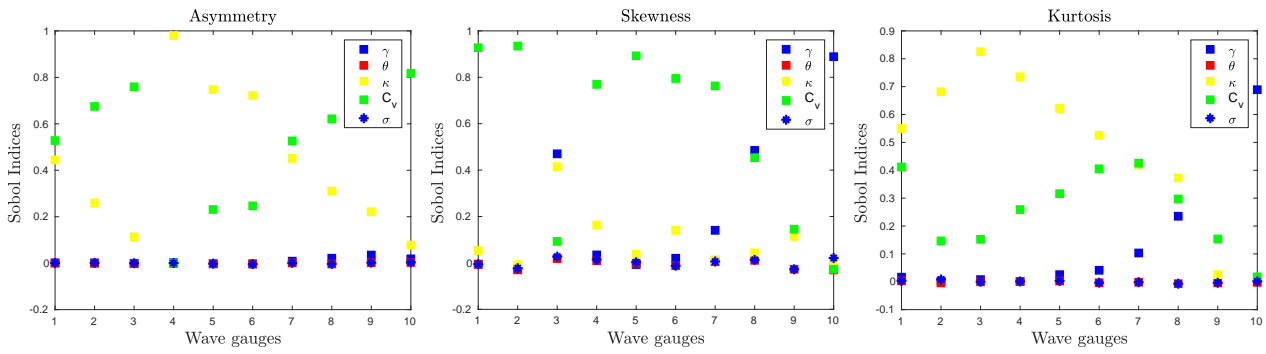


Figure 4.42: First order Sobol indices for Asymmetry, Kurtosis and Skewness measured on the wave gauges.

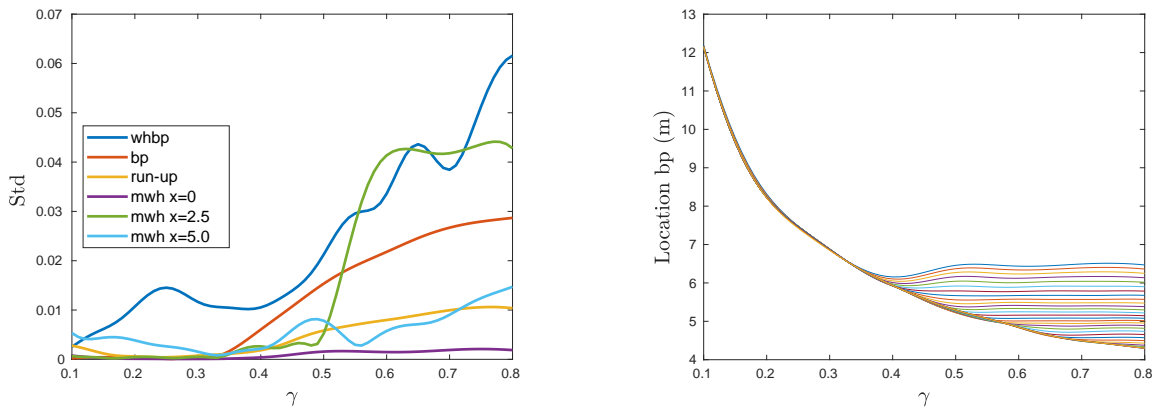


Figure 4.43: Standard deviation for the output parameters in respect to gamma (left) and evolution of the location of the bp.

in the whole domain we want to check where exactly it plays a crucial role, that is why we plot right next to the figure the absolute mean deviation of the water depth over the water depth, at $t = 6sec$. We observe that the maximum mean deviation is 25%, compared to the mean water depth, and occurs between 3m and 4m. After this region the deviation is less than 5%, so γ is still the dominant parameter but in negligible changes of the water depth. The temporal distribution 4.44 of the sensitivity indices is computed for the free surface elevation recorded at WG10 ($x = 5.0m$) and WG6 ($x = 2.5m$). Like before, θ is not the dominant parameter while the bore is breaking. To confirm how much it contributes we plot again the deviation of the free surface elevation. We can see that the maximum deviation grows as the wave propagates on shore reaching more than 90%, meaning that mainly γ is affecting the bore front.

We perform the same exercise but for the TKE closure. In 4.46 we report the spatial evolution of the water depth, sensitivity indices and absolute mean deviation of the water depth, at times representative of incipient $t = 6sec$, and after collapsing on the shore ($t = 8.2sec$). Its clear that in the early breaking time γ and κ are the predominant parameters affecting the water depth until 6m in the domain. More precisely the deviation of the water depth compared to the mean water depth

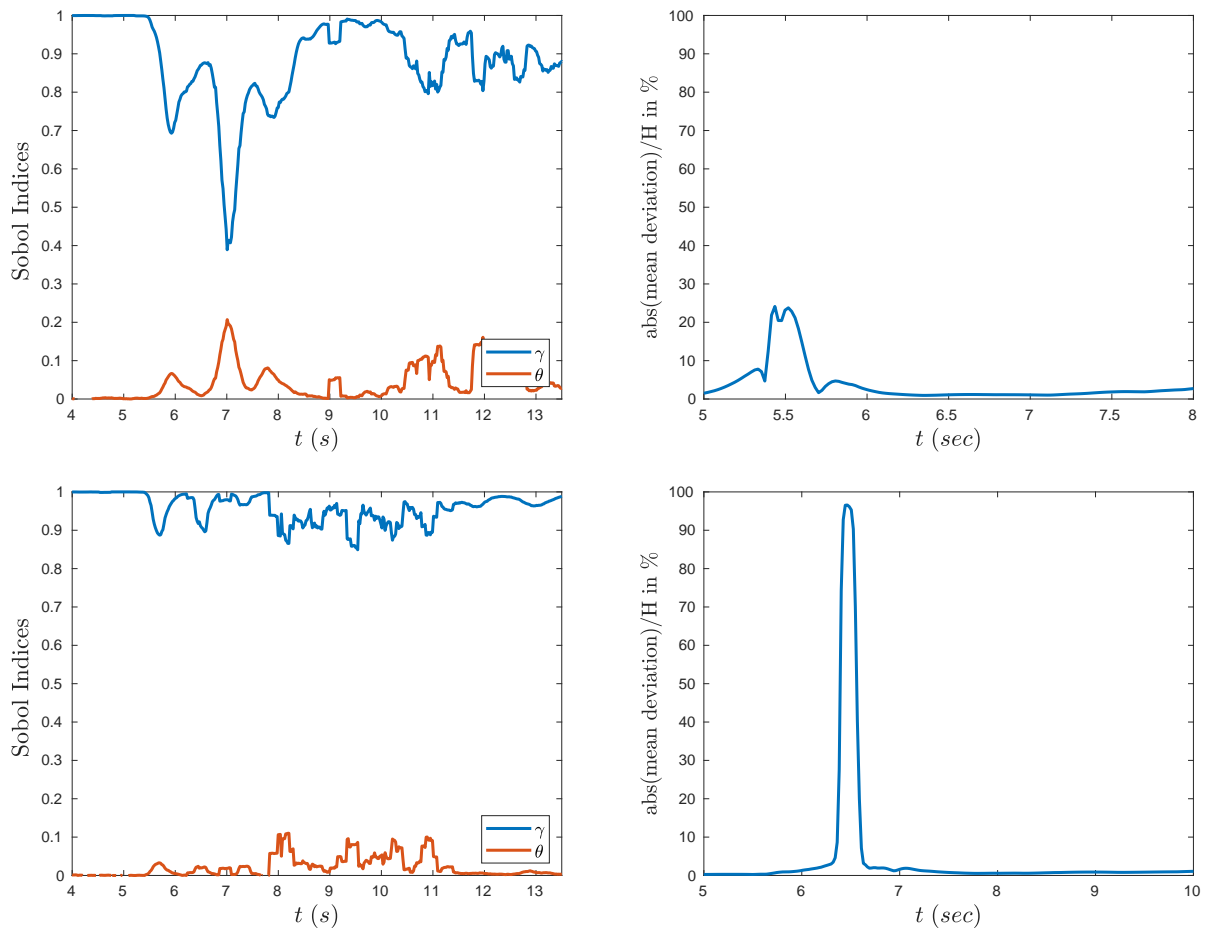


Figure 4.44: Temporal evolution of the First Order SI and deviation of the free surface elevation, at WG10 and WG 6.

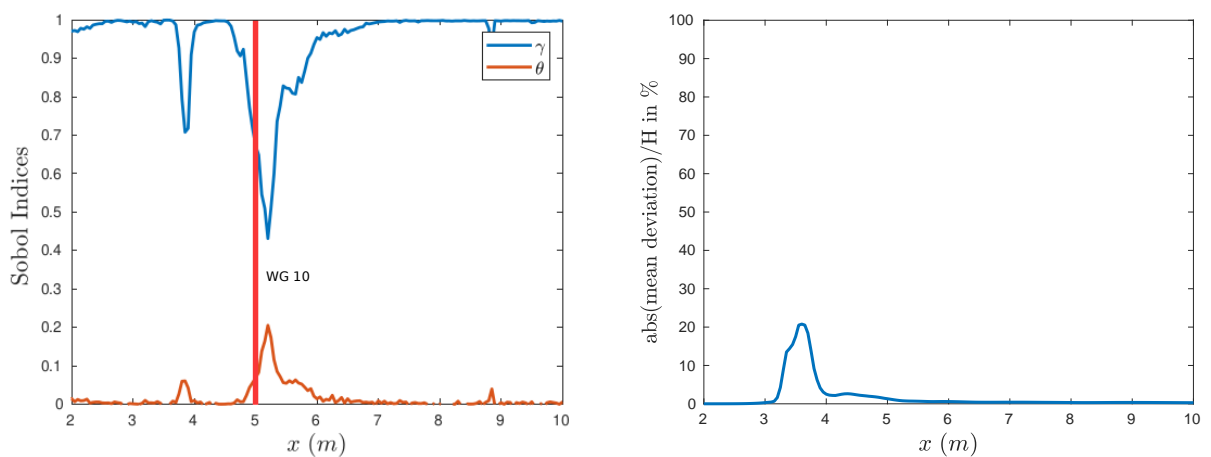


Figure 4.45: Spatial evolution of the First order SI and the deviation of water depth at $t = 6.0$ s.

is maximum 2.5%. This shows the robustness of the TKE model in contrast to the hybrid where the maximum deviation at the same time is 25%. After the collapse of the bore on the shore κ and C_v

are taking the lead and strongly affect the free surface elevation especially, the front of the wave. This is confirmed by the absolute mean deviation of the water depth shown in the low right figure of 4.46.

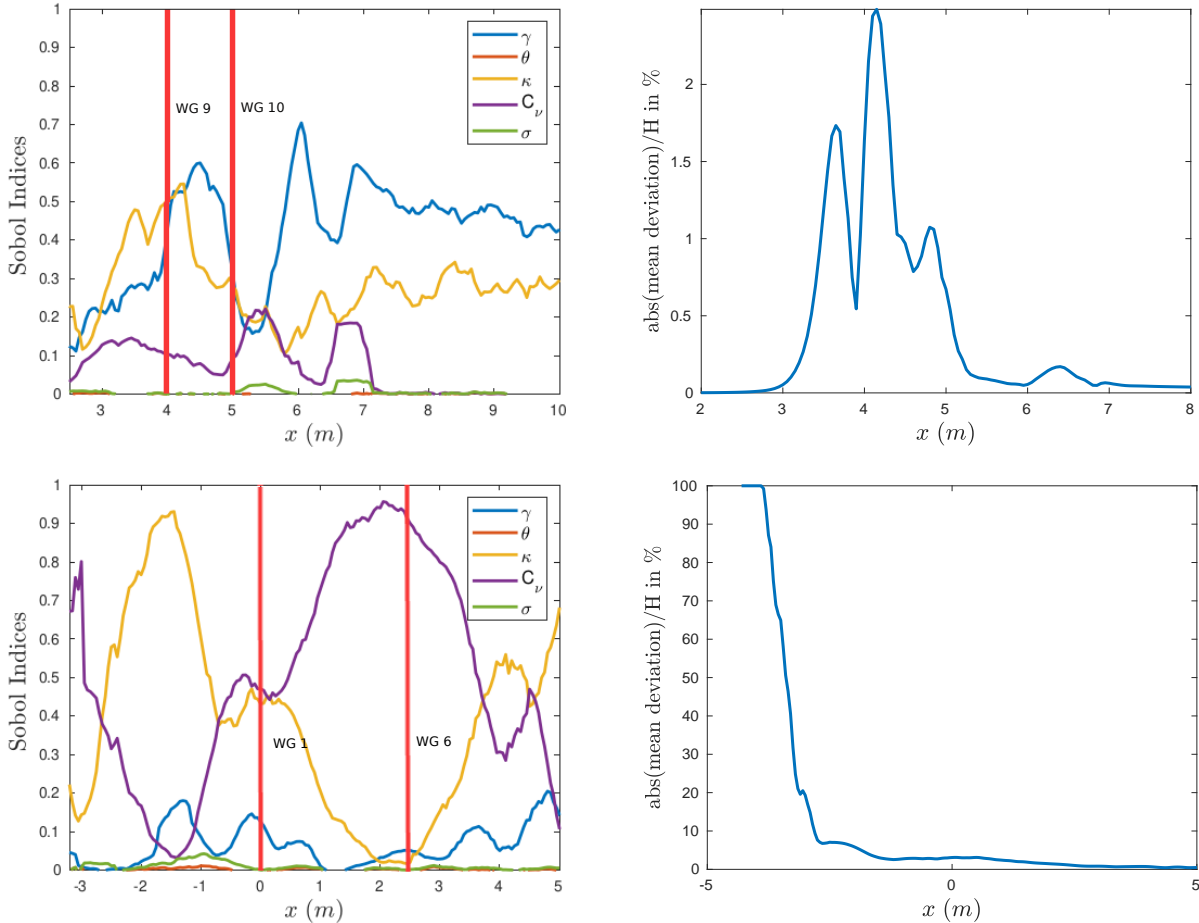


Figure 4.46: Spatial evolution of the Sobol indices and the absolute mean deviation for $t = 6, 8.2s$.

Next we study their temporal evolution in the wave gauges. For WG 10 the absolute mean deviation is almost zero, meaning that the parameters are not affecting the evolution of the free surface elevation. We report in Figure 4.47, and for the sake of completeness the results for WG6. The absolute mean deviation reaches almost 40% within the time interval 6 to 7seconds where the most important parameters are κ and C_ν . A consistent behavior is observed in all the WG's verifying that the wave-breaking mechanism is “following” the wave as it breaks until its collapse on the shore.

4.5 Summary

We have considered the issue of wave breaking closure when using weakly dispersive Boussinesq propagation models. We studied weakly and fully nonlinear models representative of classical and well known models/codes such as BOUSS-2D [67], Funwave [235], Coulawave [89, 172], BOSZ

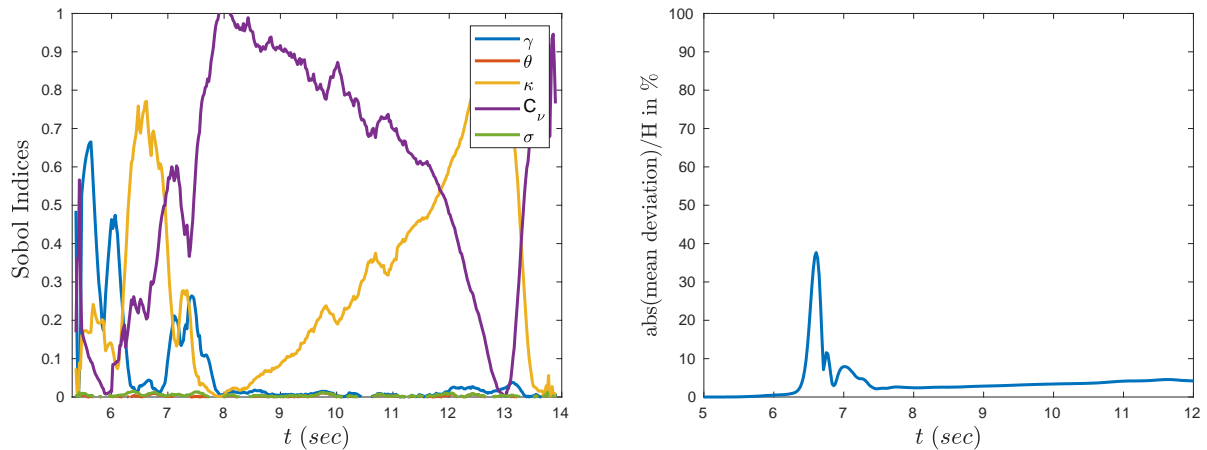


Figure 4.47: Temporal evolution of the Sobol indices and the absolute mean deviation of the free surface at WG6.

[226], MIKE21 [70], TUCWave [136, 137], and others. We have in particular focused on the enhanced equations of Nwogu [198], and on a frequency enhanced version of the Green-Naghdi system in the form proposed in [26, 97]. We have compared the now popular hybrid closure initially proposed in [252], with an eddy viscosity closure based on an adaptation of the turbulent kinetic energy closure model of [199], modified to be consistent with the detection mechanisms proposed of [137, 97], and also used here. The study performed has involved: a systematic analysis of the behaviour of the two closures for different mesh sizes; the use of dissipation monitors, consistent with the available theory of entropy dissipation for conservation laws [245], to study the dynamics of breaking for several cases; thorough evidence of the equivalent capabilities of the two approaches to provide satisfactory results.

Our results indicate that indeed, at least with the (rather standard) implementation proposed here, both closure approaches allow to describe correctly wave transformation and breaking at large scales. We have shown that when using the TKE eddy viscosity closure the numerical dissipation plays a negligible role, which motivates to look for non-dissipative/energy conserving numerical methods in the future. Also, the results clearly show the reduced sensitivity to the mesh of this approach compared to the hybrid one. The analysis of the wave breaking of solitary waves on a slope also has allowed to quantitatively study the interplay of the dissipation introduced by friction, eddy viscosity, and numerical dissipation.

Of course, one has to keep in mind that the computational cost required by the TKE closure is higher than the one of the hybrid closure. We judge this overhead justified by the increased robustness.

This preliminary study would benefit from further investigation using both improved numerics (e.g. energy preserving approximations in the propagation region), as well as improved models for both the propagation and for the breaking. The models considered at the moment present a dependence on the parameters of the detection criteria, as well as on the coefficients of the TKE equation. Improved models, including the effects of vertical variations of the flow in both the

propagation and breaking may be considered in future studies (see e.g. [33, 261, 106]).

Concerning the study on the parameters of the models using a solitary wave propagation over a slope test case, we conclude that, for the hybrid model, the initial amplitude of the wave is the most dominant parameter corresponding to almost every output metric before the run-up. The shape of the wave depends on the initial amplitude, and also on the slope of the beach during the run-up. The kurtosis of the wave is affected by mostly the slope of the beach and the friction coefficient. For the hybrid model, the statistical metrics are most affected by the wave-dependent input parameters. Among the model-specific parameters such as γ and θ , the former one has the most effect on the statistical metrics, more so after the value of $\gamma > 0.3$. θ , although not a dominant parameter for wave breaking, does contribute to the tail of the wave post breaking.

For the TKE model, the Sobol indices indicate that the wave amplitude is the most dominant parameter for the deterministic metrics, similar to the hybrid model. However, when the amplitude and the slope values are fixed, it emerges that κ and Cv are the parameters which most affect the output metrics.

It is also seen that, among the two candidate models, the hybrid model shows a significant effect of γ on the run-up of the wave, in contrast to the TKE model, which shows almost no effect of changes in γ . Further, in the case of the hybrid model, the effect of γ is less sensitive to changes in the initial amplitude when the slope and the friction parameters are fixed. This implies that, when using the hybrid model, small errors in the slope or the friction parameters may manifest into considerable errors in the prediction of the maximum run-up. On the other hand, the TKE model doesn't show a similar effect of γ on the run-up process over a range of values for the initial amplitude, friction and the slope parameters. However, once we fix the value of γ , the predicted run-up of the waves reflects a larger influence of the friction and the slope parameters compared to the initial amplitude of the wave when the TKE model parameters are varied. Thus, it can be concluded that the run-up predicted by either of the models may be more sensitive to the errors in the measurement of the friction or the slope parameters, in comparison to the initial amplitude of the waves, and will depend on the choice of γ for the hybrid model and the model parameters for the TKE model.

Finally, the absolute mean deviation of the free surface elevation measured at the wave gauges reveals that the hybrid model can lead to large differences between the observed values of the free surface elevation and the mean free surface elevation, up to 90%. On the other hand TKE model is more robust mainly on the off-shore region.

We have to note the differences of the Sobol indices for the statistical parameters between the two wave-breaking closures, see Figures 4.35 and 4.36. This is due to the fact that the wave-breaking closures simulate the breaking wave in a different way. The hybrid closure simulates the breaking wave as a traveling bore while the one obtained using the TKE closure has a smoother propagating front.

Chapter 5

Conclusions and future work

5.1 Conclusion

Over the last decade, my research has significantly contributed to the field of nonlinear water wave dynamics particularly in the context of Boussinesq-type (BT) models. The most important topics of my work during the last ten years at Inria of the University of Bordeaux are summarized in this manuscript. We can divide this work into three main areas. *The study of depth averaged asymptotic models, the development of high order numerical schemes in one and two dimensions for these models, and the study of wave breaking mechanisms for BT models.*

In the study of depth-averaged asymptotic modes, we revisited the fundamental question of the necessity of full nonlinearity in weakly dispersive BT models. Through a detailed examination and comparison of various weakly nonlinear BT models, we identified critical cases where full nonlinearity is essential, thereby advocating for a revision of benchmarking habits for BT models. This work underscored that while fully nonlinear models are crucial for addressing problems involving highly nonlinear waves, weakly nonlinear models remain effective for many practical applications not involving planar nonbreaking wavefronts reflecting on steep coastal structures.

My contributions to the development of numerical schemes have advanced the implementation of depth-averaged models. We show that hybrid schemes, that are flexible and easy to implement, is a good choice for asymptotic models. In this approach we highlighted the interaction between modeling and discretization errors, which one must take into account. Key findings include the necessity of second-order methods for elliptic components and the careful representation of data in unstructured grids. These insights are crucial to ensure accurate and stable numerical simulations of BT models.

In the study of wave breaking, our research focused on the sensitivity of wave breaking closures, particularly the hybrid and eddy viscosity approaches. We addressed the stability issues of the hybrid method and provided a quantitative description of the dissipation mechanisms. Our findings demonstrated that while both approaches can accurately model wave transformation and breaking, the eddy viscosity approach shows reduced sensitivity to mesh size and less numerical dissipation.

Overall, my contributions have advanced the formal understanding of numerical systems for

depth-averaged mathematical models and have clarified the mechanisms of wave breaking in BT models. My work has not only improved theoretical insights but also enhanced the accuracy and stability of numerical simulations in the field of nonlinear water wave dynamics.

5.2 Current activity and future work

This last section presents my current activity and what is that planned for the next 4 years. These include collaborations and activities that have already been funded or applied for funding.

5.2.1 Coupling methods of phase-resolving coastal wave models

This project lies within the framework of the PhD of Jose Galaz that Antoine Rousseau and I are co-supervising. Dr Jose Galaz defended his thesis on 26th of June 2024 and we submitted parts of this work for publication. In this work we study how to couple different phase-resolving water wave models that have been developed since the mid 19th century, namely Boussinesq-type and Saint-Venant (or Non Linear Shallow Water) that they are commonly employed in the study of nearshore wave propagation. A detailed analysis can be found in Galaz's PhD thesis [101]. Here we will attempt to highlight some parts of the work that is still ongoing.

Despite the existence of numerous models and coupling examples, there is still no clear consensus on the artifacts and issues caused by these strategies, nor is there a well-defined method for analyzing and comparing them. To address this problem, our research employs a domain decomposition approach, based on the principle that 3D water wave models (such as Euler or Navier-Stokes) are the ideal reference solution.

In particular, for one of the most popular coupling methods used for modeling wave breaking on BT equations, the hybrid model, it was noted that many authors [235, 145, 253] had reported different types of such artifacts. We categorize them in three main categories: **(I)** Oscillations, **(II)** Instabilities, and **(III)** Mesh dependent solutions. The objectives of this work are threefold.

1. Develop new couple phase-resolving coastal wave models.
2. Study and explain the source of any artifacts observed.
3. Contribute to their mathematical justification (as approximations to the 3D model).

In order to complete these goals it is necessary to define the concept of the ideal coupled model. *The ideal coupled model is the one closest to the 3D model*, with the 3D model taken, for example, as the free-surface Euler or Navier Stokes equations. This principle stems from the observation that, similar to regular BT or SV models, the primary reason for not using the highly accurate 3D model in most scenarios is its substantial complexity and computational expense. This concept is already employed in the literature to justify the use of both linear and non-linear BT models.

This work is divided in two parts. First we propose new coupled models and we evaluate them through numerical experiments. We identify specific hypotheses about their accuracy and

limitations. Subsequently, a theoretical framework is developed to prove these hypotheses mathematically, utilizing the one-way coupled model as an intermediate reference to distinguish between expected and unexpected effects and categorize errors relative to the 3D solution. The total error is split in three parts—coupling error, Cauchy-model error, and half-line-model error—and these concepts are applied to the linear coupling of Saint-Venant and Boussinesq models using the so called 'hybrid' model. The analysis confirms that the coupling error accounts for wave reflections at the interfaces, and varies with the direction of propagation. Moreover, thanks to the choice of the one-way model as the intermediate reference solution, this analysis proves several important properties such as the well-posedness and the asymptotic size of the reflections. Additionally, the work also addresses the weak-wellposedness of the Cauchy problem for the B model and its implications for mesh-dependent solutions that have been reported. As a byproduct, a new result for the half-line problem of the linear B model is obtained for a more general class of boundary data, including a description of the dispersive boundary layer, which had not been addressed in the literature yet. The proposed pragmatic definition of coupling error aligns with and extends existing notions from the literature. It can be readily applied to other BT models, discrete equations, linear and nonlinear cases (at least numerically), as well as other coupling techniques.

One overarching conclusion is that the one-way model proves to be the optimal coupled model when dealing with a vertical interface (static switch) and initial conditions located on one side of the interface. This holds true regardless of the nonlinearity regime and aligns with Dubach's observation that absorbing conditions are also the optimal choice. Beyond Dubach's statement, this model offers insight into what occurs on the other side of the interface in the reference solution. While this model has many limitations for practical computations, it is very useful for quantifying the coupling error and assessing the performance of a given coupled model. The conclusions drawn, up to now, from this study regarding the main objectives are:

1. We have studied new coupled models which they also displayed some or all of the artifacts that the hybrid model had too, that is to say: (I) Oscillations, (II) Instabilities, and/or (III) Mesh-dependent solutions.

2. We demonstrate that issue (II), Instabilities, is a problem at the discrete level, not the continuous one. This was done first numerically in the nonlinear case and then theoretically in the linear case. Additionally, it was shown that the source of problem (III), Mesh-dependent solutions, appears at the continuous level, regardless of the discrete scheme chosen. This is done both numerically and theoretically. The problem arises from the weak well-posedness of the BT models: because it is not possible to remove the term that contains the derivative of the initial data in the continuity estimate of the BT model, mesh-dependent waves that are neglectable for the SV model are significant in the BT model, leading to completely different solutions and possible negative depths and instabilities on different mesh sizes. These oscillations could be triggered by any small perturbation regardless of their source (discretization, source terms, etc), but the nonphysical amplification happens at the continuous level. This is assuming a transmission from the

SV to the B model through a horizontal interface, i.e., through the initial condition of the Cauchy problem. It is also demonstrated that the source of problem (I), Oscillations, is at the continuous level too, but it was proved that the oscillations are reflected waves emanating from the interface, that are asymptotically small at order $O(\mu^2)$. This was discovered numerically and theoretically demonstrated. It also confirms a conjecture of Shi et al. [235], observed from numerical results. It was also proved that the size of these reflections is larger when waves are initially supported in the SV subdomain than in the B subdomain.

In addition to addressing problems (I) to (III) for the second objective, we discussed other effects anticipated from the coupling of linear equations. These are presented as expected outcomes of the models, in contrast to the unexpected artifacts of the previous three problems. We examined the horizontal interface (transmission through initial conditions). Due to the causality principle, transmission can only occur one way—forward in time. Consequently, the wavelength of the waves does not change as a result of switching equations. We also studied the vertical interface (static switch) based on the behavior of the one-way model. Unlike the horizontal interface, the primary effect here is an artificial refraction that changes the wavelengths inversely to the phase speed change. Additionally, for wave propagation from SV to B subdomains, short waves that do not conform to the B model's dispersion relation are filtered out through a distance of $O(\mu^2)$. This is a characteristic of the half-line problem of the Boussinesq equations, represented by a dispersive boundary layer of length $O(\mu)$. The analysis of the half-line linear BT problems is a novel result not previously documented in the literature, although the dispersive boundary layer had been identified in the nonlinear case [32, 161]. Moreover, these findings are likely applicable to the coupling of other linear BT models.

3. The justification for coupling with a horizontal interface (initial conditions) relies solely on the existing literature that addresses the Cauchy problems, as referenced in [157]. By "justification," we mean proving the well-posedness of the model and demonstrating that its solution approximates the 3D model. To justify the coupled models in the case of a vertical interface (static switch), we proposed quantifying three types of errors: 1. *Cauchy model error*, 2. *Half-line model error* and 3. *Coupling error*. The sum of these three errors provides an upper bound for the total error relative to the 3D model. However, only the third type of error, the coupling error, is directly related to the coupling technique. The other two errors pertain to the error estimates for the Cauchy problems and half-line problems of each equation with respect to the 3D model and not directly to the coupling itself. The computation of the coupling error is straightforward and can be applied to any phase-resolving model, regardless of nonlinearity. It is simply the difference from the one-way model. One main limitation of this metric is the assumption that the support must be on one side of the vertical interface. Under the assumption of linearity, we discuss and prove that the initial support can be split into two functions, each supported on one side of the interface. These can then be used as references in the superposition of two one-way models. Whether this approach is effective with nonlinear models remains an open question.

Our analysis reveals that the coupling error is entirely due to reflections originating at the

interface. These reflections cause the mesh-independent small oscillations (problem (I) Oscillations) found in the literature. Additionally, using Fourier analysis, we obtained an explicit integral representation of the solution. This representation allows us to quantify the continuity, the asymptotic size $O(\mu^2)$ of the coupling error/reflections, and the effect of directionality.

The work that remains to be done concerns the proof of weakly well posedness on the nonlinear problem on the whole domain. We also need to examine the stability of the numerical scheme for the hybrid model using for example the weakly nonlinear BT equation and last but not least to compute the coupling error for the fully nonlinear BT equations.

5.2.2 IMEX schemes for low Froude numbers

The next project is a joint work with Martin Parisot and the PostDoc Ralph Lteif from Cardamom team at Inria of the University of Bordeaux. The objective of this work is the implementation of an Implicit-Explicit scheme (IMEX) for flows in low Froude numbers. This is in the frame of the ANR Lagoon project (2022-2026). The scope of Lagoon is to increase the computational performance of the common modeling platform UHAINA, in order to upgrade it as an efficient and accurate tool for storm-surge predictions in different future climate scenarios. To achieve this goal and produce results which go beyond the state-of-the-art, one of the planned developments is the development and analysis of a robust and efficient high order numerical scheme for the shallow water flows in the low Froude numbers. The reason is that, for oceanic and coastal simulations, the Froude number of the flow can vary from 1 near the coast to two or three orders of magnitude less offshore. In deep sea, the classical hyperbolic schemes are inadequate [114] as the time step restricted by the CFL condition is dramatically reduced and thus realistic simulations are impossible. The solution to this bottleneck is to solve a part of the system implicitly, thus leading to IMEX schemes. In the context of semi implicit discretization, advection is discretized explicitly, while pressure (i.e water level) is handled implicitly. As a result, the stability condition is constrained only by the main flow speed, which approaches zero in the low Froude limit. Therefore, semi-implicit schemes are significantly more efficient than explicit methods in the low Froude limit. Additionally, they exhibit less numerical viscosity and offer more accurate resolution since the implicit terms do not require numerical stabilization.

The idea here is to limit the size and number of linear systems to be solved so we use as a starting point the CPR scheme [208] which is first order accurate both in space and in time. The CPR approach is a fully diagonal segregated method which only relies on the implicit treatment of the water height and hybrid mass fluxes using explicit velocities. The method allows to avoid resolution of large linear systems.

In the context of IMEX schemes and to archive a high-order time integration, several Runge-Kutta schemes can be found in the literature see for example [71] and [27] and references therein. However, to limit the number of linear systems to solve, we focus on the simple Crank-Nicolson schemes. For the space discretization, a classical second order MUSCL reconstruction is used.

We implemented the scheme both in one and two horizontal dimensions. We test the convergence rates for moving and steady solutions both for high and low Froude numbers. Furthermore, we

conduct a comparative analysis of CPU times between the ImEx and explicit schemes, revealing important computational savings with the ImEx scheme particularly under the low Froude regime. We are currently working on the analysis of the scheme in its linearized version to study the stability properties.

5.2.3 Discrete well balanced schemes for hyperbolic equations

An other project that I am involved is the implementation of discrete well balanced schemes for hyperbolic equations. This is a joint work with Dr Mario Ricchiuto from Inria Bordeaux and Carlos Pares from the University of Malaga, Spain. Inspired by the approximate well-balanced schemes introduced e.g in [42] and [107] we aim at constructing a method whose discrete steady states are solutions of arbitrary very high order ODE integrators. However, as in [181] we embed this property directly in the scheme, so that the ODE integrator is never actually applied to solve the local Cauchy problem. To achieve this, we work in the WENO finite difference setting already explored in [204]. As in [54] we apply the WENO reconstruction to a global flux assembled nodewise as the sum of the physical flux and a source primitive. The novel idea is to compute the source primitive by means of very high order multi-step ODE methods applied on the finite difference grid. We obtain in this way a local well balanced splitting of a source integral with weights depending on the ODE integrator. As in [4] this approach is referred to as global flux quadrature of the source. The discrete solutions of our schemes are the solutions of the underlying ODE integrator by construction. In practice, we combine WENO flux reconstructions of orders from 3 to 7, with Adams-Moulton or Adams-Bashford methods of orders up to 8. The results confirm that the steady accuracy of the scheme is independent on the order of the WENO approximation, and only depends on the consistency of the ODE method. For our approach moreover the two are independent, which is a very interesting improvement compared to [181]. Moreover, as in the last reference our approach does not require to explicitly solve the Cauchy problem, which differentiates our approach from the one of [42, 107]. Applications to scalar balance laws and to the shallow water equations confirm all the desired properties. Other systems will also be examined.

5.2.4 On the design of an improved Boussinesq model for real applications: equilibrium between accuracy and performances

The computational cost of modeling coastal flooding using Boussinesq-type models in real scenarios is a significant limitation. Current models struggle to achieve the high resolution and extensive simulation scenarios required to assess community risks from coastal hazards and climate change. This project aims to develop an enhanced Boussinesq-type model within the UHAINA hydrodynamic code, specifically tailored for real-life applications. The focus will be on optimizing a combination of modeling choices (such as dispersive or non-dispersive, full or weak nonlinearity, scalar or vector dispersion terms) and numerical choices (including numerical dispersion/dissipation, local accuracy order in space, and local accuracy order in time) to align with the relevant physical processes. As a result, we aim to gain at least an order of magnitude in the performance of our simulations without

affecting the phenomenological representation in the context of real applications. Our progress will be evaluated by simulating coastal areas affected by strong swells in the Nouvelle-Aquitaine region (NVA). We will model the impact of historical storms in the area and compare our results with existing measurements. This project is a collaboration with BRGM, whose funding allows us to recruit a PhD student starting in April 2024. The student is being co-supervised Dr. Andrea Filippini from BRGM, Dr Mario Ricchiuto from Cardamom and myself.

The error produced by a modeling tool is the result of the composition/compensation of the error of the asymptotic model and that of the numerical scheme. To achieve our goals, we will focus on two main areas: (i) a mathematical study of the equations and analysis of their linear and non-linear properties for describing dispersive processes; (ii) the design of a new strategy for solving the mathematical model that does not aim for accuracy, but practically accepts an approximation error due to the speed of execution. More precisely, the work flow that we are currently following is:

- Benchmark the performance of the code in its current state on 2D academic test cases and on the targeted real-world application(s).
- Mathematical study of the model implemented in UHAINA [94] and analysis of its linear and non-linear properties. Construction of an improved Boussinesq model with simpler resolution, without significant loss of precision in phenomenological representation. Validation on targeted test cases.
- Final benchmarking of the code and application to the study of wave propagation and extreme events on the coast of the NVA region.

BRGM will also provide data for historical events at sites in NVA region subject to strong wave regimes.

The work to be carried out will provide an improved model, numerical scheme, and solution strategy explicitly designed to optimize the balance between accuracy and speed in real-world applications. Leveraging these combined strengths, we aim to achieve efficient numerical simulations, up to an order of magnitude faster than current capabilities, using a wave-by-wave model for the overtopping of extensive coastal sections (several tens of kilometers).

All the work will be implemented in the code UHAINA [96, 94], a phase-resolving free surface wave model. More precisely UHAINA is a 2DH hydrodynamic model for coastal applications, whose hydrostatic core is already an operational tool for real applications. Its non-hydrostatic module solves the fully non-linear and weakly dispersive enhanced Green-Naghdi equations with an efficient and flexible approach [137, 97], incorporating a local hybrid closure for wave breaking. UHAINA is built on the Aerosol platform, offering extensive capabilities such as arbitrary high-order finite element discretizations, hybrid meshes, and an advanced programming environment optimized for performance and high-performance computing (HPC). It is co-developed by Cardamom and Cagire teams of Inria and BRGM.

With these advancements, UHAINA will be capable of conducting studies over much larger areas than other currently available modeling tools. Additionally, we will be able to run simulations

in significantly shorter times and/or increase the number of simulations, which will be beneficial for probabilistic approaches (especially in the context of climate change) and for developing meta-models.

5.2.5 European project RESCUER HORIZON-MSCA-2022-DN 101119437

The Doctoral Network (DN) RESCUER (Resilient Solutions for Coastal, Urban, Estuarine and Riverine Environments) aims to train 10 young researchers (Fellows) to tackle medium to long term water challenges, focusing on forecasting and modeling of coastal, riverine, and urban flooding and associated water quality issues. The DN will leverage advances in the numerical treatment of multi-scale and multi-physics problems made in the past decade, into models to address the pressing needs in the practical modeling of hydrodynamic phenomena with the goal of improving overall safety of coastal and riverine areas.

The outcome of this project will be a suite of universal, highly efficient, and accurate numerical models covering the whole spectrum of hazards induced by sea and river forcing actions, such as wave run-up and overtopping, coastal and urban flooding, water-quality issues, bed and riverbank erosion. These multi-physics models validated using data from dedicated laboratory campaigns and collected at a selected field site (Senigallia, Italy) and put into service by our commercial partners will be able to provide a complete picture of potentially hazardous conditions on the coast. The models will be used on an operational basis as well as tools for risk assessment and mitigation planning and to provide guidance for decision makers. An Early Warning System can be envisaged as an outlook of the present work beyond the project duration.

RESCUER integrates four research themes: WP1: Coastal modeling and hazards focusing on phase-resolved wave forecasting tools such as shallow-water and Boussinesq models, and the study of wave processes and hazards related to infragravity waves and waves propagating over steep bed topography; WP2: River and estuary; dynamics focusing on flow and sediment transport in the river/estuary contact area, and to study sediment transport over saturated subsurface flow; WP3: Urban flooding focusing on the construction of numerical models; WP4: Water quality focusing on the spreading of pollutants and the kinetics of decomposition. Two more WP's complete the project. WP6: Communication, Dissemination and Exploitation and WP7: Network management and coordination. *We are leading WP6 and we are participating in WP3 with one fellow student.*

Leading WP6 requires having a comprehensive overview of the entire project and detailed information on the results of all work packages. This responsibility necessitates dedicating a portion of my working hours to ensure effective coordination and integration of findings across the project.

The scientific objective of WP3 is to improve the modeling of urban floods and include effects of small-scale, e.g. gates and openings. The objective of our work in this working package is to develop a modeling framework for urban flooding simulations that integrates precise representations of topography and built structures using the Discontinuous Galerkin (DG) numerical method. Ensuring high-resolution descriptions of both coastlines and structures, with accuracies of maybe less than a meter, is crucial for accurately depicting flooding dynamics. The primary challenge lies in managing complex and irregular bathymetric data represented by polynomials on unstructured grids. This

framework must effectively handle interactions between irregular bathymetric data and flooding fronts (wet/dry transitions), potentially incorporating non-submerged floating structures. A well-balanced scheme is imperative to avoid spurious and non-physical waves arising from numerical discretization-induced bathymetric variations.

The idea is to explore sub-cell models and sub-cell resolution strategies combined with some nonlinear numerical method. For example one avenue of exploration lies in the usage of sub-cell approximations that may allow to construct well balanced schemes preserving the high resolution see for eg [184, 100]. Further more the integration of sub cell techniques can be instrumental in maintaining water positivity around wet/dry areas [116].

It is known that high order DG methods may produce spurious oscillations in the presence of discontinuities or steeply varying gradients, i.e. Gibbs phenomenon [116], so a possible way to treat this is the sub cell nonlinear approximations for the topography, as to avoid these spurious oscillations. Furthermore, the integration of individual cell models could be extended to deal with friction phenomena and adapting to the presence of floating structures, allowing an integrated simulation framework that captures a variety of real-world scenarios [28].

Anticipated outcomes include improvement on academic tests, and applications in operational context to realistic events, and experiments from other partners benefiting from consortium data. The resulting numerical scheme will be applied to a case study of urban flooding, with comparisons made against experimental data provided by project's partners.

A PhD student, whom i will supervise, will start working on the project on October 1st.

5.2.6 Comparison of different numerical schemes for dispersive flows in real case scenarios

This work is a part of a larger project called CORALI (COⁿnaissances inteRdisciplinaires pour une meilleure Adaptation face aux risques LI^ttoraux/InteRdisciplinary knowledge for better Adaptation in the face of LI^ttoral risks) which is funded by the Regional Program of Nouvelle Aquitaine called PSGAR (Ambitious Regional Scientific Projects).

Our work lies on the region of wave transformation from the open sea to the coast. As waves propagate from the deep ocean to the coast, they undergo multiple transformations, and significant progress has been made in understanding and numerically simulating these processes over the past few decades. Different models and codes can be used for the study of waves' transformation. Codes based on phase-averaged models or on phase resolving models. The latter ones has the advantage that explicitly represent waves and allow for a much more realistic reproduction of these phenomena. In Cardamom team we developed different numerical schemes for phase-resolving models.

In this project, we will study and compare various numerical schemes for phase-resolving models. These schemes have already been developed [137],[206] or are currently in development (see Section 5.2.4). Additionally, a postdoctoral position will be available in 2025 to support this endeavor.

5.2.7 Adaptive meshes for tsunami simulations

The project is a part of the PC Outre-mer funded by the IRIMA Programme and led by IPGP. It belongs to the WP2: Tsunami risks: Estimating damage and socio-economic impacts. The challenge of WP2 is to build a toolchain and methodologies that link advanced mathematical and numerical models with geophysical, geological, civil engineering, geographical, and economic data to conduct an analysis of hazards, risks, and socio-economic impacts (including buildings and infrastructure) related to tsunamis generated by landslides in a seismo-volcanic context (including cascading effects). Distant field scenarios such as earthquakes will also be considered to complement the study.

Our part lies on the developing of accurate tsunami modeling tools by integrating adaptive meshing methods and incorporating phenomena that can affect the magnitude of a tsunami (e.g. tides, structures etc). The first step is to enhance the performance of the code that we will use, i.e UHAINA, through the implementation of dynamic and non-stationary mesh adaptation techniques, coupling with MMG. MMG is an open-source remeshing software package. It offers volatile capabilities, in 2D, 3D and in parallel capabilities. A given mesh is transformed by a series of local mesh modifications to a new mesh adapted to a given metric field, which specifies the local sizes and orientations of the orientations of the elements. MMG is being developed by an industrial consortium, which guarantees its robustness and cutting-edge capabilities.

Static meshes are inefficient for tsunami simulations, where an impulsive wave is initially concentrated in a narrow region and then propagates over a certain distance. We will investigate metric-based mesh adaptation, where the entire domain is remeshed to optimize the size and orientation of the elements. This allows us to adjust the total number of vertices throughout the simulation as the waves develop within the domain and to move vertices between remeshing steps.

The second step is the development of error models for dispersive flows. This task is very innovative, with very little or almost no prior work found in the literature. This project is a joint collaboration with Dr Nicolas Barral and Dr Mario Ricchiuto from Cardamom team.

5.2.8 Tidal bore and bathymetry

Last but not least I am participating in the ANR BABA: Tidal Bore and Bathymetry (Augmented) a research project that aims to understand the hydro-sedimentary dynamics related to the propagation of a tidal bore in internal estuaries. The author participates in WP5: Theoretical modeling and numerical simulations. In WP5, we will attempt to address numerically the question of characterizing the hydrodynamic processes and regimes having the largest potential impact on morphological modifications. The work by [49] has highlighted the existence of two modes of propagation of a bore, of which one is essentially hydrostatic, the other fully non-hydrostatic. The second mode involving vertical kinematics of much larger magnitudes is clearly more prone to produce particle suspensions and may be more interesting for morphodynamical changes. Note that these modes have been not only produced in numerical models but observed in measurements in artificial and natural environments [257, 25].

Additionally, it's essential to consider the dynamics of vorticity and its interaction with the boundary layers, which play a crucial role in the actual morphological changes caused by the bore. To address these issues, WP5 introduces additional layers of depth to the hierarchy of investigation tools used in BABA. Specifically, to complement laboratory and in situ measurements, we will employ three families of models with increasing fidelity.

The author, a postdoctoral student, and DR Mario Ricchiuto from the Cardamom team will handle the lowest fidelity level, represented by depth-integrated models. We will utilize the solver SLOWS, as referenced in [138] and [49]. This model has the advantage of a reduced computational cost, which should allow its application for all cases, including the in situ ones covered in other WPs.

5.2.9 Modeling of wave dispersion including porosity

We are currently working with Dr Nghi Vu Van from the Ho Chi Minh City University Of Transport in Vietnam on the simulation of dispersive waves in porous media. In our recent work [144] we introduced a conservative form of the extended Boussinesq equations for waves in porous media. This model can be used in both porous and non-porous media since it does not require any boundary condition at the interface between the porous and non-porous media. A hybrid Finite Volume/Finite Difference (FV/FD) scheme [135] is used to solve the conservative form of the extended Boussinesq equations for waves in porous media. The model is validated with experimental data for solitary waves interacting with porous structures and a porous dam break in a one-dimensional flow. At the moment, we are working on the two layer model with dispersion and porosity and the idea is to extend the model to 2HD.

Bibliography

- [1] MB Abbott, HM Petersen, and O Skovgaard. Computations of short waves in shallow water. In *Coastal Engineering 1978*, pages 414–433. 1978.
- [2] K.S. Abdol-Hamid. Assessments of k -Turbulence Model Based on Menter’s Modification to Rotta’s Two-Equation Model. *International Journal of Aerospace Engineering*, 2015, 2015. Article ID 987682, doi:10.1155/2015/987682.
- [3] Francisco Alcrudo and Pilar Garcia-Navarro. A high-resolution Godunov-type scheme in finite volumes for the 2D shallow-water equations. *International Journal for Numerical Methods in Fluids*, 16(6):489–505, 1993.
- [4] B. Alvarez-Samaniego and D. Lannes. A Nash-Moser theorem for singular evolution equations. Application to the Serre and Green-Naghdi equations. *Indiana University Mathematics Journal*, 57(1), 2008.
- [5] M Antuono, V Liapidevskii, and Maurizio Brocchini. Dispersive nonlinear shallow-water equations. *Studies in Applied Mathematics*, 122(1):1–28, 2009.
- [6] Luca Arpaia and Mario Ricchiuto. r - adaptation for shallow water flows: conservation, well balancedness, efficiency. *Computers & Fluids*, 160:175–203, 2018.
- [7] P. Bacigaluppi, M. Ricchiuto, and P. Bonneton. A 1D stabilized finite element model for non-hydrostatic wave breaking and run-up. In J. Fuhrmann, M. Ohlberger, and C. Rohde, editors, *Finite Volumes for Complex Applications VII*, volume 77 of *Springer Proceedings in Mathematics and Statistics*. Springer, 2014.
- [8] Paola Bacigaluppi, Mario Ricchiuto, and Philippe Bonneton. Implementation and evaluation of breaking detection criteria for a hybrid Boussinesq model. *Water waves*, 2(2):207–241, 2020.
- [9] Timothy Barth. Recent developments in high order k -exact reconstruction on unstructured meshes. In *31st Aerospace Sciences Meeting*, page 668, 1993.
- [10] Timothy Barth and Paul Frederickson. Higher order solution of the Euler equations on unstructured grids using quadratic reconstruction. In *28th aerospace sciences meeting*, page 13, 1990.

- [11] Timothy J Barth. Aspects of unstructured grids and finite-volume solvers for the Euler and Navier-Stokes equations. 1992.
- [12] T.J. Barth. Aspects of unstructured grids and finite-volume solvers for the Euler and Navier-Stokes equations. 1992. AGARD, Special Course on Unstructured Grid Methods for Advection Dominated Flows.
- [13] X Barthelemy, ML Banner, WL Peirson, F Fedele, M Allis, and F Dias. On a unified breaking onset threshold for gravity waves in deep and intermediate depth water. *Journal of Fluid Mechanics*, 841:463–488, 2018.
- [14] S Beji and Jurjen A Battjes. Numerical simulation of nonlinear wave propagation over a bar. *Coastal Engineering*, 23(1-2):1–16, 1994.
- [15] S. Beji and K. Nadaoka. A formal derivation and numerical modeling of the improved Boussinesq equations for varying depth. *Ocean Engineering*, 23:691–704, 1996.
- [16] S Beji and K Nadaoka. A formal derivation and numerical modelling of the improved Boussinesq equations for varying depth. *Ocean Engineering*, 23(8):691–704, 1996.
- [17] Michel Benoit, F Dias, J Herterich, and Yves-Marie Scolan. Un Cas-Test Discriminant pour la Simulation de la Propagation et du Run-up de Trains de vagues de Type Tsunami (A discriminating test case for simulating the propagation and run-up of a tsunami-like wave). In *Actes des 16èmes Journées de l’Hydrodynamique, proceedings of the 16th Hydrodynamics Days*, pages 1–14, Marseille, November 2018.
- [18] JCW Berkhoff, N Booy, and A C_ Radder. Verification of numerical wave propagation models for simple harmonic linear water waves. *Coastal Engineering*, 6(3):255–279, 1982.
- [19] A. Bermudez, A. Dervieux, J.-A.e Desideri, and M.E. Vazquez. Upwind schemes for the two-dimensional shallow water equations with variable depth using unstructured meshes. *Computer Methods in Applied Mechanics and Engineering*, 155(1):49–72, 1998.
- [20] A. Bermudez and M.E. Vazquez. Upwind methods for hyperbolic conservation laws with source terms. *Computers & Fluids*, 23(8):1049 – 1071, 1994.
- [21] Iooss Bertrand and Lemaître Paul. A review on global sensitivity analysis methods. *Operations Research/ Computer Science Interfaces Series*, 59:101–122, 2015.
- [22] Harsh Bhatia, Gregory Norgard, Valerio Pascucci, and Peer-Timo Bremer. The Helmholtz-Hodge decomposition—a survey. *IEEE Transactions on Visualization and Computer Graphics*, 19(8):1386–1404, 2013.
- [23] Daria Bolbot, Dimitrios Mitsotakis, and Athanasios E Tzavaras. Oscillatory and regularized shock waves for a modified Serre–Green–Naghdi system. *Studies in Applied Mathematics*, page e12694, 2024.

- [24] P. Bonneton. Modelling of periodic wave transformation in the inner surf zone. *Ocean Engineering*, 34(10):1459 – 1471, 2007.
- [25] P Bonneton, N Bonneton, J-P Parisot, and B Castelle. Tidal bore dynamics in funnel-shaped estuaries. *Journal of Geophysical Research: Oceans*, 120(2):923–941, 2015.
- [26] Philippe Bonneton, Florent Chazel, David Lannes, Fabien Marche, and Marion Tissier. A splitting approach for the fully nonlinear and weakly dispersive Green–Naghdi model. *Journal of Computational Physics*, 230(4):1479–1498, 2011.
- [27] Walter Boscheri, Maurizio Tavelli, and Cristóbal E Castro. An all Froude high order IMEX scheme for the shallow water equations on unstructured Voronoi meshes. *Applied Numerical Mathematics*, 185:311–335, 2023.
- [28] Umberto Bosi, Allan P Engsig-Karup, Claes Eskilsson, and Mario Ricchiuto. A spectral/hp element depth-integrated model for nonlinear wave–body interaction. *Computer Methods in Applied Mechanics and Engineering*, 348:222–249, 2019.
- [29] Joseph Boussinesq. Théorie des ondes et des remous qui se propagent le long d’un canal rectangulaire horizontal, en communiquant au liquide contenu dans ce canal des vitesses sensiblement pareilles de la surface au fond (Theory of waves and eddies propagating along a horizontal rectangular channel, imparting to the liquid contained therein similar velocities from the surface to bottom). *Journal de mathématiques pures et appliquées*, 17 :55–108, 1872.
- [30] Pierre Brenner. Unsteady flows about bodies in relative motion. In *1st AFOSR Conference on Dynamic Motion CFD Proceedings, Rutgers University, New Jersey, USA*, 1996.
- [31] S. Brenner and R. Scott. *The Mathematical Theory of Finite Element Methods*, volume 15 of *Texts in Applied Mathematics*. Springer, 2008.
- [32] Didier Bresch, David Lannes, and Guy Métivier. Waves interacting with a partially immersed obstacle in the boussinesq regime. *Analysis & PDE*, 14(4):1085–1124, 2021.
- [33] R Briganti, G Bellotti, R Musumeci, E Foti, and M Brocchini. Boussinesq Modelling of Breaking Waves: Description of Turbulence. In *Coastal Engineering 2004: (In 4 Volumes)*, pages 402–414. World Scientific, 2005.
- [34] R. Briganti, R. E. Musumeci, G. Belloti, M Brocchini, and E. Foti. Boussinesq modeling of breaking waves: Description of turbulence. *J. Geophys. Res.*, 109, 2004.
- [35] M. Brocchini and D.H. Peregrine. The dynamics of strong turbulence at free surfaces. part 2. free-surface boundary conditions. *J. Fluid Mech.*, 449:255–290, 2001.

- [36] Maurizio Brocchini. A reasoned overview on Boussinesq-type models: the interplay between physics, mathematics and numerics. *Proceedings of the Royal Society A: Mathematical, Physical and Engineering Sciences*, 469(2160):20130496, 2013.
- [37] Maurizio Brocchini, R Bernetti, Alessandro Mancinelli, and Gianni Albertini. An efficient solver for nearshore flows based on the WAF method. *Coastal Engineering*, 43(2):105–129, 2001.
- [38] Maurizio Brocchini and Nicholas Dodd. Nonlinear shallow water equation modeling for coastal engineering. *Journal of waterway, port, coastal, and ocean engineering*, 134(2):104–120, 2008.
- [39] P. Brufau, P. Garcia-Navarro, and M.E. Vazquez-Cendon. Zero mass error using unsteady wetting-drying conditions in shallow flows over dry irregular topography. *Int. J. Numer. Meth. Fluids*, 45:1047–1082, 2004.
- [40] P. Brufau, M. E. Vázquez-Cendón, and P. Gracia-Navarro. A numerical model for the flooding and drying of irregular domains. *Int. J. Numer. Meth. Fluids*, 39:247–275, 2002.
- [41] Saray Busto, Michael Dumbser, Cipriano Escalante, Nicolas Favrie, and Sergey Gavrilyuk. On high order adier discontinuous galerkin schemes for first order hyperbolic reformulations of nonlinear dispersive systems. *Journal of Scientific Computing*, 87(2):48, 2021.
- [42] Manuel J Castro and Carlos Parés. Well-balanced high-order finite volume methods for systems of balance laws. *Journal of Scientific Computing*, 82(2):48, 2020.
- [43] M.J. Castro, A.M. Ferreira Ferreira, J.A. Garcia-Rodriguez, J.M. Gonzalez-Vida, J. Macias, C. Pares, and M.E. Vazquez-Cendon. The numerical treatment of wet/dry fronts in shallow flows: application to one-layer and two-layer systems. *Mathematical and Computer Modelling*, 42(3-4):419 – 439, 2005.
- [44] M.J. Castro, J. Gonzalez-Vida, and C. Pares. Numerical treatment of wet/dry fronts in shallow flows with a Roe scheme. *Mathematical Models and Methods in Applied Sciences*, 16(6):897–931, 2006.
- [45] M.J. Castro, J.M. Gonzalez-Vida, and C. Pares. Numerical treatment of wet/dry fronts in shallow water flows with a modified Roe scheme. *Mathematical Models and Methods in Applied Sciences*, 16(6):897–931, 2006.
- [46] Oscar Castro-Orgaz and Hubert Chanson. Undular and broken surges in dam-break flows: a review of wave breaking strategies in a Boussinesq-type framework. *Environmental Fluid Mechanics*, 20:1383–1416, 2020.
- [47] Oscar Castro-Orgaz, Willi H Hager, and Francisco N Cantero-Chinchilla. Shallow flows over curved beds: Application of the Serre–Green–Naghdi theory to weir flow. *Journal of Hydraulic Engineering*, 148(1):04021053, 2022.

- [48] Oscar Castro-Orgaz, Willi H Hager, and Nikolaos D Katopodes. Variational models for nonhydrostatic free-surface flow: A unified outlook to maritime and open-channel hydraulics developments. *Journal of Hydraulic Engineering*, 149(7):04023014, 2023.
- [49] Rémi Chassagne, Andrea Gilberto Filippini, Mario Ricchiuto, and Philippe Bonneton. Dispersive and dispersive-like bores in channels with sloping banks. *Journal of Fluid Mechanics*, 870:595–616, 2019.
- [50] F. Chazel, D. Lannes, and F. Marche. Numerical simulation of strongly nonlinear and dispersive waves using a Green–Naghdi model. *Journal of Scientific Computing*, 48(1):105–116, 2011.
- [51] Qin Chen, James T Kirby, Robert A Dalrymple, Andrew B Kennedy, and Arun Chawla. Boussinesq modeling of wave transformation, breaking, and runup. II: 2D. *Journal of Waterway, Port, Coastal, and Ocean Engineering*, 126(1):48–56, 2000.
- [52] A. Chertock, S. Cui, A. Kurganov, and T. Wu. Steady State and Sign Preserving Semi-Implicit Runge-Kutta Methods for ODEs with Stiff Damping Term. *SIAM Journal on Numerical Analysis*, 53:2008–2029, 2015.
- [53] Vincent P Chiravalle and Nathaniel R Morgan. A 3D Lagrangian cell-centered hydrodynamic method with higher-order reconstructions for gas and solid dynamics. *Computers & Mathematics with Applications*, 78(2):298–317, 2019.
- [54] Mirco Ciallella, Davide Torlo, and Mario Ricchiuto. Arbitrary high order weno finite volume scheme with flux globalization for moving equilibria preservation. *Journal of Scientific Computing*, 96(2):53, 2023.
- [55] P.G. Ciarlet. *The finite element method for elliptic problems*, volume 4 of *Studies in Mathematics and its Applications*. North-Holland Publishing Co., 1978.
- [56] Rodrigo Cienfuegos, Eric Barthélemy, and Philippe Bonneton. A fourth-order compact finite volume scheme for fully nonlinear and weakly dispersive Boussinesq-type equations. Part I: model development and analysis. *International Journal for Numerical Methods in Fluids*, 51(11):1217–1253, 2006.
- [57] Rodrigo Cienfuegos, Eric Barthélemy, and Philippe Bonneton. A fourth-order compact finite volume scheme for fully nonlinear and weakly dispersive Boussinesq-type equations. Part II: boundary conditions and validation. *International Journal for Numerical Methods in Fluids*, 53(9):1423–1455, 2007.
- [58] Rodrigo Cienfuegos, Eric Barthélemy, and Philippe Bonneton. Wave-breaking model for Boussinesq-type equations including roller effects in the mass conservation equation. *Journal of waterway, port, coastal, and ocean engineering*, 136(1):10–26, 2010.

- [59] Didier Clamond, Denys Dutykh, and Dimitrios Mitsotakis. Conservative modified Serre–Green–Naghdi equations with improved dispersion characteristics. *Communications in Nonlinear Science and Numerical Simulation*, 45:245–257, 2017.
- [60] M. Costabel and M. Dauge. Weighted regularization of maxwell equations in polyhedral domains. a rehabilitation of nodal finite elements. *Numerische Mathematik*, 93:239–277, 2002.
- [61] Martin Costabel. A coercive bilinear form for Maxwell’s equations. *Journal of Mathematical Analysis and Applications*, 157(2):527–541, 1991.
- [62] AI Delis and M Kazolea. Finite volume simulation of waves formed by sliding masses. *International Journal for Numerical Methods in Biomedical Engineering*, 27(5):732–757, 2011.
- [63] AI Delis, Maria Kazolea, and NA Kampanis. A robust high-resolution finite volume scheme for the simulation of long waves over complex domains. *International Journal for Numerical Methods in Fluids*, 56(4):419–452, 2008.
- [64] Anargiros I Delis, Maria Kazolea, and Maria Gaitani. On the numerical solution of sparse linear systems emerging in finite volume discretizations of 2D Boussinesq-type models on unstructured grids. *Water*, 14(21):3584, 2022.
- [65] Anargiros I Delis, IK Nikolos, and M Kazolea. Performance and comparison of cell-centered and node-centered unstructured finite volume discretizations for shallow water free surface flows. *Archives of Computational Methods in Engineering*, 18(1):57–118, 2011.
- [66] A. Demirbilek, Z. Zundel and O. Nwogu. Boussinesq modeling of wave propagation and runup over fringing coral reefs, model evaluation report. coastal and hydraulics laboratory technical note chltr0712. vicksburg. IMS: U.S. Army Engineer Research and Development Center, 2007.
- [67] Zeki Demirbilek, Okey G. Nwogu, et al. Boussinesq modeling of wave propagation and runup over fringing coral reefs, model evaluation report. 2007.
- [68] Morteza Derakhti and James T Kirby. Bubble entrainment and liquid–bubble interaction under unsteady breaking waves. *Journal of fluid mechanics*, 761:464–506, 2014.
- [69] Morteza Derakhti, James T Kirby, Michael L Banner, Stephan T Grilli, and Jim Thomson. A unified breaking onset criterion for surface gravity water waves in arbitrary depth. *Journal of Geophysical Research: Oceans*, 125(7):e2019JC015886, 2020.
- [70] DHI. MIKE 21 Boussinesq waves module—Scientific Documentation. 2008.

- [71] Giacomo Dimarco, Raphaël Loubère, Victor Michel-Dansac, and Marie-Hélène Vignal. Second-order implicit-explicit total variation diminishing schemes for the Euler system in the low Mach regime. *Journal of Computational Physics*, 372:178–201, 2018.
- [72] Maarten W Dingemans. *Water wave propagation over uneven bottoms: Linear wave propagation*, volume 13. World Scientific, 2000.
- [73] M.W. Dingemans. *Water wave propagation over uneven bottoms*. Advanced Series on Ocean Engineering. 1997.
- [74] JS Antunes Do Carmo, FJ Seabra Santos, and AB Almeida. Numerical solution of the generalized Serre equations with the MacCormack finite-difference scheme. *International journal for numerical methods in fluids*, 16(8):725–738, 1993.
- [75] JS Antunes Do Carmo, FJ Seabra Santos, and E Barthélemy. Surface waves propagation in shallow water: a finite element model. *International Journal for Numerical Methods in Fluids*, 16(6):447–459, 1993.
- [76] D.A. Dunavant. High degree efficient symmetrical Gaussian quadrature rules for the triangle. *Int. J. Numer. Methods in Engrg.*, 21:1129–1148, 1985.
- [77] A. Duran. Tsunami propagation: numerical issues 1. well balancedness, positivity preservation, high order of accuracy. 2016.
- [78] A. Duran. Tsunami propagation: Numerical issues 1. well balancedness, positivity preservation, high order of accuracy. In *TANDEM and DEFIS LITTORAL Tsunami school*, Bordeaux, France, 2016.
- [79] A. Duran, F. Marche, and Q. Liang. On the well-balanced numerical discretization of shallow water equations on unstructured meshes. *J. Comput. Phys*, 235:565–586, 2013.
- [80] Arnaud Duran and Fabien Marche. A discontinuous Galerkin method for a new class of Green–Naghdi equations on simplicial unstructured meshes. *Applied Mathematical Modelling*, 45:840–864, 2017.
- [81] Walid El Asmar and Okey Nwogu. Finite volume solution of Boussinesq-type equations on an unstructured grid. In *Coastal Engineering 2006: (In 5 Volumes)*, pages 73–85. World Scientific, 2007.
- [82] A. Elnaggar, Z. Watanabe. Nonlinear Wave Dynamics in Surf and Swash Zones. In *Proceedings 27th International Conference on Coastal Engineering*, 2000.
- [83] Zakaria Elnaggar and Akira Watanabe. Nonlinear wave dynamics in surf and swash zones. In *Coastal Engineering 2000*, pages 664–677. 2001.

- [84] Allan P Engsig-Karup, Jan S Hesthaven, Harry B Bingham, and Tim Warburton. DG-FEM solution for nonlinear wave-structure interaction using Boussinesq-type equations. *Coastal Engineering*, 55(3):197–208, 2008.
- [85] K. S. Erduran, S. Ilic, and V. Kutija. Hybrid finite-volume finite-difference scheme for the solution of Boussinesq equations. *Int. J. Numer. Methods Fluids*, 49:1213–1232, 2005.
- [86] Schulz Eric, Speekenbrink Maarten, and Krause Andreas. A tutorial on Gaussian process regression: Modelling, exploring, and exploiting functions. *Journal of Mathematical Psychology*, 85:1–16, 2018.
- [87] A. Ern and J.-L. Guermond. *Theory and practice of finite elements*, volume 159 of *Applied Mathematical Sciences*. Springer, 2004.
- [88] Claes Eskilsson, SJ Sherwin, and Lars Bergdahl. An unstructured spectral/hp element model for enhanced Boussinesq-type equations. *Coastal Engineering*, 53(11):947–963, 2006.
- [89] P. Lynett *et al.* Coulwave website: http://isec.nacse.org/models/coulwave_description 2004.
- [90] Henry Favre. Etude theorique et experimental des ondes de translation dans les canaux decouverts (Theoretical and experimental study of translational waves in open channels). In Dunod, editor, *Publications du laboratoire de recherches hydrauliques annexé à l'Ecole polytechnique fédérale de Zurich*, volume 150, pages 205–209 . Dunod, Paris, 1935.
- [91] A.G. Filippini, L Arpaia, and P et al. Vincent. On an efficient operational high order DG tool for shallow water flows and coastal hazard predictions. 2024.
- [92] Andrea G Filippini, Maria Kazolea, and Mario Ricchiuto. A flexible 2D nonlinear approach for nonlinear wave propagation, breaking and run up. In *ISOPE International Ocean and Polar Engineering Conference*, pages ISOPE–I. ISOPE, 2017.
- [93] Andrea Gilberto Filippini. *Free surface flow simulation in estuarine and coastal environments: numerical development and application on unstructured meshes*. PhD thesis, Bordeaux, 2016.
- [94] Andrea Gilberto Filippini, Luca Arpaia, Vincent Perrier, Rodrigo Pedreros, Philippe Bonneton, David Lannes, Fabien Marche, Sebastien De Brye, Simon Delmas, Sophie Lecacheux, et al. An operational discontinuous galerkin shallow water model for coastal flood assessment. Available at SSRN 4808242.
- [95] Andrea Gilberto Filippini, Stevan Bellec, Mathieu Colin, and Mario Ricchiuto. On the nonlinear behaviour of Boussinesq type models: Amplitude-velocity vs amplitude-flux forms. *Coastal Engineering*, 99:109–123, 2015.

- [96] Andrea Gilberto Filippini, Sébastien De Brye, Vincent Perrier, Fabien Marche, Mario Ricchiuto, David Lannes, and Philippe Bonneton. UHAINA: A parallel high performance unstructured near-shore wave model. In *Journées Nationales Génie Côtier-Génie Civil*, volume 15, pages 47–56. Editions Paralia, 2018.
- [97] Andrea Gilberto Filippini, Maria Kazolea, and Mario Ricchiuto. A flexible genuinely nonlinear approach for nonlinear wave propagation, breaking and run-up. *Journal of Computational Physics*, 310:381–417, 2016.
- [98] U.S. Fjordholm, S. Mishra, and E. Tadmor. Well-balanced and energy stable schemes for the shallow water equations with discontinuous topography. *Journal of Computational Physics*, 230(14):5587 – 5609, 2011.
- [99] Maria Fotia. *Wave breaking onset and dissipation in a fully non-linear, staggered grid Boussinesq model*. PhD thesis, University of Delaware, Department of Civil and Environmental Engineering, 2023.
- [100] Elena Gaburro, Walter Boscheri, Simone Chiocchetti, and Mario Ricchiuto. Discontinuous galerkin schemes for hyperbolic systems in non-conservative variables: quasi-conservative formulation with subcell finite volume corrections. *arXiv preprint arXiv:2406.15644*, 2024.
- [101] José Galaz. *Coupling methods of phase-resolving coastal wave models*. PhD thesis, Université de montpellier, 2024.
- [102] Jose Galaz, Maria Kazolea, and Antoine Rousseau. Coupling dispersive shallow water models by deriving asymptotic interface operators. In Zdeněk Dostál, Tomáš Kozubek, Axel Klawonn, Ulrich Langer, Luca F. Pavarino, Jakub Šístek, and Olof B. Widlund, editors, *Domain Decomposition Methods in Science and Engineering XXVII*, pages 181–188, Cham, 2024. Springer Nature Switzerland.
- [103] Francesco Gallerano, Giovanni Cannata, and Mara Villani. An integral contravariant formulation of the fully non-linear Boussinesq equations. *Coastal Engineering*, 83:119–136, 2014.
- [104] Sergey Gavrilyuk and Christian Klein. Numerical study of the serre–green–naghdi equations in 2d. *Nonlinearity*, 37(4):045014, 2024.
- [105] Sergey Gavrilyuk and Keh-Ming Shyue. 2D Serre-Green-Naghdi Equations over Topography: Elliptic Operator Inversion Method. *Journal of Hydraulic Engineering*, 150(1):04023054, 2024.
- [106] SL Gavrilyuk, V Yu Liapidevskii, and AA Chesnokov. Spilling breakers in shallow water: applications to favre waves and to the shoaling and breaking of solitary waves. *Journal of Fluid Mechanics*, 808:441–468, 2016.

- [107] Irene Gómez-Bueno, Manuel Jesús Castro Díaz, Carlos Parés, and Giovanni Russo. Collocation methods for high-order well-balanced methods for systems of balance laws. *Mathematics*, 9(15):1799, 2021.
- [108] S. Gottlieb, C.-W. Shu, and E. Tadmor. Strong stability-preserving high-order time discretization methods. *SIAM Review*, (1):89–112, 2001.
- [109] Albert E Green and Paul M Naghdi. A derivation of equations for wave propagation in water of variable depth. *Journal of Fluid Mechanics*, 78(2):237–246, 1976.
- [110] ST Grilli, R Subramanya, IA Svendsen, and J Veeramony. Shoaling of solitary waves on plane beaches. *Oceanographic Literature Review*, 8(42):608, 1995.
- [111] Stephan T Grilli, Miguel A Losada, and Francisco Martin. Characteristics of solitary wave breaking induced by breakwaters. *Journal of Waterway, Port, Coastal, and Ocean Engineering*, 120(1):74–92, 1994.
- [112] Stéphan T Grilli and Ravishankar Subramanya. Numerical modeling of wave breaking induced by fixed or moving boundaries. *Computational Mechanics*, 17(6):374–391, 1996.
- [113] Jean-Luc Guermond, Chris Kees, Bojan Popov, and Eric Tovar. Hyperbolic relaxation technique for solving the dispersive Serre–Green–Naghdi equations with topography. *Journal of Computational Physics*, 450:110809, 2022.
- [114] Hervé Guillard and Cécile Viozat. On the behaviour of upwind schemes in the low Mach number limit. *Computers & fluids*, 28(1):63–86, 1999.
- [115] L. Hagg and M. Berggren. On the well-posedness of Galbrun’s equation. *Journal de Mathématiques Pures et Appliquées*, 150:112–133, 2021.
- [116] Ali Haidar, Fabien Marche, and Francois Vilar. A posteriori finite-volume local subcell correction of high-order discontinuous Galerkin schemes for the nonlinear shallow-water equations. *Journal of Computational Physics*, 452:110902, 2022.
- [117] Florian Haider. *Discrétisation en maillage non structuré général et applications LES*. PhD thesis, 2009.
- [118] Florian Haider, Pierre Brenner, Bernard Courbet, and Jean-Pierre Croisille. Efficient implementation of high order reconstruction in finite volume methods. In *Finite Volumes for Complex Applications VI Problems & Perspectives*, pages 553–560. Springer, 2011.
- [119] Florian Haider, Bernard Courbet, and Jean-Pierre Croisille. A high-order compact reconstruction for finite volume methods: the one-dimensional case. 2015.
- [120] J. B. Hansen and I. A. Svendsen. Regular waves in shoaling water: experimental data. Technical Report, ISVA Series Paper 21, 1979.

- [121] A. Harten. On the symmetric form of systems of conservation laws with entropy. *J. Comput. Phys.*, 49:151–164, 1983.
- [122] H el ene H ebert. Project TANDEM (Tsunamis in the Atlantic and the English Channel: Definition of the Effects through numerical Modeling) (2014-2017): main results and perspectives. In *EGU General Assembly Conference Abstracts*, EGU General Assembly Conference Abstracts, page 9511, April 2018.
- [123] H. Helmholtz. Uber integrale der hydrodynamischen gleichungen, welche den wirbelbewegungen entsprechen. *J.fur die reine und angewandte Mathematik*, 1858(55):25–55, 1858.
- [124] H. Helmholtz. On integrals of the hydrodynamical equations, which express vortex-motion. *Philosophical Magazine and J. Science*, 33(226):485–512, 1867.
- [125] M. E. Hubbard and P. Garc ıa-Navarro. Flux difference splitting and the balancing of source terms and flux gradients. *J. Comp. Phys.*, 165:89–125, 2000.
- [126] T.J.R. Hughes, G. Scovazzi, and T. Tezduyar. Stabilized methods for compressible flows. *J. Sci. Comp.*, 43:343–368, 2010.
- [127] W. Hundsdorfer, S. J. Ruuth, and R. J. Spiteri. Monotonicity-preserving linear multistep methods. *SIAM Journal on Numerical Analysis*, 41:605–623, 2003.
- [128] W. Hundsdorfer and J.G Verwer. Numerical solution of time-dependent advection-diffusion-reaction equations. In *Springer Series in Comput. Math.* Springer, 2003.
- [129] S. M. Joshi, M. Kazolea, and M. Ricchiuto. Parameter sensitivity for wave-breaking closures in Boussinesq-type models. *Water Waves*, 4(3):491–515, 2022.
- [130] B Jouy, D Violeau, M Ricchiuto, and M Le. One dimensional modelling of Favre waves in channels. *Applied Mathematical Modelling*, 2024.
- [131] Th V Karambas and Christoforos Koutitas. A breaking wave propagation model based on the Boussinesq equations. *Coastal Engineering*, 18(1-2):1–19, 1992.
- [132] Theodoros Katsaounis, Dimitrios Mitsotakis, and George Sadaka. Boussinesq-Peregrine water wave models and their numerical approximation. *Journal of Computational Physics*, page 109579, 2020.
- [133] Maria Kazakova and Pascal Noble. Discrete transparent boundary conditions for the linearized Green–Naghdi system of equations. *SIAM Journal on Numerical Analysis*, 58(1):657–683, 2020.
- [134] Maria Kazakova and Ga el Lo ic Richard. A new model of shoaling and breaking waves: one-dimensional solitary wave on a mild sloping beach. *Journal of Fluid Mechanics*, 862:552–591, 2019.

- [135] M Kazolea and AI Delis. A well-balanced shock-capturing hybrid finite volume–finite difference numerical scheme for extended 1d Boussinesq models. *Applied Numerical Mathematics*, 67:167–186, 2013.
- [136] M Kazolea, AI Delis, IK Nikolos, and CE Synolakis. An unstructured finite volume numerical scheme for extended 2d Boussinesq-type equations. *Coastal Engineering*, 69:42–66, 2012.
- [137] M Kazolea, Argiris I Delis, and Costas E Synolakis. Numerical treatment of wave breaking on unstructured finite volume approximations for extended Boussinesq-type equations. *Journal of computational Physics*, 271:281–305, 2014.
- [138] M Kazolea, AG Filippini, and M Ricchiuto. Low dispersion finite volume/element discretization of the enhanced Green–Naghdi equations for wave propagation, breaking and runup on unstructured meshes. *Ocean Modelling*, 182:102157, 2023.
- [139] Maria Kazolea. *Mathematical and computational modeling for the generation and propagation of waves in marine and coastal environments*. PhD thesis, 2013.
- [140] Maria Kazolea and AI Delis. Irregular wave propagation with a 2DH Boussinesq-type model and an unstructured finite volume scheme. *European Journal of Mechanics-B/Fluids*, 72:432–448, 2018.
- [141] Maria Kazolea, Andrea Filippini, Mario Ricchiuto, Stéphane Abadie, M Martin Medina, Denis Morichon, Camille Journeau, Richard Marcer, Kévin Pons, Sylvestre LeRoy, et al. Wave propagation, breaking, and overtopping on a 2D reef: A comparative evaluation of numerical codes for tsunami modelling. *European Journal of Mechanics-B/Fluids*, 73:122–131, 2019.
- [142] Maria Kazolea, Subodh Joshi, and Mario Ricchiuto. Sensitivity analysis for two wave breaking models used by the Green-Naghdi equation. In *WCCM-ECCOMASS 2020-14th World Congress in Computational Mechanics and Ecomass Congress 2020*, 2021.
- [143] Maria Kazolea, N Kalligeris, Nikolaos Maravelakis, CE Synolakis, Argiris I Delis, and Patrick Lynett. Numerical study of wave conditions for the old Venetian harbor of Chania in Crete, Greece. In *Proc., 36th IAHR World Congress*, 2015.
- [144] Maria Kazolea, Changhoon Lee, et al. A hybrid FV/FD scheme for a novel conservative form of extended Boussinesq equations for waves in porous media. *Ocean Engineering*, 269:113491, 2023.
- [145] Maria Kazolea and Mario Ricchiuto. On wave breaking for Boussinesq-type models. *Ocean Modelling*, 123:16–39, 2018.
- [146] Maria Kazolea and Mario Ricchiuto. Full nonlinearity in weakly dispersive Boussinesq models: Luxury or necessity. *Journal of Hydraulic Engineering*, 150(1):04023061, 2024.

- [147] Andrew B Kennedy, Qin Chen, James T Kirby, and Robert A Dalrymple. Boussinesq modeling of wave transformation, breaking, and runup. I: 1D. *Journal of waterway, port, coastal, and ocean engineering*, 126(1):39–47, 2000.
- [148] M. J. Kermani, A. G. Geber, and J. M. Stockie. Thermodynamically based moisture prediction using Roe’s scheme. In *The 4th Conference of Iranian AeroSpace Society*, 2003. Amir Kabir University of Technology, Tehran, Iran, January.
- [149] Dae-Hong Kim, Patrick J Lynett, and Scott A Socolofsky. A depth-integrated model for weakly dispersive, turbulent, and rotational fluid flows. *Ocean Modelling*, 27(3-4):198–214, 2009.
- [150] James T Kirby. Boussinesq models and their application to coastal processes across a wide range of scales. *Journal of Waterway, Port, Coastal, and Ocean Engineering*, 142(6):03116005, 2016.
- [151] James T Kirby, Ge Wei, Qin Chen, Andrew B Kennedy, and Robert A Dalrymple. FUNWAVE 1.0: fully nonlinear Boussinesq wave model-Documentation and user’s manual. *research report NO. CACR-98-06*, 1998.
- [152] J.T. Kirby. B’waves 2014 conference: open discussion session. 2014.
- [153] G.Th. Klonaris, C.D. Memos, and Th.V. Karambas. A boussinesq-type model including wave-breaking terms in both continuity and momentum equations. *Ocean Engineering*, 57:128 – 140, 2013.
- [154] J. Klosa. Extrapolated BDF residual distribution schemes for the shallow water equations. Master thesis, 2012.
- [155] D. Lannes and P. Bonneton. Derivation of asymptotic two-dimensional time-dependent equations for surface water wave propagation. *Physics of Fluids*, 21, 2009. 016601 doi:10.1063/1.3053183.
- [156] D Lannes and L Weynans. Generating boundary conditions for a Boussinesq system. *Nonlinearity*, 33(12):6868, 2020.
- [157] David Lannes. *The water waves problem: mathematical analysis and asymptotics*, volume 188. American Mathematical Soc., 2013.
- [158] David Lannes. Modeling shallow water waves. *Nonlinearity*, 33(5):R1, 2020.
- [159] David Lannes and Fabien Marche. A new class of fully nonlinear and weakly dispersive Green–Naghdi models for efficient 2D simulations. *Journal of Computational Physics*, 282:238–268, 2015.

- [160] David Lannes and Mathieu Rigal. General boundary conditions for a Boussinesq model with varying bathymetry. *arXiv preprint arXiv:2402.03859*, 2024.
- [161] David Lannes and Lisl Weynans. Generating boundary conditions for a boussinesq system. *Nonlinearity*, 33(12):6868, 2020.
- [162] C. Lataniotis, D. Wicaksono, S. Marelli, and B. Sudret. UQLab user manual – Kriging (Gaussian process modeling). Technical report, Chair of Risk, Safety and Uncertainty Quantification, ETH Zurich, Switzerland, 2019. Report # UQLab-V1.3-105.
- [163] Randall J LeVeque. *Finite volume methods for hyperbolic problems*, volume 31. Cambridge university press, 2002.
- [164] Maojun Li, Liwei Xu, and Yongping Cheng. A CDG-FE method for the two-dimensional Green-Naghdi model with the enhanced dispersive property. *Journal of Computational Physics*, 399:108953, 2019.
- [165] YS Li, S-X Liu, Y-X Yu, and G-Z Lai. Numerical modeling of Boussinesq equations by finite element method. *Coastal Engineering*, 37(2):97–122, 1999.
- [166] Q. Liang and A. G. L. Borthwick. Adaptive quadtree simulation of shallow flows with wet/dry front over complex topography. *Comput. Fluids*, 38:221–234, 2009.
- [167] Yeh H. Synolakis C. Liu, P.L.-F. Advanced numerical models for simulating tsunami waves and runup. *Adv. Coast. Ocean Engng.*, 10, 2008.
- [168] Ralph Lteif. An operator-splitting approach with a hybrid finite volume/finite difference scheme for extended Boussinesq models. *Applied Numerical Mathematics*, 196:159–182, 2024.
- [169] Aaron TL Lun. basilisk: a bioconductor package for managing python environments. *The Journal of Open Source Software*, 7(79):4742, 2022.
- [170] P. J. Lynett, T. R. Wu, and P. L. F. Liu. Modeling wave runup with depth integrated equations. *Coastal Eng.*, 46:98–107, 2002.
- [171] Patrick J Lynett. Nearshore wave modeling with high-order Boussinesq-type equations. *Journal of waterway, port, coastal, and ocean engineering*, 132(5):348–357, 2006.
- [172] Patrick J Lynett, L-F Liu Philip, Khairil Irfan Sitanggang, and Dae-Hong Kim. Modeling Wave Generation, Evolution, and Interaction with Depth-Integrated, Dispersive Wave Equations. COULWAVE Code Manual , 2008. Long and Intermediate Wave Modeling Package.
- [173] Brocchini M. Free surface boundary conditions at a bubbly/weakly splashing air-water interface. *Physics of fluids*, 14:1834–1840, 2002.

- [174] Sobol I. M. Sensitivity estimates for non linear mathematical models. *Mathematical Modelling and Computational Experiments*, (1):407–414, 1993.
- [175] Sobol I. M. Global sensitivity indices for nonlinear mathematical models and their Monte Carlo estimates. *Mathematics and Computers in Simulation*, 55:271–280, 2001.
- [176] Per A Madsen, Harry B Bingham, and Hua Liu. A new Boussinesq method for fully nonlinear waves from shallow to deep water. *Journal of Fluid Mechanics*, 462:1–30, 2002.
- [177] Per A Madsen, Russel Murray, and Ole R Sørensen. A new form of the Boussinesq equations with improved linear dispersion characteristics. *Coastal engineering*, 15(4):371–388, 1991.
- [178] Per A Madsen and Ole R Sørensen. A new form of the Boussinesq equations with improved linear dispersion characteristics. Part 2. A slowly-varying bathymetry. *Coastal Engineering*, 18(3-4):183–204, 1992.
- [179] Per A Madsen, OR Sørensen, and HA Schäffer. Surf zone dynamics simulated by a Boussinesq type model. Part i. Model description and cross-shore motion of regular waves. *Coastal Engineering*, 32(4):255–287, 1997.
- [180] Per A Madsen, OR Sørensen, and HA Schäffer. Surf zone dynamics simulated by a Boussinesq type model. Part ii: Surf beat and swash oscillations for wave groups and irregular waves. *Coastal engineering*, 32(4):289–319, 1997.
- [181] Yogiraj Mantri, Philipp Öffner, and Mario Ricchiuto. Fully well-balanced entropy controlled discontinuous galerkin spectral element method for shallow water flows: global flux quadrature and cell entropy correction. *Journal of Computational Physics*, 498:112673, 2024.
- [182] Fabien Marche. Combined hybridizable discontinuous Galerkin (HDG) and Runge-Kutta discontinuous Galerkin (RK-DG) formulations for Green-Naghdi equations on unstructured meshes. *Journal of Computational Physics*, 418:109637, 2020.
- [183] Stefano Marelli and Bruno Sudret. UQLab: A framework for uncertainty quantification in Matlab. In *Vulnerability, uncertainty, and risk: quantification, mitigation, and management*, pages 2554–2563. 2014.
- [184] Andreas Meister and Sigrun Ortleb. A positivity preserving and well-balanced DG scheme using finite volume subcells in almost dry regions. *Applied Mathematics and Computation*, 272:259–273, 2016.
- [185] Lorenzo Melito, Matteo Antuono, and Maurizio Brocchini. From boussinesq-type to quasi-3d models: A comparative analysis. *Journal of Hydraulic Engineering*, 149(8):04023025, 2023.
- [186] Amadine Menasaria. *Accurate and efficient models for the simulation of wall bounded flows*. PhD thesis, Arts et Métiers Paris Tech-Centre de Paris, 2019.

- [187] F. R. Menter and Y. Egorov. The scale-adaptive simulation method for unsteady turbulent flow predictions. part 1: Theory and model description. *Flow, Turbulence and Combustion*, 85(1):113–138, 2010.
- [188] Christopher Michalak and Carl Ollivier-Gooch. Accuracy preserving limiter for the high-order accurate solution of the Euler equations. *Journal of Computational Physics*, 228(23):8693–8711, 2009.
- [189] S.K. Misra, M. Brocchini, and J.T. Kirby. Turbulent interfacial boundary conditions for spilling breakers. In *Proceedings of the Coastal Engineering Conference*, 2007.
- [190] Dimitrios Mitsotakis, Boaz Ilan, and Denys Dutykh. On the Galerkin/finite-element method for the Serre equations. *Journal of Scientific Computing*, 61(1):166–195, 2014.
- [191] Pranab K Mohapatra and M Hanif Chaudhry. Numerical solution of Boussinesq equations to simulate dam-break flows. *Journal of Hydraulic Engineering*, 130(2):156–159, 2004.
- [192] Joaquin P Moris, Patricio A Catalán, and Rodrigo Cienfuegos. Incorporating wave-breaking data in the calibration of a Boussinesq-type wave model. *Coastal Engineering*, 168:103945, 2021.
- [193] J. Murillo, P. Garcia-Navarro, and J. Burguete. Time step restrictions for well-balanced shallow water solutions in non-zero velocity steady states. *Int. J. for Num. Meth. Fluids*, 60:1351, 2009.
- [194] J. Murillo, P. Garcia-Navarro, J. Burguete, and P. Brufau. The influence of source terms on stability, accuracy and conservation in two-dimensional shallow flow simulation using triangular finite volumes. *Int. J. for Numer. Methods in Fluids*, 54:543, 2007.
- [195] I. K. Nikolos and A. I. Delis. An unstructured node-centered finite volume scheme for shallow water flows with wet/dry fronts over complex topography. *Comput. Methods Appl. Mech. Engrg*, 198:3723–3750, 2009.
- [196] Sebastian Noelle, Martin Parisot, and Tabea Tscherpel. A class of boundary conditions for time-discrete Green–Naghdi equations with bathymetry. *SIAM Journal on Numerical Analysis*, 60(5):2681–2712, 2022.
- [197] O.G. Nwogu and Z. Demirbilek. BOUSS-2D: A Boussinesq Wave Model for Coastal Regions and Harbors". US Army Corps of Engineers, Engineering Research and Development Center - Report TR-01-25, September 2001.
- [198] Okey Nwogu. Alternative form of Boussinesq equations for nearshore wave propagation. *Journal of Waterway, Port, Coastal, and Ocean Engineering*, 119(6):618–638, 1993.
- [199] Okey NWOGU. Numerical prediction of breaking waves and currents with a Boussinesq. In *Proc. 25th Int. Conf. on Coastal Eng., ASCE*, pages 4807–4819, 1996.

- [200] Takashi Okamoto and David R Basco. The Relative Trough Froude Number for initiation of wave breaking: Theory, experiments and numerical model confirmation. *Coastal Engineering*, 53(8):675–690, 2006.
- [201] Carl F. Ollivier-Gooch. Quasi-ENO schemes for unstructured meshes based on unlimited data-dependent least-squares reconstruction. *Journal of Computational Physics*, 133(1):6–17, 1997.
- [202] Nishant Panda, Clint Dawson, Yao Zhang, Andrew B. Kennedy, Joannes J. Westerink, and Aaron S. Donahue. Discontinuous Galerkin methods for solving Boussinesq–Green–Naghdi equations in resolving non-linear and dispersive surface water waves. *Journal of Computational Physics*, 273:572–588, 2014.
- [203] Christos E Papoutsellis, Marissa L Yates, Bruno Simon, and Michel Benoit. Modelling of depth-induced wave breaking in a fully nonlinear free-surface potential flow model. *Coastal Engineering*, 154:103579, 2019.
- [204] Carlos Parés and Carlos Parés-Pulido. Well-balanced high-order finite difference methods for systems of balance laws. *Journal of Computational Physics*, 425:109880, 2021.
- [205] M. Parisot. Entropy-satisfying scheme for a hierarchy of dispersive reduced models of free surface flow. *International Journal for Numerical Methods in Fluids*, 91(10):509–531, 2019.
- [206] Martin Parisot. Entropy-satisfying scheme for a hierarchy of dispersive reduced models of free surface flow. *International Journal for Numerical Methods in Fluids*, 91(10):509–531, 2019.
- [207] Martin Parisot. Thick interfaces coupling technique for weakly dispersive models of waves. 2024.
- [208] Martin Parisot and Jean-Paul Vila. Centered-potential regularization for the advection upstream splitting method. *SIAM Journal on Numerical Analysis*, 54(5):3083–3104, 2016.
- [209] Hyongsu Park, Daniel T Cox, Patrick J Lynett, Dane M Wiebe, and Sungwon Shin. Tsunami inundation modeling in constructed environments: A physical and numerical comparison of free-surface elevation, velocity, and momentum flux. *Coastal Engineering*, 79:9–21, 2013.
- [210] M. Parsani, D.I. Ketcheson, and W. Deconinck. Optimized explicit Runge–Kutta schemes for the spectral difference method applied to wave propagation problems. *SIAM Journal on Scientific Computing*, (2):A957–A986, 2013.
- [211] D Howell Peregrine. Calculations of the development of an undular bore. *Journal of Fluid Mechanics*, 25(2):321–330, 1966.
- [212] D Howell Peregrine. Long waves on a beach. *Journal of Fluid Mechanics*, 27(4):815–827, 1967.

- [213] Marc Perlin, Wooyoung Choi, and Zhigang Tian. Breaking waves in deep and intermediate waters. *Annual review of fluid mechanics*, 45:115–145, 2013.
- [214] Jordan P.A. Pitt, Christopher Zoppou, and Stephen G. Roberts. Numerical scheme for the generalised Serre–Green–Naghdi model. *Wave Motion*, 115:103077, 2022.
- [215] Grégoire Pont, Pierre Brenner, Paola Cinnella, Bruno Maugars, and Jean-Christophe Robinet. Multiple-correction hybrid k-exact schemes for high-order compressible RANS-LES simulations on fully unstructured grids. *Journal of Computational Physics*, 350:45–83, 2017.
- [216] S. B. Pope. *Turbulent Flows*. Cambridge University Press, Cambridge, 2003.
- [217] Stéphane Popinet. A quadtree-adaptive multigrid solver for the Serre–Green–Naghdi equations. *Journal of Computational Physics*, 302:336–358, 2015.
- [218] L.L.J. Pratt and J.A. Whitehead. *Rorating Hydraulics*, volume 36 of *Atmospheric and Oceanographic Sciences Library*. Springer-Verlag, New-York, 2007.
- [219] M. Ricchiuto. An explicit residual based approach for shallow water flows. *J.Comput.Phys.*, 80:306–344, 2015.
- [220] M. Ricchiuto. An explicit residual based approach for shallow water flows. *Journal of Computational Physics*, 280:306–344, 2015.
- [221] Mario Ricchiuto and Andreas Bollermann. Stabilized residual distribution for shallow water simulations. *Journal of Computational Physics*, 228(4):1071–1115, 2009.
- [222] Mario Ricchiuto and Andrea Gilberto Filippini. Upwind residual discretization of enhanced Boussinesq equations for wave propagation over complex bathymetries. *Journal of Computational Physics*, 271:306–341, 2014.
- [223] Gaël Loïc Richard and SL Gavriluk. Modelling turbulence generation in solitary waves on shear shallow water flows. *Journal of Fluid Mechanics*, 773:49–74, 2015.
- [224] P.J. Roache. Code Verification by the Method of Manufactured Solutions . *Journal of Fluids Engineering*, 124(1):4–10, 11 2001.
- [225] Philip L Roe. Approximate Riemann solvers, parameter vectors, and difference schemes. *Journal of computational physics*, 43(2):357–372, 1981.
- [226] Volker Roeber. Boussinesq-type model for nearshore wave processes in fringing reef environment". PhD thesis, University of Hawaii at Manoa , 2010.
- [227] Volker Roeber and Kwok Fai Cheung. Boussinesq-type model for energetic breaking waves in fringing reef environments. *Coastal Engineering*, 70:1–20, 2012.

- [228] Volker Roeber, Kwok Fai Cheung, and Marcelo H Kobayashi. Shock-capturing Boussinesq-type model for nearshore wave processes. *Coastal Engineering*, 57(4):407–423, 2010.
- [229] Andrea Saltelli. Making best use of model evaluations to compute sensitivity indices. *Computer Physics Communications*, 145(2):280–297, 2002.
- [230] Hemming A Schäffer, Per A Madsen, and Rolf Deigaard. A Boussinesq model for waves breaking in shallow water. *Coastal engineering*, 20(3-4):185–202, 1993.
- [231] François Serre. Contribution à l'étude des écoulements permanents et variables dans les canaux (Contribution to the study of steady and variable channel flows). *La Houille Blanche*, (6):830–872, 1953.
- [232] Florian Setzwein, Peter Ess, and Peter Gerlinger. High-order k-exact finite volume scheme for vertex-centered unstructured grids. In *AIAA Scitech 2020 Forum*, page 1785, 2020.
- [233] Florian Setzwein, Moritz Spraul, Peter Ess, and Peter M Gerlinger. On the structure of correction matrices for a k-exact high-order finite-volume scheme on vertex-centered unstructured grids. In *AIAA Scitech 2021 Forum*, page 1548, 2021.
- [234] Fengyan Shi, James T. Kirby, Jeffrey C. Harris, Joseph D. Geiman, and Stephan T. Grilli. A high-order adaptive time-stepping TVD solver for Boussinesq modeling of breaking waves and coastal inundation. *Ocean Modelling*, 43-44:36–51, 2012.
- [235] Fengyan Shi, James T Kirby, Babak Tehranirad, Jeffrey C Harris, and ST Grilli. FUNWAVE-TVD, fully nonlinear Boussinesq wave model with TVD solver, documentation and user's manual. *Center Appl. Coastal Res., Univ. Delaware, Newark, DE, USA, Res. Rep. No CACR-11-04*, 2:1, 2011.
- [236] Jon B Shiach and Clive G Mingham. A temporally second-order accurate Godunov-type scheme for solving the extended Boussinesq equations. *Coastal Engineering*, 56(1):32–45, 2009.
- [237] Ole R Sørensen, Hemming A Schäffer, and Lars S Sørensen. Boussinesq-type modelling using an unstructured finite element technique. *Coastal Engineering*, 50(4):181–198, 2004.
- [238] OR Sørensen, HA Schäffer, and PA Madsen. Surf zone dynamics simulated by a Boussinesq type model. III. Wave-induced horizontal nearshore circulations. *Coastal Engineering*, 33(2-3):155–176, 1998.
- [239] J. J. Stoker. *Water Waves: The Mathematical Theory with Applications*. Pure and Applied Mathematics. Interscience Publishers, New York, USA, 1957.
- [240] G. Strang. On the construction and comparison of difference schemes. *SIAM Journal on Numerical Analysis*, 5:506–517, 1968.

- [241] Ib A Svendsen. Mass flux and undertow in a surf zone. *Coastal engineering*, 8(4):347–365, 1984.
- [242] Costas Emmanuel Synolakis. The runup of solitary waves. *Journal of Fluid Mechanics*, 185:523–545, 1987.
- [243] E. Tadmor. Skew-selfadjoint form for systems of conservation laws. *J. Math. Anal. Appl.*, 103:428–442, 1984.
- [244] E. Tadmor and W. Zhong. *Energy-Preserving and Stable Approximations for the Two-Dimensional Shallow Water Equations*, pages 67–94. Springer Berlin Heidelberg, Berlin, Heidelberg, 2008.
- [245] Eitan Tadmor. The numerical viscosity of entropy stable schemes for systems of conservation laws. i. *Mathematics of Computation*, 49(179):91–103, 1987.
- [246] Benjamin Tatlock, Riccardo Briganti, Rosaria E Musumeci, and Maurizio Brocchini. An assessment of the roller approach for wave breaking in a hybrid finite-volume finite-difference Boussinesq-type model for the surf-zone. *Applied Ocean Research*, 73:160–178, 2018.
- [247] Sasan Tavakkol and Patrick Lynett. Celeris: A GPU-accelerated open source software with a Boussinesq-type wave solver for real-time interactive simulation and visualization. *Computer Physics Communications*, 217:117–127, 2017.
- [248] Sasan Tavakkol and Patrick Lynett. Celeris base: An interactive and immersive Boussinesq-type nearshore wave simulation software. *Computer Physics Communications*, 248:106966, 2020.
- [249] M Tissier, P Bonneton, F Marche, F Chazel, and D Lannes. A new approach to handle wave breaking in fully non-linear Boussinesq models. *Coastal Engineering*, 67:54–66, 2012.
- [250] Sergey Tkachenko, Sergey Gavriluk, and Jacques Massoni. Extended Lagrangian approach for the numerical study of multidimensional dispersive waves: Applications to the Serre-Green-Naghdi equations. *Journal of Computational Physics*, 477:111901, 2023.
- [251] Sergey Tkachenko, Sergey Gavriluk, and Jacques Massoni. Extended lagrangian approach for the numerical study of multidimensional dispersive waves: Applications to the serre-green-naghdi equations. *Journal of Computational Physics*, 477:111901, 2023.
- [252] Mara Tonelli and Marco Petti. Hybrid finite volume–finite difference scheme for 2DH improved Boussinesq equations. *Coastal Engineering*, 56(5):609–620, 2009.
- [253] Mara Tonelli and Marco Petti. Finite volume scheme for the solution of 2D extended Boussinesq equations in the surf zone. *Ocean Engineering*, 37(7):567–582, 2010.

- [254] Mara Tonelli and Marco Petti. Simulation of wave breaking over complex bathymetries by a Boussinesq model. *Journal of Hydraulic Research*, 49(4):473–486, 2011.
- [255] Mara Tonelli and Marco Petti. Shock-capturing Boussinesq model for irregular wave propagation. *Coastal Engineering*, 61:8–19, 2012.
- [256] Eleuterio Francisco Toro et al. *Shock-capturing methods for free-surface shallow flows*. Wiley and Sons Ltd., 2001.
- [257] Andreas Treske. Undular bores (Favre-waves) in open channels–Experimental studies. *Journal of Hydraulic Research*, 32(3):355–370, 1994.
- [258] D Violeau, R Ata, M Benoit, A Joly, S Abadie, L Clous, M Martin Medina, D Morichon, J Chicheportiche, M Le Gal, et al. A database of validation cases for tsunami numerical modelling. In *Sustainable Hydraulics in the Era of Global Change: Proceedings of the 4th IAHR Europe Congress (Liege, Belgium, 27-29 July 2016)*, page 377. CRC Press, 2016.
- [259] Damien Violeau. Serre equations in channels and rivers of arbitrary cross section. *Journal of Hydraulic Engineering*, 149(7):04023021, 2023.
- [260] Claudio Viotti, Francesco Carbone, and Frédéric Dias. Conditions for extreme wave runup on a vertical barrier by nonlinear dispersion. *Journal of Fluid Mechanics*, 748:768–788, 2014.
- [261] Antonino Viviano, Rosaria E Musumeci, and Enrico Foti. A nonlinear rotational, quasi-2DH, numerical model for spilling wave propagation. *Applied Mathematical Modelling*, 39(3-4):1099–1118, 2015.
- [262] Mark Walkley and Martin Berzins. A finite element method for the two-dimensional extended Boussinesq equations. *International Journal for Numerical Methods in Fluids*, 39(10):865–885, 2002.
- [263] Qian Wang, Yu-Xin Ren, and Wanai Li. Compact high order finite volume method on unstructured grids II: extension to two-dimensional Euler equations. *Journal of Computational Physics*, 314:883–908, 2016.
- [264] Qian Wang, Yu-Xin Ren, Jianhua Pan, and Wanai Li. Compact high order finite volume method on unstructured grids III: Variational reconstruction. *Journal of Computational physics*, 337:1–26, 2017.
- [265] Z.J. Wang. Spectral (finite) volume method for conservation laws on unstructured grids. basic formulation: Basic formulation. *Journal of Computational Physics*, 178(1):210–251, 2002.
- [266] R.F Warming and B.J Hyett. The modified equation approach to the stability and accuracy analysis of finite-difference methods. *Journal of Computational Physics*, 14(2):159–179, 1974.

- [267] N.P. Waterson and H. Deconinck. Design principles for bounded higher-order convection schemes ? a unified approach. *J.Comput.Phys.*, 224(1):182 – 207, 2007.
- [268] G. Wei, J. T. Kirby, and A. Sinha. Generation of waves in Boussinesq models using a source function approach. *Coastal Eng.*, 36:271, 1999.
- [269] Ge Wei and James T Kirby. Time-dependent numerical code for extended Boussinesq equations. *Journal of waterway, port, coastal, and ocean engineering*, 121(5):251–261, 1995.
- [270] Ge Wei, James T Kirby, Stephan T Grilli, and Ravishankar Subramanya. A fully nonlinear Boussinesq model for surface waves. Part 1. Highly nonlinear unsteady waves. *Journal of Fluid Mechanics* , 294:71–92, 1995.
- [271] Ge Wei and James Thornton Kirby. *A coastal processes model based on time-domain Boussinesq equations*. Center for Applied Coastal Research, Department of Civil Engineering ... , 1996.
- [272] Robert W Whalin. The limit of applicability of linear wave refraction theory in a convergence zone. Technical report, Army Engineer Waterways Experiment Station Vicksburg Miss, 1971.
- [273] N. Wintermeyer, A.R. Winters, G.J. Gassner, and D.A. Kopriva. An entropy stable nodal discontinuous Galerkin method for the two dimensional shallow water equations on unstructured curvilinear meshes with discontinuous bathymetry. *Journal of Computational Physics*, 340:200 – 242, 2017.
- [274] Y. Xing, X. Zhang, and C.-W. Shu. Positivity-preserving high order well-balanced discontinuous Galerkin methods for the shallow water equations. *Advances in Water Resources*, 33(12):1476 – 1493, 2010.
- [275] JA Zelt. The run-up of nonbreaking and breaking solitary waves. *Coastal Engineering*, 15(3):205–246, 1991.
- [276] X. Zhang, Y. Xia, and C.-W. Shu. Maximum-principle-satisfying and positivity-preserving high order discontinuous Galerkin schemes for conservation laws on triangular meshes. *Journal of Scientific Computing*, (50):29–62, 2012.
- [277] Yao Zhang, Andrew B Kennedy, Aaron S Donahue, Joannes J Westerink, Nishant Panda, and Clint Dawson. Rotational surf zone modeling for $O(\mu^4)$ Boussinesq–Green–Naghdi systems. *Ocean Modelling*, 79:43–53, 2014.
- [278] Yu-Si Zhang, Yu-Xin Ren, and Qian Wang. Compact high order finite volume method on unstructured grids IV: Explicit multi-step reconstruction schemes on compact stencil. *Journal of Computational Physics*, 396:161–192, 2019.